Karlsruher Institut für Technologie

Institut für Mikro- und Nanoelektronische Systeme

Development, modeling, deployment, and K_u band operation of microwave SQUID multiplexers for microcalorimeter readout

Zur Erlangung des akademischen Grades eines
DOKTORS DER NATURWISSENSCHAFTEN
von der KIT-Fakultät für Physik des
Karlsruher Instituts für Technologie (KIT)

angenommene

DISSERTATION

von

M.Sc. Martin Neidig
aus Schwetzingen

Tag der mündlichen Prüfung:	08.05.2026
Referent:	Prof. Dr. Sebastian Kempf
Korreferent:	Prof. Dr. Reinhold Kleiner

Abstract

Superconducting microcalorimeters are cryogenic particle detectors offering excellent energy resolution and near-unity quantum efficiency. Advances in fabrication enable large detector arrays, creating the need for suitable multiplexed readout techniques. Microwave SQUID multiplexing (µMUXing) is the state-of-the-art approach, but its present performance often limits applications, making it of utmost importance to understand and mitigate existing limitations. In this respect, we show how microwave losses in the µMUX dc circuitry reduce the intrinsic quality factor and thereby µMUX noise performance and provide a quantitative description of how different dc loads affect µMUX characteristics. Moreover, we deployed the first full-fledged µMUX system for magnetic microcalorimeters, demonstrating full functionality with a mean noise level of $1.4\,\mu\Phi_0/\sqrt{\mathrm{Hz}}$ and improving former systems by 44 %. To further optimize future µMUX designs, we developed a numerical model describing µMUX characteristics and performance for the entire parameter range of non-hysteretic rf-SQUIDs, accepting arbitrary current-phase relations of the Josephson junctions. This allows us to quantify the effects of tunnel barrier inhomogeneities, which are similar but distinct from those of an increased screening parameter, making them essential to accurate µMUX characterization. Finally, we demonstrate a novel approach operating a µMUX in the $\mathrm{K_u}$ band, enabling lower noise, better time resolution, higher multiplexing factor, and smaller device footprint. These devices are feasible, agree well with our models, and achieve dimensions smaller than typical microcalorimeter absorbers. In addition, they demonstrate open-loop readout noise as low as $0.27\,\mu\Phi_0/\sqrt{\mathrm{Hz}}$, comparable to levels otherwise attained only with kinetic-inductance traveling-wave parametric amplifiers in the cryogenic readout chain.

Kurzfassung

Supraleitende Mikrokalorimeter sind kryogene Teilchendetektoren, die eine hervorragende Energieauflösung und nahezu 100 % Quanteneffizienz bieten. Fortschritte in der Fertigung ermöglichen große Detektorarrays, wodurch geeignete Multiplex-Auslesetechniken erforderlich werden. Mikrowellen-SQUID-Multiplexing (µMUXing) stellt den aktuellen Stand der Technik dar, aber sein Rauschverhalten schränkt die Anwendungsmöglichkeiten oft ein, sodass es von größter Bedeutung ist, die bestehenden Einschränkungen zu verstehen und zu mindern. In diesem Zusammenhang zeigen wir, wie Mikrowellenverluste in der µMUX-Gleichstromschaltung den intrinsischen Qualitätsfaktor und damit das Rauschverhalten des µMUX verschlechtern, und liefern eine quantitative Beschreibung, wie sich unterschiedliche Gleichstromlasten auf die Eigenschaften des µMUX auswirken. Darüber hinaus haben wir das erste vollwertige µMUX-System für magnetische Mikrokalorimeter eingesetzt, dessen volle Funktionsfähigkeit mit einem mittleren Rauschpegel von $1.4\,\mu\Phi_0/\sqrt{\mathrm{Hz}}$ nachgewiesen wurde, was einer Verbesserung um 44 % gegenüber früheren Systemen entspricht. Um zukünftige µMUX-Designs weiter zu optimieren, haben wir ein numerisches Modell entwickelt, das die Eigenschaften und die Leistung von µMUX für den gesamten Parameterbereich von nicht-hysteresen rf-SQUIDs beschreibt und beliebige Strom-Phasen-Relationen der Josephson-Kontakte akzeptiert. Dies ermöglicht es uns, die Auswirkungen von Inhomogenitäten der Tunnelbarriere zu quantifizieren. Diese ähneln denen eines erhöhten Abschirmungsparameters, unterscheiden sich jedoch und sind daher für eine genaue µMUX-Charakterisierung entscheidend. Schließlich demonstrieren wir einen neuartigen Ansatz für den Betrieb eines µMUX im K_u-Band, der ein geringeres Rauschen, höhere Zeitauflösung, größere Multiplexfaktoren und kleinere Geräteabmessungen ermöglicht. Diese Geräte sind realisierbar, stimmen gut mit unseren Modellen überein und erreichen Abmessungen, die kleiner sind als typische Mikrokalorimeterabsorber. Darüber hinaus weisen sie ein Open-Loop-Ausleserauschen von nur $0.27\,\mu\Phi_0/\sqrt{\mathrm{Hz}}$ auf, was mit Werten vergleichbar ist, die sonst nur mit kinetisch-induktiven Wanderwellen-Verstärkern in der kryogenen Auslesekette erreicht werden.

Contents

1. Introduction

Progress in modern physics increasingly relies on the precise measurement of extremely small energy deposits. Probing rare processes or resolving subtle spectral features requires detectors that combine sub-electronvolt energy resolution with near-unity quantum efficiency. Superconducting microcalorimeters are cryogenic, energy-dispersive single particle detectors that represent one of the most advanced detector technologies developed to meet these demands.

A superconducting microcalorimeter is operated at millikelvin temperatures and generally consists of a particle absorber that is thermally coupled to a temperature sensor, which is weakly coupled to a thermal heat bath. The energy of an incident particle is absorbed and converted into a temperature rise of the detector. By monitoring the detector's temperature rise, the energy deposited by the particle can be determined. Thermalization of the entire system is guaranteed by a weak thermal link to a heat bath.

Microcalorimeters are classified by the type of temperature sensor employed. The most mature ones are superconducting transition-edge sensors (TESs) [Irw05, Ull15] and magnetic microcalorimeters (MMCs) [Fle05, Kem18]. TESs utilize the strong temperature dependence of the electrical resistivity of a superconducting film biased within its transition region, while MMCs utilize the temperature dependence of the magnetization of a paramagnetic material placed in a weak external magnetic field. In both cases, the temperature change is ultimately converted into a change in current or magnetic flux, which can be read out using a superconducting quantum interference device (SQUID) [Fag06].

The combination of outstanding energy resolution, fast signal rise time, almost ideal linearity, and near-unity quantum efficiency makes these microcalorimeters an excellent choice for a broad range of applications. These include neutrino mass determination [Gas17, Alp25, Kov25], dark matter searches [Rot18, Kro23], cosmic microwave background polarization measurements [Ham24, Man25], radionuclide metrology [Fit21, Mül24], searches for neutrinoless double beta decay [Kim23, Agr25], and nuclear safeguards [Cro12, Kim18], among others. Moreover, latest advances in modern micro- and nanofabrication technologies enable the realization of TES and MMC arrays of virtually any size, facilitating future experiments that require high statistics or angular resolution.

A small number of detectors can be read out individually using two-stage dc-SQUIDs [Dru07], which amplify the current signal of a front-end sensing SQUID, employing a SQUID array operated as a highly sensitive low-noise amplifier. However, this approach becomes infeasible for large arrays comprising hundreds or even thousands of detectors due to the linear increase in system cost and complexity, as

well as the parasitic heat load on the millikelvin temperature experiment platform, caused by the readout wiring and SQUID Joule power dissipation. To address these challenges, suitable SQUID-based multiplexing schemes are developed to read out multiple detector channels through a single broadband readout line [Irw09, Aka23].

Several SQUID-based multiplexing approaches have been demonstrated, including time-division [Che99, Dor06], code-division [Nie10, Irw10], and frequency-division multiplexing in the megahertz [Yoo01, Ric21a] and gigahertz regimes [Irw04, Mat08, Kem17a]. The latter, referred to as microwave SQUID multiplexing (µMUXing), represents the current state of the art [Koh14, Dob21, Ric23, Sch25]. Due to its high multiplexing factors, low on-chip power dissipation, and large bandwidth per readout channel, µMUXing, along with hybrid multiplexing schemes [Ben19, Sch22] built upon it, is widely regarded as the most promising approach for scaling microcalorimeter arrays towards megapixel arrays.

In µMUX readout, each detector is inductively coupled to an unshunted, non-hysteretic rf-SQUID, which is in turn coupled to a superconducting microwave resonator capacitively connected to a common transmission line. A detector signal modifies the magnetic flux threading the rf-SQUID and thereby its effective inductance. This inductance change shifts the resonance frequency of the coupled resonator. The signal is encoded as a resonance frequency shift and can be detected by applying a probe tone close to resonance and monitoring the transmitted amplitude or phase. By assigning distinct resonance frequencies to multiple resonators, all coupled to the same transmission line, hundreds or thousands of channels can be read out simultaneously.

Although µMUX has enabled the simultaneous readout of hundreds of detectors [Kem17a, Szy23], its noise performance remains approximately an order of magnitude inferior to that of optimized two-stage SQUID systems [Ric23, Man21], currently limiting the achievable energy resolution for MMC readout. Numerical simulations predict a substantially lower theoretical noise floor [Sch23b], indicating that state-of-the-art µMUX are not yet fundamentally limited. A key parameter affecting noise performance is the resonance depth [Hir13, Koh14, Ric23], which is directly linked to microwave losses within the individual µMUX channels. These losses typically exceed those of bare superconducting resonators by about an order of magnitude [Dob21, Ric23], suggesting the presence of additional dominant loss mechanisms. A detailed understanding of these mechanisms is therefore essential for further noise performance improvements. In this thesis, we investigate the losses introduced by integrating the rf-SQUID into the resonator and by coupling the microcalorimeter to the µMUX input coil, with the aim of identifying and mitigating the dominant contributions.

Beyond resonance depth, µMUX noise performance depends sensitively on the chosen design parameters and on the power and frequency of the applied probe tone. Optimization presently relies on numerical simulation frameworks [Sch23b, Red24] based on an analytical model [Weg22] describing the probe tone power-dependence arising from the nonlinear current-flux relation of the rf-SQUID. While this model accurately repro-

duces the behavior of many µMUX devices, its validity is restricted to a small parameter range, which has constrained parameter optimization within simulation-frameworks. In this thesis, we present an extended µMUX model that overcomes this limitation and provides a power-dependent description for the full parameter range of µMUX. The model further allows for arbitrary current-phase relations of the Josephson junctions, enabling, for the first time, the systematic investigation of junction inhomogeneities and their impact on µMUX performance.

In parallel to design optimization, several approaches have been pursued to improve µMUX noise performance. These include the use of kinetic-inductance traveling-wave parametric amplifiers (KITWPAs) as the first cryogenic amplification stage [Mal23] and tone-tracking readout schemes [Ker18, Yu23]. While both approaches offer significant potential, they introduce additional major technical challenges, such as elaborate biasing networks, limited saturation power, and demanding requirements for room temperature control electronics. In this thesis, we explore a complementary strategy based on increasing the µMUX operating frequency beyond the established 4–8 GHz range and enlarging the channel bandwidth. Operation at higher frequencies enables reduced readout noise, increased multiplexing factors, improved time resolution, and smaller device dimensions. The latter facilitates the realization of densely packed arrays with full focal-plane coverage without complex multilayer wiring schemes [Tol16, Ste19]. We demonstrate the feasibility of µMUX devices operating in the K_u band (12–18 GHz), achieving device dimensions smaller than a typical microcalorimeter absorber, and show that their behavior is well described by our µMUX models. First noise measurements demonstrate that their noise performance is comparable to that achieved with KITWPAs as the first-stage cryogenic amplifier.

In chapter 2, we introduce the theory of µMUXing. We describe the two types of microwave resonators employed in this work and summarize the essential properties of non-hysteretic rf-SQUIDs. Building on these elements, we present the operating principle of µMUX, analyze the relevant noise contributions, introduce flux-ramp modulation for linearization, and outline the room-temperature electronics used for tone generation and signal demodulation. Finally, we discuss the limitations of state-of-the-art µMUX devices and how increasing the µMUX operation frequency could overcome many of these limitations.

In chapter 3, we detail the infrastructure, design methodology, and fabrication processes developed in this thesis, enabling the development of µMUX devices. We describe the simulations performed as the basis for our microwave resonator design, as well as the simulations to adapt the rf-SQUID layout for µMUX channels with almost arbitrary design parameters. The µMUX chip architecture and the established microfabrication process are presented in detail. We further introduce the sample housing designed for mounting our µMUX chips in a dilution refrigerator and the cryogenic readout chain implemented for µMUX characterization measurements at millikelvin temperatures. The chapter concludes with a description of the measurement setups and the key data analysis algorithms used throughout this work.

In chapter 4, we analyze the loss mechanisms that presently limit the intrinsic quality factor of µMUX channels. We first consider the fundamental losses of a superconducting microwave resonator and then examine additional losses introduced by the coupled rf SQUID. Measurements demonstrate that rf-SQUID integration gives rise to dominant loss contributions that exceed those of the bare resonator. In particular, we provide a quantitative description of the flux-dependent losses introduced by a filter resistor in the rf SQUID input coil and verify this model experimentally. We further investigate how different loads applied to the µMUX input circuitry modify the resonance depth. Based on these studies, we develop a model describing the influence of filter resistors and arbitrary input load impedances on the resonance characteristics. The model shows that the input circuitry does not merely reduce resonance depth but can substantially alter the overall µMUX behavior.

In chapter 5, we present measurements performed with a state-of-the-art full-fledged µMUX readout system for MMCs that enables, for the first time, the simultaneous readout of up to 400 channels. We describe in detail the software-defined radio platform used for probe-tone generation and signal decoding, as well as the custom µMUX chip and the cryogenic measurement setup developed for these measurements. We confirm that the system is fully functional and demonstrate record-low noise levels in µMUX-based MMC readout.

In chapter 6, we present our advanced model for the µMUX power-dependence. After discussing the limitations of the established analytical model, we detail how our numerical approach extends its range of validity and enables accurate modeling for the full parameter range of non-hysteretic rf-SQUIDs. The superiority of the numerical model is demonstrated through its application to a µMUX device with an extreme parameter set. Furthermore, the model allows for the incorporation of arbitrary current-phase relations for the Josephson junctions of the rf-SQUID. This capability enables a systematic treatment of inhomogeneous tunnel barriers and their impact on µMUX characteristics. We show that accounting for such inhomogeneities is essential for accurate modeling and characterization.

In chapter 7, we show how our µMUX models and the simulations based on them predict improved noise performance for devices operated at elevated resonance frequencies and increased channel bandwidths. We describe the design iterations that resulted in the first µMUX devices operating in the K_u band, a development that required a complete redesign of the coupled rf-SQUIDs. Based on this new rf-SQUID design, we realized two K_u-band µMUX implementations: one employing $\lambda/4$-resonators and one based on lumped-element resonators. We demonstrate the full functionality of both designs and confirm that their behavior is accurately captured by our µMUX models, thereby establishing the feasibility of µMUX operation in the K_u frequency band. Finally, we present open-loop noise measurements of one device and obtain noise levels otherwise only achieved with the inclusion of KITWPAs in the cryogenic readout chain. These results verify that practical µMUX systems operating at elevated resonance frequencies can indeed improve readout noise performance compared to state-of-the-art devices.

2. Basics of microwave SQUID multiplexing

Recent advances in micro- and nanofabrication of state-of-the-art cryogenic microcalorimeters have enabled the realization of large-scale detector arrays of virtually arbitrary size, allowing for next-generation experiments that require high statistics, imaging capabilities, or spatial resolution. The readout of such large arrays, however, remains challenging and is the subject of ongoing research [Man21, Aka23, Ric23]. Single cryogenic microcalorimeters or small-scale detector arrays are typically read out using two-stage dc superconducting quantum interference device (SQUID) setups [Fag06, Dru07]. However, this approach does not scale to large channel counts, as it requires dedicated wiring and readout electronics for each detector channel. The resulting large number of wires rapidly increases system complexity and, because they connect the low-temperature stage to room-temperature electronics, introduces a significant heat load. This heat load, together with the power dissipation of 1 nW to 10 nW per SQUID array, can, especially for MMC based experiments, degrade detector performance [Kra24] and may even exceed the typical dilution refrigerator cooling power of approximately 10 µW at 10 mK. Additionally, the high cost and power consumption of room-temperature electronics can impose further limitations, especially for TES based satellite experiments.

Consequently, multiplexing techniques are required that ideally use a single set of room-temperature electronics to read out multiple detectors, while minimizing the number of connections to the low-temperature stage. A variety of SQUID-based multiplexing schemes have been demonstrated, including time-division multiplexing [Che99, Dor16], code-division multiplexing [Nie10, Irw10], frequency-division multiplexing in the MHz [Yoo01, Ric21a] or GHz [Irw04, Mat08, Kem17a] regimes, and hybrid multiplexing schemes [Ben19, Sch22]. Frequency-division multiplexing in the GHz regime is referred to as microwave SQUID multiplexing (µMUXing) [Irw04, Mat08, Kem17a] and represents the current state of the art, offering a high multiplexing factor, low on-chip power dissipation, and a large bandwidth per readout channel. Today, µMUXs employ rf-SQUIDs to read out detector signals, resulting in a low power dissipation per channel of only a few picowatts. Each channel signal is frequency-encoded using a superconducting microwave resonator coupled to a broadband transmission line, enabling the readout of hundreds to thousands of detectors through a single readout line.

In this chapter, we present the theoretical background of the two essential building blocks of microwave SQUID multiplexers: the superconducting microwave resonator and the non-hysteretic rf-SQUID. Based on these components, we explain the operating principle of the µMUX and introduce state-of-the-art models that describe its behavior as a function of readout power, magnetic flux bias, and device parameters. We then introduce flux-ramp modulation to linearize the SQUID response and explain the working principle of the software-defined radio used to operate a µMUX system. Finally, we discuss the limitations of current µMUX devices and present novel µMUXing concepts that promise to overcome these limitations.

2.1 Microwave properties of superconductors

One of the two integral components of a µMUX is the superconducting microwave resonators. In this section, we introduce the microwave properties of superconductors and introduce superconducting coplanar waveguides as the selected transmission line type for the µMUX designs discussed in this thesis. Finally, we discuss the two types of resonators used in this thesis: the $\lambda/4$ transmission line resonator and the lumped-element LC resonator, both of which are capacitively coupled to a transmission line and terminated by a load inductor, connecting them to ground.

2.1.1 Superconductors at microwave frequencies

The BCS theory describes the macroscopic effects of superconductivity at a microscopic level [Bar57]. Two electrons at the Fermi surface can interact weakly and attractively through the virtual phonon exchange, forming a Cooper pair. Breaking a Cooper pair requires a minimum energy of 2Δ, where Δ is the superconducting energy gap. This pair-breaking energy decreases with increasing temperature T, reaching zero at the critical temperature T_c of the superconductor. The related temperature dependence of the energy gap $\Delta(T)$ can be derived from the expression [Bar57]

$$\frac{1}{N(0)\mathcal{V}} = \int_0^{\hbar\omega_\mathrm{D}} \tanh\left(\frac{\sqrt{\epsilon^2+\Delta^2(T)}}{2k_\mathrm{B}T}\right)\frac{\mathrm{d}\epsilon}{\sqrt{\epsilon^2+\Delta^2(T)}}, \tag{2.1}$$

where ω_D denotes the Debye frequency, $\hbar$ the reduced Planck constant, k_B represents the Boltzmann constant, and $N(0)\mathcal{V}$ the BCS coupling constant, comprising $\mathcal{V}$, the strength of the attractive phonon-mediated interaction, and $N(0)$ the density of states at the Fermi level. The coupling constant can be calculated by evaluating equation 2.1 at the critical temperature T_c, where the energy gap vanishes:

$$\frac{1}{N(0)\mathcal{V}} = \int_0^{\hbar\omega_\mathrm{D}} \tanh\left(\frac{\epsilon}{2k_\mathrm{B}T_\mathrm{c}}\right)\frac{\mathrm{d}\epsilon}{\epsilon}. \tag{2.2}$$

While dc currents in a superconductor below T_c are carried entirely by Cooper pairs, resulting in zero dc resistance, ac currents with an angular frequency ω experience a finite surface impedance $Z_\mathrm{s} = R_\mathrm{s} + i\omega L_\mathrm{s}$ [Mat58], which consists of the surface resistance R_s and surface inductance L_s.

The surface resistance R_s arises from quasiparticles in the superconductor, which are accelerated by the applied alternating electric fields. These quasiparticles are subject to the same scattering mechanisms as conduction electrons, leading to ohmic losses. Cooper pairs do not scatter, causing them to continue building momentum and storing kinetic energy when an electric field is applied. The Cooper pairs cannot change their

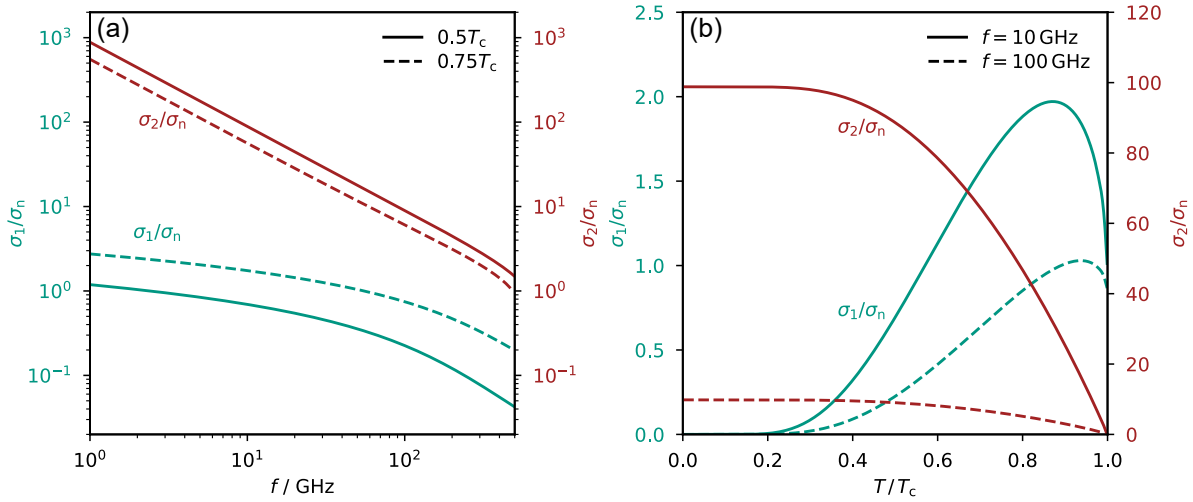

Fig. 2.1: Complex conductivity as a function of (a) frequency and (b) temperature. The curves were calculated using equations 2.1 to 2.5 for a 100 nm thick niobium thin film with a critical temperature of $T_c = 8.6\,\mathrm{K}$, which is the typical material and film thickness used for the resonators through out this thesis.

momentum instantaneously when the electric field is changed, resulting in a kinetic inductance L_{kin}. Together with the magnetic inductance L_{m}, which depends on the geometrical arrangement of the superconducting structure, this results in the total surface inductance $L_{\mathrm{s}} = L_{\mathrm{m}} + L_{\mathrm{kin}}$. The quasiparticle density decreases exponentially with temperature, resulting in negligible ohmic losses at temperatures far below the critical temperature, i.e. $T \ll T_c$, and the surface impedance Z_{s} is dominated by the surface inductance L_{s}. This enables the development of superconducting resonators that exhibit very low losses.

The surface impedance can be derived from the complex conductivity of the superconductor,

$$\sigma_{\mathrm{S}}(\omega,T) = \sigma_1(\omega,T) - i\sigma_2(\omega,T), \tag{2.3}$$

that depends on temperature and angular frequency $\omega = 2\pi f$ [Glo57]. The real and imaginary part of σ_{S} can be derived using the Mattis-Bardeen theory [Mat58]. For low angular frequencies $\omega < 2\Delta(T)/\hbar$, where a single photon does not possess the required energy to break Cooper pairs, these quantities can be calculated with

$$\frac{\sigma_1}{\sigma_{\mathrm{n}}} = \frac{2}{\hbar\omega} \int_{\Delta(T)}^{\infty} \frac{[f(\epsilon) - f(\epsilon - \hbar\omega)][\epsilon^2 + \Delta^2(T) + \hbar\omega\epsilon]}{\sqrt{\epsilon^2 - \Delta^2(T)}\sqrt{[\epsilon + \hbar\omega]^2 - \Delta^2(T)}} \mathrm{d}\epsilon \tag{2.4}$$

$$\frac{\sigma_2}{\sigma_{\mathrm{n}}} = \frac{1}{\hbar\omega} \int_{\Delta(T)-\hbar\omega}^{\Delta(T)} \frac{[1 - 2f(\epsilon - \hbar\omega)][\epsilon^2 + \Delta^2(T) + \hbar\omega\epsilon]}{\sqrt{\Delta^2(T) - \epsilon^2}\sqrt{[\epsilon + \hbar\omega]^2 - \Delta^2(T)}} \mathrm{d}\epsilon \tag{2.5}$$

where $f(\epsilon) = [1 + \exp(\epsilon/k_{\mathrm{B}}T)]^{-1}$ denotes the Fermi-Dirac distribution. Both parts are depicted in figure 2.1 as a function of temperature and frequency.

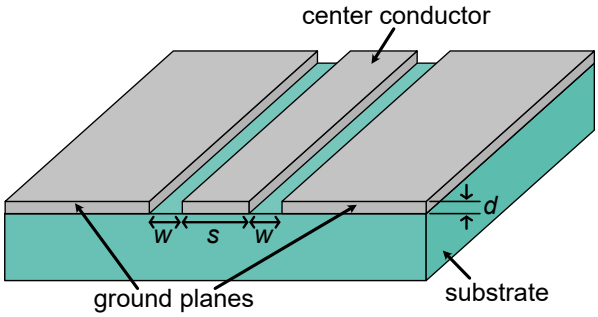

Fig. 2.2: Schematic illustration of a coplanar waveguide. The center conductor and ground planes are depicted in gray and are part of the same metal layer with thickness d. The metal layer is placed onto an infinitely thick dielectric substrate with permittivity ϵ_r.

The expression relating the equations 2.4 and 2.5 with the surface impedance depends on the characteristic lengths of the superconductor used. The superconducting niobium thin films used through out this thesis can be described in the local dirty limit, where the electron mean free path l_e is much smaller than the coherence length ξ_0 as well as the magnetic penetration depth λ. In this limit, the surface impedance of a film with thickness d can be expressed as [Kau78]

$$Z_\mathrm{s} = \sqrt{\frac{i\omega\mu_0}{\sigma_\mathrm{S}(\omega,T)}}\coth\left(d\sqrt{i\omega\mu_0\sigma_\mathrm{S}(\omega,T)}\right), \tag{2.6}$$

where μ_0 denotes the vacuum permeability. In the limit of temperatures far below the critical temperature, i.e. $T \ll T_\mathrm{c}$, we obtain $\sigma_2 \gg \sigma_1$, and equation 2.6 can be simplified to [Bar09]

$$R_\mathrm{s} = \mu_0\omega\lambda_\mathrm{eff}\beta\frac{\sigma_1}{2\sigma_2} \tag{2.7}$$

$$L_\mathrm{s} = \mu_0\lambda_\mathrm{eff}. \tag{2.8}$$

Here, the parameter $\beta = 1 + \frac{2d/\lambda}{\sinh(2d/\lambda)}$ accounts for the film thickness d and the effective magnetic penetration depth $\lambda_\mathrm{eff} = \lambda\coth(d/\lambda)$ given through

$$\lambda = \sqrt{\frac{1}{\mu_0\omega\sigma_2}}. \tag{2.9}$$

Using the relations presented in this section, we can numerically calculate the surface impedance of our superconducting thin films, depending on temperature, frequency, and film thickness, if the quantities ω_D, T_c, and σ_n are known.

2.1.2 Superconducting coplanar waveguides

The transmission line type used throughout this thesis is the coplanar waveguide (CPW), as schematically depicted in figure 2.2. Many different types of CPWs exist, which are discussed in detail in [Sim01]. Here, we will only introduce the conventional CPW on a single layer substrate. It consists of a center conductor with width s, which is surrounded on both sides by ground planes, separated by a slot width w. The

conductor and ground planes are placed on a dielectric substrate with permittivity ϵ_r. An electromagnetic wave traveling along the CPW is described by a quasi-transverse electromagnetic mode (quasi-TEM), which is defined by field vectors $\boldsymbol{E}$ and $\boldsymbol{B}$ for the electric and magnetic fields, which are approximately transverse to the wave vector $\boldsymbol{k}$ and orthogonal to each other.

The characteristic impedance Z_0 of the ideal CPW is defined solely by the ratio $k = s/(s+2w)$ and the substrate's permittivity ϵ_r, allowing for the combination of transmission lines of virtually any width on the same substrate without altering Z_0. Since a CPW comprises only a single metal layer, fabrication is simple, and shunts to ground are easy to realize, requiring no via holes through the substrate [Sim01].

The CPW has a magnetic inductance per unit length L'_m and a capacitance per unit length C', both of which can be calculated using conformal mapping techniques. In the case of an infinitely thin metal layer, wide ground planes, and a thick substrate, this results in [Sim01]

$$L'_\mathrm{m} = \frac{\mu_0}{4}\frac{\mathrm{K}(k')}{\mathrm{K}(k)} \tag{2.10}$$

$$C' = 4\epsilon_0\epsilon_\mathrm{r,eff}\frac{\mathrm{K}(k)}{\mathrm{K}(k')}, \tag{2.11}$$

where ϵ_0 denotes the vacuum permittivity and $\mathrm{K}(x)$ is the complete elliptic integral of the first kind. The parameters $k = s/(s+2w)$ and $k' = \sqrt{1-k^2}$ take the CPW geometry into account, and the effective permittivity $\epsilon_\mathrm{r,eff} \approx (\epsilon_\mathrm{r}+1)/2$ accounts for the fact that only half of the space around the CPW is filled with the dielectric substrate.

The total inductance per unit length $L' = L'_\mathrm{m} + L'_\mathrm{kin}$ consists of an additional kinetic inductance component $L'_\mathrm{kin} = (g_\mathrm{c} + g_\mathrm{s})L_\mathrm{g}$ [Gao08a], which comprises a contribution g_c by the center conductor and g_g by the ground planes. In the case of a thin metal layer with a thickness of $d < 0.05s$ and $k < 0.8$, these contributions can be approximated as [Col00]

$$g_\mathrm{c} = \frac{1}{4s(1-k^2)\mathrm{K}(k)^2}\left[\pi + \ln\left(4\pi\frac{s}{d}\right) - k\ln\left(\frac{1+k}{1-k}\right)\right] \tag{2.12}$$

$$g_\mathrm{g} = \frac{1}{4s(1-k^2)\mathrm{K}(k)^2}\left[\pi + \ln\left(4\pi\frac{s+2w}{d}\right) - \frac{1}{k}\ln\left(\frac{1+k}{1-k}\right)\right]. \tag{2.13}$$

With the total inductance and capacitance per unit length, we can finally determine the characteristic impedance Z_0 and the phase velocity v_p along the CPW:

$$Z_0 = \sqrt{\frac{L'}{C'}} \tag{2.14}$$

$$v_\mathrm{p} = \frac{1}{\sqrt{L'C'}} = \frac{c_0}{\sqrt{\epsilon_\mathrm{r,eff}}}. \tag{2.15}$$

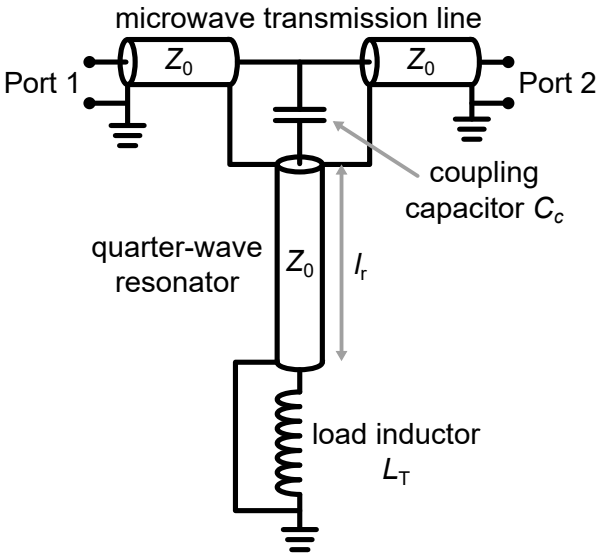

Fig. 2.3: Schematic of $\lambda/4$ resonator capacitively coupled to a microwave transmission line by a coupling capacitor C_c and terminated by a load inductor L_T. The $\lambda/4$ resonator has length of l_r and characteristic impedance Z_0, which, for simplicity, is chosen to be equivalent with the characteristic impedance of the microwave transmission line. Ground connections at ports and along the transmission line are shown explicitly in this figure but omitted in subsequent figures for clarity.

Here, c_0 denotes the speed of light in vacuum. Both quantities are essential when designing $\lambda/4$ transmission line resonators.

2.1.3 Superconducting $\lambda/4$ transmission line resonators

The most common resonator type employed for microwave SQUID multiplexers is a $\lambda/4$ transmission line resonator[1]. It consists of a transmission line of length l_r that is open at one end and connected to ground at the other. A standing wave with wavelength λ can form on the resonator if the resonance condition $l_\mathrm{r} = (2n-1)\lambda/4$ with $n \in \mathbb{N}$ is met. For the fundamental mode $n = 1$, the resonance frequency is given by

$$f_0 = \frac{v_\mathrm{p}}{4l_\mathrm{r}}, \tag{2.16}$$

where v_p represents the phase velocity on the transmission line.

The $\lambda/4$ resonators used in microwave SQUID multiplexers are coupled via a coupling capacitor C_c to a microwave transmission line and are terminated to ground by a load inductor L_T, as depicted in figure 2.3. Ground connections of the transmission lines are explicitly shown only in figure 2.3 and are omitted in all subsequent schematics for clarity. By coupling the resonator to the microwave transmission line, also referred to as the feedline, we can read out the resonator by measuring the scattering parameter S_{21} between the two ports of the feedline, resulting in a resonance curve whose bandwidth can be set by adjusting C_c. The characteristic impedance Z_0 of resonator and feedline do not have to match, however, for simplicity, they are assumed to be equivalent throughout this work. The load inductor L_T can be used to inductively couple other devices, such as an rf-SQUID, to our resonator. The total impedance Z_tot of the resonator, from the

[1] referred to in the following as $\lambda/4$ resonator

feedline to ground, is given by [Col00]

$$Z_{\mathrm{tot}} = \frac{1}{i\omega C_{\mathrm{c}}} + Z_0 \frac{i\omega L_{\mathrm{T}} + Z_0 \tanh(\gamma l_{\mathrm{r}})}{Z_0 + i\omega L_{\mathrm{T}} \tanh(\gamma l_{\mathrm{r}})}. \tag{2.17}$$

Here, $\gamma = \alpha + i\beta$ represents the propagation constant, which consists of the attenuation constant α and the phase constant $\beta = \omega/v_{\mathrm{p}}$. Using Z_{tot}, we can calculate the scattering parameter S_{21} through the feedline [Poz98]:

$$S_{21} = \frac{2}{2 + Z_0/Z_{\mathrm{tot}}}. \tag{2.18}$$

The resonance condition of the total resonator is satisfied when $\mathrm{Im}[Z_{\mathrm{tot}}] = 0$. In the limit $Z_0 \ll 1/2\pi f_0 C_{\mathrm{c}}$ and $2\pi f_0 L_{\mathrm{T}} \ll Z_0$, the resonance frequency can be calculated as [Mat11]

$$f_{\mathrm{r}} = \frac{f_0}{1 + 4f_0(C_{\mathrm{c}} Z_0 + L_{\mathrm{T}}/Z_0)}. \tag{2.19}$$

The scattering parameter around the resonance frequency, i.e. $f \approx f_{\mathrm{r}}$ can be approximated by [Maz04]

$$S_{21}(f) = \frac{S_{21}^{\mathrm{min}} + 2iQ_{\mathrm{l}}\frac{f - f_{\mathrm{r}}}{f_{\mathrm{r}}}}{1 + 2iQ_{\mathrm{l}}\frac{f - f_{\mathrm{r}}}{f_{\mathrm{r}}}}. \tag{2.20}$$

Here, $S_{21}^{\mathrm{min}} = Q_{\mathrm{l}}/Q_{\mathrm{i}}$ is the minimum of the resonance curve, or resonance depth, which occurs at the resonance frequency f_{r}. The quantities Q_{l} and Q_{i} represent the loaded and intrinsic quality factors, which are related through

$$\frac{1}{Q_{\mathrm{l}}} = \frac{1}{Q_{\mathrm{i}}} + \frac{1}{Q_{\mathrm{c}}} \tag{2.21}$$

with the coupling quality factor Q_{c}. The loaded quality factor Q_{l} is the ratio of the energy stored in the resonator to the energy lost per oscillation. Each loss mechanism can be attributed its own quality factor. The intrinsic quality factor Q_{i} represents undesired losses within the resonator, such as those caused by radiation, two-level systems, or quasiparticles, and will be discussed in more detail in chapter 4. The coupling quality factor Q_{c} describes the intentional energy loss through the coupling capacity C_{c} and is given by [Mat11]

$$Q_{\mathrm{c}} = \frac{\pi}{2Z_0^2 \omega_{\mathrm{r}}^2 C_{\mathrm{c}}^2}. \tag{2.22}$$

For superconducting microwave resonators, Q_{i} is typically much larger than Q_{c}, resulting in deep resonance curves. In this case, we can approximate $Q_{\mathrm{l}} \approx Q_{\mathrm{c}}$, which allows for the setting of the resonance bandwidth

$$\Delta f_{\mathrm{BW}} = \frac{f_{\mathrm{r}}}{Q_{\mathrm{l}}} \approx \frac{f_{\mathrm{r}}}{Q_{\mathrm{c}}} \tag{2.23}$$

through the coupling capacitor C_{c}.

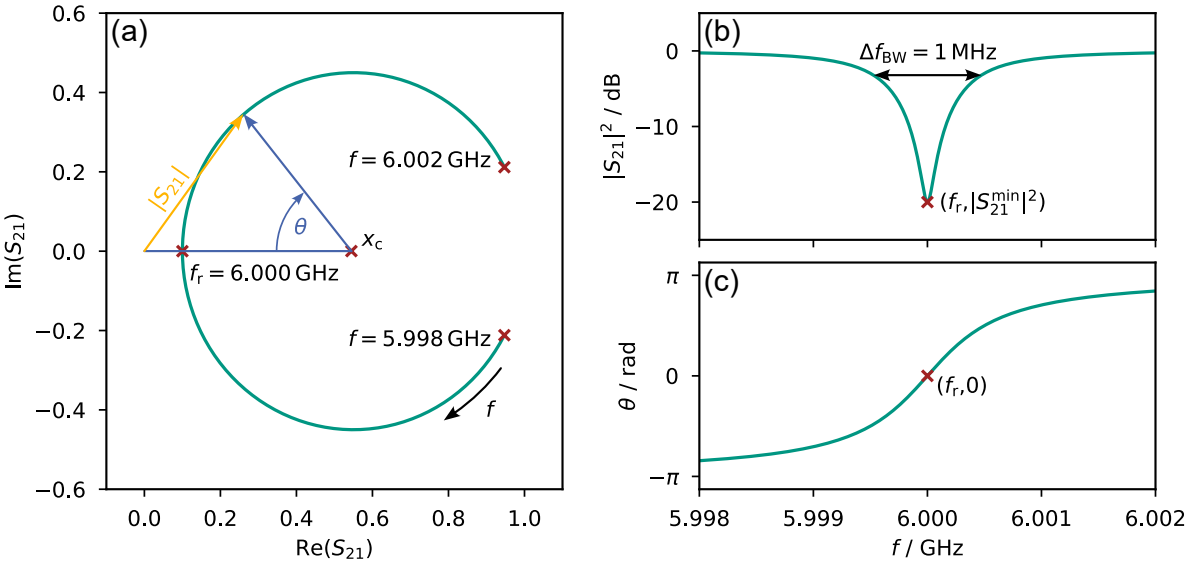

Fig. 2.4: Different representations of the scattering parameter S_{21} of a $\lambda/4$ resonator calculated from equation 2.20 with $f_\mathrm{r} = 6\,\mathrm{GHz}$, $Q_\mathrm{l} = 6000$ and $S_{21}^\mathrm{min} = 0.1$. The parameters f_r, Δf_BW and S_{21}^min characterizing the resonance curve are marked in the corresponding panel. (a) Complete representation of S_{21}. (b) Transmission parameter $|S_{21}|$ as function of frequency. (c) Phase θ as a function of frequency.

Figure 2.4 shows different representations of a resonance curve calculated using equation 2.20, with all characteristic parameters marked. In the complex plane, the resonance curve forms a circle in complex space with its center at $(x_\mathrm{c},0)$ and $x_\mathrm{c} = (1 + S_{21}^\mathrm{min})/2$. The resonator bandwidth is defined at half the resonance depth corresponding to $-3\,\mathrm{dB}$, if $S_{21}^\mathrm{min} \ll -3\,\mathrm{dB}$. The phase shown in figure 2.4(c) is calculated using $\tan(\theta) = \mathrm{Im}[S_{21}]/(x_\mathrm{c} - \mathrm{Re}[S_{21}])$ corresponding to the angle sketched in figure 2.4(a). Actual measured resonance curves deviate significantly from the curve depicted in figure 2.4, which is due to factors such as cable attenuation, cable delay, or impedance mismatch. In section 3.8.1, we will discuss how the characteristic resonator parameters can still be extracted.

For an applied microwave tone far off resonance with power P_rf, no power couples into the resonator, resulting in $|S_{21}|^2 = 1$. However, on resonance, the tone couples into the resonator, inducing a sinusoidal current with amplitude

$$I_\mathrm{T} = \sqrt{\frac{16}{\pi}\frac{Q_\mathrm{l}^2}{Q_\mathrm{c}}\frac{P_\mathrm{rf}}{Z_0}} \tag{2.24}$$

in the load inductor L_T [Kem12].

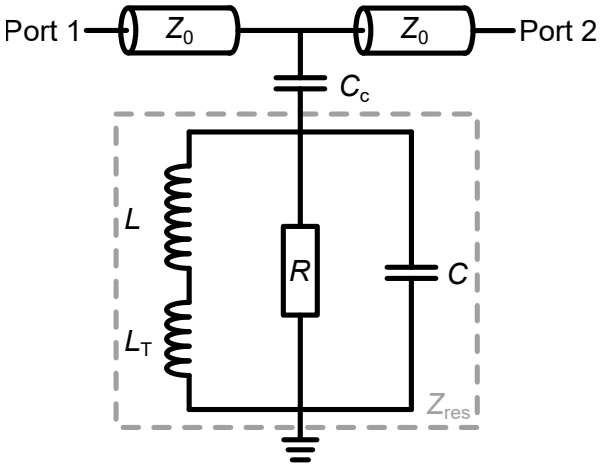

Fig. 2.5: Schematic of a lumped-element resonator coupled with a coupling capacitor C_c to a microwave transmission line with characteristic impedance Z_0. The resonator consists of parallel circuit of a capacitor C, resistance R and the inductors L and L_T, resulting in a total resonator impedance Z_{res}.

2.1.4 Superconducting lumped-element resonators

Microwave resonators based on lumped elements represent an alternative to the $\lambda/4$ resonators discussed in the previous section. Lumped-element circuits offer the advantage of significantly smaller device dimensions compared to distributed elements, as each lumped-element is inherently much smaller than the applied signal wavelength λ. Generally, this means keeping the maximum dimension l_{max} less than $\lambda/20$ [Bah03]. Additionally, lumped-element resonators exhibit no higher modes, allowing for the coupling of several resonators to the same feedline over a broad frequency range without the higher modes of lower frequency resonators interfering with the high resonance frequency resonators.

In the $\lambda/4$ resonator, the coupling capacitor C_c and the load inductor L_T are already implemented with lumped-elements. The lumped-element resonator also replaces the $\lambda/4$ transmission line with a parallel circuit of lumped-elements, as depicted in figure 2.5. The inductance of the resonator $L + L_T$ is connected in parallel with the capacitance of the resonator C. The resistance R is not implemented as a physical element, but rather signifies losses in the resonator.

In the case of the lumped-element resonator, the total impedance Z_{tot} of the resonator is given by

$$Z_{tot} = \frac{1}{i\omega C_c} + \left(\frac{1}{R} + i\omega C + \frac{1}{i\omega(L + L_T)} \right)^{-1}. \tag{2.25}$$

By solving $\mathrm{Im}(Z_{tot}(\omega_r)) = 0$, we can derive the resonance frequency $f_{r,0}$ [Poz98]

$$f_{r,0} = \frac{1}{2\pi\sqrt{(L + L_T)(C + C_c)}}. \tag{2.26}$$

The resonance curve of the lumped-element resonator can also be calculated with equa-

tion 2.20. However, the quality factors are given by [Poz98, Ahr22]

$$Q_\mathrm{i} = \frac{R}{\omega_{\mathrm{r},0}(L + L_\mathrm{T})} \tag{2.27}$$

$$Q_\mathrm{c} = \frac{2}{Z_0 \omega_{\mathrm{r},0}^3 (L + L_\mathrm{T}) C_\mathrm{c}^2}. \tag{2.28}$$

In the lumped-element resonator-based µMUX we couple an rf-SQUID to the inductor L_T. To describe the readout power dependence of the µMUX characteristics, we need knowledge of the amplitude I_T of the current induced in L_T by a readout tone with power P_rf, which has been derived (see appendix A.1) as

$$I_\mathrm{T} = \sqrt{4 \frac{Q_\mathrm{l}^2}{Q_\mathrm{c}} \frac{P_\mathrm{rf}}{\omega_{\mathrm{r},0}(L + L_\mathrm{T})}} \tag{2.29}$$

if the probe tone is applied on resonance. This expression deviates from that presented in [Ahr22] by a factor of 2. However, the calculation presented in section A.1 and the agreement with experimental data in chapter 7.4 verify that the expression presented here holds true.

2.2 Non-hysteretic rf-SQUIDs

The second essential component of a µMUX is the non-hysteretic, unshunted rf-SQUID, which is inductively coupled to the load inductor L_T of the superconducting microwave resonator. An rf-SQUID consists of a superconducting loop with inductance L_S, which is interrupted by a single Josephson tunnel junction, as depicted in figure 2.6(a). The non-linear magnetic flux-dependent inductance of this rf-SQUID enables the modulation of a microwave probe tone applied to the µMUX channel resonance curves depending on the applied magnetic flux.

The non-linear behavior of the rf-SQUID arises from the Josephson tunnel junction (JJ). It consists of two superconducting electrodes separated by a thin insulating layer. The macroscopic wave functions of the two superconductors overlap if the insulating layer is thin enough. As a result, Cooper pairs can tunnel without loss of coherence through the barrier and carry a superconducting current $I_\mathrm{S,JJ}$, which depends on the gauge invariant phase difference

$$\varphi = \varphi_2 - \varphi_1 - \frac{2\pi}{\Phi_0} \int_1^2 \boldsymbol{A}(\mathbf{r}) \mathrm{d}\boldsymbol{r} \tag{2.30}$$

between the two superconducting electrodes. Here, $\Phi_0 = h/2e$ is the magnetic flux quantum, and φ_1 and φ_2 denote the phases of the macroscopic wave function of the two superconductors, taken close to the barrier. Additionally, $\boldsymbol{A}(\boldsymbol{r})$ denotes the magnetic vector potential, which is integrated along an arbitrary path connecting the two points

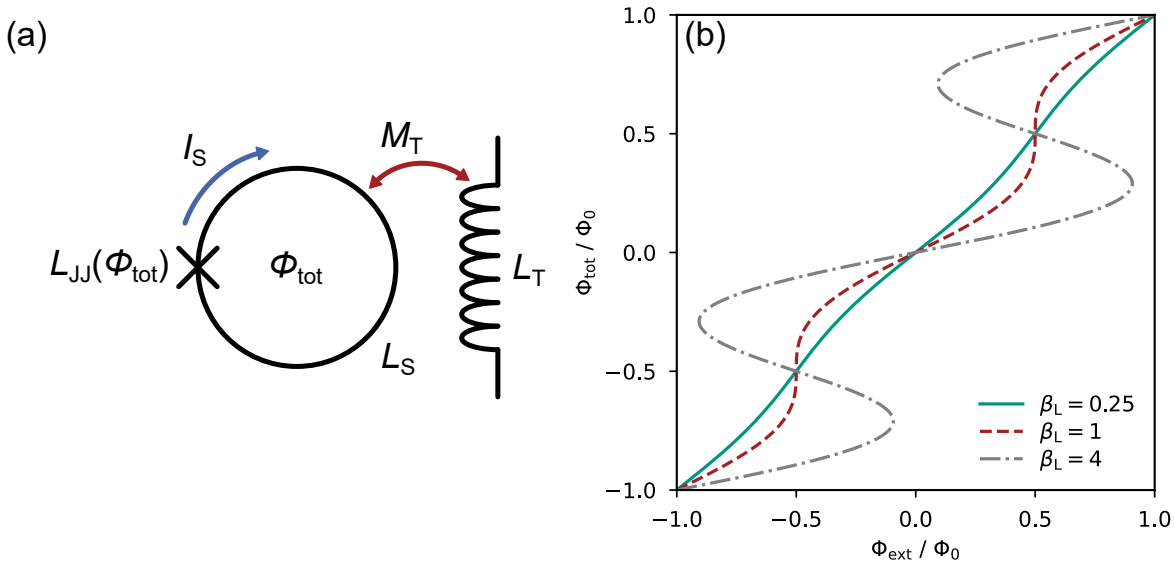

Fig. 2.6: (a) Schematic of an unshunted rf-SQUID inductively coupled to an inductor L_T. The coupling is quantified by the mutual inductance M_T. The rf-SQUID loop is threaded by a magnetic flux Φ_{tot}. (b) Relation between the total magnetic flux Φ_{tot} threading the SQUID loop and the magnetic flux Φ_{ext} that is externally applied to the SQUID. The rf-SQUID is hysteretic for a screening parameter $\beta_L > 1$, where the relation becomes multi-valued.

where the phases were taken.

The current-phase relation is 2π-periodic, and in the simplest case, it can be represented by the first Josephson equation [Jos62, Jos64]

$$I_{S,JJ}(\varphi) = I_c \sin(\varphi), \tag{2.31}$$

where I_c denotes the critical current of the Josephson junction. This approximation is valid in the limit of low tunneling probabilities across the barrier, which is generally the case for homogeneous insulating barriers in tunnel JJs.

The voltage V across the junction is related to the time derivative of the phase difference through the second Josephson equation [Jos62, Jos64]:

$$\dot{\varphi} = \frac{2\pi}{\Phi_0} V. \tag{2.32}$$

Using equations 2.31 and 2.32, we can introduce a parametric inductance

$$L_{JJ}(\varphi) = \frac{V}{\dot{I}_{S,JJ}} = \frac{L_J}{\cos(\varphi)} \tag{2.33}$$

of the junction, with the Josephson inductance $L_J = \Phi_0/(2\pi I_c)$.

For an rf-SQUID, the two junction electrodes are connected by a superconducting loop with inductance L_S. By considering equation 2.30 and the quantization of magnetic flux threading a superconducting loop, we can derive a relation between the gauge-invariant phase difference and the total magnetic flux Φ_tot threading the SQUID loop

$$\varphi + 2\pi\frac{\Phi_\mathrm{tot}}{\Phi_0} = 2\pi n \quad \text{with} \quad n \in \mathbb{Z} \tag{2.34}$$

which gives us the current-flux relation of the rf-SQUID:

$$I_\mathrm{S} = -I_\mathrm{c}\sin\left(2\pi\frac{\Phi_\mathrm{tot}}{\Phi_0}\right). \tag{2.35}$$

The magnetic flux $\Phi_\mathrm{tot} = \Phi_\mathrm{ext} + L_\mathrm{S}I_\mathrm{S}$ consists of a component Φ_ext, which is the sum of all externally applied fluxes to the rf-SQUID, and $\Phi_\mathrm{scr} = L_\mathrm{S}I_\mathrm{S}$, which represents the flux generated by the current I_S through the SQUID loop. By introducing the normalized magnetic flux $\varphi_\mathrm{tot} = 2\pi\Phi_\mathrm{tot}/\Phi_0$ and $\varphi_\mathrm{ext} = 2\pi\Phi_\mathrm{ext}/\Phi_0$, we can write

$$\varphi_\mathrm{tot} = \varphi_\mathrm{ext} - \beta_\mathrm{L}\sin\left(\varphi_\mathrm{tot}\right) \tag{2.36}$$

with the screening parameter

$$\beta_\mathrm{L} = 2\pi\frac{L_\mathrm{S}I_\mathrm{c}}{\Phi_0}. \tag{2.37}$$

As shown in figure 2.6(b), the screening parameter has a significant impact on the relation between Φ_tot and Φ_ext. For $\beta_\mathrm{L} > 1$, Φ_tot is no longer uniquely defined by Φ_ext and the rf-SQUID becomes hysteretic. In this regime, the rf-SQUID can switch between the different flux states, which leads to a dissipative behavior [Cla04]. In a µMUX, however, we use non hysteretic rf-SQUIDs ($\beta_\mathrm{L} < 1$), resulting in non-dissipative behavior with flux dependent inductance across the Josephson junction

$$L_\mathrm{JJ}(\varphi_\mathrm{tot}) = \frac{\Phi_0}{2\pi I_\mathrm{c}\cos(\varphi_\mathrm{tot})}. \tag{2.38}$$

It is this flux dependent inductance in the rf-SQUID that enables the modulation of the resonance frequency of the superconducting resonator of a µMUX channel.

2.3 Principle of microwave SQUID multiplexing

Figure 2.7 shows an equivalent circuit diagram of a single CPW-based µMUX channel. It combines the non-hysteretic rf-SQUID with the superconducting resonator by inductively coupling the SQUID via the mutual inductance M_T to the load inductor L_T. In this configuration, the resonator termination can be described by an effective load inductance $L_\mathrm{T,eff}(\varphi_\mathrm{tot})$, which varies periodically with the magnetic flux applied to the rf-SQUID. The magnetic flux through the rf-SQUID is controlled through the input coil L_in and the modulation coil L_mod, which are inductively coupled to the rf-SQUID via the

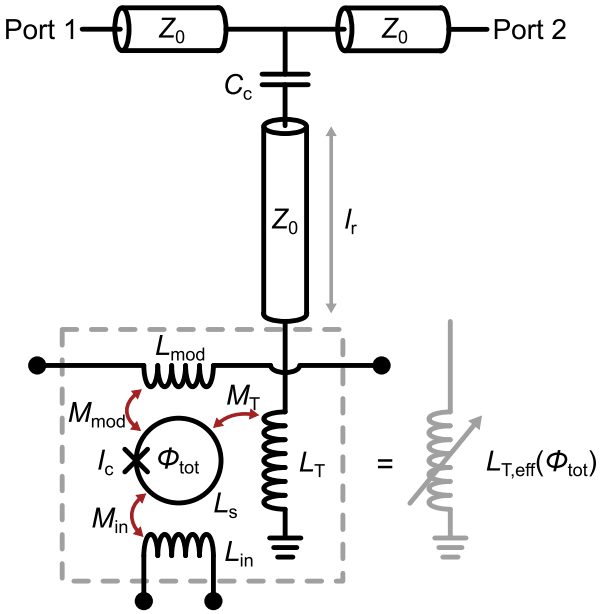

Fig. 2.7: Circuit diagram of a single µMUX channel. The channel comprises an rf-SQUID coupled to the input coil L_{in} and the inductor L_{T}, which loads a superconducting $\lambda/4$ microwave resonator. The resonator is coupled to the feedline via the coupling capacitor C_{c}. Additionally, a modulation coil L_{mod} is coupled to the SQUID for flux-ramp modulation (see section 2.6). Owing to the mutual couplings, the load inductor can be described by an effective inductance $L_{\mathrm{T,eff}}(\Phi_{\mathrm{tot}})$ that depends on the total magnetic flux Φ_{tot} through the SQUID.

mutual inductances M_{in} and M_{mod}, respectively. The modulation coil is used for flux-ramp modulation (FRM), a linearization method that will be discussed in section 2.6. The input coil is used to couple a detector to the rf-SQUID. As a result, a detector signal alters the current through the input coil, which changes the normalized magnetic flux φ_{tot} through the rf-SQUID and consequently modifies the effective load inductance $L_{\mathrm{T,eff}}(\varphi_{\mathrm{tot}})$ of the resonator, leading to a shift in its resonance frequency $f_{\mathrm{r}}(\varphi_{\mathrm{tot}})$ and resonance curve, as depicted in figure 2.8(a). Like the rf-SQUID inductance, this resonance frequency shift is periodic in Φ_{tot} and therefore in Φ_{ext}, with the maximum resonance frequency being reached for an externally applied flux of $\Phi_{\mathrm{ext}} = n\Phi_0$ and the minimum for $\Phi_{\mathrm{ext}} = (n + 1/2)\Phi_0$.

The original detector signal can be determined by monitoring the resonance frequency shift. In principle, this could be achieved by continuously measuring the resonance curve of the µMUX channel using a vector network analyzer. However, this method is slow and would significantly limit the achievable sampling rate. Instead, the transmission parameter S_{21} is measured at a single frequency only. A probe tone is applied at the frequency f_{exc} on the flank of the resonance curve, which, as depicted in figure 2.8(b), alters its transmitted amplitude $|S_{21}(f_{\mathrm{exc}})|$ based on the position of the resonance curve and, consequently, on the applied magnetic flux. This method is significantly faster than measuring the entire resonance curve and is still sufficient to monitor the input signal generated by the detector in the input coil.

The most essential relation characterizing a µMUX channel is the relationship $f_{\mathrm{r}}(\varphi_{\mathrm{tot}})$ between resonance frequency and magnetic flux. If the effective load inductance $L_{\mathrm{T,eff}}(\varphi_{\mathrm{tot}})$ is known, this relationship is given by equation 2.19 yielding

$$f_{\mathrm{r,CPW}}(\varphi_{\mathrm{tot}}) = \frac{f_0}{1 + 4f_0[C_{\mathrm{c}}Z_0 + L_{\mathrm{T,eff}}(\varphi_{\mathrm{tot}})/Z_0]}. \tag{2.39}$$

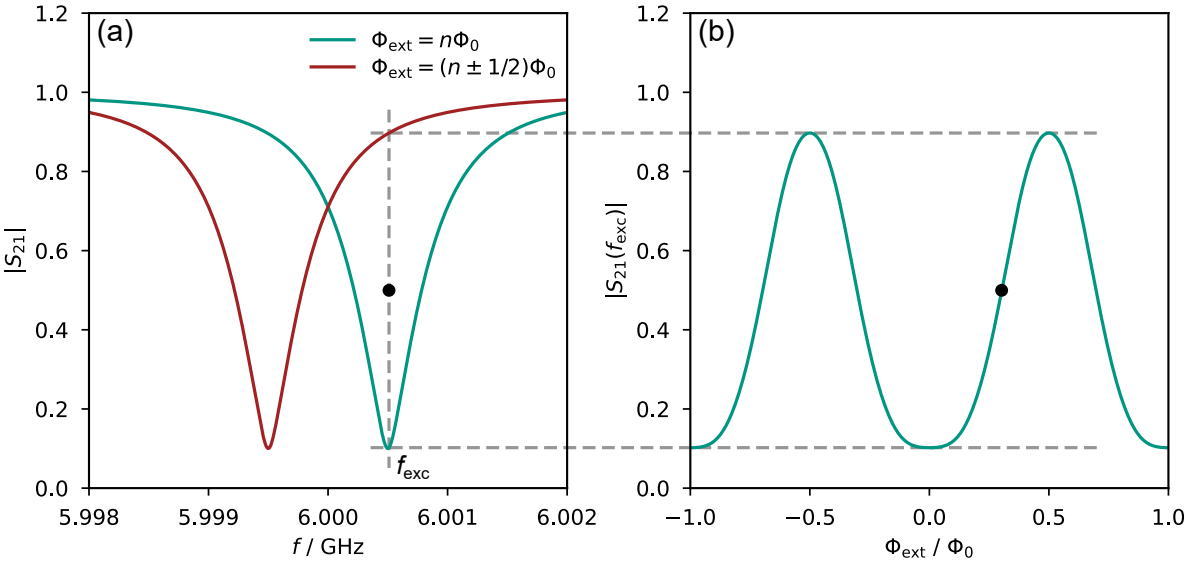

Fig. 2.8: (a) Resonance curve of a µMUX channel, assuming an externally applied flux of $\Phi_{ext} = n\Phi_0$ and $\Phi_{ext} = (n \pm 1/2)\Phi_0$, respectively, corresponding to the flux states with the maximum and minimum resonance frequency. For readout, a probe tone with frequency f_{exc} is applied. (b) Transmission parameter $|S_{21}(f_{ext})|$ of the probe tone as a function of the external magnetic flux Φ_{ext}.

Alternatively, a µMUX can be realized with a lumped-element resonator by coupling the rf-SQUID to its inductor L_T. In this case, we can use equation 2.26 to obtain

$$f_{r,LEMWR}(\varphi_{tot}) = \frac{1}{2\pi\sqrt{(L + L_{T,eff}(\varphi_{tot}))(C + C_c)}}. \tag{2.40}$$

To determine $L_{T,eff}(\varphi_{tot})$, we must consider the currents running through the load inductor. The total current $i_{tot}(t) = i_T(t) + i_{ind}(t)$ is time dependent and is composed of two components. The current $i_T = I_T \sin(\omega t)$ is generated by the probe tone, with an amplitude I_T determined by the probe tone power P_{rf} (see equations 2.24 and 2.29). The second component ,

$$i_{ind}(t) = -\frac{M_T}{i\omega L_T}\frac{dI_S(t)}{dt}, \tag{2.41}$$

represents the current that is induced by the current $I_S(t)$ running in the SQUID loop, which is given by

$$I_S(t) = -I_c \sin\left[\varphi_{ext} + \varphi_{rf}\sin(\omega t) + \beta_L \frac{I_S(t)}{I_c}\right]. \tag{2.42}$$

which is derived from equation 2.35, where we consider that the total normalized magnetic flux $\varphi_{tot} = \varphi_{ext} + \varphi_{rf}\sin(\omega t) + \varphi_{scr}(t)$ is composed of three components: the normalized magnetic flux φ_{ext}, which is applied externally through the input and modulation coil, the normalized magnetic flux $\varphi_{rf} = 2\pi M_T I_T/\Phi_0$ which is induced by the

current $i_\mathrm{T}(t)$ in the load inductor, and $\varphi_\mathrm{scr}(t) = \beta_\mathrm{L} I_\mathrm{S}(t)/I_\mathrm{c}$, induced by the SQUID screening current. Since the signals applied through the input coil and modulation coil are typically significantly slower than the probe tone frequency, φ_ext is treated as a quasi-static, time independent flux contribution, i.e. $\varphi_\mathrm{ext} \approx \mathrm{const.}$.

While $i_\mathrm{ind}(t)$ can consist of multiple frequency components, due to the resonance condition of equation 2.39, only the fundamental mode ω populates the resonator, as the higher harmonics interfere destructively within the resonator. The fundamental modes of $i_\mathrm{ind}(t)$ and $i_\mathrm{T}(t)$ are in phase [Weg22], and we can write the effective load inductance as [Weg22]

$$L_\mathrm{T,eff} = L_\mathrm{T} \frac{i_\mathrm{tot}(t)}{i_\mathrm{T}(t)} = L_\mathrm{T} \left(1 + \frac{i_\mathrm{ind}(t)}{i_\mathrm{T}(t)}\right). \tag{2.43}$$

The main challenge in modeling the dependence of the resonance frequency shift on the external magnetic flux φ_ext and readout power φ_rf lies in solving the implicit equation 2.42. In fact, no general analytical solution for I_S exists. Instead, existing µMUX models describe the limit of low readout powers $\varphi_\mathrm{rf} \to 0$ [Mat11, Kem17a] or provide a more general approximation for the power dependence. However, this is for a limited parameter space of $\beta_\mathrm{L} < 0.6$ [Weg22].

2.3.1 Flux-dependence of the resonance frequency in the limit of low readout powers

In the limit of low readout powers, i.e. $\varphi_\mathrm{rf} \to 0$, the contribution of the rf-flux $\varphi_\mathrm{rf}\sin(\omega t)$ to the total normalized flux φ_tot threading the SQUID loop can be neglected, and an analytical solution for the effective load inductance can be found [Weg22]:

$$L_\mathrm{T,eff}(\varphi_\mathrm{tot}) = L_\mathrm{T} - \frac{M_\mathrm{T}^2}{L_\mathrm{S}} \frac{\beta_\mathrm{L}\cos(\varphi_\mathrm{tot})}{1 + \beta_\mathrm{L}\cos(\varphi_\mathrm{tot})}. \tag{2.44}$$

This solution is valid for any choice of the screening parameter β_L, but only for vanishing readout powers P_rf. While this is typically not the case during µMUX operation, it still provides a valuable approximation for µMUX characterization, which is often performed at sufficiently low readout power. By inserting this solution into equation 2.39, assuming $\omega_0 L_\mathrm{T,eff} \ll Z_0$ and $Z_0 \gg 1/(\omega_0 C_\mathrm{c})$ and performing a first order Taylor expansion, the flux-dependence of the resonance frequency of a CPW-based µMUX can be expressed as

$$f_\mathrm{r,CPW}(\varphi_\mathrm{tot}) \approx f_0 - 4f_0^2 \left[C_\mathrm{c} Z_0 + \frac{L_\mathrm{T}}{Z_0} - \frac{M_\mathrm{T}^2}{Z_0 L_\mathrm{S}} \frac{\beta_\mathrm{L}\cos(\varphi_\mathrm{tot})}{1 + \beta_\mathrm{L}\cos(\varphi_\mathrm{tot})}\right], \tag{2.45}$$

from which we can determine the maximum resonance frequency shift

$$\Delta f_\mathrm{r,CPW}^\mathrm{max} \approx \frac{4 f_0^2 M_\mathrm{T}^2}{Z_0 L_\mathrm{S}} \frac{2\beta_\mathrm{L}}{1 - \beta_\mathrm{L}^2}. \tag{2.46}$$

Similarly, we can find an approximate solution for the lumped-element-based µMUX

by inserting $L_{\mathrm{T,eff}}$ into equation 2.40:

$$f_{\mathrm{r,LEMWR}}(\varphi_{\mathrm{tot}}) \approx f_{\mathrm{r},0}\left[1+\frac{M_{\mathrm{T}}^2}{2L_{\mathrm{S}}(L+L_{\mathrm{T}})}\frac{\beta_{\mathrm{L}}\cos(\varphi_{\mathrm{tot}})}{1+\beta_{\mathrm{L}}\cos(\varphi_{\mathrm{tot}})}\right]. \tag{2.47}$$

where $f_{\mathrm{r},0}$ represents the resonance frequency without an rf-SQUID coupled to the resonator, as given by equation 2.26. With this, we can calculate the maximum resonance frequency shift of the lumped-element-based µMUX:

$$\Delta f_{\mathrm{r,LEMWR}}^{\mathrm{max}} \approx \frac{f_{\mathrm{r},0}M_{\mathrm{T}}^2}{2L_{\mathrm{S}}(L+L_{\mathrm{T}})}\frac{2\beta_{\mathrm{L}}}{1-\beta_{\mathrm{L}}^2}. \tag{2.48}$$

2.3.2 Analytical model of the readout power dependence

During actual µMUX readout, the normalized rf-flux contribution φ_{rf} is typically finite and cant be neglected. Thus, a µMUX model that accounts for power dependence is essential for accurately predicting the behavior of a µMUX-based readout system. In the most advanced µMUX model described in [Weg22], equation 2.35 was solved by consecutively applying a 2nd-order and a 10th-order Taylor expansion in β_{L}, yielding

$$L_{\mathrm{T,eff}}(\varphi_{\mathrm{ext}},\varphi_{\mathrm{ext}}) = L_{\mathrm{T}} - \frac{M_{\mathrm{T}}^2}{L_{\mathrm{S}}}\frac{2\beta_{\mathrm{L}}}{\varphi_{\mathrm{rf}}}\sum_{i,j} p_{i,j}(\varphi_{\mathrm{ext}},\varphi_{\mathrm{rf}}) \tag{2.49}$$

with

$$p_{i,j}(\varphi_{\mathrm{ext}},\varphi_{\mathrm{rf}}) = a_{i,j}\beta_{\mathrm{L}}^{b_{i,j}}\cos(c_{i,j}\varphi_{\mathrm{ext}})J_1(c_{i,j}\varphi_{\mathrm{rf}}). \tag{2.50}$$

The coefficients $a_{i,j}$, $b_{i,j}$, and $c_{i,j}$ are listed in table 2.1 and $J_1(x)$ denotes the Bessel function of the first kind and order one. Inserting equation 2.49 into equation 2.39, we obtain the power dependence of the resonance frequency of a CPW based µMUX:

$$f_{\mathrm{r,CPW}}(\varphi_{\mathrm{ext}},\varphi_{\mathrm{rf}}) \approx f_0 - 4f_0^2\left[C_{\mathrm{c}}Z_0 + \frac{L_{\mathrm{T}}}{Z_0} - \frac{M_{\mathrm{T}}^2}{Z_0L_{\mathrm{S}}}\frac{2\beta_{\mathrm{L}}}{\varphi_{\mathrm{rf}}}\sum_{i,j} p_{i,j}(\varphi_{\mathrm{ext}},\varphi_{\mathrm{rf}})\right] \tag{2.51}$$

Similarly, we can insert equation 2.49 into equation 2.40, yielding the power dependence of the resonance frequency of a lumped-element resonator based µMUX:

$$f_{\mathrm{r,LEMWR}}(\varphi_{\mathrm{ext}},\varphi_{\mathrm{rf}}) \approx f_{\mathrm{r},0}\left[1+\frac{M_{\mathrm{T}}^2}{2L_{\mathrm{S}}(L+L_{\mathrm{T}})}\frac{2\beta_{\mathrm{L}}}{\varphi_{\mathrm{rf}}}\sum_{i,j} p_{i,j}(\varphi_{\mathrm{ext}},\varphi_{\mathrm{rf}})\right]. \tag{2.52}$$

Since the Bessel function of the first kind $J_1(x)$ approximately resembles a sine that decays with $1/\sqrt{x}$, the total resonance frequency shift decreases with increasing readout power, allowing us to find the maximum peak-to-peak resonance frequency shift $\Delta f_{\mathrm{r}}^{\mathrm{max}}$ in the low power limit according to equation 2.46 and 2.48.

Due to the inherent limitations of Taylor expansions, this power dependent model is

Tab. 2.1: Coefficients used for calculating $p_{i,j}(\varphi_{\mathrm{ext}},\varphi_{\mathrm{tot}})$ in equation 2.50 [Weg22].

$p_{i,j}$	$a_{i,j}$	$b_{i,j}$	$c_{i,j}$	$p_{i,j}$	$a_{i,j}$	$b_{i,j}$	$c_{i,j}$
$p_{0,0}$	$+1$	0	1	$p_{7,2}$	$+137/512$	7	6
$p_{1,0}$	$-1/2$	1	2	$p_{7,3}$	$-267/1024$	7	8
$p_{2,0}$	$-1/8$	2	1	$p_{8,0}$	$+21/1024$	8	1
$p_{2,1}$	$+3/8$	2	3	$p_{8,1}$	$-35/512$	8	3
$p_{3,0}$	$+1/8$	3	2	$p_{8,2}$	$+103/512$	8	5
$p_{3,1}$	$-5/16$	3	4	$p_{8,3}$	$-651/2048$	8	7
$p_{4,0}$	$+1/16$	4	1	$p_{8,4}$	$+547/2048$	8	9
$p_{4,1}$	$-5/32$	4	3	$p_{9,0}$	$-63/2048$	9	2
$p_{4,2}$	$+9/32$	4	5	$p_{9,1}$	$+27/256$	9	4
$p_{5,0}$	$-5/64$	5	2	$p_{9,2}$	$-1089/4096$	9	6
$p_{5,1}$	$+3/16$	5	4	$p_{9,3}$	$+193/512$	9	8
$p_{5,2}$	$-17/64$	5	6	$p_{9,4}$	$-1139/4096$	9	10
$p_{6,0}$	$-15/512$	6	1	$p_{10,0}$	$-105/8192$	10	1
$p_{6,1}$	$+57/512$	6	3	$p_{10,1}$	$+435/8192$	10	3
$p_{6,2}$	$-115/512$	6	5	$p_{10,2}$	$-2595/16384$	10	5
$p_{6,3}$	$+133/512$	6	7	$p_{10,3}$	$+5705/16384$	10	7
$p_{7,0}$	$+21/512$	7	2	$p_{10,4}$	$-7317/16384$	10	9
$p_{7,1}$	$-77/512$	7	4	$p_{10,5}$	$+4807/16384$	10	11

not valid for arbitrary values of the screening parameter β_{L}, but only up to $\beta_{\mathrm{L}} \leq 0.6$. Consequently, it does not cover the full parameter range $\beta_{\mathrm{L}} < 1$ of interest for designing a µMUX. In theory, the model could be expanded. However, this would require a substantially higher order of Taylor expansion, rendering the approach impractical. Instead, we will present a numerical model in chapter 6 that accounts for the power dependence of the resonance frequency shift for screening parameters up to $\beta_{\mathrm{L}} \leq 1$.

2.3.3 Input circuit of the rf-SQUID

The input coil of each µMUX channel is equipped with an additional low pass filter, which minimizes microwave power leakage from the µMUX into the detector. In the case of µMUXs designed for the readout of magnetic microcalorimeters (MMCs), this filter typically consists of a single resistor R_{f} shunting the input coil, as depicted in figure 2.10. The resistor, together with the detector coil inductance L_{det} and total parasitic inductance L_{p} of the wiring connecting the detector and input coil, forms a first-order low pass filter with a cut-off frequency of [Kem12]

$$f_{\mathrm{cut}} = \frac{R_{\mathrm{f}}}{2\pi} \frac{L_{\mathrm{in}} + L_{\mathrm{det}} + L_{\mathrm{p}}}{L_{\mathrm{in}}(L_{\mathrm{det}} + L_{\mathrm{p}})}. \tag{2.53}$$

The cut-off frequency cannot be set arbitrarily low, as it will also affect the signal originating from the detector. Additionally, in the case of the MMC readout, the

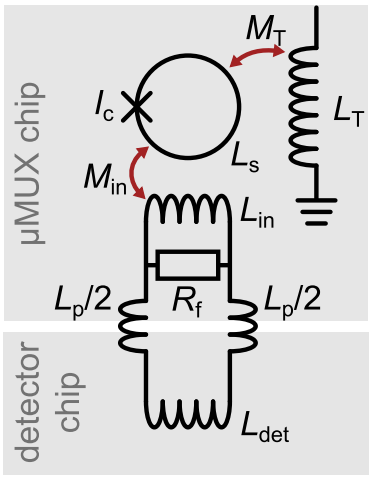

Fig. 2.9: Schematic of the input circuit of a μMUX channel with filter resistor R_f shunting the input coil and a detector with inductance L_{det} connected to the input. μMUX chip and detector chip are typically connected through bond wires which introduce an parasitic inductance L_p.

inductance of the input coil must be matched to the MMC (see section 5.1). Hence, low cut-off frequencies require small filter resistances, which generate increased current noise that affects the overall noise performance. Consequently, a compromise must be made when designing the input circuit filter.

2.4 Microwave SQUID multiplexing of large detector arrays

So far, we have considered only a single μMUX channel capable of reading out one detector. For practical multiplexing, however, we aim to read out multiple detectors using a single set of wiring. Figure 2.10 shows the equivalent circuit of a μMUX that can simultaneously read out N individual detectors. Here, many μMUX channels, as discussed in the previous section 5.6.3, are coupled to a common feedline, with each channel having a unique resonance frequency f_i. A detector is connected to the input coil of each channel, while the modulation coils of all channels are connected in series. For readout, not a single probe tone, but a comb of probe tones is applied to the feedline. Each tone is placed at the flank of one of the μMUX channel resonance curves and is amplified by a high mobility electron transistor (HEMT) amplifier before being measured at room temperature. As a result, if, for example, an event occurs only in the detector of channel 3, only the amplitude of the corresponding probe tone at f_3 will be affected, allowing us to read out this detector signal and assign it to the corresponding detector.

The total number of channels that can be read out using a single feedline is limited by several factors, including the resonance frequency spacing, the HEMT amplifier bandwidth, and the HEMT amplifier saturation power. The resonance frequency spacing of the μMUX channels is determined by the required channel bandwidth and the acceptable level of crosstalk between neighboring channels. The maximum achievable sampling rate with a μMUX is determined by its settling time $\tau_{res} = 1/(\pi \Delta f_{BW})$ and, consequently, its bandwidth Δf_{BW}. Therefore, the requirement for the readout bandwidth of a detector also imposes a requirement on the μMUX channel bandwidth. For a

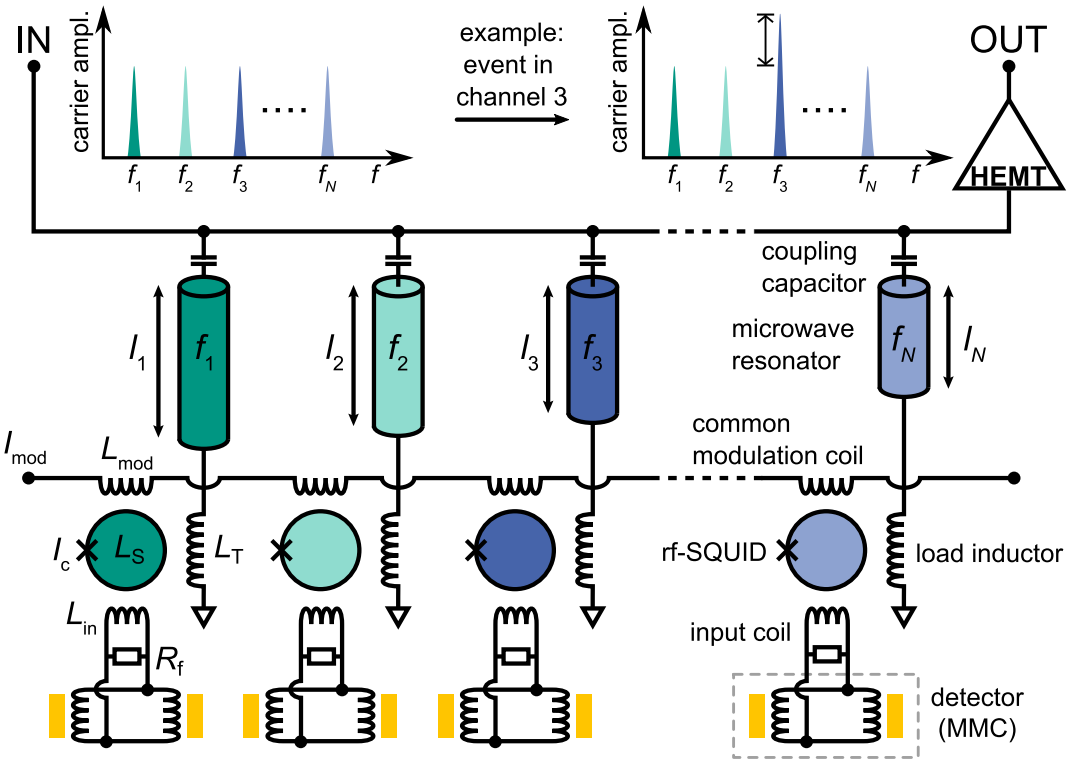

Fig. 2.10: Equivalent circuit diagram of a microwave SQUID multiplexer with N readout channels. The channels are based on CPW $\lambda/4$ resonators, each with its own resonance frequency f_i, and are coupled to a common feedline. A detector, here a MMC comprising a gradiometric pixel pair, is coupled to the input coil of each channel, and the modulation coils are connected in series. For readout, a comb of probe tones is applied to the feedline input and is amplified by a HEMT amplifier before being read out at the feedline output.

given µMUX resonance frequency spacing, however, increasing the bandwidth results in an increasing overlap of the resonance curves of neighboring channels. As a result, the resonance frequency shift of one channel can affect the transmitted probe tone power of the neighboring channel, leading to crosstalk. To decrease this Lorentzian crosstalk, the ratio $\Delta n = (f_{i+1} - f_i)/\Delta f_{\mathrm{BW}}$ must be increased. Typically, a ratio of $\Delta n = 10$ with a crosstalk of $< 0.1\,\%$ is chosen as a compromise [Weg18, Mat19]. Other sources of crosstalk, due to inter channel electromagnetic coupling and nonlinear mixing in the broadband components of the readout chain, can be minimized by increasing the spatial distance between channels on the chip and by selecting broadband components with a higher third-order intercept point (IP3) [Hir17, Mat19].

The frequency spacing, combined with the HEMT bandwidth Δf_{HEMT}, limits the maximum number of channels per feedline to $N = \Delta f_{\mathrm{HEMT}}/(\Delta n\,\Delta f_{\mathrm{BW}})$. Typically, HEMT amplifiers with a bandwidth of 4-8 GHz are employed, yielding, for example, a multiplexing factor of $N = 400$ for µMUX with $\Delta f_{\mathrm{BW}} = 1\,\mathrm{MHz}$ and a crosstalk of $0.1\,\%$. Additionally, the multiplexing factor N can be limited by the saturation power of the

HEMT amplifier, which restricts the total number of probe tones that can be amplified for readout. This restriction, however, also depends on the power required for each probe tone.

2.5 Noise contributions

An important parameter that characterizes any readout system is the noise contribution it introduces. Ideally, the total noise in a detector system is dominated by the detector itself. While this is typically achieved for superconducting transition-edge sensors (TES) [Irw05], the performance of magnetic microcalorimeters (MMCs) [Fle05, Kem18] is usually limited by the SQUIDs used for readout [Kem18]. This is primarily due to the required impedance matching between the µMUX input coil and the MMC pickup coil, which limits the mutual inductance M_{in} and, consequently, the amplitudes of the flux signals generated by the MMC in the SQUID. Thus, optimizing the readout system noise is a key challenge when designing a µMUX system.

The total system noise in a µMUX-based readout system consists of multiple contributions. The most significant source of noise is introduced by the cryogenic readout chain, contributing a voltage noise of $S_{V,\mathrm{system}} = 4k_{\mathrm{B}}T_{\mathrm{N,system}}Z_0$ to the voltage amplitude of the probe tone. For a well designed readout chain, the system noise temperature $T_{\mathrm{N,system}}$ is dominated by the noise temperature of the first amplifier on the receiving side of the readout chain, which is typically a cryogenic low noise HEMT amplifier $T_{\mathrm{N,HEMT}} \approx T_{\mathrm{N,system}}$. By determining the maximum transfer coefficient $V_\Phi^{\max}$ between transmitted probe tone amplitude and applied magnetic flux Φ_{ext}, we can derive the equivalent flux noise as $S_{\Phi,\mathrm{HEMT}} = S_{\mathrm{V,HEMT}}/(V_\Phi^{\max})^2$, yielding

$$S_{\Phi,\mathrm{system}}^{\mathrm{CPW}} = \frac{k_{\mathrm{B}}T_{\mathrm{N,system}}}{\pi\eta_0 f_{\mathrm{r}}}\frac{Q_{\mathrm{c}}}{Q_{\mathrm{l}}}\frac{L_{\mathrm{S}}}{\beta_{\mathrm{L}}-\beta_{\mathrm{L}}^3}\left(\sum_{ij}\left.\frac{\partial p_{i,j}}{\partial\varphi_{\mathrm{ext}}}\right|_{\Phi_{\mathrm{ext}}=\Phi_{\mathrm{ext}}^{\mathrm{opt}}}\right)^{-2}\left(\frac{f_{\mathrm{r}}}{f_0}\right)^2 \tag{2.54}$$

for a µMUX based on CPW resonators and

$$S_{\Phi,\mathrm{system}}^{\mathrm{LEMWR}} = \frac{k_{\mathrm{B}}T_{\mathrm{N,system}}}{\pi\eta_0 f_{\mathrm{r}}}\frac{Q_{\mathrm{c}}}{Q_{\mathrm{l}}}\frac{L_{\mathrm{S}}}{\beta_{\mathrm{L}}-\beta_{\mathrm{L}}^3}\left(\sum_{ij}\left.\frac{\partial p_{i,j}}{\partial\varphi_{\mathrm{ext}}}\right|_{\Phi_{\mathrm{ext}}=\Phi_{\mathrm{ext}}^{\mathrm{opt}}}\right)^{-2} \tag{2.55}$$

for µMUX based on lumped-element resonators[2]. Here, $\Phi_{\mathrm{ext}}^{\mathrm{opt}}$ refers to the flux bias of the rf-SQUID at which the resonance frequency shift is steepest, i.e., where $|\partial f_{\mathrm{r}}/\partial\Phi_{\mathrm{ext}}|$ is maximized, and $\eta_0 = \Delta f_{\mathrm{r}}^{\max}/\Delta f_{\mathrm{BW}}$ denotes the ratio of peak-to-peak resonance frequency shift in the limit of low readout power to the resonator bandwidth. The flux noise level, as calculated from equation 2.54, is plotted in figure 2.11. Initially, as the probe tone power P_{rf} increases, the flux noise level decreases. However, since the

[2]This expression for $S_{\Phi,\mathrm{system}}^{\mathrm{LEMWR}}$ deviates from the expression found in [Ahr22] by a factor of 4, which can be traced back to the additional factor of 2 in equation 2.29.

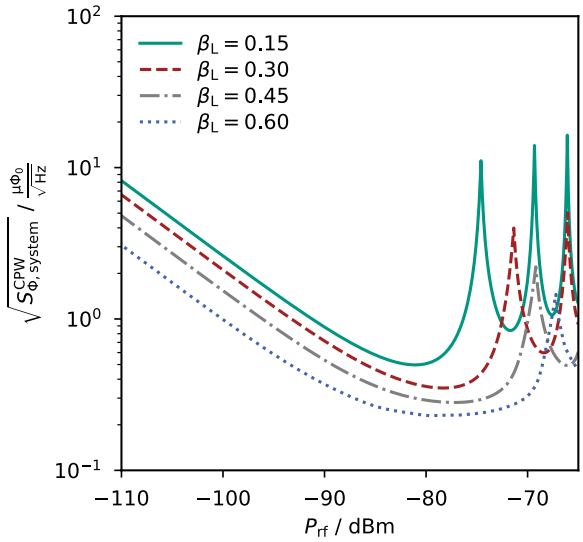

Fig. 2.11: Equivalent flux noise level corresponding to the system noise temperature, dominated by the HEMT amplifier. The noise levels are calculated from equation 2.54. The µMUX parameters are chosen to correspond to the 6 GHz µMUX described in chapter 5, however with varying screening parameter β_L. The system noise temperature is assumed to be $T_{N,system} = 4\,K$, and $Q_c = Q_l$ corresponding to negligible losses inside the resonator.

total resonance frequency shift and, therefore, V_Φ^{max} decreases towards higher readout power, the noise level increases again, and we observe an optimal readout power. For the µMUX design we will discuss in chapter 5, this results in a theoretical minimum flux noise of $\sim 0.2\,\mu\Phi_0/\sqrt{Hz}$ in open-loop readout. The flux noise level decreases with increasing screening parameter β_L, as the resonance frequency shift becomes steeper around $\Phi_{ext} = \Phi_0/2$. However, as a result, the resonance frequency shift also becomes less sinusoidal, which we will see in section 2.6 degrades the achievable noise performance in flux-ramp modulated readout.

The resonator exhibits a $1/f$-like frequency noise S_{f_r} [Gao07] induced by two-level systems [And72] in the dielectric and metal oxides on its surface [Phi87, Gao08c]. The resulting fluctuations of the resonance frequency affect the amplitude of a transmitted probe tone, leading to an equivalent flux noise contribution of

$$S_{\Phi,TLS} = \left[\frac{Q_c \Phi_0}{\pi \eta_0 (1-\beta_L^2)}\right]^2 \frac{S_{f_r}}{f_r^2} \tag{2.56}$$

for a bias flux of $\Phi_{ext} = \Phi_0/4$ [Kem12]. For Nb resonators on silicon substrates operated at 100 mK with a readout power of $P_{rf} = -72\,dBm$, an average frequency noise of $S_{f_r}/f_r^2 \approx 10^{-20}\,Hz^{-1}$ has been found in the range of 200 Hz to 300 Hz [Kum08]. For the µMUX design presented in chapter 5, this results in a noise level of $\sqrt{S_{\Phi,TLS}} \approx 0.1\,\mu\Phi_0/\sqrt{Hz}$, which is smaller than typical HEMT noise contributions. Additionally, as we will see in section 2.6, this low frequency noise contribution is suppressed when performing flux-ramp modulated readout.

The filter resistor R_f, which shunts the input coil, introduces Johnson current noise in the µMUX input circuit, resulting in a magnetic flux noise of [Kem12]

$$S_{\Phi,R_F} = M_{in}^2 \left(\frac{L_{det} + L_p}{L_{in} + L_{det} + L_p}\right)^2 \frac{4 k_B T}{R_F} \tag{2.57}$$

in open-loop readout, where L_{det} denotes the detector inductance and L_{p} the parasitic inductance of the wiring connecting the detector and µMUX. This contribution is typically small, and in the case of the µMUX system presented in chapter 5, it results in a noise contribution of $\sim 0.01\,\mu\Phi_0/\sqrt{\mathrm{Hz}}$ at an operation temperature of 10 mK.

Furthermore, the SQUID contributes several noise components. The intrinsic noise of the rf-SQUID is limited by the quantum-limited energy sensitivity $\hbar/2$ and thermal fluctuations, both of which contribute to white noise [Lik86] and can be neglected for high quality Josephson tunnel junctions and millikelvin operation temperatures. Additionally, the rf-SQUID exhibits $1/f$ excess flux noise [Kem16], which can originate from various sources, including fluctuations in the junctions critical current [Wel04], magnetic flux vortices penetrating the conductor of the SQUID loop [Sta04], or the random filling and emptying of charge traps near the superconducting surfaces, with spin locked carriers and randomly oriented magnetic moments [Koc07]. However, these contributions are expected to be insignificant compared to the typical low frequency noise of the microcalorimeter [Weg18, Mat11].

2.6 Flux-ramp modulation

The relation between the transmitted probe tone power and the magnetic flux applied to the rf-SQUID is periodic with period Φ_0 and therefore highly non-linear (see figure 2.8(b)). The probe tone power can be assumed to be proportional to the input signal only when the magnetic flux amplitudes applied to the µMUX's rf-SQUID are sufficiently small. In this case, to maximize the transfer coefficient $\mathrm{d}|S_{21}(f_{\mathrm{exc}},\varphi_{\mathrm{ext}})|/\mathrm{d}\varphi_{\mathrm{ext}}$, the flux bias of the rf-SQUID is adjusted for maximum flux sensitivity

$$V_\Phi^{\max} = \frac{\mathrm{d}}{\mathrm{d}\varphi_{\mathrm{ext}}}|S_{21}(f_{\mathrm{exc}},\varphi_{\mathrm{ext}})|\bigg|_{\varphi_{\mathrm{ext}}=\varphi_{\mathrm{ext}}^{\mathrm{opt}}}, \tag{2.58}$$

at an optimal externally applied flux $\varphi_{\mathrm{ext}}^{\mathrm{opt}}$. This readout mode is referred to as open-loop readout. Typically, however, the input signal amplitudes are a significant portion of a magnetic flux quantum or may even correspond to multiple Φ_0. Consequently, a linearization scheme is necessary. In principle, this could be achieved through a flux-locked loop [Cla04]. However, this would require an individual set of wires for a feedback coil coupled to each rf-SQUID, thereby eliminating the multiplexing idea. Instead, flux-ramp modulated readout is used, which requires only a single set of wires that connects multiple modulation coils in series [Mat12].

The principle of FRM readout is depicted in figure 2.12. The modulation coil can be used to continuously apply a sawtooth flux signal with a repetition rate of f_{ramp} to the rf-SQUID. If the ramp amplitude is $N\Phi_0$, this will result in N oscillations of the transmitted probe tone amplitude per ramp repetition and a SQUID oscillation frequency $f_{\mathrm{c}} = Nf_{\mathrm{ramp}}$, referred to as the carrier frequency. If we sample this SQUID oscillation over one ramp at the times t_i with the transmitted probe tone am-

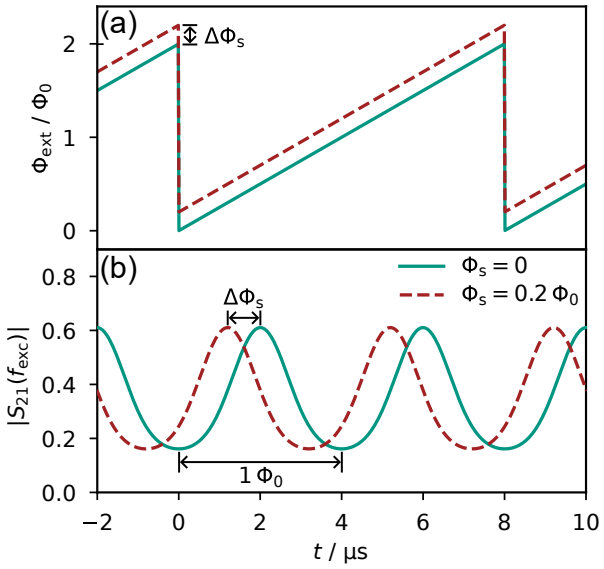

Fig. 2.12: Illustration of the principle of flux-ramp modulation. A sawtooth-shaped flux signal depicted in (a) is applied to the rf-SQUID through the modulation coil. This results in a periodic oscillation of the transmitted probe tone amplitude depicted in (b), where each oscillation corresponds to $1\,\Phi_0$ of change in applied flux. An additional signal $\Delta\Phi_\mathrm{S}$, generated in the input coil of the rf-SQUID and quasi-static within one flux ramp, results in the red dashed lines. The applied flux to the rf-SQUID is offset by $\Delta\Phi_\mathrm{S}$, while the oscillation of the probe tone amplitude is phase shifted proportionally to $\Delta\Phi_\mathrm{S}$.

plitudes $|S_{21}(f_\mathrm{exc},\varphi_\mathrm{ext}(t_i))|$, we can determine the phase ϕ of this oscillation with the relation [Mat12]

$$\phi = \arctan\left(\frac{\sum_i |S_{21}(f_\mathrm{exc},\varphi_\mathrm{ext}(t_i))| \sin(\omega_\mathrm{c} t_i)}{\sum_i |S_{21}(f_\mathrm{exc},\varphi_\mathrm{ext}(t_i))| \cos(\omega_\mathrm{c} t_i)}\right) \tag{2.59}$$

where $\omega_\mathrm{c} = 2\pi f_\mathrm{c}$. A detector signal $\Delta\Phi_\mathrm{s}$ is typically much slower than the applied flux-ramp and can, therefore, be considered as a constant flux offset of the flux-ramp signal applied to the rf-SQUID. This offset results in a phase shift $\Delta\phi = 2\pi\Delta\Phi_\mathrm{s}/\Phi_0$ of the probe tone amplitude oscillation, which is proportional to the detector signal $\Delta\Phi_\mathrm{s}$. Consequently, we can use the phase of the carrier signal as linearized output signal.

Since this method calculates only one phase per acquired flux ramp, the sampling rate in FRM readout is determined by the ramp repetition rate f_ramp and is reduced to the sampling rate in open-loop readout. Additionally, the noise performance is degraded. One reason for this degradation is that typically the entire acquired ramp cannot be used for flux-ramp demodulation due to the transient region at every ramp reset. Instead, only a fraction α of the flux ramp samples is used, where $N\alpha$ must be an integer, leading to an increase in noise by a factor of $1/\sqrt{\alpha}$ [Mat12]. Furthermore, over the duration of one flux-ramp, the µMUX is operated at its optimum flux bias with maximum transfer coefficient V_Φ^max only for a fraction of time. Consequently, the effective transfer coefficient is reduced [Mat12], which worsens all noise which is added in the readout chain after the µMUX, such as the dominant amplifier noise (see section 2.5), by a factor of [Ric21b]:

$$b = \sqrt{\frac{(V_\Phi^\mathrm{max})^2}{\langle V_\Phi^2\rangle}} \quad \text{with} \quad \langle V_\Phi^2\rangle = \frac{1}{2\pi}\int_0^{2\pi}\left(\frac{\mathrm{d}}{\mathrm{d}\varphi_\mathrm{ext}}|S_{21}(f_\mathrm{exc},\varphi_\mathrm{ext})|\right)^2 \mathrm{d}\varphi_\mathrm{ext}. \tag{2.60}$$

In the ideal case, $|S_{21}(f_{\mathrm{exc}},\varphi_{\mathrm{ext}})|$ is a sine function in φ_{ext}, resulting in $b = \sqrt{2}$. Therefore, in FRM readout, the noise performance degrades by a factor of $b/\sqrt{\alpha}$, or in the ideal case, by a factor of $\sqrt{2/\alpha}$.

Although the overall noise performance is degraded in FRM readout, it mitigates low frequency noise contributions outside the rf-SQUID, such as those arising from two-level systems (TLS) in the resonator. Such low frequency noise, far below f_{ramp}, effectively results in a constant offset in the amplitude oscillation of the transmitted probe tone and therefore does not affect the measured phase change $\Delta\phi$.

2.7 Software Defined Radio

The generation of the probe tone frequency comb is typically accomplished using a software defined radio (SDR) [Maz06, Mat17, Ric21b]. In this approach, rather than generating each probe tone individually, an arbitrary waveform generator produces a frequency comb in the MHz range, which is subsequently block-upconverted to the desired probe tone frequency comb. After transmission through the readout chain, the frequency comb with modulated probe tone amplitudes is block-downconverted back into the MHz range and digitized for processing using software-programmable digital signal processing techniques.

In figure 2.13, the working principle of an SDR used for µMUX readout is depicted. It uses a field programmable gate array (FPGA) to control a set of digital-to-analog converters (DACs). One DAC generates the flux ramp applied to the modulation line of the µMUX. Two additional DACs generate the in-phase (I) and quadrature (Q) components, $s_{\mathrm{I}}(t)$ and $s_{\mathrm{Q}}(t)$, of a complex signal $s(t) = s_{\mathrm{I}}(t) + i s_{\mathrm{Q}}(t)$. This signal corresponds to a frequency comb in the MHz range, which is mixed into the GHz range to the desired probe tone frequencies using an IQ-mixer and a local oscillator placed on the SDR's rf-frontend. The sign of the I and Q components of each tone determines whether the corresponding GHz tone appears above or below the local oscillator frequency.

The probe tone frequency comb is sent into the transmission (TX) side of the cryogenic readout chain, passing through the µMUX chip where the probe tone amplitudes are modulated according to the detector and flux-ramp signal. The frequency comb with the altered probe tone amplitudes is sent back through the receiving (RX) side of the cryogenic readout chain and mixed down again using an IQ-mixer. The frequency comb in the MHz range is then digitized using two analog-to-digital converters (ADCs). On the FPGA, the different frequency components of the frequency comb are separated using digital band-pass filters, allowing for the readout of the amplitude of each individual probe tone. For each channel, flux-ramp demodulation is performed, yielding the phase shift of each ramp and, consequently, the detector signal. Using this phase data, the FPGA also manages event detection and data acquisition.

Typically, the available DACs do not provide sufficient bandwidth to cover the full operation bandwidth of the µMUX. Instead, the operation bandwidth is divided into

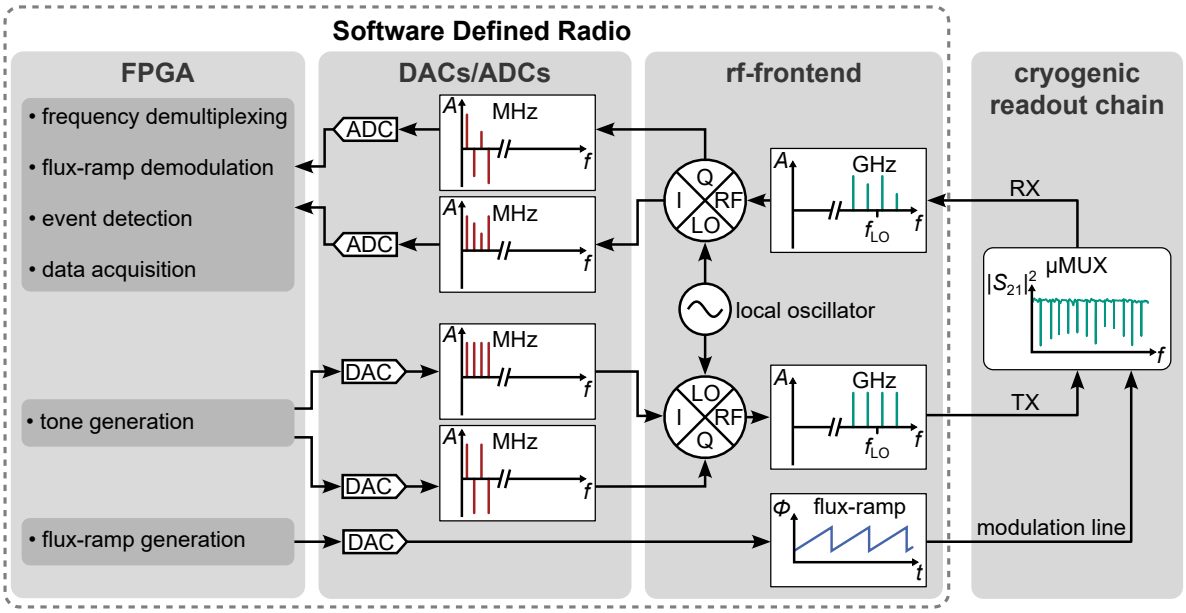

Fig. 2.13: Schematic of an SDR used for µMUX operation. The FPGA controls the digital-to-analog converters (DACs) to directly generate the flux-ramp signal, as well as a MHz range frequency comb of probe tones which gets mixed up into the GHz range on the rf-frontend using a local oscillator and an IQ-mixer. After transmission through the µMUX, the frequency comb is mixed back into the MHz range and digitized using analog-to-digital converters (ADCs). The FPGA discerns the individual probe tone amplitudes, performs flux-ramp demodulation, and handles the data acquisition.

multiple subbands, which are combined prior to transmission through the cryogenic readout chain and separated again afterwards [Kar22]. For each of these subbands, an individual set of ADCs, DACs, IQ-mixers, and local oscillators is used to generate and digitize a probe tone frequency comb in the corresponding range.

2.8 Limitations of state-of-the-art µMUX devices

While microwave SQUID multiplexing enables the simultaneous readout of hundreds or thousands of individual detectors, it has thus far remained a limiting factor in terms of energy resolution when deploying MMC-based high-resolution experiments. Based on simulations using currently established µMUX concepts, a theoretical white noise performance in FRM readout of $\sqrt{S_{\Phi,\mathrm{white}}} \approx 0.6\,\mu\Phi_0/\sqrt{\mathrm{Hz}}$ is achievable for µMUX devices optimized for MMC readout [Sch23b]. Moreover, as demonstrated in chapter 5, state-of-the-art µMUX systems still exhibit white noise levels that are more than twice as high as those predicted by simulations, indicating significant potential for further improvements. Exceeding this theoretical limit, which is predominantly set by the noise contribution of the cryogenic HEMT amplifier, requires the development of novel concepts. One such concept is the use of a quantum-limited amplifier as the first amplifier

in the microwave readout chain to significantly reduce the contribution of the amplifier arrangement to the overall system noise. By implementing kinetic-inductance traveling-wave parametric amplifiers (KITWPAs) [Eom12] into the readout chain, a reduction by a factor of ~ 2 in the added noise from the amplifier chain has been achieved [Mal21]. When employed for the readout of µMUX devices, flux noise levels have been halved to $0.77\,\mu\Phi_0/\sqrt{\text{Hz}}$ in FRM and $0.2\,\mu\Phi_0/\sqrt{\text{Hz}}$ in open-loop readout [Mal23]. However, the use of these amplifiers in µMUX-based readout systems presents several major challenges. They require complex biasing circuits to supply the KITWPA with its pump tone and to filter leakage of this tone from the subsequent amplifier. Additionally, the development of KITWPAs with adequate bandwidth, gain flatness, and saturation power remains an ongoing area of research [Mal23, Gia24, Far24].

The requirements for the saturation power of the KITWPAs may be reduced through the method of tone tracking [Ker18, Yu23]. In this method, the frequency of the probe tone applied to each µMUX channel is dynamically adjusted to ensure it remains at the minimum of the resonance curve at all times. As a result, the power per tone transmitted to the first amplifier stage is significantly reduced, depending on the resonance depth (a reduction of $\sim 9\,\text{dB}$ has been demonstrated [Ker18]), thereby relaxing the requirements for its input saturation power or, alternatively, permitting a larger multiplexing factor. Additionally, in conjunction with an increased resonance shift to resonance bandwidth ratio η, this method promises improved readout noise performance. However, this approach necessitates sophisticated room temperature electronics, and due to the finite reaction time of the electronics, it has so far been limited to flux-ramps with a slope of $< 100\,\Phi_0/\text{ms}$ and, therefore, ramp repetition rates of $< 100\,\text{kHz}$. Consequently, this limitation currently restricts the readout bandwidth compared to fixed probe tone readout, which permits flux-ramp repetition rates of up to 5 MHz [Hay24].

Beyond its noise performance, the µMUX device also imposes significant constraints on the detector array layout. The stringent requirements for the energy resolution of microcalorimeters demand that absorbers and sensors have low heat capacity, which in turn limits the absorber dimensions. Additionally, some experiments require high spatial resolution, which further constrains the absorber size to typically $\sim 250\,\mu\text{m} \times 250\,\mu\text{m}$. In contrast, the connected µMUX channels remain comparatively large, with widths of several hundred micrometers and lengths of a few millimeters (see section 5.3). This configuration poses a major challenge in experiments employing large arrays of low-temperature detectors, especially in imaging experiments, where a high fill factor of the focal plane is desired [Kem17a, Li18, Ben19]. Ideally, the focal plane fill factor should approach unity, as depicted in figure 2.14. If the readout electronics are larger than the microcalorimeter absorbers, this necessitates a complex multilayer wiring scheme [Tol16, Ste19], the complexity of which increases with the number of detectors. This is not the case if the readout electronics for each channel have a footprint similar to or smaller than the area of the microcalorimeter absorber. As seen in existing µMUX systems, the readout electronics can be positioned underneath the substrate that hosts the detector pixels, where they can be read out using a single transmission line [McC21]. In such a configuration, combined with superconducting through-silicon

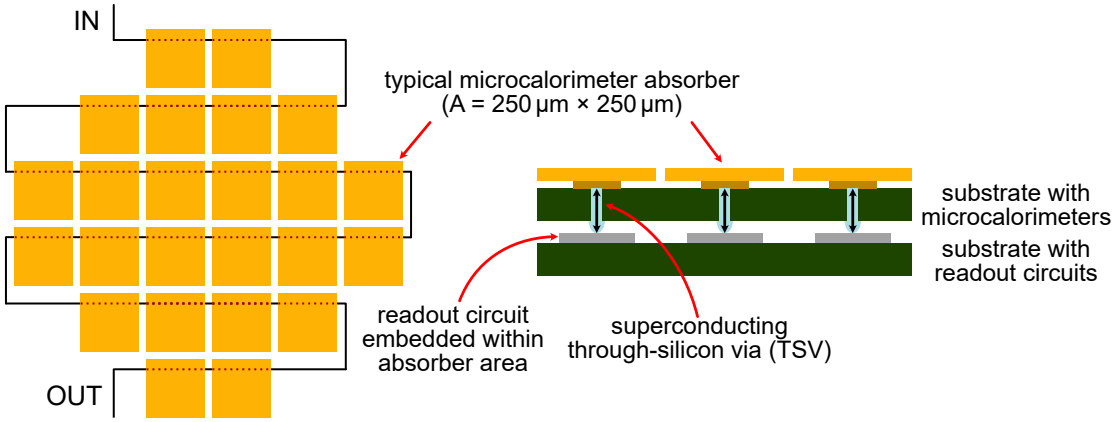

Fig. 2.14: Schematic illustration of a possible focal-plane arrangement for a large microcalorimeter array. The top view (left) shows a single feedline reading out the entire array, with the readout circuits integrated within the absorber area of each pixel. The cross-sectional view (right) demonstrates how sufficiently compact readout circuits can be located on a separate substrate below the microcalorimeters and connected by superconducting through-silicon vias (TSVs).

vias (TSVs), which have already been demonstrated as effective tools for the 3D integration of qubit circuits [Yos20], the complexity of the wiring between the detector and readout SQUIDs can be further reduced.

To achieve the desired focal plane configuration, it is essential to significantly minimize the footprint of a single µMUX channel. This reduction requires a decrease in length for coplanar waveguide (CPW) resonators and a reduction in the footprint of the capacitor and inductor for lumped-element resonators. Unless the capacitance is raised again through the use of high-κ materials, this miniaturization results in an increase in the resonance frequency, surpassing the currently established frequency band for µMUXing.

Raising the operational frequency of µMUX devices offers several advantages. Most notably, higher resonance frequencies expand the accessible frequency range within which a µMUX can operate. With the increased bandwidth of the common transmission readout line, the bandwidth of each individual channel can also be enlarged, thereby improving its time resolution. Larger bandwidths additionally increase the Lorentzian crosstalk between channels. However, this effect can be mitigated by exploiting the broader available frequency range to increase the spacing between channels while preserving the total channel count. Alternatively, or in combination, the number of channels coupled to the transmission line can be increased, thereby enhancing the multiplexing factor. The implications of elevated operation frequencies for noise performance are less clear and require further investigation. At the same time, the design and fabrication of µMUX devices at higher frequencies are increasingly challenging due to tighter fabrication tolerances, higher sensitivity to parasitic capacitances and inductances, impedance mismatches, and increased resonator losses. The practical feasibility of high-frequency

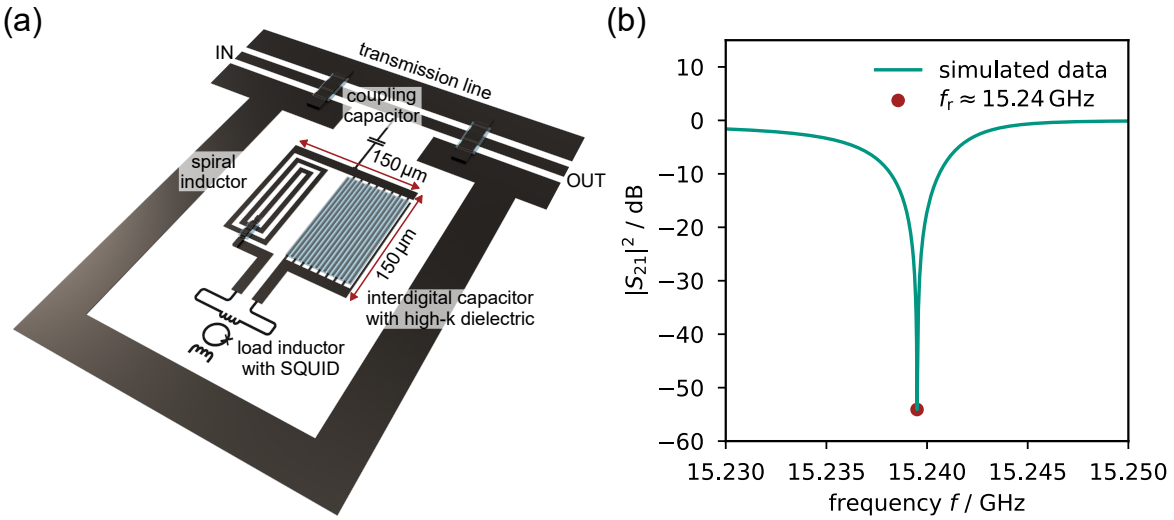

Fig. 2.15: (a) Potential Design of a lumped-element resonator patterned into a NbTiN layer sputtered on on oxidized silicon wafer. The design was evaluated in Sonnet resulting in the transmission spectrum shown in (b) with a resonance frequency of $\sim 15.24\,\mathrm{GHz}$.

µMUX devices has yet to be demonstrated. Both the investigation of noise performance and the demonstration of practical feasibility are presented in chapter 7.

To estimate the resonance frequency at which µMUX devices can be scaled down to fit beneath a typical microcalorimeter absorber, enabling the previously described focal plane arrangement, we simulated a lumped-element resonator design in Sonnet®, as depicted in figure 2.15(a). The resonator area was constrained to $150\,\mu\mathrm{m} \times 150\,\mu\mathrm{m}$, with a 100 nm NbTiN metal layer and oxidized silicon as the substrate. The operating temperature was set to 10 mK. To enhance the capacitance of the interdigital capacitor within the resonator, its fingers were coated with 150 nm of aluminum oxide, leaving one finger uncovered to allow resonance frequency adjustment using a tile-and-trim technique [Ahr22]. This design results in a resonance frequency of approximately 15.24 GHz (see figure 2.15(b)), neglecting the additional inductance introduced by the load inductor. The resonance frequency of complete µMUX devices would be lower, depending on rf-SQUID design. Further reductions could be achieved by exploiting the high kinetic inductance of NbTiN at reduced film thickness, in combination with increased dielectric thickness over the interdigital capacitor. Nonetheless, these simulations indicate that µMUX operating frequencies around 15 GHz in the $\mathrm{K_u}$ frequency band (12–18 GHz) are already sufficient to reduce the device footprint below the size of a typical microcalorimeter absorber.

3. Experimental methods

The development of microwave SQUID multiplexers comprises multiple steps, ranging from design to device characterization. In this chapter, we describe the design process for the µMUX devices developed within this thesis. We begin with electromagnetic simulations of the superconducting microwave resonators, followed by inductance simulations of the rf-SQUID design. Based on these simulations, the design parameters of the µMUX channels are determined. We then present the microfabrication process developed for the µMUX devices, detailing the fabrication of an example µMUX wafer produced during the course of this thesis. The sample holder designed to house the µMUX chips during cryogenic measurements is described, along with the cryogenic microwave setup we installed for µMUX characterization and optimization measurements in a dilution refrigerator with a base temperature below 10 mK. Finally, we introduce the measurement setup used for µMUX characterization and outline the circle-fit algorithms employed to extract characteristic resonator parameters. A brief introduction to Welch's method is also provided, which is used to calculate noise spectra from acquired timestream data.

3.1 Design of superconducting $\lambda/4$ resonators

The superconducting microwave resonator design we chose for most µMUX devices in this thesis is the quarterwave resonator, with the transmission lines of the resonator and feedline realized as a coplanar waveguide (CPW). The targeted characteristic impedance of both transmission lines is 50 Ω. To achieve this, the center line width s and slot width w must be optimized. The optimization was performed using the high-frequency electromagnetic simulation software Sonnet®[1], which enables the simulation of planar multiport microwave layouts that exceed the complexity of the CPW described in section 2.1.2, such as multilayered substrates, ground bridges crossing a CPW, or lumped elements integrated in the transmission line.

The planar layout consists of an arbitrary number of stacked layers placed inside a six sided metal box. The layer stack used for the simulations in this thesis is depicted in figure 3.1 (a). Our µMUX devices are placed in a copper housing. Consequently, the metal box in the simulations was assumed to be made of copper with a standard conductivity of 58 MS/m as provided by Sonnet. The substrate on which our µMUX devices are fabricated is thermally oxidized silicon with a silicon (Si) layer thickness of 279 µm and a dielectric constant of $\epsilon_r = 11.9$, and a thin 250 nm thick silicon oxide (SiO_2) layer on top with a dielectric constant of $\epsilon_r = 3.9$. Both dielectric constants were also taken from the Sonnet library and are assumed to be lossless with negligible

[1] https://www.sonnetsoftware.com/, Syracuse, NY, USA

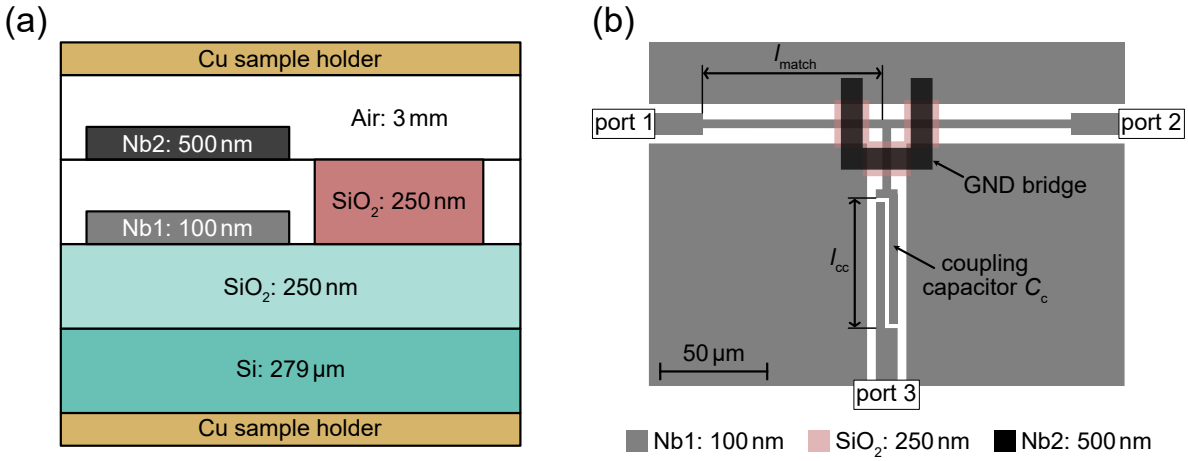

Fig. 3.1: (a) Layer stack used in the Sonnet simulations. The substrate is depicted in green and consists of two materials silicon and silicon oxide. The sputtered silicon oxide is depicted in red, whereas the niobium metal layers are depicted in gray and black. The niobium layers Nb1 and Nb2 are connected with losses vias, if no sputtered SiO_2 is drawn between them in the design layout. (b) Design layout used for the Sonnet simulations of the T-junction. We simulated the circuit for various lengths l_{cc} of the coupling capacitor as well as the length l_{match} of the slimmed down feedline.

dielectric loss tangent $\tan\delta = 0$. A 100 nm thick niobium (Nb) layer is sputtered onto the substrate, which is isolated from a second 500 nm thick Nb layer by a sputtered 250 nm thick SiO_2 layer that shares the same dielectric constant as the SiO_2 layer of the substrate. Connections between the second Nb layer and the bottom Nb layer are assumed to be perfectly conducting, while the Nb layers are characterized by their surface impedance, derived from equations 2.1 to 2.6 as a function of frequency. The required conductivity σ_n in the normal conducting state and the critical temperature of a 100 nm thick niobium layer were measured in [Maa22] and are listed in table 3.1. The operation temperature of our µMUX devices when used for magnetic microcalorimeter readout is ~ 10 mK. At this temperature, the surface resistance R_s of Nb is negligible. We describe the frequency dependence of the surface inductance L_s with a third order polynomial of frequency. However, in the range from 4-20 GHz, the variation in L_s, extracted from the derived surface impedance, is less than 0.02 % around 216.6 fH/□.

Tab. 3.1: Parameters used for the calculation of the surface impedance of the Nb layers. T_c and σ_n were measured in [Maa22], while ω_D was taken from [Hoe64].

Parameter	Value
Operation temperature T	10 mK
Layer thickness d	100 nm
Frequency range f	4-20 GHz
Critical temperature T_c	8.55 K
Conductivity σ_n	9.12 MS/m
Debye frequency ω_D	36 THz

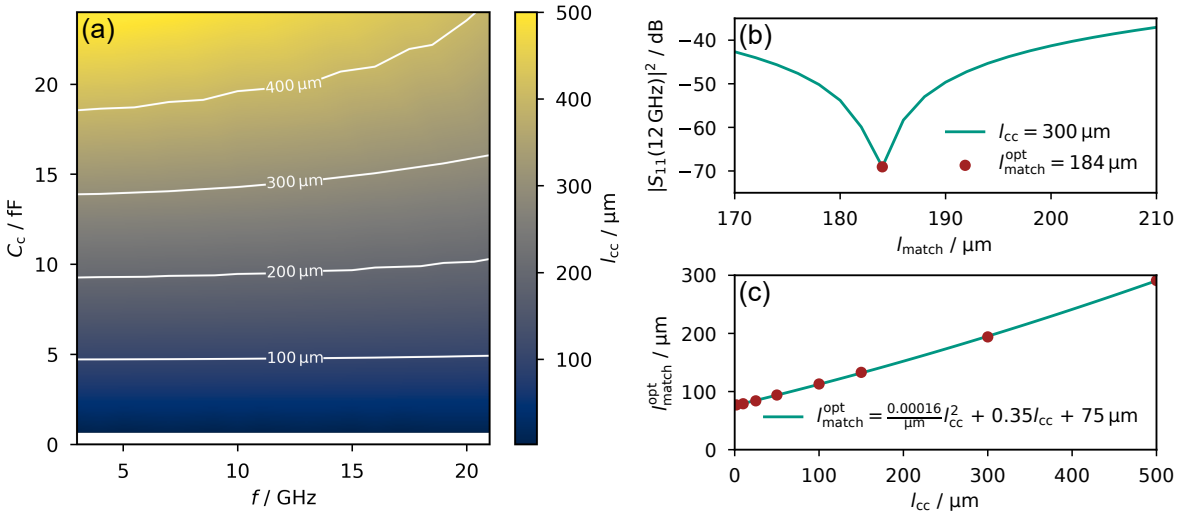

Fig. 3.2: (a) Capacitance of the coupling capacitor C_c as a function of frequency for various coupler lengths l_{cc}. The values have been simulated in Sonnet using the geometry depicted in figure 3.1. (b) Reflection coefficient $|S_{11}|^2$ of a 12 GHz signal applied to port 1 as a function of the matching length l_{match} for a coupling capacitor length of $l_{cc} = 300\,\mu m$. The best matching is achieved at minimum reflection at l^{opt}_{match} marked with a red circle. (c) Relation between the coupler length and the optimum matching length. The explicitly simulated values of l^{opt}_{match} are marked by red circles. The relation can be approximated by a linear function.

Using these layer settings, we determined the slot width of a CPW with a center conductor width of $s = 10\,\mu m$ for a target characteristic impedance of $50\,\Omega$. The slot width was varied in $1\,\mu m$ steps, yielding the best agreement for $w = 4\,\mu m$, corresponding to $Z_0 = 51.4\,\Omega$ and an effective dielectric constant of $\epsilon_{r,eff} = 6.15$. The deviation in characteristic impedance from the target value is less than 3 %, which is considered acceptable given fabrication tolerances and possible deviations of the assumed dielectric constants from those of the actual substrate. These CPW parameters are used for both the resonators and the feedline.

The capacitor C_c coupling the resonator to the feedline is realized in a layout designed in [Maa22], as depicted in figure 3.1 (b). In this T-junction layout, the resonator is connected to port 3, while the feedline extends from port 1 to port 2. The capacitor is implemented as an interdigital capacitor, where the length l_{cc} can be adjusted to achieve the desired capacitance. Since the T-junction interrupts the ground plane on one side along the feedline, a ground bridge is realized in the second Nb layer across the coupling capacitor, allowing currents at the CPW edge to flow uninterrupted along the feedline. Additionally, ground bridges connect the ground planes on both sides of the feedline, avoiding imbalances in potential and suppressing the occurrence of parasitic coupled slot-line modes [Ste02]. These ground bridges, however, introduce excess capacitance between the inner conductor and the ground plane, affecting the characteristic impedance of the transmission line. To compensate for this capacitance,

the inductance of the CPW is increased in close proximity to the ground bridges by decreasing the width of the center line. By adjusting the length l_{match} of this narrowed line, the characteristic impedance of the circuit can be modified.

The layout depicted in figure 3.1 was initially used to simulate the capacitance between the feedline and the resonator at port 3 while varying the finger length l_{cc}. The result is depicted in figure 3.2. The capacitance was calculated from the admittance parameters Y_{31} and Y_{32} with $C_{\mathrm{c}} = -\mathrm{Im}[Y_{31} + Y_{32}]/\omega$. The capacitance is treated as frequency dependent, capturing the full reactive behavior of the coupling capacitor and accounting for parasitic inductances that arise as device dimensions and frequency increase. Based on these simulations, the required finger length l_{cc} can be determined to achieve a target capacitance at a given frequency.

The fingers of the coupling capacitor couple not only to the resonator but also to the surrounding ground plane, thereby introducing an excess capacitance in addition to that introduced by the ground bridges, both of which must be compensated for using a narrowed feedline. We optimized the matching length l_{match} for minimum reflection in port 1, as depicted in figure 3.2 (b). The optimal matching length $l_{\mathrm{match}}^{\mathrm{opt}}(l_{\mathrm{cc}})$ as a function of the finger length l_{cc} is shown in figure 3.2 (c). The relation can be described by a quadratic function, allowing us to adjust l_{match} for arbitrary finger lengths.

3.2 Design of the rf-SQUID

For our rf-SQUIDs, we adapted the design from [Ric21b]. The layout of a single rf-SQUID is depicted in figure 3.3 (a), and its equivalent circuit model is shown in (b). The rf-SQUID is implemented in a gradiometric layout, which decreases the sensitivity of the SQUID loop to homogeneous magnetic background fields. The CPW transmission line of the resonator ends at the top of the depicted layout, where it connects to the surrounding ground plane through the load inductor. The modulation line runs along the bottom of the depicted layout and can be connected in series with other µMUX channels to the left and right. The majority of the SQUID loop is dedicated to coupling with the input coil. The Josephson junction is realized as a window-type tunnel

Tab. 3.2: Inductance and mutual inductance values of the rf-SQUID for a coupler length of $l_{\mathrm{MT}} = 15\,\mu\mathrm{m}$. The values were extracted from simulations in InductEx. $M_{\mathrm{p},X\leftrightarrow Y}$ denotes the parasitic mutual inductance between the inductors L_X and L_Y.

Parameter	Value	Parameter	Value
L_{T}	122 pH	M_{T}	3.67 pH
L_{in}	1.44 nH	M_{in}	153 pH
L_{mod}	268 pH	M_{mod}	34.1 pH
L_{S}	40.3 pH	$M_{\mathrm{p,T}\leftrightarrow\mathrm{in}}$	6.71 pH
		$M_{\mathrm{p,T}\leftrightarrow\mathrm{mod}}$	0.14 pH
		$M_{\mathrm{p,in}\leftrightarrow\mathrm{mod}}$	15.8 pH

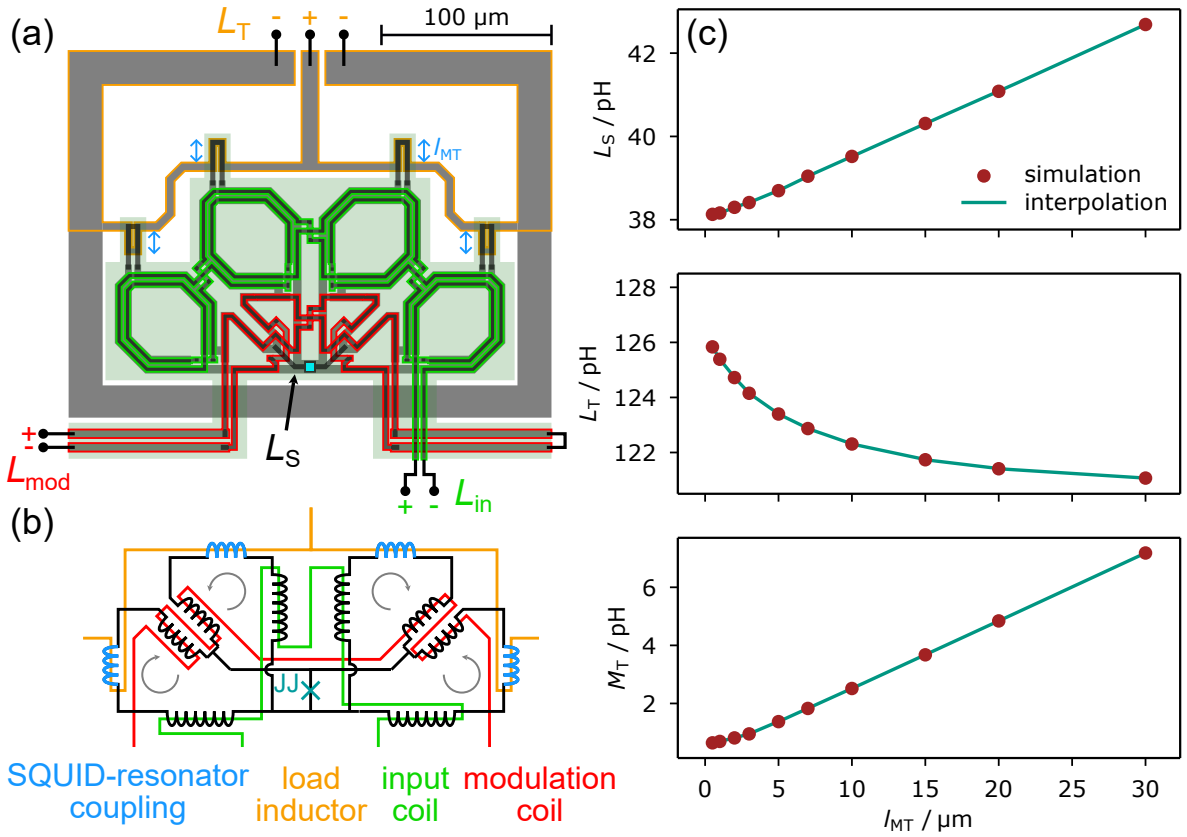

Fig. 3.3: (a) Layout of the rf-SQUID as simulated in InductEx. The bottom niobium layer is depicted in grey, the top niobium layer in black, while the insulation layer between them is depicted in a transparent green. The virtual pins across which the different inductances and couplings were simulated are marked as L_T, L_{mod}, and L_{in} and the corresponding structures are highlighted according to the color scheme depicted in (b). (b) Equivalent circuit model of the rf-SQUID. (c) Linear interpolation of the simulated SQUID inductance L_S, load inductance L_T and SQUID-resonator coupling M_T as a function of the length l_{MT} of the coupler depicted in blue in (a).

junction. Apart from the additional layers required for the trilayer of this junction, the design follows the same layer stack as described for the superconducting resonator in figure 3.1. The SQUID loop is defined in the bottom niobium layer, except for the connection to the top electrode of the junction. The input coil and modulation coil are defined in the second niobium layer and run on top of the SQUID coil.

The major differences between this design and our adapted design include changes in layer thicknesses and adjustments to the SQUID-resonator coupler. From equation 2.46, we can see that $\Delta f_{r,CPW}^{max} \propto f_0^2 M_T^2$. Consequently, the SQUID-resonator coupling M_T must be reduced as the µMUX operation frequency is increased if a constant peak-to-peak resonance frequency shift is to be maintained, which becomes especially relevant for µMUX operating at 16 GHz, such as those presented in chapter 7. In our adapted design, M_T is adjusted by modifying the length l_{MT}. However, this length significantly affects not only M_T but also the SQUID inductance L_S and the load inductance L_T. To

determine the relation between l_{MT} and the various inductances of the rf-SQUID, we simulated the circuit in InductEx®[2], while varying l_{MT}. The extracted inductances are listed in table 3.2 for a coupler length $l_{\mathrm{MT}} = 15\,\mu\mathrm{m}$, and the parameters L_{S}, L_{T}, and M_{T} are plotted as a function of l_{MT} in figure 3.3 (c)-(e). The data are linearly interpolated, allowing for the evaluation of the rf-SQUID parameters for arbitrary coupler lengths.

3.3 Design procedure of a µMUX chip

Using the interpolated simulation data from section 3.1 and 3.2, we can design µMUX channels with a wide range of parameters. To draw a µMUX channel design with a given resonance frequency f_{r}, bandwidth Δf_{BW}, peak-to-peak resonance frequency shift $\Delta f_{\mathrm{r}}^{\mathrm{max}}$, and screening parameter β_{L}, we must determine the coupling capacitor finger length l_{cc}, matching length l_{match}, SQUID-resonator coupler length l_{MT}, resonator length l_{r}, and the area A_{JJ} of the Josephson junction. The procedure to determine these design values is illustrated in figure 3.4. Given a set of design parameters, we can calculate the coupling capacitor capacitance C_{c} using equations 2.22 and 2.23, and the characteristic impedance Z_0 extracted from the Sonnet simulation of the CPW. With C_{c} fixed, we can determine the finger length $l_{\mathrm{cc}}(C_{\mathrm{c}})$ and the required matching length $l_{\mathrm{match}}(l_{\mathrm{cc}})$ using the Sonnet simulations of the T-junction. Additionally, given C_{c} and the simulations of the rf-SQUID, we can use equation 2.46 to express the peak-to-peak resonance frequency shift $\Delta f_{\mathrm{r}}^{\mathrm{max}}(l_{\mathrm{MT}})$ as a function of the SQUID-resonator coupler length and solve it numerically to determine the required l_{MT}. With l_{MT}, we can determine the load inductor inductance L_{T}, which, combined with equations 2.19 and 2.16, allows for the calculation of the resonator length l_{r}. Finally, we can use L_{S} and equation 2.37 to calculate the critical current I_{c} of the Josephson junction to achieve the desired screening parameter, which, combined with the critical current density j_{c} of the employed junction fabrication process, enables the calculation of the junction area A_{JJ}.

Following this procedure, we automated the layout drawing for individual µMUX channels and arranged the channels on a $15.5\,\mathrm{mm} \times 5\,\mathrm{mm}$ µMUX chip, as depicted in figure 3.5. The feedline crosses the chip from left to right. At the edges of the chip, the CPW of the feedline increases in size to tapered bondpads, where we connect the feedline to external rf wiring using wire bonds. The individual µMUX channels are placed below the feedline, with the $\lambda/4$ transmission line arranged in a meander shape, ensuring that all rf-SQUIDs are positioned at the same height at the bottom of the chip. The ground plane covers most of the chip and ends at the bottom, just above the modulation line, which crosses the chip from left to right, connecting the modulation coils of all rf-SQUIDs in series. The input coils of the µMUX channels are connected through the bondpads at the bottom of the chip. With the bondpads of the feedline and modulation line placed on the right and left sides, the chips can easily be daisy-chained, allowing the readout of many µMUX chips using a single readout chain.

[2]https://www.sun-magnetics.com/, Stellenbosch, South Africa

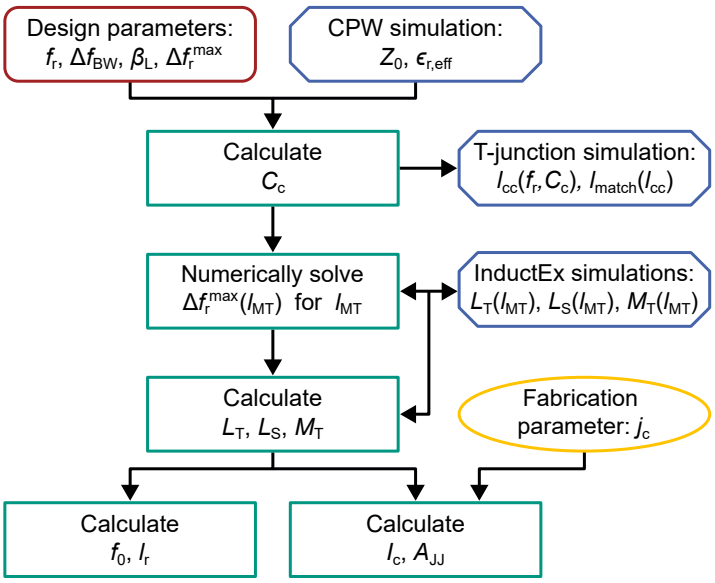

Fig. 3.4: Flowchart of the procedure used to calculate the relevant device parameter of a single µMUX channel. Given a set of design parameters, the critical current density j_c set by the Josephson junction fabrication process, and the simulations described in section 3.1 and 3.2, we can calculate the required coupling capacitor length l_{cc}, matching length l_{match}, resonator length l_r, and Josephson junction area A_{JJ}.

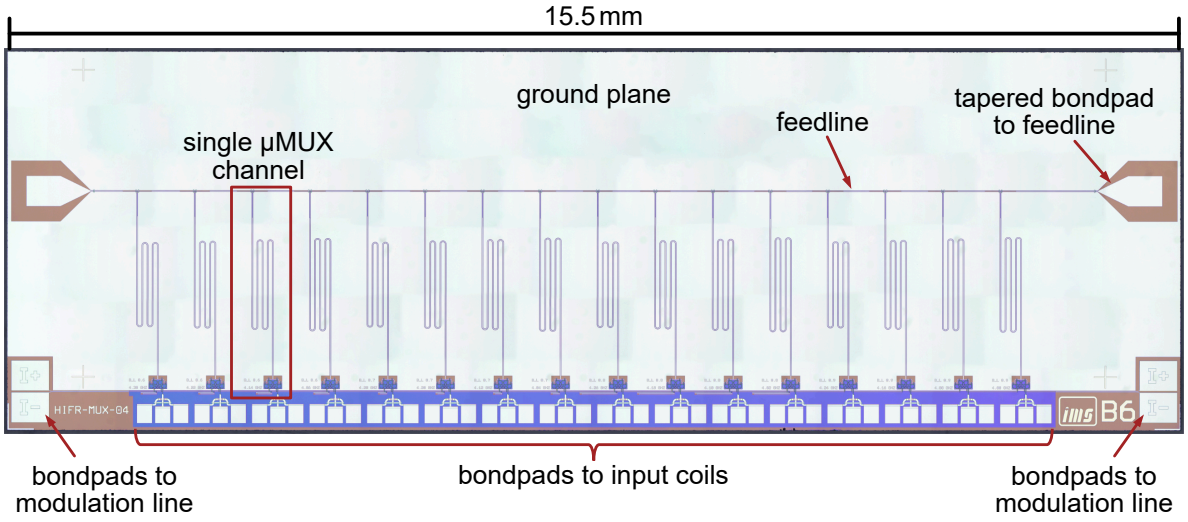

Fig. 3.5: Micrograph of a typical µMUX chip layout fabricated during the course of this thesis. An identical design was used for the measurements presented in chapter 6. The chip measures 15.5 mm × 5 mm. The substrate shows in brown and the niobium layers in white. The insulating SiO_2 layer covers only a small portion on the bottom of the chip where it shows in blue when sputtered directly onto the substrate. The image is a composite assembled from multiple micrographs, which leads to visible brightness variations in the ground plane at the boundaries where individual images were stitched together.

3.4 Microfabrication

As part of this thesis, we fabricated several µMUX designs in the cleanroom facility of the Institute of Micro- and Nanoelectronic Systems at the Karlsruhe Institute of Technology. The different thin-film layers comprising the µMUX devices are listed in table 3.3. The µMUX are fabricated on two-inch high-resistivity ($\rho > 1\,\mathrm{k\Omega\,cm}$) Si(100) wafers, which are covered with a 250 nm thick thermally oxidized SiO_2 layer. The metal layers were deposited using dc magnetron sputtering, while the isolation layers were deposited using rf magnetron sputtering, both in the institute's custom high vacuum sputter chambers.

Initially, the Nb/Al-AlO_x/Nb trilayer, comprising the first three layers, is deposited in situ. Before the first Nb deposition, the substrate is surface cleaned by exposing it to a mild Ar plasma, generated by applying a 34 W rf signal to the two-inch substrate holder at an Ar pressure of $p_{\mathrm{Ar}} = 40\,\mu\mathrm{bar}$. Subsequently, the first 100 nm thick Nb layer is deposited using a three-inch sputter gun with a power of $P_{\mathrm{dc}} = 300\,\mathrm{W}$, at an Ar pressure of $p_{\mathrm{Ar}} = 8.3\,\mathrm{mTorr}$, and a rate of $\dot{d_{\mathrm{Nb}}} = 1.06\,\mathrm{nm\,s^{-1}}$. The 7 nm thick aluminum layer is also deposited using a three-inch sputter gun with a power of $P_{\mathrm{dc}} = 100\,\mathrm{W}$, at an Ar pressure of $p_{\mathrm{Ar}} = 5.4\,\mathrm{mTorr}$, and a rate of $\dot{d_{\mathrm{Al}}} = 0.64\,\mathrm{nm\,s^{-1}}$. Before sputtering the 100 nm thick top Nb layer of the trilayer, the Al layer is oxidized by exposing it for $t_{\mathrm{ox}} = 3.5\,\mathrm{h}$ to a $p_{\mathrm{ox}} = 80\,\mathrm{mbar}$ O_2 atmosphere, resulting in a critical current density of the Josephson junction of $j_{\mathrm{c}} = 23\,\mathrm{A\,cm^{-2}}$. The trilayer is completed by depositing the top Nb layer using the same parameters as those applied to the first layer.

In the first etching step, the top Nb layer is structured. For this purpose, we apply the positive photoresist AZ MIR 701 (29 CPS)[3] , and expose it using a maskless aligner MLA150[4]. After developing the resist in AZ Developer[3] diluted 1:1 in water, the top electrodes of the Josephson junctions are plasma etched in a PlasmaPro 100 Cobra[5] ICP-RIE[6] system. The substrate surface is first cleaned for $\sim 5\,\mathrm{s}$ in a pure Ar plasma with an Ar pressure of $p_{\mathrm{Ar}} = 15\,\mathrm{mTorr}$, an Ar flow of $\dot{V}_{\mathrm{Ar}} = 50\,\mathrm{sccm}$, and a power of $P_{\mathrm{rf,plasma}} = 600\,\mathrm{W}$ to sustain a high density plasma, along with a power of $P_{\mathrm{rf,table}} = 50\,\mathrm{W}$ to control the energy of the ions striking the substrate. Subsequently, the Nb layer is etched for $\sim 30\,\mathrm{s}$ in an SF_6 plasma, with $p_{SF_6} = 15\,\mathrm{mTorr}$, $\dot{V}_{SF_6} = 20\,\mathrm{sccm}$, $P_{\mathrm{rf,plasma}} = 300\,\mathrm{W}$, and $P_{\mathrm{rf,table}} = 10\,\mathrm{W}$. After etching the top Nb layer, the photoresist is removed using acetone and isopropanol in an ultrasonic bath.

The top Nb layer defines the area of the Josephson junctions and serves as a hard mask for the wet etching of the Al layer. We use a solution based on phosphoric and nitric acids as the etchant for Al. After the wet etching step, the bottom Nb layer is structured using the same procedure as that used for the top Nb layer.

All subsequent layers are structured using a lift-off process. For this, we apply the

[3]Merck KGaA, Darmstadt, Germany
[4]Heidelberg Instruments Mikrotechnik GmbH, Heidelberg, Germany
[5]Oxford Instruments Plasma Technology, Bristol, UK
[6]ICP is the abbreviation for Inductively Coupled Plasma - Reactive Ion Etching

Tab. 3.3: Overview of the thin-film layers comprising the µMUX devices fabricated in this work. he first three layers are sputtered in situ, forming the trilayer.

Layer	Material	Thickness	Process	Structures
1	Nb	100 nm	dry etching	CPWs, SQUID washers, electrical leads
2	Al-AlO_x	7 nm	wet etching	Josephson junction tunnel barrier
3	Nb	100 nm	dry etching	Josephson junction top electrode
4	SiO_2	125 nm	lift-off	first isolation layer
5	SiO_2	125 nm	lift-off	second isolation layer
6	Au:Pd	140 nm	lift-off	filter resistors
7	Nb	500 nm	lift-off	ground bridges, input and modulation coil, junction wiring

photoresist AZ nLOF 2020[3], expose it using the maskless aligner, and develop it with AZ 2026 MIF[3] prior to sputter deposition. The SiO_2 isolation layer is divided into two 125 nm thick layers, with separate sputter deposition processes and lithography steps. This enhances isolation, as defects in the first isolation layer can be covered by the second deposition. The SiO_2 is rf sputtered using a three-inch sputter gun with a power of $P_{\mathrm{rf}} = 200\,\mathrm{W}$ in a mixed atmosphere of Ar and O_2 with $p_{\mathrm{Ar}} = 3.6\,\mu\mathrm{bar}$ and $p_{\mathrm{O_2}} = 2.4\,\mu\mathrm{bar}$, at a rate of $\dot{d}_{\mathrm{SiO_2}} = 0.076\,\mathrm{nm\,s^{-1}}$. After each deposition, the photoresist is removed along with the material sputtered on top. The substrate is placed in a bath of the stripper TechniStrip Micro D350[7] on a hotplate at $\sim 90\,^{\circ}\mathrm{C}$ for 90 min. This is followed by two additional megasonic baths in the stripper for 5 min at 55 °C. Finally, the substrate is cleaned in two ultrasonic baths with acetone and isopropanol.

Following the same lift-off procedure, the 140 nm thick resistive Au:Pd layer is deposited. The deposition of Au:Pd requires a sticking layer, for which we employ a thin $\sim 2\,\mathrm{nm}$ Nb layer sputtered in situ both above and below the Au:Pd layer. The Au:Pd layer is dc sputtered using a two-inch sputter gun, with $P_{\mathrm{dc}} = 70\,\mathrm{W}$, at a pressure of $p_{\mathrm{Ar}} = 5\,\mu\mathrm{bar}$ and at a rate of $\dot{d}_{\mathrm{Au:Pd}} = 0.52\,\mathrm{nm\,s^{-1}}$. The layer thickness is chosen to yield a resistivity of $2\,\Omega/\square$.

Before the final 500 nm thick Nb layer is deposited, the wafer is cleaned in situ with an Ar ion source, exposing it to an ion beam with a beam current $I_{\mathrm{beam}} = 20\,\mathrm{mA}$ and a beam voltage $V_{\mathrm{beam}} = 275\,\mathrm{V}$ at an Ar pressure of $p_{\mathrm{Ar}} = 1.3\,\mu\mathrm{bar}$. Applying this ion beam for 5 min physically etches $\sim 10\,\mathrm{nm}$ of the exposed Nb surfaces, removing resist residues and surface oxides that might otherwise degrade the quality of superconducting vias. Finally, the Nb layer is dc sputtered using a two-inch sputter gun with a power of $P_{\mathrm{dc}} = 60\,\mathrm{W}$, at a pressure of $p_{\mathrm{Ar}} = 5\,\mu\mathrm{bar}$, and at a rate of $\dot{d}_{\mathrm{Nb}} = 0.32\,\mathrm{nm\,s^{-1}}$.

After lift-off of the final metal layer, the wafer is coated with a thick protective resist layer and diced into individual chips using a wafer saw outside the cleanroom. Before measurement, the chips are cleaned in two baths of acetone and isopropanol in an ultrasonic bath.

[7] Technic France, Saint-Denis, France

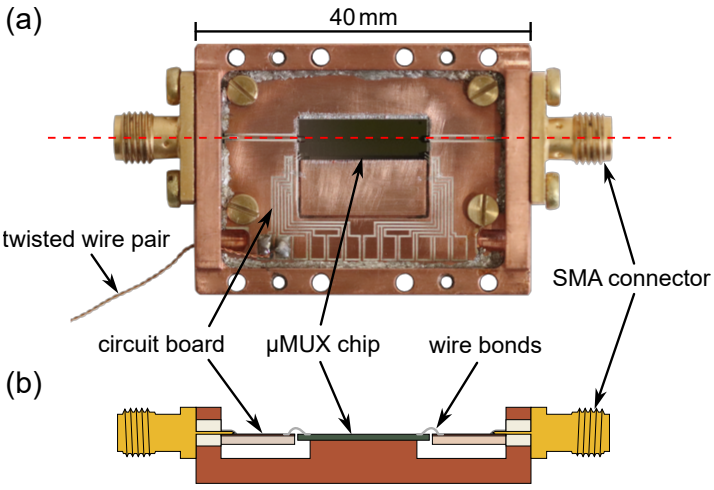

Fig. 3.6: (a) Photograph of the copper µMUX sample holder used for all samples in this thesis. A circuit board mounted inside the copper housing interfaces the rf and dc wiring to the µMUX chip, which is glued at the center. The red dashed line indicates the cross section shown in (b). (b) Cross section of the sample holder along the CPW feedline. A gap in the copper housing is left below the circuit-board CPW and the tapered feedline bondpads of the µMUX chip. The circuit board and µMUX are connected by aluminum wire bonds.

3.5 Cryogenic µMUX housing

After fabrication, the µMUX wafer is cut into individual µMUX chips, which must be mounted in a housing for installation in a cryostat and connection to the cryogenic readout chain. The µMUX housing designed for the µMUX samples fabricated during this thesis is shown in figure 3.6. The housing is constructed from copper, which provides an electrical ground for the rf circuits and also offers good thermal conductivity for thermalizing the µMUX chips in the cryostat. The µMUX must be connected to the cryogenic readout chain, which employs the SMA standard for its connectors. Consequently, we designed the µMUX housing to adhere to the same standard, utilizing SMA connectors with a gold plated brass body and gold plated beryllium copper contacts to interface with the CPW line of the circuit board within the housing.

The circuit board provides an interface between the rf and dc circuitry of the µMUX chip and the external electronics. It is fabricated from a 635 µm thick Rogers TMM 10i[8] laminate with an 18 µm copper foil cladding. The board is attached to the housing using brass screws, with a thin layer of Apiezon N[9] vacuum grease to improve thermal contact. At the edges, the ground plane is electrically connected to the housing using indium. The center pin of the SMA connector is soldered to the CPW on the board, which has a 450 µm wide center conductor and a slot width of 200 µm. The CPW runs across the housing from left to right, leaving a gap in the center for the µMUX chip. At the bottom of the board, the dc wiring provides connections to the modulation line and optional detector chips and can be soldered to the external electronics.

[8]Rogers Corporation, Chandler, AZ, USA
[9]M&I Materials Ltd, Manchester, United Kingdom

Below the CPW of the circuit board and below the tapered bondpads of the µMUX chip, we left a gap in the copper housing, reducing the capacitive coupling between the CPW center conductor and the housing ground below. Without this gap, the housing would significantly contribute to the characteristic impedance of the wide CPW, leading to an impedance mismatch between it and the connected 50 Ω network.

The µMUX chip is placed in the center of the housing, attached using GE-7031 low temperature varnish[10]. Electrical connections between the µMUX chip and the circuit board are established with aluminum wire bonds. Since a wire bond has an inductance of $\sim 1\,\mathrm{nH\,mm^{-1}}$ [Rog03], it introduces an impedance mismatch when connecting the feedline of the µMUX chip to the circuit boards CPW. To minimize this mismatch, we keep the wire bonds as short as possible and place at least five wire bonds in parallel when connecting the CPW center conductor, along with an additional five wire bonds for the ground plane on each side. The dc lines are connected twice for redundancy.

Special attention must be paid to the connection of the ground plane. Insufficient grounding can lead to the occurrence of parasitic modes along the edge of the ground plane of the µMUX chip, which can be suppressed by increasing the density of placed grounding wire bonds and keeping their spacing homogeneous [Wen11]. The ground plane of the µMUX couples capacitively to the µMUX housing underneath and is simultaneously connected inductively through the grounding wire bonds. Using a simple impedance-ladder model, we can calculate the resonance frequency f_{par} of this circuit, above which the parasitic modes become significant [Wen11], affecting transmission through our µMUX chip and the resonance depth of our µMUX channels. With the Inductance L_{w} per wire bond and the capacitance C_{w} between the housing and the µMUX ground plane between adjacent wire bonds, we can calculate

$$f_{\mathrm{par}} = \frac{1}{2\pi\sqrt{L_{\mathrm{w}}C_{\mathrm{w}}}}. \tag{3.1}$$

The ground plane of our µMUX chip forms a plate capacitor with the µMUX housing, resulting in a capacitance of $C_{\mathrm{GND}} \approx 30\,\mathrm{pF}$. Assuming this capacitance is evenly distributed among a total of N wire bonds, we obtain $C_{\mathrm{w}} = C_{\mathrm{GND}}/N$. Furthermore, assuming a wire bond inductance of $L_{\mathrm{w}} = 0.75\,\mathrm{nH}$, we can approximate the minimum number of wire bonds required for the desired µMUX operation frequency. For frequencies up to 20 GHz, this results in a requirement of over 350 wire bonds. However, in reality, this number is further increased due to the inhomogeneous wire bond spacing enforced by the bondpads at the edge of the chip [Wen11]. Hence, we placed more than 350 wire bonds for the measurements presented in this thesis.

After installing the µMUX chip, the housing is closed with a copper lid. To suppress box resonances inside the housing, we designed the lid to occupy the majority of the interior volume, leaving only an open space of $17\,\mathrm{mm} \times 7\,\mathrm{mm} \times 2.5\,\mathrm{mm}$ above the µMUX chip, which results in the lowest box resonance at 23 GHz.

[10] Von Roll USA Inc., Schenectady, NY, USA

3.6 Cryogenic microwave readout chain

In section 2.5, we discussed the various contributions to the total noise of a µMUX-based readout system. At present, the noise performance is ultimately limited by the noise temperature $T_{\mathrm{N,system}}$ of the cryogenic readout chain. Therefore, the layout of the readout chain is critical when designing a µMUX system. Since microcalorimeters are typically operated at millikelvin temperatures, all measurements presented in this thesis were performed inside a ^{3}He/^{4}He dilution refrigerator[11], which can cool its experimental stage, the mixing chamber (MXC) stage, to temperatures $T < 7\,\mathrm{mK}$. We designed and installed two readout channels for unidirectional transmission measurements in the cryostat, considering noise performance and heat load on the cryostat's cooling stages. Both channels are depicted schematically in figure 3.7. One channel provides a bandwidth of 6-20 GHz for measurements of µMUX devices operating in the $\mathrm{K_u}$ frequency band, while the other offers a bandwidth of 4-8 GHz in exchange for an improved noise temperature.

To estimate the noise temperature of our readout chain, we can model it as a cascade of n two-port networks with noise temperatures $T_{\mathrm{N},i}$ and power gain/attenuation G_i. With this, we can calculate the total input-referred noise temperature using the Friis formula [Fri44]:

$$T_{\mathrm{N,tot}} = T_{\mathrm{N},1} + \frac{T_{\mathrm{N},2}}{G_1} + \frac{T_{\mathrm{N},3}}{G_1 G_2} + ... + \frac{T_{\mathrm{N},n}}{G_1 G_2 ... G_{n-1}}. \tag{3.2}$$

The noise temperature $T_{\mathrm{N},i}$ of an attenuator with an attenuation G_i is calculated using its physical temperature T with $T_{\mathrm{N},i} = T(1 - G_i)/G_i$, whereas the noise temperature of an amplifier is a characteristic quantity typically provided by its manufacturer. From this and from equation 3.2, it is apparent that attenuation is ideally implemented at low temperatures. In a cascade of amplifiers, the amplifier with the lowest noise temperature should be installed first.

In our readout chains, we must install attenuation on the transmitting (TX) side to reduce the power of the probe tones generated by the SDR electronics for optimal µMUX readout power and noise performance. On the receiving (RX) side, the probe tones must be amplified before measurement at room temperature, such that the noise temperature of the room temperature electronics becomes negligible. All cables and components in our readout chains utilize SMA connectors. In total, three different types of coaxial cables are employed to connect the room temperature electronics to the device under test (DUT) at the MXC-stage. We use semirigid beryllium copper cables with silver plated inner conductor[12] as a compromise between cable attenuation and heat conductivity. Below, the 4 K stage, we also employ semirigid superconducting NbTi cables[13], which provide negligible attenuation with minimal thermal conductivity.

[11] LD250, Bluefors, Helsinki, Finland
[12] BCB018 - 0.085" Diameter SP BeCuBeCu, CryoCoax, Crossville, TN, USA
[13] BCB012 - 0.034" Diameter NbTi/NbTi, CryoCoax, Crossville, TN, USA

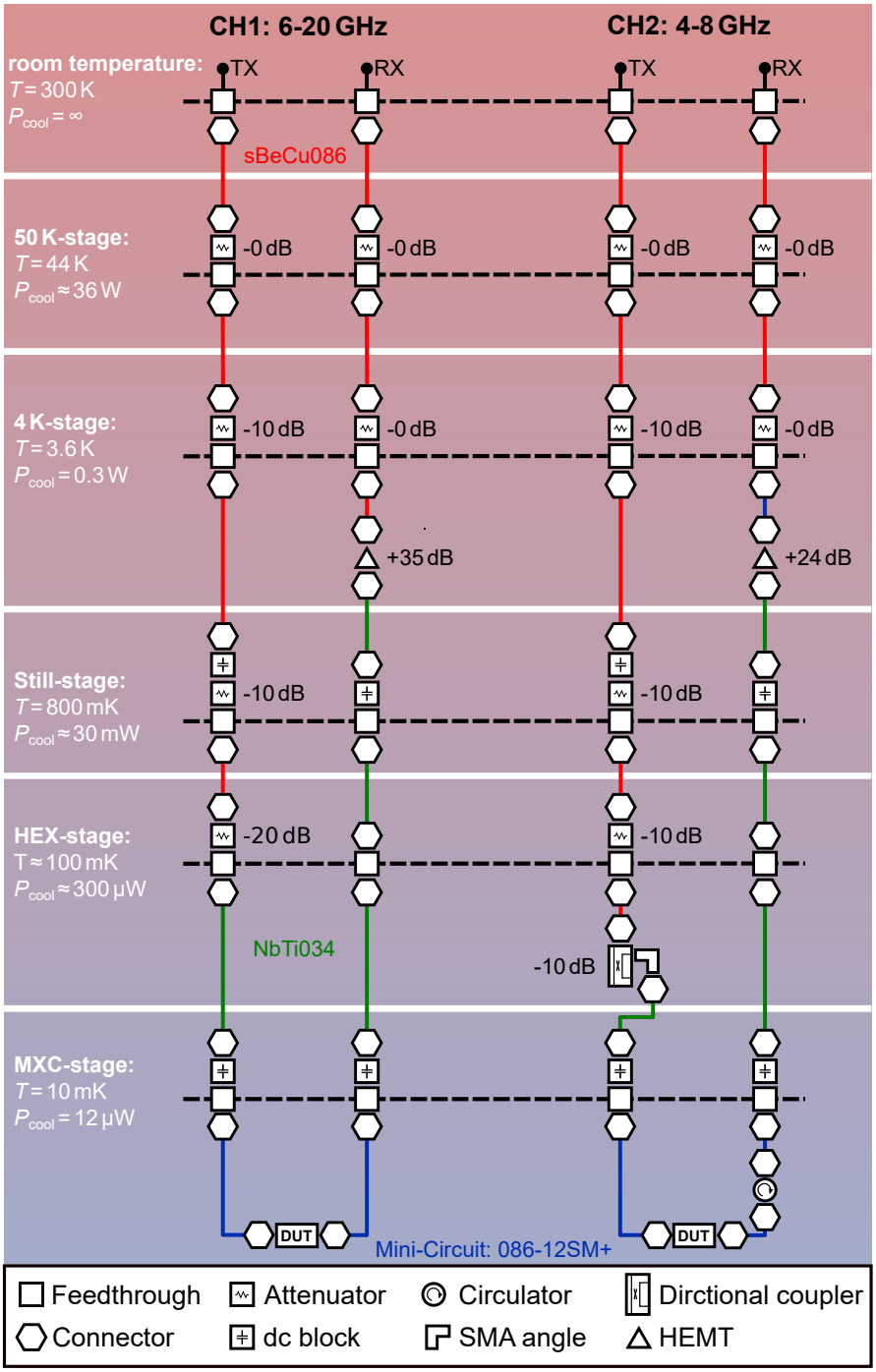

Fig. 3.7: Schematic of the rf wiring inside the dilution refrigerator. Two readout chains are installed: Channel 1 (CH1) with a bandwidth of 6–20 GHz and channel 2 (CH2) with a bandwidth of 4–8 GHz. Components at the different cooling stages are identified in the legend. Cable types are color-coded: beryllium copper (sBeCu086, red), niobium titanium (NbTi034, green), and Mini-Circuits flexible cables (Mini-Circuit: 086-12SM+, blue).

When connecting components on the same cryostat stage, thermal conductivity does not have to be considered, and we can employ standard flexible coaxial cables[14].

For optimal noise performance, it is ideal to install all attenuation on the MXC-stage. However, the power dissipated from the attenuated probe tones and the cooling power of the cryostat's individual cooling stages must be taken into account. Thus, we distributed the attenuators[15] across the RX side. The attenuators also electrically connect the inner and outer conductors and, therefore, the inner conductor and the cryostat cooling stage, improving the thermalization of the inner conductor. Thus, we installed 0 dB attenuators on both the RX and TX paths.

On the still-stage and the MXC-stage, we installed dc-blocks[16], which interrupt the inner and outer conductors of the coaxial cables, providing thermal isolation from the warmer cryostat stages. In the 4-8 GHz channel, we installed a directional coupler[17] on the heat exchanger stage (HEX-stage). The directional coupler is terminated with 50 Ω in two of its ports. The attenuated power is dissipated in the first termination, while the second termination, connected to the ongoing transmission line, remains cold, thereby keeping the noise temperature of the final attenuation stage low.

On the RX side, we installed cryogenic low noise HEMT[18] amplifiers, as the first amplification stage. As the amplifiers dissipate several milliwatts of power, they must be installed on the 4 K-stage, where sufficient cooling power is provided. In the 4-8 GHz channel, the amplifier[19] exhibits a noise temperature of $T_{\mathrm{N,HEMT}} \approx 2\,\mathrm{K}$ at 6 GHz, while the amplifier[20] in the 6-20 GHz channel exhibits a noise temperature of $T_{\mathrm{N,HEMT}} \approx 5\,\mathrm{K}$ at 16 GHz. In the 4-8 GHz channel, we installed a circulator[21] between DUT and amplifier, with its third port terminated with 50 Ω. In this configuration, we isolate the DUT from noise, back action, and reflected signals coming from the HEMT amplifier, such that the noise seen by the DUT is determined by the cold 50 Ω termination in the circulator. Since no cryogenic circulators or directional couplers were available for the 6-20 GHz frequency range at the time of designing the readout chains, the corresponding channel is not equipped with either.

Assuming an attenuation of −0.1 dB per feedthrough, −0.5 dB per dc block and circulator, and a true attenuation of −0.3 dB for each 0 dB attenuator, we can estimate the system noise temperatures of our channels using equation 3.2. For both channels, the TX side contributes a noise temperature of $< 100\,\mathrm{mK}$ referred to the DUT input. The RX side is the major contributor to the system noise, with $\sim 6.9\,\mathrm{K}$ at 16 GHz for channel 1 and $\sim 3.3\,\mathrm{K}$ at 6 GHz for channel 2, yielding a total system noise of $T_{\mathrm{N,CH1}}(16\,\mathrm{GHz}) \approx 7\,\mathrm{K}$ for channel 1 and $T_{\mathrm{N,CH2}}(6\,\mathrm{GHz}) \approx 3.4\,\mathrm{K}$ for channel 2.

[14] 086-12SM+, Mini-Circuits, Brooklyn, NY, USA
[15] 18AH-0, Inmet by Spectrum Control, Fairview, PA, USA
[16] dc block 8039, Inmet by Spectrum Control, Fairview, PA, USA
[17] QMC-CRYOCOUPLER-10, Quantum Microwave Components, Hingham, MA, USA
[18] High-Electron-Mobility Transistor
[19] LNF-LNC4_8C_LG, Low Noise Factory AB, Göteborg, Sweden
[20] LNF-LNC6_20D, Low Noise Factory AB, Göteborg, Sweden
[21] LNF-CIC4_8A, Low Noise Factory AB, Göteborg, Sweden

To increase the capacity for measuring different samples during a single cryostat cooldown and to enable normalization measurements, we installed two cryogenic rf-switches[22] in the cryostat. The switches can be connected to the RX and TX sides of either channel on the MXC-stage. The latching switches are controlled through short current pulses, which are applied through a set of twisted, normal conducting CuNi and superconducting NbTi wire pairs, generated by a custom controller at room temperature (see section A.2).

3.7 Room temperature setup for µMUX characterization

For µMUX characterization measurements throughout this thesis, we used a vector network analyzer[23] (VNA) in the setup depicted in figure 3.8 (a). The VNA is connected to the cryogenic readout chain using a set of flexible coaxial cables[24]. To avoid ground loops, we connect these cables to the cryostat through the same dc-blocks used in the cryogenic readout chain. We installed an additional amplification stage after the HEMT amplifier at room temperature. The amplifier[25] for the 4-8 GHz channel has a noise temperature of $\sim 130\,\mathrm{K}$, raising the system noise temperature to $T_{\mathrm{N,CH2}} \approx 4.3\,\mathrm{K}$, the amplifier[26] for the 6-20 GHz channel has a noise temperature of $\sim 275\,\mathrm{K}$, raising the noise temperature to $T_{\mathrm{N,CH1}} \approx 7.1\,\mathrm{K}$.

To modulate the applied magnetic flux to the µMUX channels of the rf-SQUID, we use a set of SQUID electronics[27] that generates a dc current, which can be applied to the µMUX chip's modulation line through a set of twisted CuNi wire pairs. To vary the readout power P_{rf} applied to the µMUX channels, we adjust the VNA output power P_{VNA}. The VNA, as well as the SQUID electronics, is controlled from a PC, enabling automated measurements of the S_{21} parameter as a function of the applied magnetic flux. Additionally, the VNA (as well as the SDR electronics in chapter 5 and the signal generator and analyzer in section 7.3.3) is supplied with an external reference frequency generated by a rubidium frequency standard[28]. The µMUX chip to be characterized is connected to one of the rf-switch channels in parallel to a simple through line. In this way, we can measure the transmission through the setup without the µMUX sample, which can be used to normalize the S_{21} data, correcting for attenuation and amplification in the RX and TX branches.

We used the setup depicted in figure 3.8 to characterize a µMUX with $f_{\mathrm{r}} = 3.9\,\mathrm{GHz}$ connected to the 6-20 GHz cryogenic readout channel. Even though the amplifiers in this setup are only specified down to 6 GHz, we found them still sufficient to perform S_{21} measurements down to $\sim 3.5\,\mathrm{GHz}$. We measured the dependence of the µMUX

[22] R583423141, Radiall, Tempe, AZ, USA
[23] P5024B, Keysight Technologies, Santa Rosa, CA, USA
[24] ST18/SMAM/SMAM/72IN, Huber+Suhner, Herisau, Switzerland
[25] ZX60-83LN-S+, Mini-Circuits, Brooklyn, NY, USA
[26] ZX60-06203ALN+, Mini-Circuits, Brooklyn, NY, USA
[27] XXF-1, Magnicon, Hamburg, Germany
[28] FS725, Stanford Research Systems, Sunnyvale, CA, USA

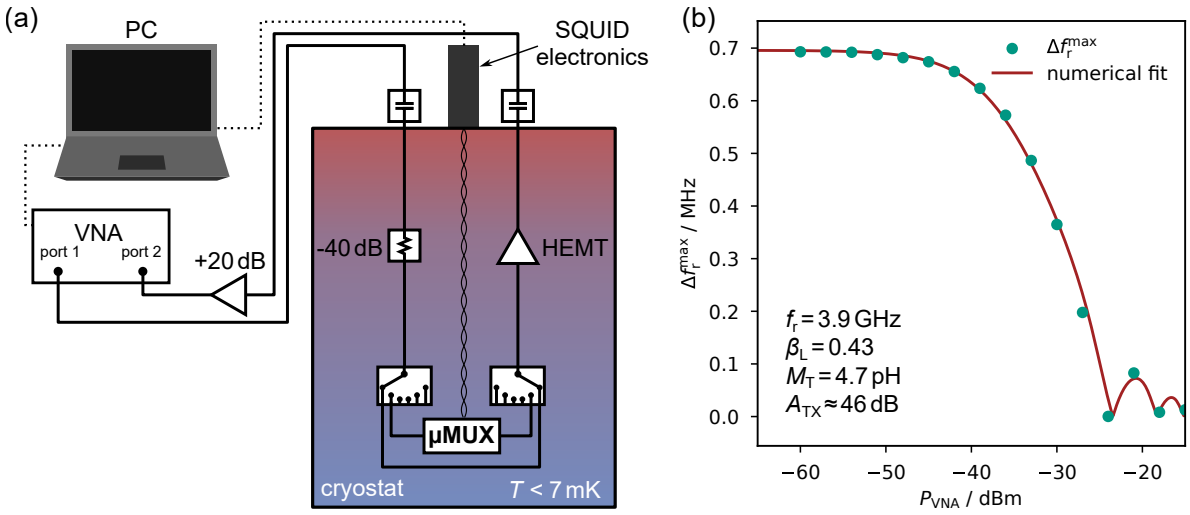

Fig. 3.8: (a) Measurement setup for μMUX characterization. Two rf-switches connect the μMUX to one of the two cryogenic readout chains, while a second switch path provides a through connection without a device under test. The transmission parameter S_{21} is measured with a VNA. A room-temperature amplifier is placed before VNA port 2 to compensate for the installed attenuation. The SQUID electronics applies the modulation current to the rf-SQUIDs via a copper–nickel twisted-pair connection to the μMUX. (b) Total resonance frequency shift of a μMUX channel as a function of readout power P_{VNA}. Equation 2.19 is numerically fitted to the data to extract the total transmission side attenuation at 3.9 GHz, yielding $A_{\mathrm{TX}} \approx 46\,\mathrm{dB}$.

channels peak-to-peak resonance frequency shift Δf_{r} as a function of the applied VNA output power P_{VNA}, which is depicted in figure 3.8 (b). From this, we can derive the power applied to the μMUX on-chip, using equation 2.51, which allows us to determine the actual attenuation installed in the TX branch of this setup. We determine a total attenuation of $A_{\mathrm{TX}} \approx 46\,\mathrm{dB}$ at 3.9 GHz. Consequently, we can attribute 6 dB of attenuation to ideally lossless components, such as the cables and dc-blocks. Since the TX branches of both readout channels are mostly identical, we expect the same total attenuation for the 4-8 GHz channel.

3.8 Algorithms employed for data analysis

In the following, we provide a brief introduction to the circle-fit algorithm and Welch's method, which we employed when characterizing most of our measurement data. The circle-fit was utilized to extract characteristic resonance parameters, such as the resonance frequency f_{r} and the quality factors Q_{l}, Q_{c}, and Q_{i}, while we applied Welch's method to calculate the power spectral densities from measured noise traces of any quantity, such as those presented in section 5.6.3 and 7.3.3.

3.8.1 Circle-fit algorithm for microwave resonators

The S_{21} parameter of resonance curves measured with a VNA typically deviates significantly from equation 2.20 due to the additional influences of cable length, attenuation, and delay, as well as the effects of impedance mismatches in proximity to the resonator. We use the algorithm described in [Pro15] to fit the function

$$S_{21}(f) = ae^{i\alpha}e^{-2\pi i f\tau}\left[1 - \frac{(Q_\mathrm{l}/|Q_\mathrm{c}|)e^{i\theta}}{1 + 2iQ_\mathrm{l}\frac{f-f_\mathrm{r}}{f_\mathrm{r}}}\right] \tag{3.3}$$

to the complex resonance circle and extract our characteristic resonance parameters. Here, a accounts for the net attenuation or amplification present in the transmission line. τ represents the finite run time of a signal along the transmission line, resulting in a phase delay that is proportional to frequency. An additional quantity, α, is included to account for any phase delay that might arise from the various components in the readout chain. Lastly, the real valued coupled quality factor Q_c is replaced by a complex quality factor $|Q_\mathrm{c}|e^{-i\theta}$, where θ quantifies the impedance mismatch, which causes asymmetric resonance curves.

3.8.2 Welch's method for estimating spectral densities

For a measured sequence $X(j)$ with $j \in \{0,\ldots,N-1\}$, resulting from sampling a continuous-time signal $X(t)$ at a uniform sampling frequency f_s, we can estimate the power spectrum using Welch's method [Wel67]. In this method, we subdivide the sampled signal time trace $X(j)$ into K overlapping segments of length L, with an overlap of $L - D$ data points:

$$X_k(j) = X(j + kD) \quad \text{with} \quad k \in \{0,\ldots,K-1\} \quad \text{and} \quad j \in \{0,\ldots,L-1\}. \tag{3.4}$$

For each segment, we apply a window function $W(j)$ and calculate the periodogram

$$S_{XX}^{(k)}(f) = \frac{2}{LUf_\mathrm{s}}\left|\sum_{j=0}^{L-1} X_k(j)W(j)e^{-2\pi ijf/f_\mathrm{s}}\right|^2, \tag{3.5}$$

where $f = (n/L)f_\mathrm{s}$ is the frequency, and $n \in \{1,\ldots,L/2-1\}$. Here, U is a normalization factor for the applied window function and is derived from

$$U = \frac{1}{L}\sum_{j=0}^{L-1} W^2(j) \tag{3.6}$$

Finally, the Welch power spectrum is obtained by averaging the individual modified periodograms

$$\langle S_{XX} \rangle (f) = \frac{1}{K} \sum_{k=0}^{K-1} S_{XX}^{(k)}(f). \tag{3.7}$$

For the power spectra calculated in this thesis, we used a minimum 4-term Blackman-Harris window, as implemented in the Python library *SciPy*[29] and a segment overlap of $D = L/2$. While a larger number of short segments results in higher fidelity of the estimated power spectrum, it also reduces frequency resolution. On the other hand, a low number of long segments enhances frequency resolution. However, this comes at the cost of power spectrum fidelity. To obtain both, a power spectrum estimate at low frequencies and high fidelity at high frequencies, we stitch together multiple Welch spectra calculated using varying window lengths for the same acquired time trace.

[29]SciPy 1.17.1, scipy.org

4. Intrinsic quality factor of µMUX devices

The noise performance of a microwave SQUID multiplexer strongly depends on the signal induced total change in amplitude of the probe tones. Maximizing this change requires deep resonance curves, ideally approaching full suppression of probe tone transmission, i.e. $S_{21}^{\mathrm{min}} = 0$, at the resonance frequency. The depth of the resonance is primarily determined by the intrinsic quality factor Q_{i}, which quantifies energy dissipation within the resonator. Previous works have shown that Q_{i} represents a dominant limitation on the achievable noise performance of µMUX-based readout systems [Ric21b]. A detailed understanding of the underlying loss mechanisms and strategies to mitigate them is therefore essential for maximizing the µMUX performance.

In this chapter, we examine the loss mechanisms that limit the intrinsic quality factor of µMUX resonators. We will also present measurements investigating the impact of the µMUX dc circuitry and discuss how the microwave properties of modulation and input lines affect both the resonance depth and the resulting resonance frequency shift.

4.1 Loss mechanisms in superconducting microwave resonators

The losses in superconducting microwave resonators have been investigated in great detail over the past two decades [Zmu12, McR20]. While the total loss within the resonator is determined by various loss mechanisms, the combination of quasiparticle losses Q_{MB}^{-1}, two-level system losses Q_{TLS}^{-1}, radiation losses Q_{rad}^{-1}, and vortex induced losses Q_{v}^{-1} generally dominates.

In an alternating electric field, both superconducting Cooper pairs and normal conducting quasiparticles contribute to the current in the superconductor, with the latter resulting in ohmic losses. The corresponding quality factor can be derived from the Mattis-Bardeen integrals (see equation 2.7 and 2.8) as follows:

$$Q_{\mathrm{MB}} = \frac{2}{\alpha\beta}\frac{\sigma_2}{\sigma_1}. \tag{4.1}$$

Here, $\alpha = L_{\mathrm{kin}}/L_{\mathrm{tot}}$ is the ratio of the resonator's kinetic inductance L_{kin} to its total inductance L_{tot}, and the parameter $\beta = 1 + \frac{2d/\lambda}{\sinh 2d/\lambda}$ accounts for the dependence of the magnetic penetration depth λ on the film thickness d. As the temperature decreases, the quasiparticle number density and, hence, the real part of the complex conductivity σ_1 decrease exponentially. Consequently, losses due to thermally excited quasiparticles can be neglected at temperatures $T \ll T_{\mathrm{c}}$. Quasiparticles can also be generated through infrared stray light [Bar11] as well as high readout powers P_{rf}, even at frequencies well below the gap energy of the superconductor, resulting in losses with $Q_{\mathrm{MB}}^{-1} \propto P_{\mathrm{rf}}^{1/2}$ [Vis14]. However, these effects can be mitigated through multilayered radiation shields and by limiting the readout power.

In amorphous solids, such as many dielectrics, at surfaces, interfaces, and in photoresist residues, two-level systems (TLS) can occur [Phi87, Gao08c, Mac10, Qui14]. TLS couple to the resonator's electric field and contribute to its effective dielectric constant $\epsilon_{\mathrm{r,eff}}$, which leads to a temperature dependent resonance frequency as well as resonance frequency noise [Gao08b]. Additionally, these TLS introduce power and temperature dependent loss that can be described by [Gao08a]:

$$Q_{\mathrm{TLS}}^{-1} = F\delta_{\mathrm{TLS}}^{0}\frac{\tanh\left(\frac{\hbar\omega}{2k_{\mathrm{B}}T}\right)}{\sqrt{1+\frac{P_{\mathrm{rf}}}{P_{\mathrm{c}}}}}. \tag{4.2}$$

Here, $\delta_{\mathrm{TLS}}^{0}$ is the TLS loss tangent in the low power and low temperature limit, and F is the filling factor, which accounts for the spatial distribution of TLS within the resonator's electric field. The TLS losses decrease as the readout power P_{rf} is increased due to TLS saturation effects. P_{c} is the critical power that defines this saturation power-dependence. In µMUX readout, we typically operate above P_{c}, yet TLS losses still represent a significant contribution to the total resonator loss [Loh24].

Radiation losses refer to the microwave power radiating from the resonator into free space, as well as dissipation induced by the resonators field far from the device, such as currents in the normalconducting microwave housing. These losses increase with device dimensions and the resonance frequency [Maz04]:

$$Q_{\mathrm{rad}}^{-1} \propto \omega^2(s+w)^2 \tag{4.3}$$

with s and w denoting the CPW center line width and slot width, respectively. Consequently, these losses can be reduced by decreasing the CPW dimensions [Sag11]. However, a compromise must be made, as TLS losses increase with smaller slot widths, as smaller slot widths concentrate the electric field close to the substrate surface, where the TLS density is typically the highest. Further methods for reducing radiation losses include the use of high kinetic inductance materials [Häh20] and the mitigation of dissipative currents in the microwave housing through superconducting screening layers [Goe16].

Vortices typically occur when a type-II superconducting thin film is exposed to a perpendicular magnetic field. Above a magnetic field of $B_{\mathrm{m}} \approx \Phi_0/W^2$, where W denotes the smallest width of the thin film structure, vortices may enter the superconducting film [Sta04]. Since the centers of these vortices are normal conducting, they can dissipate power as they move through the superconducting layer. This movement is caused by the Lorentz force induced by the currents in the superconducting layer. Therefore, they degrade the intrinsic quality factor of the resonator [Son09], particularly when near the current antinodes [Nsa14]. The occurrence of vortices can be minimized by magnetic shielding, which screens external fields, such as the Earth's magnetic field, from the sample. Additionally, incorporating a lattice of holes into the superconducting structures provides artificial pinning sites that trap vortices and prevent their motion [Bot11].

4.2 rf-SQUID contribution to the intrinsic quality factor

Superconducting microwave resonators, including lumped-element and transmission line resonators, routinely achieve intrinsic quality factors $Q_\mathrm{i} > 10^5...10^6$ [Sag11, Nar20]. However, the intrinsic quality factors observed in practical µMUX devices are typically one order of magnitude lower [Hir13, Koh14, Dob21, Ric23]. Additionally, a substantial reduction in the intrinsic quality factor is often observed for those µMUX channels for which a detector is connected to the input coil [Ric23, Gro25].

Connecting the load inductor and coupling to the rf-SQUID, along with the input and modulation coils to the resonator, introduces additional elements through which power can be dissipated and microwave leakage into external electronics can occur. Within the rf-SQUID, losses can arise in the Josephson junction. By employing the RCSJ model and incorporating a sub-gap resistance R_sg shunting the ideal Josephson junction, it is possible to derive the quality factor Q_sg that accounts for the µMUX channel losses within the Josephson junction [Weg18, Kem17b]:

$$Q_\mathrm{sg}(\varphi_\mathrm{tot}) = \frac{\pi Z_0 R_\mathrm{sg}(1+\beta_\mathrm{L}\cos\varphi_\mathrm{tot})^2}{4(\omega M_\mathrm{T})^2}. \tag{4.4}$$

As a result, the intrinsic quality factor becomes flux dependent through $\varphi_\mathrm{tot}(\varphi_\mathrm{ext})$, and the resonance depth is generally reduced, particularly for magnetic flux biases approaching $(n \pm 1/2)\Phi_0$. However, for the high-quality Josephson junctions used in this thesis, the junctions typically exhibit normal resistance to sub-gap resistance ratios of $R_\mathrm{sg}/R_\mathrm{N} \geq 30$, resulting in sub-gap resistances on the order of $\gtrsim 1\,\mathrm{k\Omega}$. Consequently, the sub-gap-related quality factor takes values of $Q_\mathrm{sg} > 10^5$ and is not expected to be a dominant effect in our µMUX devices.

Additionally, losses can occur within the filter resistor R_f that shunts the input coil. Although this filter primarily functions to prevent the leakage of microwave power into the connected detector, a portion of the filtered microwave power is dissipated within the filter resistor itself. Analogous to the losses attributed to the sub-gap resistance, the losses incurred by the filter resistor are dependent on the magnetic flux. These losses can be quantified using a quality factor Q_f (see section A.4):

$$Q_\mathrm{f}(\varphi_\mathrm{tot}) \approx \frac{\pi Z_0}{4R_\mathrm{f}} \frac{[L_\mathrm{in}L_\mathrm{SQ}(\varphi_\mathrm{tot}) - M_\mathrm{in}^2]^2}{M_\mathrm{T}^2 M_\mathrm{in}^2 + L_\mathrm{SQ}(\varphi_\mathrm{tot})[M_\mathrm{p}^2 L_\mathrm{SQ}(\varphi_\mathrm{tot}) - 2M_\mathrm{in}M_\mathrm{T}M_\mathrm{p}]}. \tag{4.5}$$

with

$$L_\mathrm{SQ}(\varphi_\mathrm{tot}) := L_\mathrm{S}(1 + [\beta_\mathrm{L}\cos\varphi_\mathrm{tot}]^{-1}). \tag{4.6}$$

We assumed that only the filter resistor R_f shunts the input coil, with no detector connected. Furthermore, R_f is selected to satisfy the condition $\omega_\mathrm{c} = R_\mathrm{f}/L_\mathrm{in} \ll \omega$, ensuring that the filter effectively attenuates the excitation tone to prevent microwave leakage into the detector. The mutual inductance M_p represents the parasitic coupling between the load inductor and the input coil. Similar to the sub-gap resistance, this

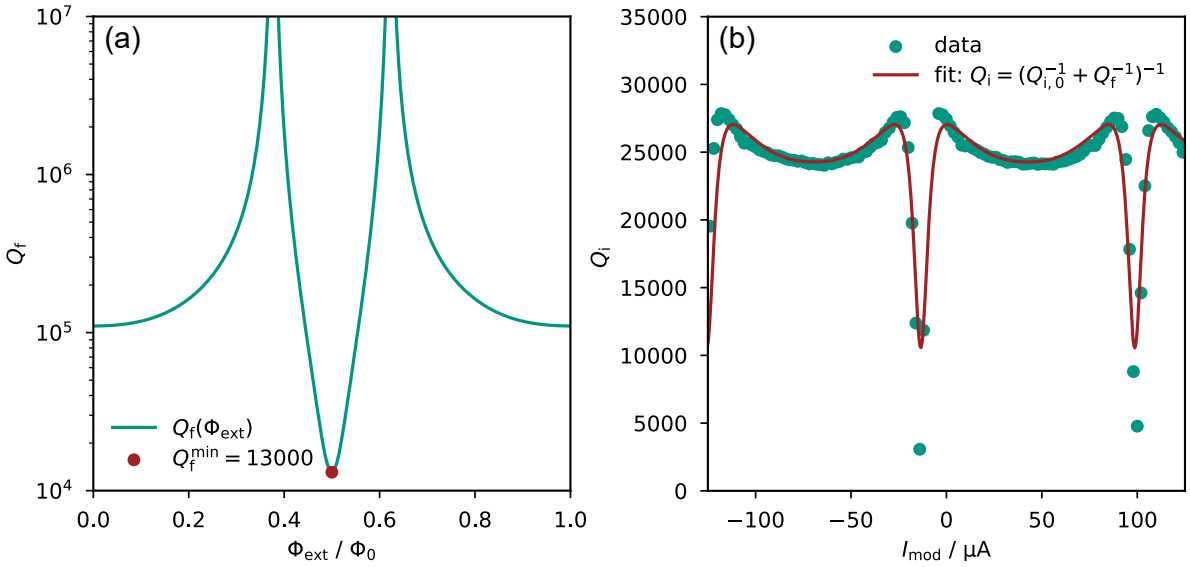

Fig. 4.1: (a) Calculated dependence of the intrinsic quality factor of the 5.5 GHz µMUX channel from *Hifr-Mux-06* chip *A4* (see section 5.3) as a function of the applied external magnetic flux. The lowest filter-related quality factor Q_f^{min} is marked with a red circle at $\Phi_{ext} = \Phi_0/2$. Above and below $\Phi_0/2$ the quality factor diverges for a single flux bias value, when assuming a negligible parasitic coupling M_p. (b) Measured Q_i data as a function of magnetic flux, for the same µMUX channel (see section 5.5). The data was fitted using the flux dependent quality factor Q_f from (a), combined with a flux independent quality factor $Q_{i,0}$.

results in degradation of Q_i for magnetic flux values of $\Phi_{tot} \approx (n \pm 1/2)\Phi_0$. Typically, Q_f assumes values around 10^5. However, it is highly dependent on the specific design parameters of the rf-SQUID and filter resistor. Moreover, the expression for Q_f changes once an actual detector is connected to the input coil. In section 4.3, we will consider the influence of the filter on the resonance frequency shift, as well as the more general case of an arbitrary complex impedance connected to the input coil, which can be used to describe arbitrary circuits connected to the input coil.

In figure 4.1 (a), the filter-related quality factor is plotted as a function of magnetic flux, calculated using equation 4.5. The rf-SQUID inductances and filter resistor parameters are chosen to match the design of the 5.5 GHz µMUX channel of *Hifr-Mux-06* chip *A4* (see section 5.3), with the determined screening parameter of $\beta_L = 0.8$ (see section 5.5). The quality factor reaches its global minimum at $\Phi_{tot} \approx (n \pm 1/2)\Phi_0$, and when assuming negligible parasitic coupling M_p, it diverges for one magnetic flux value between $n\Phi_0$ and $(n \pm 1/2)\Phi_0$. The position of this divergence is primarily defined by the screening parameter β_L. Using this flux dependent quality factor, we fitted the measured total intrinsic quality factor as a function of modulation current I_{mod} (see section 5.5), assuming that all other loss mechanisms are flux independent. The fit is plotted in figure 4.1 (b). We observe the expected minimum in the intrinsic quality factor at $\sim -15\,\mu A$, corresponding to a flux bias of $(n \pm 1/2)\Phi_0$. We also observe maxima in Q_i for magnetic flux values slightly above and below, corresponding to the diverging

Q_f, which cannot be explained by the flux dependent losses in the sub-gap resistance. We selected the mutual inductances M_p and M_T, as well as a flux independent intrinsic quality factor $Q_{\mathrm{i},0}$, as free fit parameters and found $Q_{\mathrm{i},0} = 27\,000$, $M_\mathrm{p} \approx 0\,\mathrm{pH}$, and $M_\mathrm{T} = 6.2\,\mathrm{pH}$. The latter deviates from the expected parameter $M_\mathrm{T} = 4.2\,\mathrm{pH}$ from section 5.5. Similarly, the fit itself does not perfectly agree with the measured Q_i data. Both aspects can likely be traced back to a slightly non-sinusoidal current-phase relation of the Josephson junction, caused by inhomogeneities in the tunnel barrier. The effect of these inhomogeneities will be discussed in greater detail in section 6.3.

4.2.1 Integration of the rf-SQUID into the µMUX

The degraded Q_i observed in full µMUX devices compared to bare resonators can be attributed to several factors. The rf-SQUID introduces additional losses not only through the sub-gap resistance and filter resistor but also through its geometry, which can enhance radiation losses. The free space radiation resistance of a short dipole $R_\mathrm{rad} \propto (\omega l)^2$ and a small loop $R_\mathrm{rad} \propto (\omega l)^4$ increases with device dimensions l and frequency ω [Kra88]. Consequently, these losses become increasingly relevant when raising µMUX operation frequency and can be compensated for by miniaturizing the rf-SQUID design. Additionally, portions of the microwave power from the excitation tone applied to the resonator can couple into the modulation line and the input line, leading to microwave leakage and losses in the connected dc wiring. In the case of the input line, the leakage of microwave power is expected to be suppressed by the filter resistor.

Bare resonators included on a µMUX chip also might not achieve the same Q_i values as those on a resonator chip. The deployment of a µMUX chip typically requires a larger measurement housing, which provides additional box modes at lower frequencies. Furthermore, the dc-wiring required for detector operation can introduce parasitic modes to which the microwave circuits of the chips may couple [She17], and irregular spacing in the grounding wire bonds, enforced by the bond pads of the modulation and input coils, might introduce additional parasitic resonances [Wen11].

To investigate the severity in Q_i degradation of bare resonators on a µMUX chip and the effects of coupling the rf-SQUID, chip *A4* of wafer *Hifr-Mux-02* included 4 µMUX channel designs of varying complexity: A full µMUX channel with modulation line connected to external electronics and a filter resistor shunting the input coil, a channel with a full rf-SQUID design with the input and modulation coils disconnected from the on chip input and modulation lines, a channel with only a load inductor, and a channel consisting only of the bare resonator (the equivalent circuit diagrams are depicted in figure 4.2). One of these channels was placed around 9.5 GHz, 12.5 GHz, 15.5 GHz, and 18.5 GHz. The sample was characterized with a VNA in the dilution refrigerator using the setup described in section 3.7 at a temperature of $T \approx 9\,\mathrm{mK}$ with a VNA output power of $P_\mathrm{VNA} = -30\,\mathrm{dBm}$ corresponding to an on-chip power of $P_\mathrm{chip} \approx -80\,\mathrm{dBm}$. Only for the resonances around 9.5 GHz and 12.5 GHz all channels could be identified. In the case of the 15.5 GHz channels, the resonance corresponding to the full µMUX

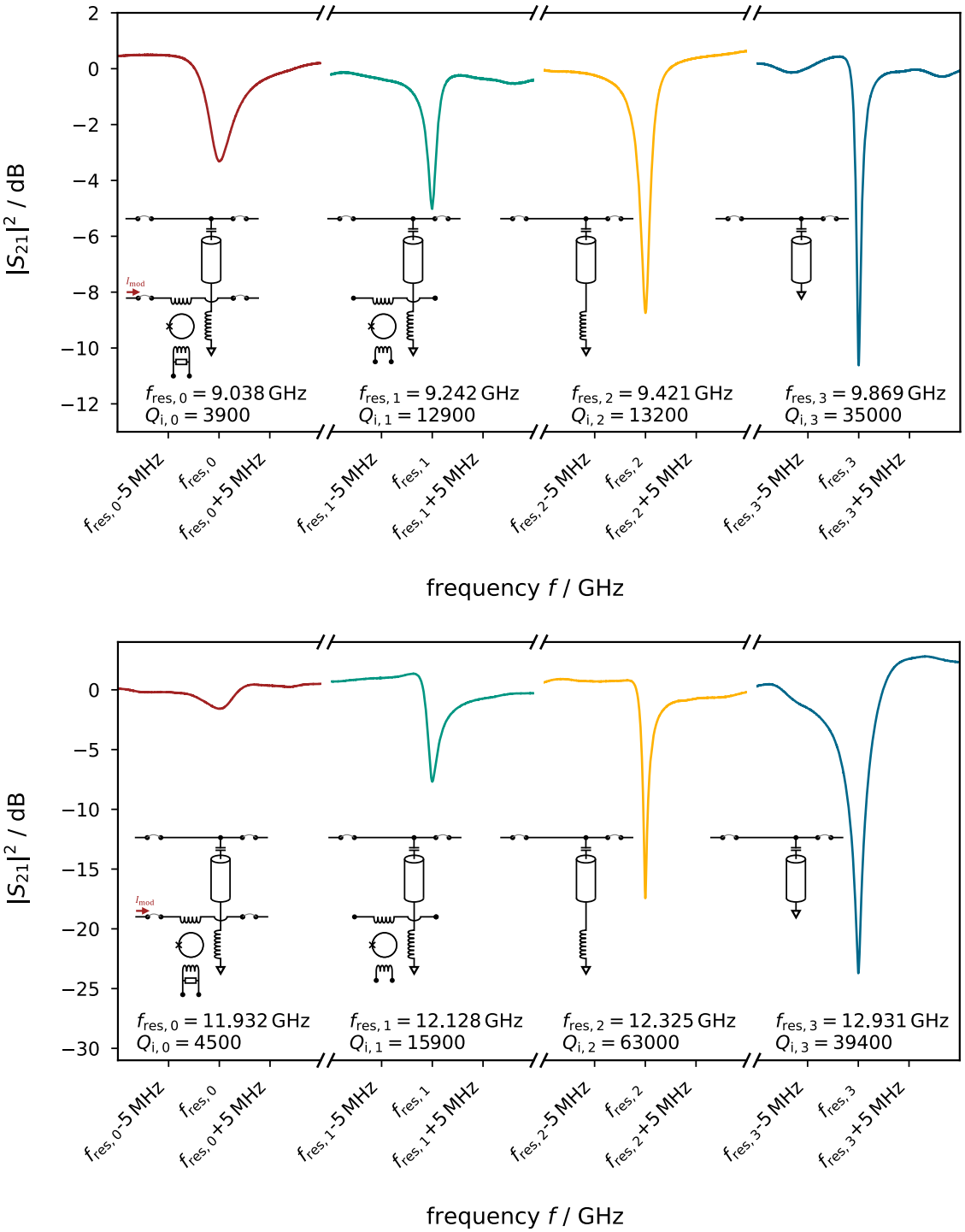

Fig. 4.2: Resonance curves measured on chip *A4* of wafer *Hifr-Mux-02* with a VNA output power of $P_{\mathrm{VNA}} = -30\,\mathrm{dBm}$ at a temperature of $T \approx 9\,\mathrm{mK}$. The top plot shows the resonances around 9.5 GHz, and the bottom plot those around 12.5 GHz. Below each resonance curve, a schematic of the corresponding resonator circuit is shown together with its resonance frequency and intrinsic quality factor.

channel could not be identified. For the channels around 18.5 GHz, only the bare resonator could be discerned from the baseline ripple.

Figure 4.2 illustrates the measurement of the transmission parameter across the µMUX channels surrounding 9.5 GHz and 12.5 GHz. The baseline ripple was corrected by applying a second-order Savitzky–Golay filter with a 50 MHz window size and subtracting the filtered data from the unfiltered data. Since the resonance curves with $\Delta f_{\mathrm{BW}} = 1\,\mathrm{MHz}$ are significantly narrower than the filter window, they remain largely unaffected by this process. For each resonance, the characteristic parameters, such as the intrinsic quality factor, were determined using the circle-fit algorithm described in section 3.8.1.

We observe a decrease in Q_{i} as the complexity of the load circuit increases. While the bare resonators (depicted in figure 4.2 in blue) and those with only the load inductor connected (yellow) achieved intrinsic quality factors of $\mathcal{O}(5 \cdot 10^4)$, the complete µMUX channels (red) reached only ~ 5000. The decrease from the disconnected µMUX (green) ($Q_{\mathrm{i}} \approx 14\,000$) to the complete µMUX is particularly significant, corresponding to an additional loss mechanism with a quality factor of $Q \approx 6000$, which dominates all other loss mechanisms. Since the connection to external devices for actual detector readout cannot be avoided, it is essential to understand and mitigate this effect.

The design *Hifr-Mux-02* was the first design in this thesis to employ CPW dimensions of $w = 4\,\mu\mathrm{m}$ for the slot width and $s = 10\,\mu\mathrm{m}$ for the center conductor width. The resonator lengths were designed assuming an effective dielectric constant of $\epsilon_{\mathrm{r,eff}} = 6.15$, as obtained from Sonnet simulations. However, the measured resonance frequencies of the bare resonators on this chip are approximately 2.6 % higher than expected, with a frequency spacing of $(3.07 \pm 0.01)\,\mathrm{GHz}$ instead of the designed 3 GHz. Using equations 2.15, 2.16, 2.19, and 2.22, together with the designed resonator length l_{res} and the measured resonance parameters f_{r} and Q_{c}, we determine an effective dielectric constant of $\epsilon_{\mathrm{r,eff}} = 5.86 \pm 0.02$ for the fabricated CPWs. This value was used for all subsequent µMUX designs.

4.2.2 Influence of loading the dc circuitry

To better understand the reduction in Q_{i} when connecting the rf-SQUID to external circuits, additional measurements were performed using a µMUX chip from wafer *ECHo-Mux-04*, which is described in detail in [Ric21b]. Since the rf-SQUID geometry used throughout this work was adapted from wafer *ECHo-Mux-04*, results obtained with that chip are expected to qualitatively represent the other devices. The µMUX chip was cooled to $T \leq 10\,\mathrm{mK}$ in multiple subsequent measurements using different configurations of connections to the dc circuitry. The resulting resonance curves of one of the µMUX channels are displayed in figure 4.3. The difference in resonance frequency can be attributed to the differing load impedances of the resonator due to the changing dc connections, as well as a random flux bias of the rf-SQUID caused by background fields.

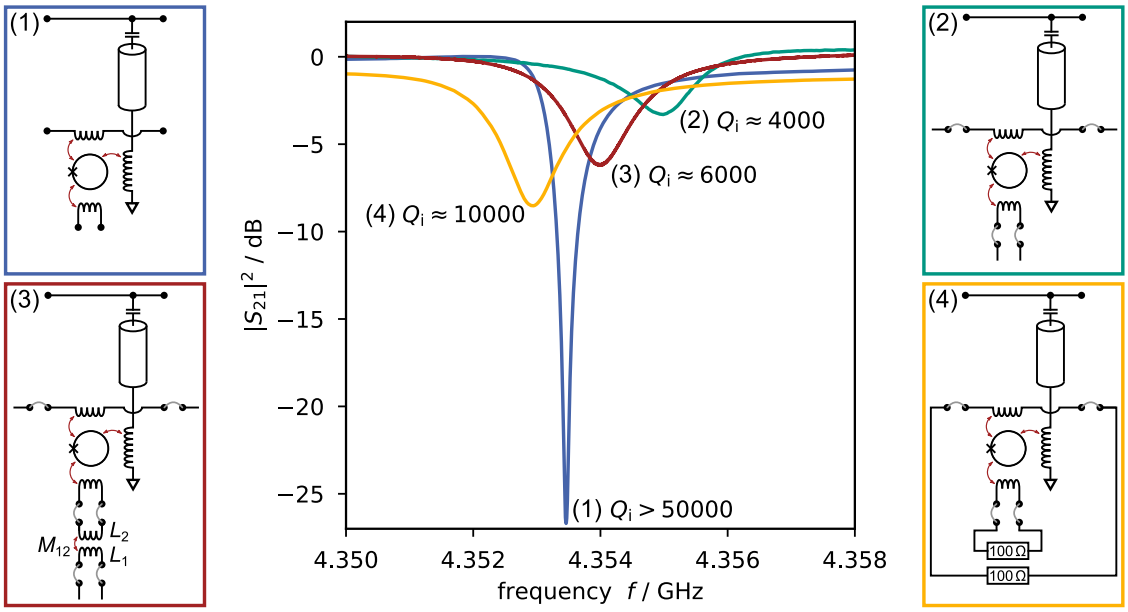

Fig. 4.3: Resonance curve of channel 14 on chip *4C* of wafer *ECHo-Mux-04* as described in [Ric21b]. The measurements were performed with a VNA output power of $P_{\mathrm{VNA}} = -27\,\mathrm{dBm}$ at $T \leq 10\,\mathrm{mK}$. Across consecutive cool-downs, the connection to the dc circuits of the µMUX channel was varied, resulting in significant changes in the intrinsic quality factor. The configuration corresponding to each resonance curve is illustrated schematically to the left and right of the plot.

In the initial measurement, neither the modulation line nor any of the input lines on the chip were connected to the housings dc circuit board through bond wires. In this configuration, the channel reached an internal quality factor $Q_i > 50\,000$. This value is higher than the measured value of the µMUX channels on wafer *Hifr-Mux-02*. However, it should be noted that the operating frequency of this multiplexer device is significantly lower than 9.5 GHz, which makes loss mechanisms such as radiation losses and coupling to parasitic modes less prominent. Therefore, the determined Q_i values are not directly comparable.

In the second cool down, the input coil of the depicted channel and the common modulation coil were connected to the dc circuit board, which was in turn linked via twisted pair CuNi cables to the room temperature electronics. This configuration resulted in a pronounced reduction of the intrinsic quality factor. This drop could be caused by microwave power leakage through the dc wiring to the room temperature electronics. Interfering signals originating at room temperature might couple into our rf-SQUID, affecting the performance of µMUX channels. Additionally, the connected electronics might lead to a significant change in the effective load impedance of the resonator and suppress the resonance.

To reduce microwave power leakage and suppress potential interference signals from room temperature, we fabricated a flux transformer consisting of two magnetically

coupled coils, with inductances $L_1 = 800\,\mathrm{pH}$ and $L_2 = 1.5\,\mathrm{nH}$, and mutual inductance $M_{12} = 500\,\mathrm{pH}$, as depicted in the equivalent circuit marked in red in figure 4.3. In a subsequent measurement, this flux transformer was inserted into the input line between room temperature electronics and the rf-SQUID, reducing the effective coupling strength between the input circuit and the external electronics from 155 pH to 25 pH. Combined with the modulation coil coupling, this results in a total reduction of the coupling strength between the rf-SQUID and the external electronics by a factor of ~ 3.8, from 176 pH to 46 pH. This configuration resulted in a modest improvement in Q_i by a factor of 1.5 compared to the directly connected µMUX measurement. However, this increase is far smaller than the coupling reduction, suggesting that microwave power leakage or external interference are unlikely to be the dominant mechanisms limiting Q_i.

This observation is further supported by a fourth measurement. Here, the modulation coil and input coil were shunted with a $100\,\Omega$ resistor connected at millikelvin temperatures via the µMUX housings dc circuit board. In this configuration, parasitic signals originating from external electronics are nearly completely suppressed. However, the intrinsic quality factor remains significantly lower than that of a fully disconnected µMUX. Therefore, changes in the effective load impedance must significantly influence the intrinsic quality factor, either by increasing dissipation in the load circuit or by altering the phase shift of the oscillating signal within the resonator.

In the final measurement, the µMUX was reset to its original configuration without any dc connections. In this setup, a $Q_\mathrm{i} > 50\,000$ was once again achieved, thereby verifying that the observed changes in Q_i were not due to device damage or degradation between cool-downs.

4.2.3 Contribution of the input filter placement to the intrinsic quality factor

Typically, we consider the dc circuitry of the µMUX to be independent of the microwave circuitry. In the case of the input coil, the filter resistor R_f serves to attenuate any microwave signals that might couple into a connected detector, assuming that the detector impedance is significantly larger than R_f. However, this calculation is always performed under the assumption of lumped-element behavior within the input circuit, necessitating progressively smaller circuit sizes as the operating frequency increases.

In the first two wafer designs, *Hifr-Mux-01* and *Hifr-Mux-02*, we fabricated as part of this thesis, we integrated the filter resistor into the bondpad design at the edge of the µMUX chip. This resulted in a significant distance $l_\mathrm{filter} \approx 1.5\,\mathrm{mm}$ between the rf-SQUID and the filter resistor (as shown, for example, in figure 4.4(b)). At this distance, the line connecting the input coil and the filter resistor must be treated as a transmission line. We simulated a 17 GHz µMUX channel design of *Hifr-Mux-02* in Sonnet for varying lengths l_filter with a $R_\mathrm{f} = 3\,\Omega$ filter resistor terminating the input line and a simple via replacing the Josephson junction. From the resulting transmission curves, we extracted the intrinsic quality factor. As shown in figure 4.4(c), the intrinsic quality

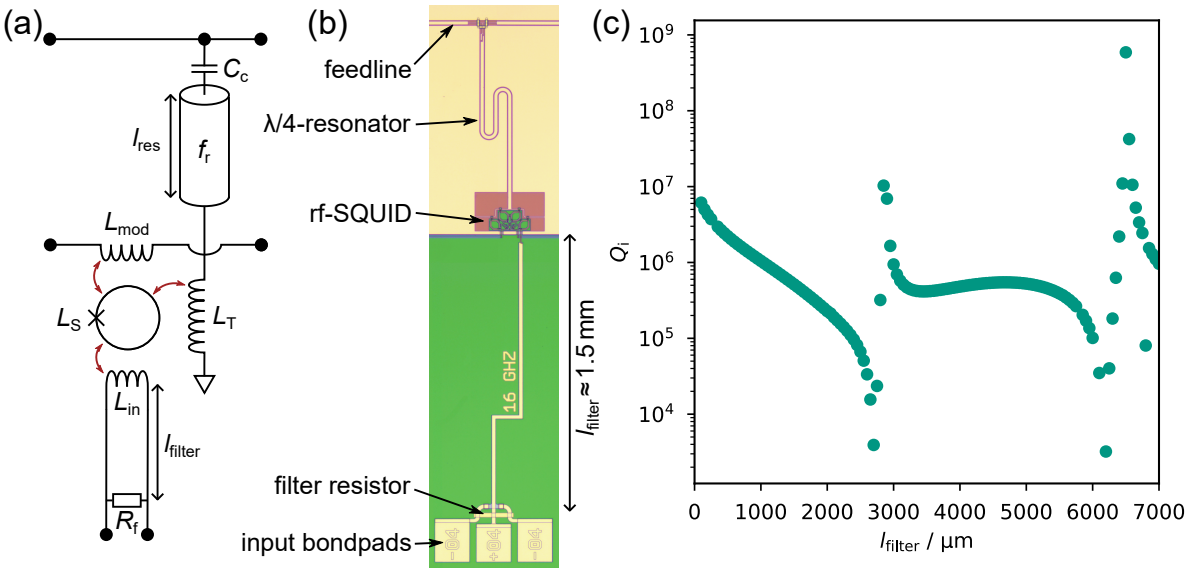

Fig. 4.4: (a) Equivalent circuit diagram of the µMUX channel simulated in Sonnet. The simulation yielded the resonance curve of the circuit for varying distances l_{filter} between the rf-SQUID's input coil and the filter resistor R_{f}. (b) Micrograph of a µMUX channel on wafer *Hifr-Mux-01*. The image shows the filter resistor placed above the bondpads at a significant distance from the rf-SQUID. (c) Intrinsic quality factor of the µMUX channel extracted from the Sonnet simulations as a function of the filter distance R_{f}. The simulations were performed for a 17 GHz µMUX channel with a 3 Ω filter resistor assuming an operation temperature of $T = 10$ mK.

factor decreases and increases periodically with l_{filter}, demonstrating the influence of distributed element behavior. To mitigate these effects, the distance between the rf-SQUID and the filter resistor was kept small in the following designs. Following the design rules for lumped element components, the filter resistor was positioned directly beneath the SQUID, significantly closer than the microwave signal wavelength.

4.3 Impact of complex input coil shunt impedances on the intrinsic quality factor

As discussed in the previous sections 4.2.2 and 4.2.3, the impedance of the circuits connected to the input and modulation coils can affect the intrinsic quality factor of the µMUX. In fact, the resonance frequency shift is also affected by these impedances, as we will see in the following. Since the coupling between the input coil and the SQUID is typically larger than that between the modulation coil and the SQUID, we will focus on the input circuit in the following discussion.

We can represent our µMUX with the equivalent circuit diagram shown in figure 4.5, where the impedance Z_{in} shunts the input coil and can take arbitrary complex val-

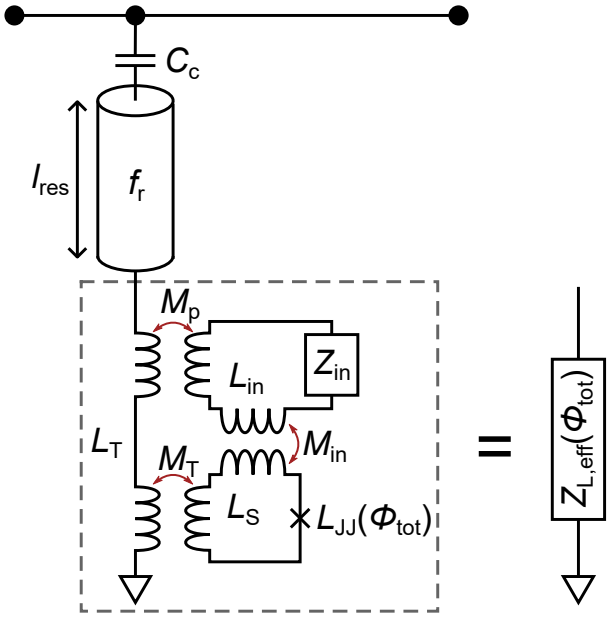

Fig. 4.5: Equivalent circuit diagram of a µMUX channel with only an input coil L_{in} but no modulation coil coupled to the rf-SQUID. The input coil is terminated with an unknown, complex impedance Z_{in}, representing an arbitrary detector circuit. For the analytical derivation of the µMUX channel properties, the load circuit is replaced by a flux-dependent effective load impedance $Z_{\mathrm{L,eff}}(\Phi_{\mathrm{tot}})$.

ues. Using this circuit, we can derive an effective load impedance $Z_{\mathrm{L,eff}}(\varphi_{\mathrm{tot}})$ (see section A.3), which terminates the resonator:

$$Z_{\mathrm{L,eff}}(\varphi_{\mathrm{tot}}) = i\omega \left[L_{\mathrm{T}} - \frac{M_{\mathrm{p}}^2 L_{\mathrm{s}}(1 + [\beta_{\mathrm{L}} \cos\varphi_{\mathrm{tot}}]^{-1}) + M_{\mathrm{T}}^2 (L_{\mathrm{in}} + \frac{Z_{\mathrm{in}}}{i\omega}) - 2M_{\mathrm{in}} M_{\mathrm{T}} M_{\mathrm{p}}}{L_{\mathrm{s}}(1 + [\beta_{\mathrm{L}} \cos\varphi_{\mathrm{tot}}]^{-1})(L_{\mathrm{in}} + \frac{Z_{\mathrm{in}}}{i\omega}) - M_{\mathrm{in}}^2} \right] \tag{4.7}$$

In case that no detector is connected, the input coil is shunted by the filter resistor $Z_{\mathrm{in}} = R_{\mathrm{f}}$ only. The real part of this equation results through $Q_{\mathrm{f}} = \pi Z_0/(4\Re[Z_{\mathrm{L,eff}}])$ in equation 4.5, while the imaginary part can be used to derive the effective load inductance $L_{\mathrm{T,eff}} = \Im[Z_{\mathrm{L,eff}}]/\omega$ and, therefore, the resonance shift. In the limit of very large filter resistances, i.e., an open input circuit, using equation 4.7 yields the established effective load inductance as represented by equation 2.44:

$$L_{\mathrm{T,eff}}(\varphi_{\mathrm{tot}}) = L_{\mathrm{T}} - \frac{M_{\mathrm{T}}^2}{L_{\mathrm{S}}} \frac{\beta_{\mathrm{L}} \cos\varphi_{\mathrm{tot}}}{1 + \beta_{\mathrm{L}} \cos\varphi_{\mathrm{tot}}} \tag{4.8}$$

However, the filter resistor is typically selected to achieve a cutoff frequency $\omega_{\mathrm{c}} = R_{\mathrm{f}}/L_{\mathrm{in}}$ that is significantly smaller than the µMUX resonance frequency. Consequently, the filter resistor is negligibly small, yielding (see section A.4)

$$L_{\mathrm{T,eff}}(\varphi_{\mathrm{tot}}) \approx L_{\mathrm{T}} - \frac{M_{\mathrm{p}}^2 L_{\mathrm{S}} + \beta_{\mathrm{L}} \cos\varphi_{\mathrm{tot}} (M_{\mathrm{p}}^2 L_{\mathrm{S}} + M_{\mathrm{T}}^2 L_{\mathrm{in}} - 2M_{\mathrm{in}} M_{\mathrm{T}} M_{\mathrm{p}})}{L_{\mathrm{S}} L_{\mathrm{in}} + \beta_{\mathrm{L}} \cos\varphi_{\mathrm{tot}} (L_{\mathrm{S}} L_{\mathrm{in}} - M_{\mathrm{in}}^2)}. \tag{4.9}$$

Therefore, the shift in resonance frequency is altered compared to the typically assumed resonance shift derived from equation 2.44. Figure 4.6 shows the calculated resonance frequency shift for the 4.5 GHz µMUX channel of *Hifr-Mux-06* chip *A4*, which was used for the measurements presented in chapter 5. The resonance curves were calculated

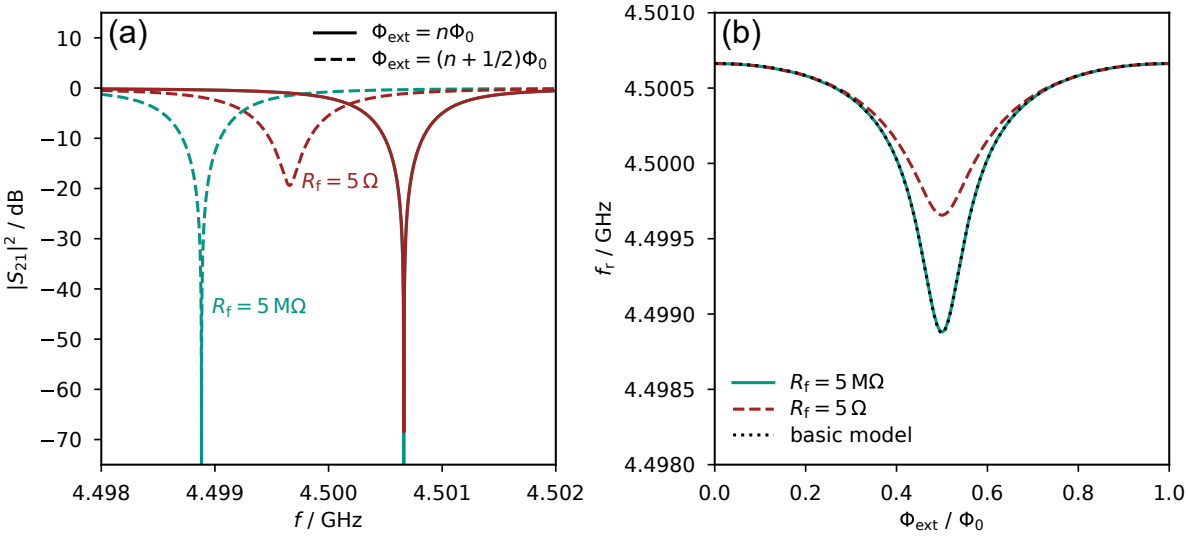

Fig. 4.6: Calculated resonance frequency shift of the 4.5 GHz µMUX channel of *Hifr-Mux-06* chip *A4*, discussed in chapter 5. (a) Calculated resonance curves of the µMUX channel for the flux states corresponding to the highest (solid lines) and lowest (dashed lines) resonance frequencies. The red curves account for the 5 Ω filter resistor, whereas in the green curves the filter resistor is set to 5 MΩ, corresponding to an open input circuit. The solid green curve is obscured by the red curve, as the resonance frequency at a flux bias of $n\Phi_0$ is almost unaffected by the filter resistor. (b) Resonance frequency shift as a function of the applied flux Φ_{ext}. The red dashed curve accounts for the filter resistor, while in the green solid curve the filter resistor is set to 5 MΩ. The resonance frequency shift with the 5 MΩ resistor is virtually identical to that predicted by equations 2.44 and 2.39, shown as the black dotted curve.

using equations 4.7, 2.17, and 2.18. The resonance frequency shift in the case of an unshunted input coil was calculated using equation 4.7 by setting the filter resistance to $R_f = 5\,M\Omega$ and using inductances determined through InductEx simulations. As expected, the resulting shift in resonance frequency agrees with the shift predicted by equation 2.44. It is important to note that the total peak-to-peak resonance frequency shift calculated is only 1.8 MHz, while the design parameter is 2 MHz. This deviation can be traced back to the use of equation 2.46, which is an approximation of equation 2.39, during device design.

When accounting for the filter resistor, the total shift in resonance frequency is reduced, resulting in a shift of only 1 MHz. Assuming that the parasitic coupling M_p between the load inductor and the input coil can be avoided, the total shift is reduced to about 1.3 MHz. Consequently, the change in resonance frequency shift will result in systematic errors when estimating M_T^2/L_S and β_L during characterization if the filter resistor is not taken into account.

As discussed in section 4.2.3, at high frequencies and for long dc lines, it is necessary to consider the input circuit, which includes the detector in parallel with the filter

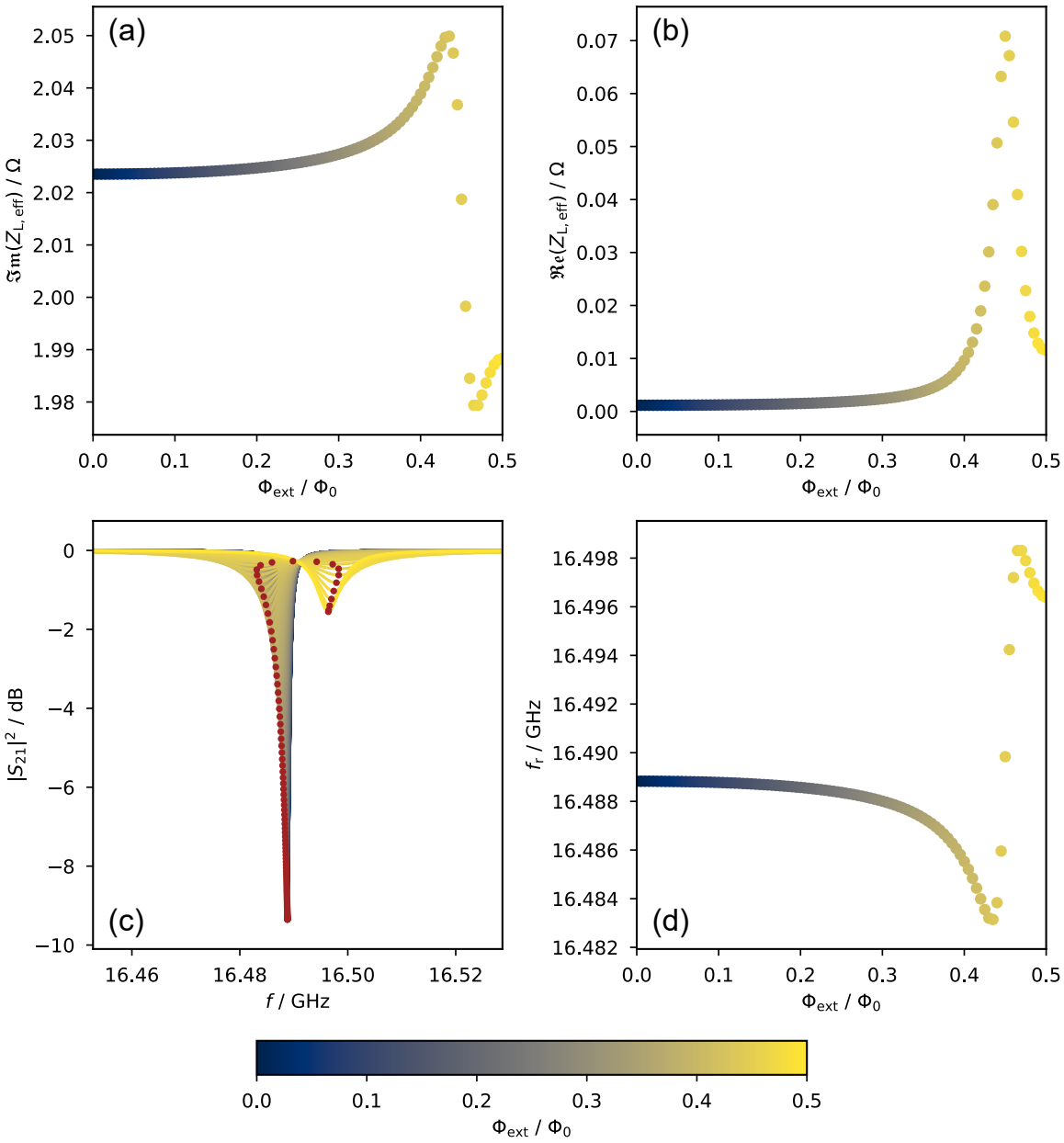

Fig. 4.7: Analytically derived µMUX characteristics of a µMUX channel as depicted in figure 4.5. The µMUX parameters were chosen to resemble those of a µMUX channel of the design *Hifr-Mux-03*, described in chapter 7.2. For the input circuit termination, $Z_{\mathrm{in}} = (1 - 20i)\,\Omega$ was assumed. (a) Dependence of the imaginary component of $Z_{\mathrm{L,eff}}$ on the externally applied magnetic flux Φ_{ext}. (b) Dependence of the real component of $Z_{\mathrm{L,eff}}$ on the applied magnetic flux. (c) Resulting resonance curves for each flux state, with the resonance minima marked by red circles. (d) Dependence of the resonance frequency on the applied magnetic flux.

resistor, as distributed elements. Consequently, Z_{in} can take a wide range of complex values and can even exhibit capacitive behavior at the µMUX operation frequency. This can lead to the dc circuitry itself exhibiting a flux dependent resonance and unexpected µMUX behavior. One example is displayed in figure 4.7, which shows the calculated complex load impedance of a 16.5 GHz µMUX channel from the design *Hifr-Mux-03* (see chapter 7). We observe a jump in the real component of $Z_{\mathrm{L,eff}}$ and a spike in its imaginary component for a flux bias of $\Phi_{\mathrm{ext}} \approx 0.45\,\Phi_0$, indicating that parts of the load circuit resonate at the operation frequency for this flux bias. The resulting resonance curves and the resonance frequency shifts are displayed in figure 4.7 (c) and (d). The resonance frequency shift exhibits atypical behavior, with the resonance frequency first decreasing simultaneously with a decrease in resonance depth, followed by a jump in resonance frequency around $\Phi_{\mathrm{ext}} \approx 0.45\Phi_0$ to higher frequencies. Here, the resonance curve becomes deeper again, and the resonance frequency decreases. Ultimately, the resonance frequency at $\Phi_{\mathrm{ext}} = \Phi_0/2$ is greater than the resonance frequency at $\Phi_{\mathrm{ext}} = 0$. A model that includes the modulation coil circuit might exhibit additional resonance frequency jumps due to resonances in the modulation line circuitry, which is particularly nontrivial due to the flux dependent impedances of the coupled rf-SQUIDs.

Multiple channels of the characterized µMUX chip *A4* of design *Hifr-Mux-03* , discussed in chapter 7.2, exhibited atypical jumps in resonance frequency. However, fitting the model described here to the measured data is highly challenging, as it would require, on one hand, the inclusion of the modulation coil, as well as a precise description of the impedances describing the input and modulation lines at the µMUX operation frequency. Nonetheless, the model described herein can be employed to qualitatively explain the observed behavior.

A jump in resonance frequency is highly undesirable in FRM readout, as it degrades the signal of the fundamental harmonic of the transmitted readout tone and, consequently, the achievable noise performance. Therefore, these resonances should be suppressed in practice. The resonances occur when the real part of the denominator in equation 4.7 is zero, necessitating a strongly capacitive behavior of Z_{in}. These resonances can be mitigated by selecting a sufficiently small filter resistor R_{f}. Consequently, to suppress such resonances on the input line, as well as the modulation line, future µMUX designs should also incorporate filter resistors in the modulation line. However, considering equation 2.57, a compromise must be made since additional small filter resistors will also increase flux noise in the rf-SQUID.

Since equation 4.9 for $L_{\mathrm{T,eff}}$ and its subsequent resonance frequency shift depend on a large number of parameters, it is challenging to fit actual data with the model described here. Additionally, this µMUX model does not yet include the readout power dependence of the rf-SQUID. For these reasons, and to maintain consistency with previous works, all analyzes of the µMUX devices presented in the following will be conducted using the established µMUX model. This choice may introduce systematic errors in the determination of β_{L} and $M_{\mathrm{T}}^2/L_{\mathrm{S}}$, as well as in derived parameters such as the attenuation of the cryogenic readout chain.

5. Deployment of a full-scale µMUX readout system for magnetic microcalorimeters

The simultaneous readout of a large number of µMUX channels requires complex room-temperature electronics that generate the probe tone frequency comb, perform the digital demultiplexing, and detect detector events. As described in chapter 2.7, this is commonly implemented with a software defined radio (SDR) system. For the ECHo experiment [Gas17], an SDR system optimized for the readout of magnetic microcalorimeters (MMCs) has been developed [San19, Kar22]. The latest generation of this system is the first fully equipped and configured version [Mus24], capable of reading out 400 µMUX channels in the 4 GHz to 8 GHz range.

In this chapter, we report on the performance of our latest generation of a full-scale µMUX-based readout system optimized for MMC readout. This system comprises the ECHo SDR electronics and a µMUX optimized for MMC readout. The system has been deployed in conjunction with an MMC detector and a radioactive source, allowing for the full demonstration of the systems functionality and the characterization of the entire readout chain. A description of the setup and its performance has been published in [Nei25a]. The complete content of that publication is revisited and discussed in detail in the following chapter.

5.1 Basics of magnetic microcalorimeters

Magnetic microcalorimeters (MMCs) are energy-dispersive, cryogenic single-particle detectors that offer excellent energy resolution, fast signal rise time, and high linearity over a wide dynamic range [Fle05, Kem18]. According to the schematic layout in figure 5.1(a), an MMC consists of a particle absorber thermally coupled to a paramagnetic temperature sensor, which is itself weakly coupled to a heat bath. An incident particle deposits an energy δE inside the absorber, leading to a temperature rise of the detector

$$\delta T \simeq \frac{\delta E}{C_{\mathrm{tot}}}, \tag{5.1}$$

where $C_{\mathrm{tot}} = C_{\mathrm{a}} + C_{\mathrm{s}}$ denotes the total heat capacity of the MMC, determined by the absorber heat capacity C_{a} and the sensor heat capacity C_{s}. Following this temperature rise, the detector returns to the bath temperature T_0, thermalized through the weak thermal link. The time constant $\tau_1 = C_{\mathrm{tot}}/G$ of the exponentially decreasing detector temperature (see figure 5.1(b)) is set by the total heat capacity of the detector and the thermal conductance G of the weak thermal link. The deposited energy can be reconstructed from the measured signal amplitude and shape.

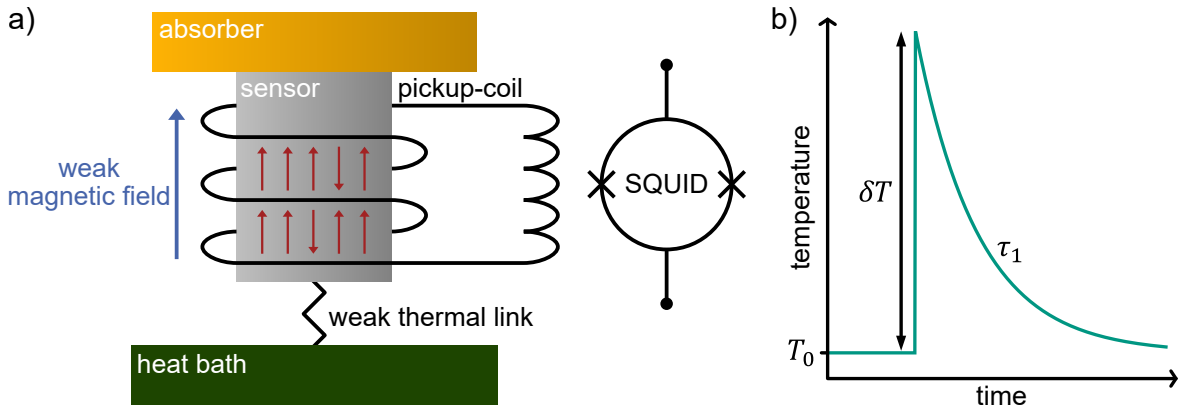

Fig. 5.1: (a) Schematic layout of a magnetic microcalorimeter. The absorber is thermally coupled to a paramagnetic temperature sensor, which is weakly linked to a heat bath. Variations in the sensor's magnetization are read out via a superconducting pickup coil connected to a current sensing dc-SQUID. (b) Typical temperature time trace of the sensor following a particle absorption. The signal starts with a rapid exponential signal rise $\mathcal{O}(100\,\mathrm{ns})$ to its amplitude, set by the deposited energy, and ends with a exponential decay with $\mathcal{O}(1\,\mathrm{ms})$ to the bath temperature T_0.

The paramagnetic sensor typically consists of a host material, either Au or Ag, doped with several hundred ppm of Er atoms. The Er atoms occupy regular lattice sites and donate three electrons to the host electron gas, forming Er^{3+} ions that give rise to the paramagnetic properties of the sensor material. Under an applied external magnetic field, the magnetic moments of the Er^{3+} ions partially align, resulting in a temperature-dependent magnetization $M(T)$. For a small temperature change δT, the corresponding change in magnetization is $\delta M \simeq (\partial M/\partial T)\delta T$. This change in magnetization is detected by a superconducting pickup coil as a change in magnetic flux $\delta\Phi$. The pickup coil is connected to the input coil of a current sensing SQUID, forming a closed superconducting loop. Due to flux conservation, the flux change $\delta\Phi$ is converted into a current change δI through the pickup and input coil:

$$\delta I = \frac{\delta\Phi}{L_{\mathrm{tot}}} \propto \frac{\partial M}{\partial T}\frac{\delta E}{C_{\mathrm{tot}}}. \tag{5.2}$$

Here, L_{tot} is the total inductance of the pickup and input coil. This current generates magnetic flux $\delta\Phi_{\mathrm{S}} = M_{\mathrm{in}}\delta I$ in the SQUID loop. In addition to transducing changes in magnetic flux into changes in current, the pickup coil can also generate the weak magnetic field applied to the paramagnetic temperature sensor. Using a heater based superconducting switch, a persistent current can be trapped in the pickup coil, generating the bias field [Bur08]. This method of biasing the MMC has the advantages of being dissipation-free and reducing noise compared to an active flux bias.

To maximize the signal size generated by an absorbed particle, the temperature dependence of the magnetization $\partial M/\partial T$ should be large, while the total heat capacity C_{tot} should be small. This condition is met at operating temperatures $T < 100\,\mathrm{mK}$, where

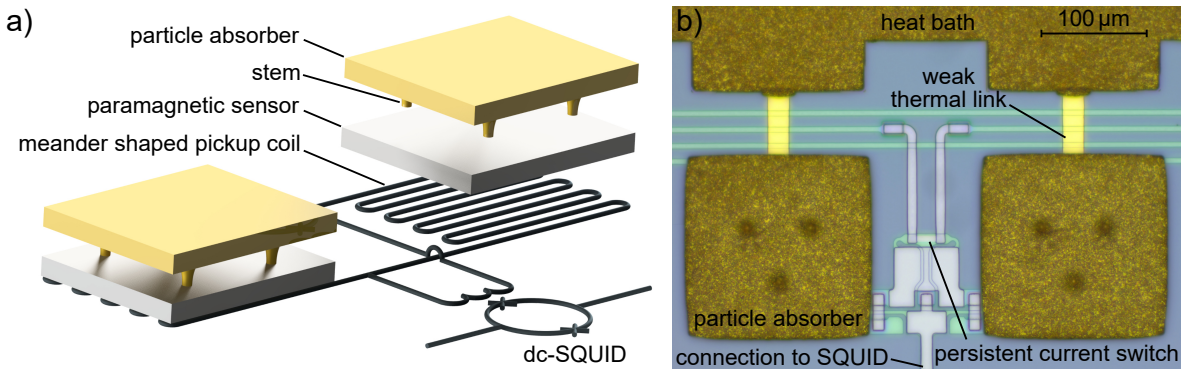

Fig. 5.2: (a) Schematic illustration of a magnetic microcalorimeter with meander-shaped pickup coils, comprising a gradiometric pixel pair. (b) Micrograph of a concrete realization of an MMC with the detector geometry shown in (a). The sensor and pickup coil is hidden beneath the particle absorber. The three gray dots in each absorber are caused by the stems supporting the freestanding absorber [Mül25].

the magnetization, following the Curie law $M \propto 1/T$, has its steepest temperature dependence, and both the phonon ($c_{\mathrm{ph}} \propto T^3$) and electronic ($c_{\mathrm{el}} \propto T$) heat capacities are small. In addition, thermal noise is reduced at these temperatures, improving the signal-to-noise performance of the MMC. It is therefore essential to provide sufficient thermalization to the heat bath to maintain operation at the lowest achievable temperature.

The MMCs used within this thesis are based on meander-shaped pickup coils and are designed in a gradiometric fashion, as shown in figure 5.2(a). Two detector pixels are connected in parallel to the SQUID input coil, forming a superconducting flux transformer. A magnetic flux signal applied to both meander-shaped coils induces currents of opposite polarity in the input coil. Consequently, this design is less susceptible to variations in externally applied magnetic fields or temperature drifts of the MMC sensor material. Additionally, this layout enables the readout of two pixels using a single SQUID, allowing the pixel in which the particle is absorbed to be determined by the signal polarity. In this pickup coil configuration, the effective magnetic flux coupling between sensor and SQUID is

$$\frac{\delta\Phi_{\mathrm{S}}}{\delta\Phi} = \frac{M_{\mathrm{in}}}{L_{\mathrm{m}} + 2(L_{\mathrm{par}} + L_{\mathrm{in}})}, \tag{5.3}$$

where L_{m} is the inductance of a single meander-shaped coil, L_{in} is the inductance of the input coil, and L_{par} is the inductance introduced by the wire bonds and on-chip wiring, both connecting the MMC to the input coil. To achieve the optimal effective coupling, the input coil must be impedance matched to the connected MMc, i.e. $L_{\mathrm{in}} = L_{\mathrm{m}}/2 + L_{\mathrm{par}}$. This restricts the design of the SQUIDs input circuitry, ruling out, for example, the inclusion of additional inductors placed in series with the input coil for signal conditioning.

The particle absorbers are typically placed on stems (see figure 5.2) to reduce losses of athermal phonons. When a particle deposits its energy in the absorber, it generates high-energy, athermal phonons that move ballistically through the absorber and may be lost to the substrate below the detector, significantly diminishing the achievable energy resolution [Koz12]. The stems minimize the interface between the absorber and the sensor, thereby greatly reducing athermal phonon loss [Kem18].

The MMCs used for the measurements within this thesis are described in detail in [Mül24]. A top view micrograph of one of the MMCs is shown in figure 5.2(b). It is identical to the ^{55}Fe design described in [Mül24], but without ^{55}Fe implantation. Each absorber is freestanding on stems and consists of 170 µm × 170 µm wide and 12 µm thick electroplated gold. The sensor is made of Ag:$\mathrm{Er}_{475\,\mathrm{ppm}}$ and is thermalized to the chips heat bath via a weak thermal link, resulting in an expected signal shape characterized by a rise time of 1 µs and a decay time of 1 ms. The inductance of a single meander-shaped pickup coil was simulated in InductEx, resulting in $L_\mathrm{m} = 1.12\,\mathrm{nH}$ [Mül25]. Assuming a total wire bond inductance of $L_\mathrm{par} \approx 0.25\,\mathrm{nH}$, this results in an optimal input coil inductance of $L_\mathrm{in}^\mathrm{opt} \approx 0.81\,\mathrm{nH}$. However, even an input inductance twice as large will only result in a reduction of the signal by $< 6\,\%$.

5.2 Description of the software defined radio system

The ECHo SDR electronics have been developed in close cooperation with the Institute for Data Processing and Electronics (IPE) at KIT [San19, Sch23a, Mus24]. The system includes all required electronics for room-temperature control and readout of a µMUX (see chapter 2.7), covering the 4 GHz to 8 GHz range and enabling the readout of up to 400 µMUX channels. It consists of three distinct boards (see figure 5.3): an analog rf front-end handling MHz and GHz analog signals, an *AMD Zynq US+ MPSoC* FPGA board responsible for digital processing, and an analog/digital conversion board that acts as a bridge, converting signals between the two domains. The probe-tone frequency combs are generated digitally and converted into the analog regime by the analog/digital conversion board, resulting in five distinct microwave signals, each spanning 800 MHz. The analog front-end board processes these signals and converts them into a single 4 GHz wide output signal ranging between 4 GHz and 8 GHz using IQ mixers [Gar22]. The generated probe-tone frequency comb is transmitted through the cryostat and the µMUX back to the RX port of the analog rf front-end, where it is divided and converted into the 5 original 800 MHz subbands, which are subsequently digitized and processed.

To digitize the 800 MHz wide signals for processing on the FPGA board, the analog/digital conversion board employs five dual-channel ADC with a sampling rate of 15.625 MHz. Analogously, the digitally generated frequency comb is converted using three four-channel DACs. Two additional DACs are used to generate a sawtooth-shaped voltage signal for flux-ramp modulation. All ADCs and DACs are operating at 1 GSPS.

On the FPGA, the signals are processed in real-time. To separate the individual

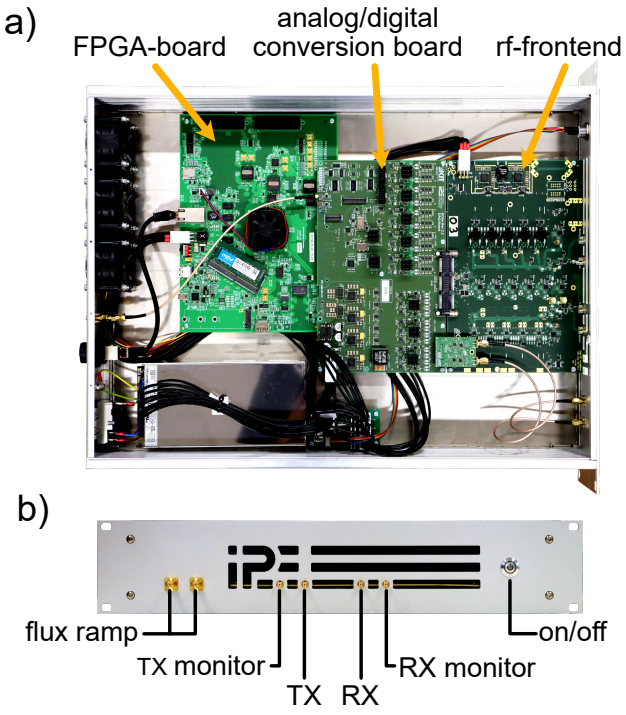

Fig. 5.3: Images of the SDR system used for the room-temperature control of the µMUX. (a) Inside view showing the analog rf front-end handling MHz and GHz analog signals, an FPGA board responsible for digital processing, and an analog/digital conversion board that acts as a bridge, converting signals between the two domains. (b) Front panel with the TX and RX ports, two flux-ramp outputs, and a monitor output for the TX and RX signals. An additional input for an external 10 MHz frequency standard and an Ethernet port are located on the systems back panel.

µMUX channels into the subbands, a digital down-conversion (DDC) stage followed by a polyphase channelizer and a filter bank [Mus24] is employed, dividing the signal into 10 MHz wide channels. Therefore, the minimum frequency spacing between µMUX channels is limited to 10 MHz. The raw amplitude signal of each channel is FRM-demodulated to reconstruct the original detector response. Here, the mixing frequency and the cut transient region following each ramp reset can be independently adjusted, thereby compensating for variations in individual SQUID responses. A trigger can be set on the demodulated signals to extract detector events, along with pre-trigger samples and additional metadata, such as a timestamp and the channel index. Alternatively, the system can acquire snapshots of raw or FRM-demodulated data. The recorded data can be transferred to a PC for post-processing via Ethernet. The PC can also be used to configure the various modules of the SDR boards at runtime according to the specific requirements of the experiment.

5.3 Description of the microwave SQUID multiplexer

We designed and fabricated a dedicated µMUX chip for measurements with the full-scale µMUX system, following the procedures described in section 3.3 and 3.4. The chip design is illustrated in figure 5.4. It comprises 18 µMUX channels with resonance frequencies between 4.25 GHz and 7.75 GHz, thereby covering each of the five 800 MHz subbands of the SDR system. The channels are based on CPW quarter wavelength resonators, which are terminated by the rf-SQUID design presented in section 3.2 and shown again in figure 5.5. The frequency spacing between neighboring resonators was

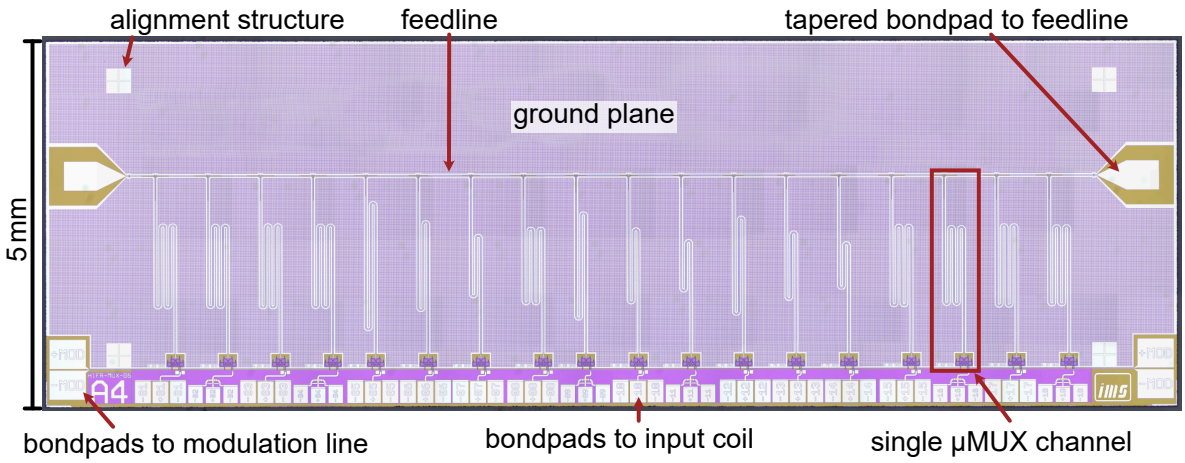

Fig. 5.4: Micrograph of the µMUX chip employed for the measurements presented in this chapter. The chip measures 15.5 mm × 5 mm. The substrate shows in brown and the niobium layers in white. The insulating SiO_2 layer covers only a small portion at the bottom of the chip where it shows in pink when sputtered directly onto the substrate. The ground plane is perforated to trap magnetic flux vortices and covers most of the chip. A zoomed in view of a single µMUX channel is depicted in figure 5.5.

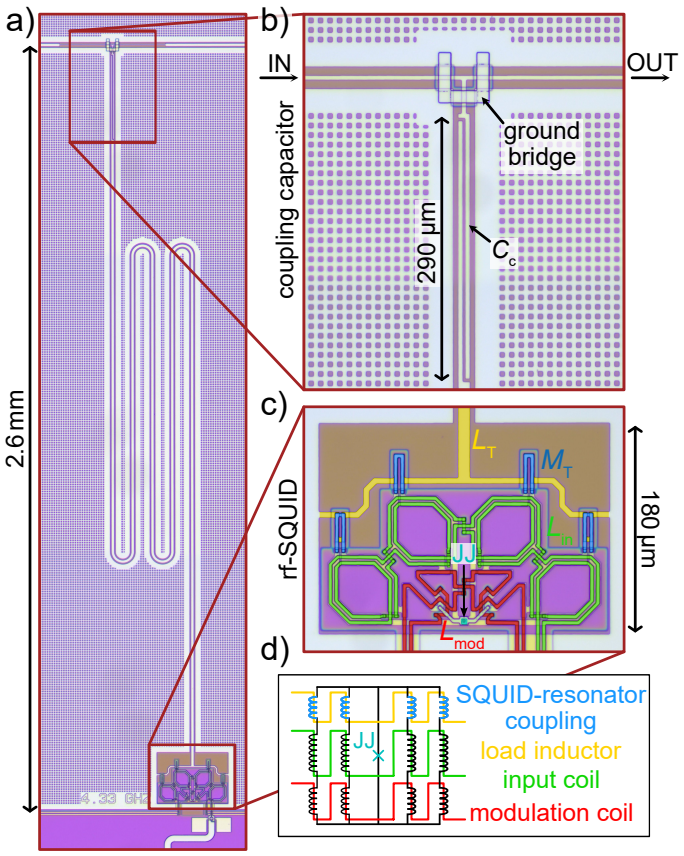

Fig. 5.5: a) Micrograph of the 4.33 GHz µMUX channel of the chip employed for the measurements presented in this chapter. b) Zoomed-in view of the coupling capacitor connecting the µMUX channel to the feedline. c) Zoomed-in view of the rf-SQUID terminating the µMUX channel resonator. The load inductor is highlighted in yellow, the input coil in green, the modulation coil in red, the Josephson junction in turquoise, and the SQUID–resonator coupling in blue. d) Equivalent circuit diagram of the second-order gradiometric rf-SQUID shown in c).

Tab. 5.1: Design parameters of the dedicated µMUX chip, developed for the measurements in this chapter. The critical current of the Josephson junction is individually tuned to yield $\beta_L = 0.6$ for all channels. The capacitance C_c and the mutual inductance M_T are chosen to achieve a channel bandwidth of 1 MHz and a peak-to-peak resonance frequency shift of 2 MHz. Here, f_r denotes the resonance frequency of the full µMUX channel, f_0 the theoretical resonance frequency of the bare resonator, and l_{res} the resonator length.

channel	f_r / GHz	f_0 / GHz	C_c / fF	l_{res} / µm	L_T / pH	M_T / pH	L_S / pH
1	4.25	4.485	14.01	6739	121.34	5.31	41.41
2	4.26	4.496	13.96	6722	121.34	5.30	41.40
3	4.27	4.507	13.91	6706	121.34	5.28	41.39
4	4.28	4.518	13.86	6690	121.35	5.27	41.38
5	4.30	4.540	13.77	6657	121.35	5.24	41.36
6	4.33	4.572	13.62	6610	121.36	5.21	41.33
7	4.37	4.616	13.44	6547	121.36	5.15	41.30
8	4.42	4.671	13.21	6470	121.37	5.09	41.25
9	4.50	4.759	12.86	6351	121.39	4.99	41.19
10	5.00	5.311	10.98	5690	121.52	4.45	40.83
11	5.50	5.869	9.52	5150	121.64	4.02	40.54
12	5.75	6.150	8.90	4914	121.69	3.83	40.41
13	6.00	6.432	8.35	4699	121.75	3.65	40.30
14	6.50	7.001	7.41	4317	121.90	3.35	40.09
15	6.75	7.289	7.00	4147	121.96	3.21	40.00
16	7.00	7.576	6.63	3989	122.03	3.09	39.91
17	7.50	8.157	5.98	3705	122.14	2.86	39.76
18	7.75	8.449	5.69	3577	122.19	2.76	39.69

varied between 10 MHz and 500 MHz, allowing for testing of the system with its target resonance frequency spacing of 10 MHz and, in principle, enabling frequency spacing dependent crosstalk measurements. On chip, the µMUX channels are shuffled such that two channels with neighboring resonance frequencies are not directly placed next to each other. This minimizes crosstalk due to inter-channel capacitive coupling.

The resonance frequency and other relevant design parameters of all µMUX channels are listed in table 5.1. The coupling capacitance C_c was varied among the channels to achieve a 1 MHz bandwidth for each channel, and the SQUID-resonator coupling M_T was adjusted to yield an optimal resonance frequency shift of 2 MHz. Changing the mutual inductance M_T also affects the SQUID inductance L_S and load inductance L_T, which was accounted for during the design process. Using the simulation framework in [Sch23b], the optimal screening parameter for minimizing flux noise was found to be $\beta_L = 0.6$. Therefore, the critical current of the rf-SQUID was tuned for each channel to yield a screening parameter of $\beta_L = 0.6$. This required a variation in the Josephson junction sidelength of only 0.1 µm, which is well below the resolution of 0.6 µm, typically

achieved during the corresponding fabrication step. Similarly, the variations in the coupling between the SQUID and the modulation coil, as well as the input coil, are negligibly small. Therefore, the same flux-ramp modulation signal was used for all channels.

The total chip measures 15.5 mm × 5 mm. As shown in figure 5.4, the feedline crosses the chip in a straight line, with all µMUX channels coupled from the same side. To connect the feedline, two tapered bondpads are located at both ends of the chip. The wire bonds used for the connection between the chip and the rf-circuit board of the chip housing introduce an impedance mismatch in the feedline. To suppress the resulting parasitic modes, the ground planes on both sides of the feedline are interconnected through a ground bridge immediately after the bondpad taper, as well as through a ground connection at the edge of the chip. To provide artificial pinning sites and mitigate losses due to the movement of magnetic vortices, the ground plane of the chip has been equipped with a lattice of 4 µm × 4 µm holes, arranged in a regular 8 µm spacing. The ground plane also includes four alignment crosses that can be used during photolithography for alignment if a post processing step of a single chip is required.

The MMC array connected to the µMUX is of a similar scale as the µMUX chip (15.3 µm × 5.1 µm). The bondpads of the input coils are placed along the bottom edge of the µMUX chip according to the spacing set by the MMC chip. The MMC array contains only 12 pixel pairs, thus requiring just 12 µMUX readout channels. Consequently, 6 out of the 18 µMUX channels were not connected to an MMCs but were used to demonstrate the functionality of the SDR systems in the corresponding frequency range. The rf-SQUID is coupled to the input coil with $M_{\mathrm{mod}} = 153\,\mathrm{pH}$, and an input inductance of $L_{\mathrm{in}} = 1.4\,\mathrm{nH}$ introduces a slight impedance mismatch between the µMUX and the MMC, which, as discussed in section 5.1, results in a reduction in signal amplitude by $< 6\,\%$, thereby slightly negatively affecting the achievable energy resolution. To suppress microwave power leakage from the resonators into the detector, a $5\,\Omega$ shunt resistor was placed in parallel with the input coil, forming a first-order LR low-pass filter. The placement of the filter was varied for every second µMUX channel with a connected MMC. In one case, the filter resistor was positioned close to the rf-SQUID, thereby avoiding distributed-circuit behavior in the input line (see section 4.2.3). In the other case, the filter resistor was integrated into the bondpads, following the design in [Ric21b].

5.4 Description of the cryogenic setup

Both the MMC chip and the µMUX chip are mounted inside a µMUX housing as described in chapter 3.5 using GE / IMI 7031 varnish (see figure 5.6 (b) and (c)). The µMUX chip is aligned with the transmission line on the circuit board of the housing, while the MMC chip is placed directly below the µMUX chip to maintain short electrical connections and hence minimal parasitic inductance. Electrical connections between the chips and the circuit board are established via aluminum wire bonds. For

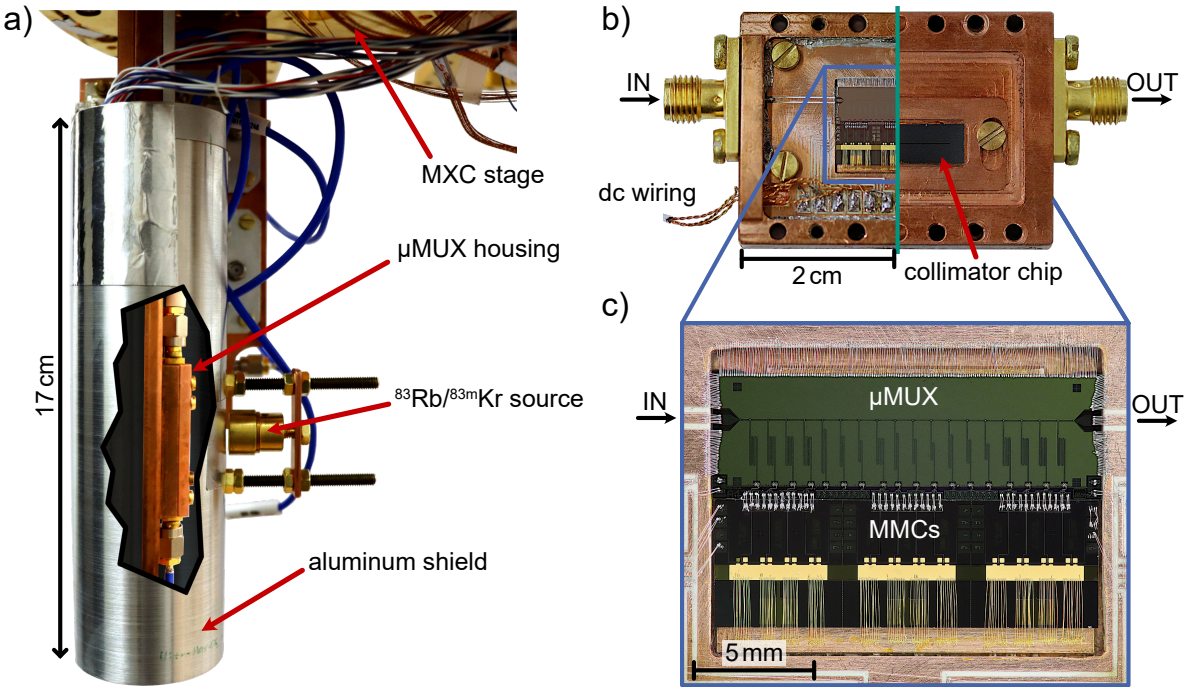

Fig. 5.6: Photographs of the experimental setup mounted in the cryostat. a) Final setup mounted on the MXC stage. The image is edited to reveal the µMUX housing inside the aluminum shield. b) Photograph of the µMUX housing, with one half covered by the copper lid and collimator chip and the other half open, showing the MMC array and µMUX. c) Zoomed-in view of the MMC array and µMUX chip inside the housing. Electrical connections are made via aluminum bonds, and the MMC heat baths are connected to the µMUX housing with gold wire bonds.

redundancy, each connection is made at least twice; to minimize impedance mismatch on the feedline, these wires are placed five times, and to ensure sufficient grounding and suppress parasitic modes along the µMUX chip edge, the ground plane is connected to the housings circuit board with > 300 wire bonds. Due to a defect in the modulation line, only one half of the modulation coil could be connected to external electronics, resulting in a reduced mutual inductance of $M_{\mathrm{mod}} = 17\,\mathrm{pH}$ ($M_{\mathrm{mod}}^{-1} = 121\,\mu\mathrm{A}/\Phi_0$). Similarly, an open circuit in the heater renders the injection of a persistent current in 4 out of 12 MMC pixel pairs impossible. For the thermalization of the individual heat baths of the MMC chip, gold wire bonds were used to connect the on-chip heat bath to the copper µMUX housing.

The µMUX housing is mounted to the MXC stage of the dilution refrigerator, which is used to cool the setup down to $T < 7\,\mathrm{mK}$. It is placed inside a superconducting aluminum shield, as displayed in figure 5.6 (a) and figure 5.7, to screen the setup against variations in external magnetic fields. The cycles of the pulse tube cooler, pre-cooling the cryostat's 4 K stage, can stimulate vibrations in the vertically mounted setup. To suppress relative vibrations between the µMUX housing and the aluminum shield, the bottom of the shield is fitted with foamed plastic, which is compressed between the

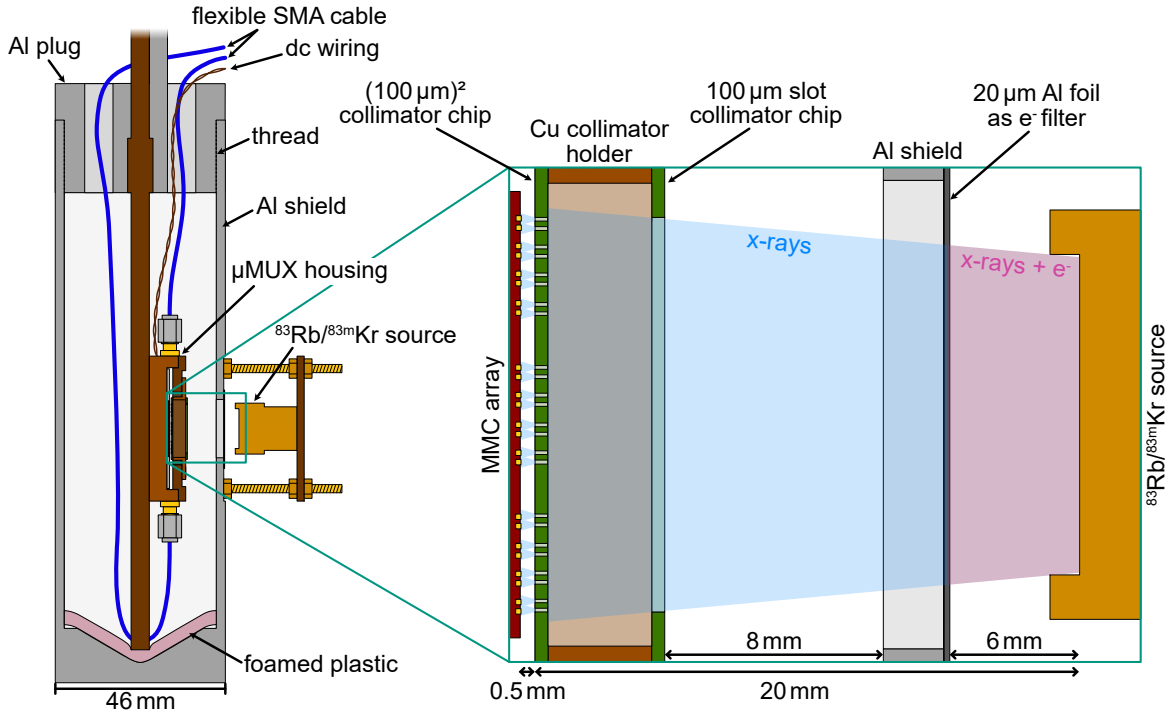

Fig. 5.7: Schematic cross section of the cryogenic measurement setup shown in figure 5.6. The zoomed-in view illustrates the arrangement of the series of collimators. The conversion electrons generated by the ^{83}Rb/^{83m}Kr source are absorbed by a $\sim 20\,\mu$m aluminum foil, which leaves the generated x-rays largely unaffected.

aluminum shield and the copper plate to which the housing is attached.

The µMUX is connected through flexible SMA cables[1] to the cryogenic rf-switch[2], which is connected to the 4 GHz to 8 GHz readout chain of the cryostat (see chapter 3.6). Another channel of the transmitting side rf-switch is shorted to a channel of the receiving side switch without a Device Under Test (DUT), allowing for the acquisition of a calibration transmission curve, which can be used to correct the baseline of the transmission curves measured through the µMUX. The modulation line and the MMC bias lines for the heater and field current are connected to room temperature with CuNi[3] twisted wire pairs.

Since the MMCs are not implanted with a radioactive source, an external source is needed to generate events. For this a ^{83}Rb/^{83m}Kr source was used, as standard calibration surces, e.g., ^{55}Fe or ^{241}Am have not yet been available. Here, ^{83}Rb, having a half-life of three months, decays by electron capture and thereby continuously produces ^{83m}Kr. ^{83m}Kr is an intermediate state with a short half-life of 1.8 h and decays into stable ^{83}Kr. During this decay several x-rays and γ-rays are emitted with energies around

[1] Mini-Circuits, 086-12SM+
[2] Radiall, R583423141
[3] ELSCHUKOM GmbH. The wire is made of 98 % copper and 2 % nickel.

∼9.4 keV, ∼12.6 keV and ∼14.1 keV, as well as conversion and Auger electrons [Vén18] with energies up to ∼32 keV. The source is mounted outside the aluminum shield, and a series of collimators provides a line of sight between the MMCs and the source. The arrangement of collimators is illustrated in figure 5.7. Electrons hitting the MMC absorber do not necessarily deposit all their energy due to back-scattering. To measure only sharp lines in the decay spectrum, enabling the determination of the systems energy resolution, the electrons must be filtered before reaching the absorber. This is accomplished by covering the first collimator with a thin aluminum foil that is ∼20 µm thick. While photons with energies above 9.4 keV pass through the foil with a probability $> 83.6\,\%$, the most energetic electrons, on average, will only penetrate 10 µm before being stopped. After passing through the aluminum foil, the photons pass through a slot in the aluminum shield and a slot in the lid of the µMUX housing directly above the MMCs. To minimize the number of photon hits in the substrate adjacent to the MMCs, two collimator chips, 500 µm silicon substrates, patterned by deep reactive-ion etching, were employed. One has 100 µm square holes above the MMC absorbers, and the other has a single 100 µm wide slot.

5.5 Characterization of the microwave SQUID multiplexer

Before biasing the MMC array, we comprehensively characterized the µMUX using a VNA and the measurement setup described in section 3.7. The measurements were conducted at the cryostats base temperature $T < 7\,\mathrm{mK}$. Figure 5.8 shows the transmission spectrum of the µMUX, measured with a VNA output power of $P_{\mathrm{VNA}} = -25\,\mathrm{dB}$, corresponding to an on-chip power level of $P_{\mathrm{chip}} \approx -72\,\mathrm{dB}$. All 18 µMUX channels can be identified. However, three of these channels did not exhibit any shift in resonance frequency with the modulation current and were therefore not operational for SDR-based readout. The resonances show a mean resonator bandwidth of $\langle \Delta f_{\mathrm{BW}} \rangle = (1.3 \pm 0.4)\,\mathrm{MHz}$ and a mean intrinsic quality factor of $\langle Q_{\mathrm{i}} \rangle = (19\,400 \pm 13\,000)$. While the variation of Q_{i} across channels is large, we observe on average lower intrinsic quality factors $\langle Q_{\mathrm{i}} \rangle_{\mathrm{MMC}} = (17\,000 \pm 10\,000)$ in channels with coupled MMC than in those without $\langle Q_{\mathrm{i}} \rangle_{\mathrm{no\ MMC}} = (26\,000 \pm 20\,000)$. The intrinsic quality factors here are greater than those observed in previous measurements with similar setups [Weg18, Ric21b]. Nevertheless, they remain significantly smaller than the target value of 10^5 as typically assumed in simulations [Sch23b]. Overall, this leads to increased resonance bandwidths.

The resonance frequency shift of each channel was determined as a function of the modulation current. Figure 5.9(a) shows the resonance curves of µMUX channel 13, with a resonance frequency of $\sim 6\,\mathrm{GHz}$, for various flux biases between $n\Phi_0$ and $(n + 1/2)\Phi_0$. This channel exhibits the deepest resonance curves between these flux limits, an effect that can be explained by the flux-dependent loss induced by the filter resistor, as described in section 4.2. From the individual resonance curves, the resonance frequency is determined and plotted as a function of the modulation current in figure 5.9(b). By applying the power-independent µMUX model from equation 2.45, we determine the

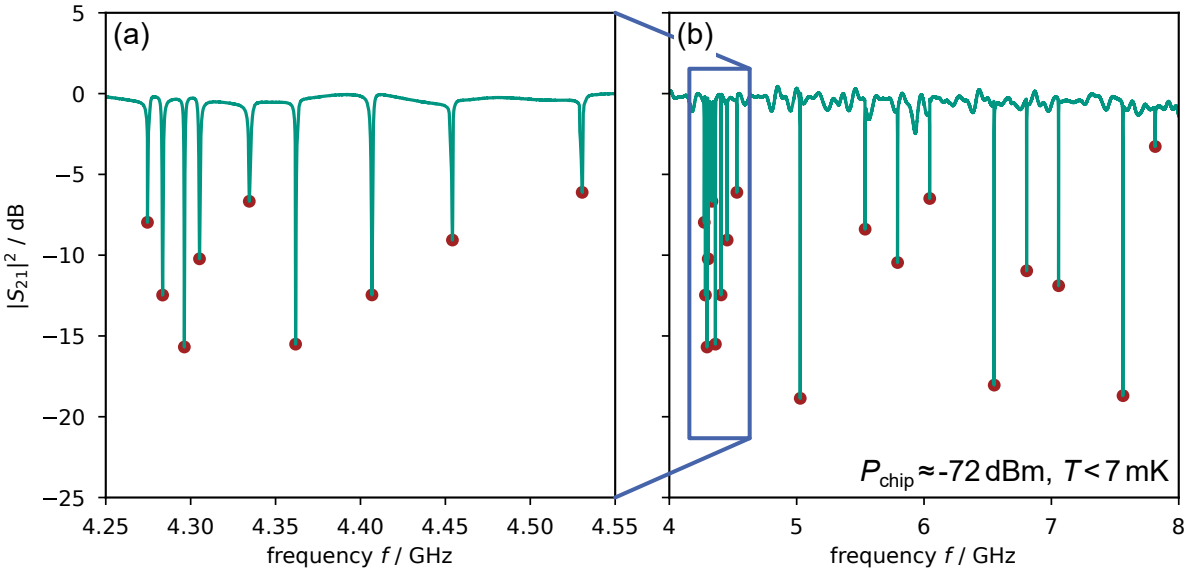

Fig. 5.8: Transmission spectrum of the µMUX chip installed in the our µMUX system. (a) shows the frequency range from 4.25 to 4.55 GHz, while (b) shows the full frequency range of the µMUX system. The baseline of the transmission spectrum was corrected using a second spectrum measured through the rf-switch channel with no DUT.

screening parameter β_L for each channel [Weg18]:

$$f_\mathrm{r}(I_\mathrm{mod}) = f_\mathrm{r}^\mathrm{off} + f_\mathrm{r}^\mathrm{amp} \frac{\beta_\mathrm{L} \cos\left(\varphi_\mathrm{tot}(I_\mathrm{mod})\right)}{1 + \beta_\mathrm{L} \cos\left(\varphi_\mathrm{tot}(I_\mathrm{mod})\right)}. \tag{5.4}$$

Here $\varphi_\mathrm{tot}(I_\mathrm{mod})$ denotes the normalized total magnetic flux threading the rf-SQUID, generated by the current I_mod in the modulation line, the screening currents in the SQUID loop, and external parasitic fields that generate a flux Φ_off. Since no analytical expression for the total magnetic flux as a function of the externally applied flux exists, we iteratively approximate φ_tot as $\varphi_{\mathrm{tot},N}$, with the n-th iteration given by

$$\varphi_{\mathrm{tot},n} = \tfrac{2\pi}{\Phi_0}(M_\mathrm{mod} I_\mathrm{mod} + \Phi_\mathrm{off}) - \beta_\mathrm{L} \sin\left(\varphi_{\mathrm{tot},n-1}\right) \tag{5.5}$$

with $\varphi_{\mathrm{tot},0} = 0$ and $N = 100$. While β_L determines the asymmetry of the resonance frequency shift, the factors $f_\mathrm{r}^\mathrm{off} \approx f_0 - 4f_0^2(C_\mathrm{c} Z_0 + L_\mathrm{T}/Z_0)$ and $f_\mathrm{r}^\mathrm{amp} \approx 4f_0^2 M_\mathrm{T}^2/(L_\mathrm{S} Z_0)$ determine the frequency around which the shift occurs and the amplitude of the shift. The determined µMUX channel parameters are presented in table 5.2.

The resonance frequency $f_\mathrm{r}^\mathrm{off}$ of the µMUX channels is, on average, (0.7 ± 0.1) % higher than designed, likely due to slight deviations in the estimate of the CPWs effective permittivity $\epsilon_\mathrm{r,eff}$. Additionally, the resonance frequency spacing deviates, on average, by (2 ± 4) MHz from the design values, which could be significantly improved in a tile-and-trim post processing step [Ahr22]. However, for the intended measurements, the achieved resonance frequency precision is sufficient, as the µMUX channels cover the majority of the SDR systems 4 GHz to 8 GHz range.

Tab. 5.2: Parameters of all µMUX channels of our µMUX system, obtained from circle fits and fits to the resonance-frequency dependence on the modulation current. The parameters were determined with an on-chip power of $P_{\mathrm{chip}} \approx -83\,\mathrm{dBm}$. An exception are Q_{i} and Δf_{BW}, which are determined at a typical readout power of $P_{\mathrm{chip}} \approx -68\,\mathrm{dBm}$ and averaged over the modulation current.

channel	$f_{\mathrm{r}}^{\mathrm{off}}$ / GHz	$\Delta f_{\mathrm{r}}^{\mathrm{max}}$ / MHz	β_{L}	$\frac{M_{\mathrm{T}}^2}{L_{\mathrm{S}}}$ / pH	M_{mod}^{-1} / $\frac{\mu\mathrm{A}}{\Phi_0}$	Δf_{BW} / MHz	Q_{i}	MMC
1	4.275	1.85	0.76	0.43	114.3	1.19	10500	defect
2	4.283	-	-	-	-	1.17	15000	defect
3	4.296	5.08	0.78	0.72	116.1	0.81	22400	defect
4	4.305	-	-	-	-	1.25	10600	defect
5	4.335	2.94	0.71	0.82	112.4	1.96	4500	✓
6	4.362	2.61	0.67	0.85	112.6	1.12	21000	✓
7	4.407	-	-	-	-	1.62	11400	✓
8	4.455	3.82	0.73	0.86	115.1	1.42	9100	✓
9	4.532	3.56	0.81	0.51	115.9	1.51	6400	✓
10	5.028	0.99	0.66	0.25	117.1	1.23	42400	-
11	5.538	4.37	0.80	0.41	113.5	0.86	20800	✓
12	5.793	1.85	0.75	0.18	119.1	1.59	8700	-
13	6.045	1.18	0.66	0.15	118.8	0.76	54700	-
14	6.551	4.23	0.80	0.27	115.5	1.20	32500	✓
15	6.806	0.93	0.64	0.10	116.7	0.92	21700	-
16	7.057	0.88	0.62	0.09	117.0	0.96	24500	-
17	7.562	3.27	0.81	0.16	112.5	2.10	26200	✓
18	7.815	1.03	0.65	0.09	119.0	1.51	6800	-

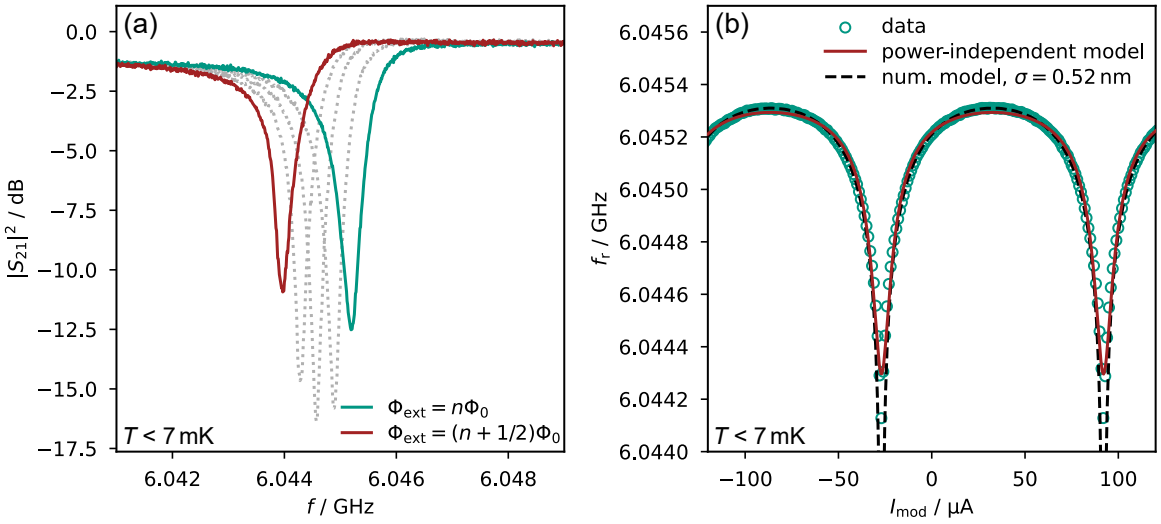

Fig. 5.9: (a) Transmission spectrum of µMUX channel 13 acquired at $T < 7\,\mathrm{mK}$ with a VNA output power of $P_{\mathrm{VNA}} = -40\,\mathrm{dBm}$ corresponding to an on chip power of $P_{\mathrm{chip}} \approx -87\,\mathrm{dBm}$. The red and green curves show the resonance for the flux state $\Phi_{\mathrm{ext}} = (n + 1/2)\Phi_0$ and $\Phi_{\mathrm{ext}} = n\Phi_0$, respectively. They grey dotted curves show intermediate flux states. The transmission baseline was corrected using a second spectrum acquired through the rf-switch channel without a DUT. (b) Resonance frequency shift as a function of the modulation current, measured at the same power and temperature. The data has been fitted with equation 5.4 and also the advanced numerical model described in chapter 6.

The average screening parameter $\langle \beta_{\mathrm{L}} \rangle = (0.72 \pm 0.07)$ is slightly higher than designed. The scatter of the parameter corresponds to a variation in the critical current of 0.5 µA, which can be explained by inhomogeneities in the critical current density across the chip, combined with variations in the side length of the Josephson junction. The average resonance frequency shift $\langle \Delta f_{\mathrm{r}}^{\mathrm{max}} \rangle = (2.6 \pm 1.4)\,\mathrm{MHz}$ aligns with the design parameter of 2 MHz. However, the variation in $\Delta f_{\mathrm{r}}^{\mathrm{max}}$ among the channels is significant. Similarly, the ratios $M_{\mathrm{T}}^2/L_{\mathrm{S}}$, determined from the amplitude $f_{\mathrm{r}}^{\mathrm{amp}}$, deviate on average from design by $(80 \pm 30)\,\%$. One possible explanation for this variation is that the measurement underestimates the actual total resonance frequency shift, as the resonance frequency shift around $\Phi_{\mathrm{ext}} = (n + 1/2)\Phi_0$ is very steep, and the modulation current steps might have been too coarse to resolve the actual minimum resonance frequency.

As shown in figure 5.9(b), the fit function given in equation 5.4 does not accurately reproduce the measured resonance frequency shift of µMUX channel 13. Similar deviations are observed for all µMUX channels. As discussed in section 4.3, both the filter resistor and the coupled MMCs are expected to influence the µMUX characteristics. Additionally, as will be discussed in section 6.3, inhomogeneities in the Josephson junction tunnel barrier can affect the resonance frequency shift. Indeed, figure 5.9 (b) shows that the resonance frequency shift of µMUX channel 13 is more accurately de-

scribed by assuming a tunneling barrier thickness of 2 nm with a Gaussian variation of $\sigma = 0.52\,\mathrm{nm}$, and a reduced screening parameter of $\beta_\mathrm{L} = 0.55$ ($\beta_\mathrm{L} = 0.66$ when using equation 5.4). Consequently, the values of $M_\mathrm{T}^2/L_\mathrm{S}$ and β_L listed in Table 5.2 are expected to be affected by these unaccounted factors in the applied fit function, too. To avoid barrier inhomogeneities in future devices, the thickness of the aluminum layer in the trilayer could be increased, which has been shown to also result in more consistent screening parameters β_L across many devices [Jon24].

5.6 Simultaneous multi-channel readout

After comprehensively characterizing the µMUX chip, we performed multi-channel readout using the SDR electronics described in section 2.7. While the MMC array was active for all measurements presented in this section, during the readout tone optimization and the noise measurements, we operated the cryostat at $T = 600\,\mathrm{mK}$, where the paramagnetic response of the MMC sensor material is suppressed, avoiding detector events that interfere with these measurements. The SDR electronics are connected to the TX and RX ports of the cryogenic readout chain of the dilution refrigerator, as shown in figure 5.10. The µMUX readout is entirely handled by the SDR board, so no additional devices are required. However, the flux-ramp signal generated by the SDR board is a voltage signal, whereas the µMUX modulation line requires a current signal. Therefore, the flux-ramp output of the SDR board was connected to a commercially available SQUID electronics[4]), providing a signal line with an inline resistor of $R = 2.5\,\mathrm{k\Omega}$. These SQUIDs electronics also serve as an auxiliary current source capable of generating simple flux signals in the rf-SQUIDs of the µMUX channels via the modulation coil. Both the SDR electronics and the SQUID electronics are software-controlled from a PC. To ensure stable operation on the SDR board during long measurements, a rubidium frequency standard[5] is connected to the SDR board, providing a stable 10 MHz reference signal.

The probe tone signals are amplified after passing through the µMUX, first by the cryogenic low-noise HEMT amplifier and then by a low-noise room-temperature amplifier[6]. Although the resulting amplification of $\sim 44\,\mathrm{dB}$ is comparable to the sending-side attenuation ($A_\mathrm{TX} \approx -46\,\mathrm{dB}$ at 4 GHz), we found that the noise performance of the readout system is still limited by the SDR system itself. In fact, a probe tone transmitted through the cryogenic readout chain exhibits the same noise level as a tone sent in loop-back through a simple flexible coaxial cable from the SDR output directly to its input. As depicted in figure 5.11 (a) and (b), we measured the absolute voltage noise $\sqrt{S_A}$ at the SDR electronics input for multiple probe tone frequencies f_exc. For each tone, we measured the noise at the SDR input when the tone was transmitted through the rf-switch channel without the DUT, through the rf-switch channel with

[4]XXF-1, Magnicon GmbH, Hamburg, Germany
[5]FS725 Rubidium Frequency Standard, Scientific Instruments GmbH, Gilching, Germany
[6]ZX60-83LN-S+, Mini-Circuits®, Brooklyn, NY, USA

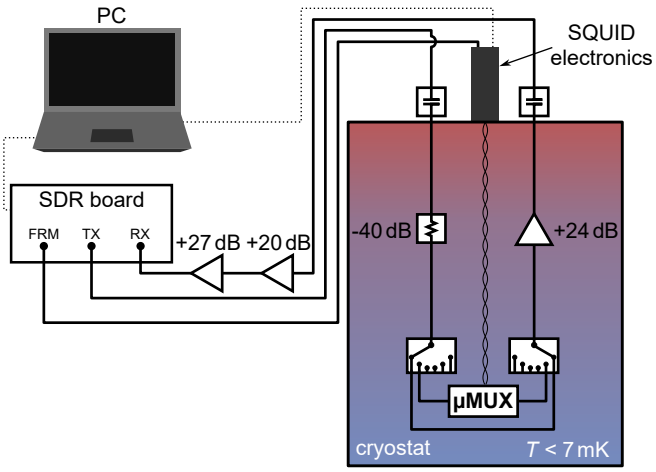

Fig. 5.10: Sketch of the setup used for the multi-channel readout with the SDR electronics. The installed attenuators, combined with the cable attenuation in the transmitting path results in a total attenuation of $A_{\mathrm{TX}} \approx -46\,\mathrm{dB}$ at 4 GHz. The voltage flux-ramp signal generated by the SDR electronics is converted into a current signal through the SQUID electronics, providing a signal line with an inline resistor of $R = 2.5\,\mathrm{k\Omega}$. Both, SDR electronics and SQUID electronics are software-controlled from the PC.

the µMUX, or in loop-back directly to the SDR input. While the tone amplitude generated by the SDR system was kept constant for each measurement, the tone amplitude received at the SDR input varied with probe tone frequency f_{exc} and the configuration of the readout chain. The absolute noise, however, appears unaffected by variations in the transmitted tone amplitude and the readout chain configuration, implying that the dominant noise contribution occurs not in the readout chain but in the input of the SDR electronics itself. The limitation imposed by this noise can be mitigated by increasing the amplification in the TX path of the readout chain. To this end, we installed an additional amplifier[7] following the existing room-temperature amplifier, resulting in a total amplification of $\sim 71\,\mathrm{dB}$ that is significantly larger than the installed attenuation.

The time-intensive acquisition of detector events, as well as the probe tone optimization presented in section 5.6.1, was performed before this issue was identified. However, the noise performance investigations presented in sections 5.6.3 and 5.7 were conducted with the additional amplifier, resulting in an improvement in noise performance of approximately a factor of two.

To determine the initial probe tone frequencies for µMUX readout, we used the transmission spectra acquired in section 5.5. For each µMUX channel's resonance curve, the frequency exhibiting the largest change in $|S_{21}|$ with varying I_{mod} was identified. For the 7.815 GHz channel, this variation was minimal, and no suitable parameters for successful FRM were found. The remaining 14 channels were successfully read out simultaneously. Of these, seven channels had a functional two-pixel MMC connected, two had a defective MMC in which no persistent current could be trapped, and five had no detector coupled to their input coil.

While the system is capable of simultaneously generating and reading up to 400 channels, the maximum output power provided by the SDR electronics was found to be insufficient to achieve the optimum readout power for all channels in this setup. Fu-

[7] ZVA-183-S+, Mini-Circuits®, Brooklyn, NY, USA

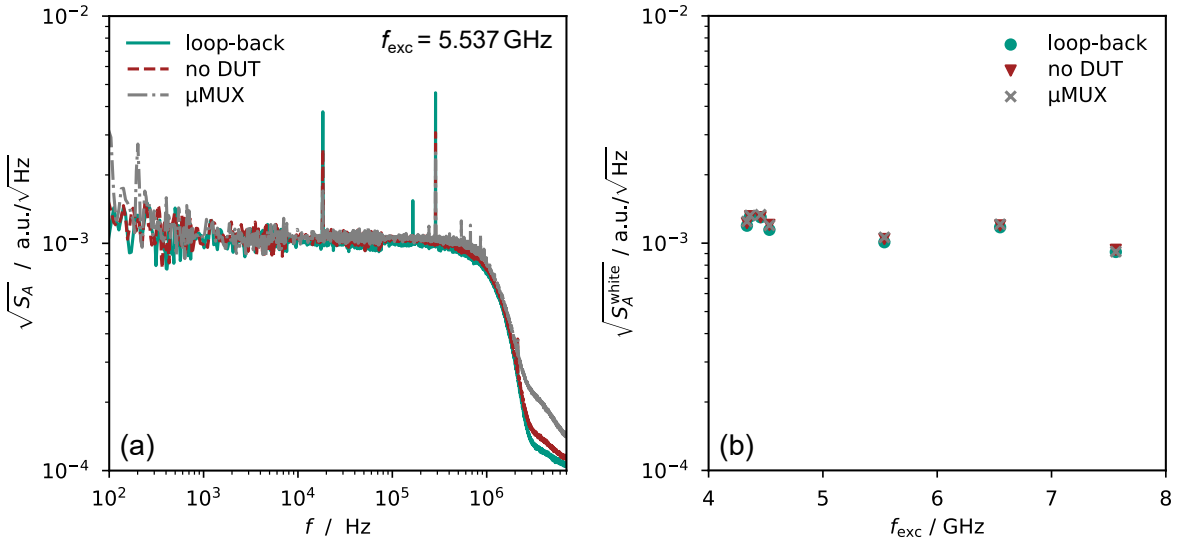

Fig. 5.11: (a) Voltage noise of a probe tone applied at $f_{\text{exc}} = 5.537\,\text{GHz}$, measured at the SDR input. The tone was measured (i) in loop-back via a flexible coaxial cable, (ii) through the cryogenic readout chain and rf-switch without a DUT, and (iii) with the μMUX installed. The ADC-to-voltage conversion has not been determined. Hence, the noise is given in arbitrary units. (b) Extracted white-noise levels for all probe tones measured as in (a). No significant difference is observed between the readout configurations at any frequency.

ture iterations of the SDR system will need to either provide increased output power or incorporate an additional amplifier after the SDR output. The output power was sufficient to read out the available 14 channels simultaneously. However, the output power did not allow for probe tone power sweeps with all 14 tones applied simultaneously. Consequently, the probe tone optimization and noise measurements discussed below were performed in two steps. First, we measured the seven channels connected to the MMCs, and then the remaining seven channels.

All FRM measurements presented here were conducted with a flux-ramp repetition rate of $f_{\text{ramp}} = 122\,\text{kHz}$ and a ramp amplitude of $\Phi_{\text{ramp}} \approx 3.75\,\Phi_0$, with minor variations arising from differences in M_{mod} among the channels. This corresponds to a carrier frequency of $f_{\text{carr}} \approx 457\,\text{kHz}$, which is the oscillation frequency of each resonance and is more than a factor of two below the maximum frequency set by the μMUX channel bandwidth. Only an integer number of flux quanta can be used for demodulation. Therefore, the transient region following each ramp reset is excluded from the analysis. Consequently, only the remaining $\sim 80\,\%$ of the ramp, i.e. $\alpha = 0.8$, is used for demodulation. Both the carrier frequency and the extent of the excluded transient region are set individually for each channel.

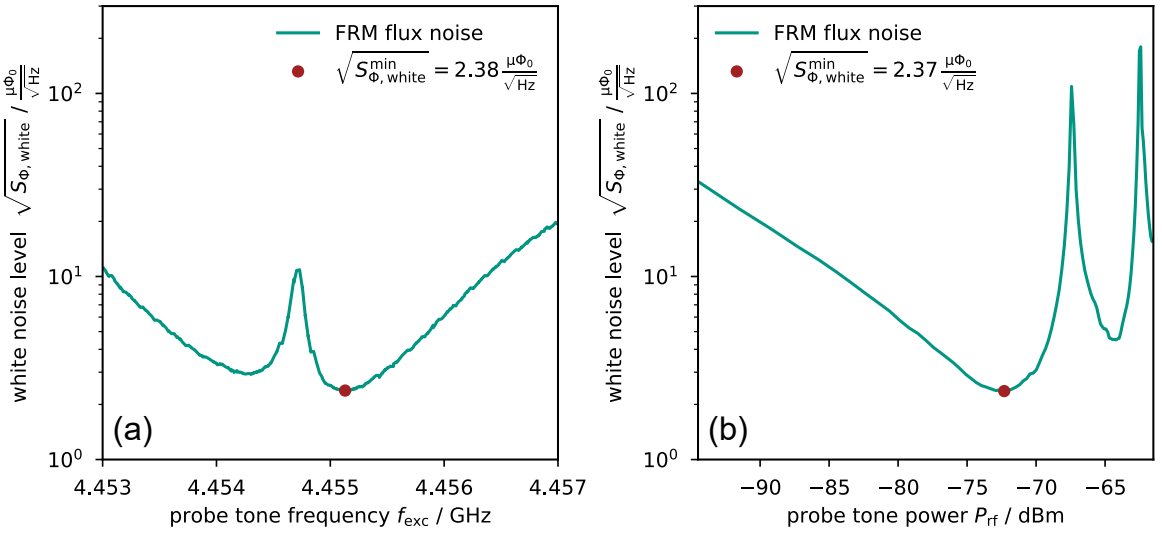

Fig. 5.12: Probe tone optimization of µMUX channel 8, at 4.455 GHz. Noise data were acquired at $T = 600\,\text{mK}$, where where the paramagnetic response of the MMC sensor material is suppressed, to avoid detector signals from interfering with our measurement. (a) Flux-ramp-demodulated white noise level as a function of probe tone frequency for a probe tone power of $P_{\text{rf}} \approx -72\,\text{dBm}$. The tone frequency at $\sqrt{S^{\min}_{\Phi,\text{white}}}$ is used for the probe tone power optimization. (b) flux-ramp-demodulated white noise level as a function of probe tone power. The power at the minimum noise level $P^{\text{opt}}_{\text{rf}} \approx -72\,\text{dBm}$ is used for all subsequent measurements.

5.6.1 Optimization of the readout tone parameters

The noise performance of each µMUX channel depends on both the probe tone detuning from the resonance frequency and the probe tone power. Consequently, both parameters must be optimized to achieve the best possible noise performance for each channel. For each combination of probe tone frequency and power, we acquired a flux-ramp–demodulated time trace containing 10^5 samples. From this time trace, we calculated the flux noise spectrum using Welch's method (see section 3.8.2). We then used the white noise level extracted from the noise spectrum as optimization criterion. In the following, we describe the optimization procedure for a single µMUX channel, which is then repeated for all channels.

First, we optimize the probe tone frequency f_{exc} by sweeping the frequency around the initial estimate obtained from the VNA measurement, covering a substantial portion of the channel's resonance curve. For each value of the probe tone frequency f_{exc}, we determine the white noise level, resulting in the plot shown in figure 5.12 (a). The frequency optimization shown in figure 5.12 was performed without the additional amplifier in the RX path of the readout chain. Consequently, the noise levels are higher than those presented in sections 5.6.3 and 5.7.

The noise levels in figure 5.12 (a) exhibit two minima, corresponding to probe tone placement on either flank of the resonance curve. The central maximum arises when the probe tone is positioned near the center of the resonance frequency shift. As the resonance frequency shifts, the resonance minimum sweeps across the fixed probe tone frequency, so that the tone alternately probes the left and right flanks of the resonance, depending on the flux bias. In this configuration, the noise performance is degraded because the total probe tone amplitude modulation is reduced. Likewise, the noise performance far off resonance is significantly degraded since the transmission of the probe tone is only weakly affected by the µMUX channel's resonance curve. For channel 8, with a resonance frequency of $f_\mathrm{r} = 4.455\,\mathrm{GHz}$, the optimal probe tone frequency $f_\mathrm{exc}^\mathrm{opt}$ is found on the right flank of the resonance curve, in agreement with simulations [Sch23b]. However, we also observed channels for which the optimal frequency was located on the left flank.

Following the frequency optimization, we swept the probe tone power P_rf. At the optimal frequency determined in the previous step, the probe tone amplitude was varied linearly around the initial estimate of $P_\mathrm{rf} \approx -70\,\mathrm{dBm}$, resulting in the data shown in figure 5.12 (b). The quoted values of P_rf refer to the on-chip power, which can only be estimated due to the lack of precise attenuation measurements at the µMUX channel frequency. The TX attenuation of the nearly identical readout chain with a bandwidth of $4-20\,\mathrm{GHz}$ was determined to be $A_\mathrm{TX}(4\,\mathrm{GHz}) \approx -46\,\mathrm{dB}$ (see section 3.6) and $A_\mathrm{TX}(16\,\mathrm{GHz}) \approx -53\,\mathrm{dB}$ (see section 7.3.2). Assuming an identical attenuation for the $4-8\,\mathrm{GHz}$ readout chain and a linear increase in attenuation with frequency, this results in a slope of $0.6\,\mathrm{dB/GHz}$, corresponding to an estimated attenuation of $\sim -46\,\mathrm{dB}$ for this channel. As the probe tone power is increased, the noise performance of the µMUX channel initially improves. The dominant noise contribution is the system noise temperature, which is set by the HEMT amplifier and is independent of the probe tone power. Consequently, the signal-to-noise ratio (SNR) increases with increasing probe tone amplitude. At high probe tone powers, however, the power dependence of the µMUX becomes relevant. This reduces the total resonance frequency shift and, in turn, the amplitude modulation of the probe tone, leading to a degradation of the SNR and the flux noise performance. The optimal probe tone power, $P_\mathrm{rf}^\mathrm{opt} \approx -67\,\mathrm{dBm}$, is found at the minimum point where the power dependence becomes relevant. To verify that the previously determined optimal probe tone frequency remains optimal at this probe tone power, we repeated the entire optimization procedure starting from $P_\mathrm{rf}^\mathrm{opt}$. However, no significant changes in the probe tone parameters or further improvements in noise performance were observed.

5.6.2 Acquisition of detector events

All further measurements performed in flux-ramp-demodulated readout were performed with optimized probe tone parameters. To demonstrate the acquisition of detector events, the cryostat was cooled to $T < 7\,\mathrm{mK}$[8]. To enable the generation of detector

[8]The calibration range of the thermometer installed in the dilution refrigerator ends at 7 mK.

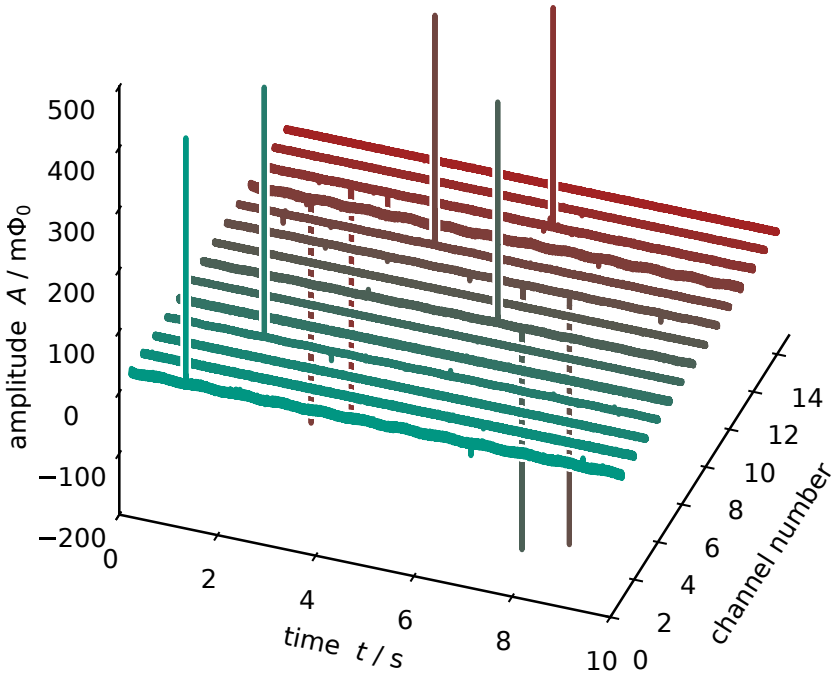

Fig. 5.13: FRM-demodulated time-stream data of 14 simultaneously operated µMUX channels. Seven channels are connected to a two-pixel MMC and exhibit detector signals appearing as spikes in the time stream. The pixels of each MMC can be distinguished by the signal polarity.

signals in the MMCs, a persistent current was prepared in the meander-shaped pickup coils, thereby providing the required magnetic field for the paramagnetic temperature sensor. Figure 5.13 shows several time traces from the 14 simultaneously operated µMUX channels. Detector signals were observed in all seven channels with MMCs connected, appearing as positive and negative spikes in the time traces.

The total number of channels used in this measurement was limited by the number of available µMUX channels. Nevertheless, the system was operated with 400 probe tones generated by the SDR electronics. Of these, 14 tones were placed on resonance for the readout of the installed µMUX channels, while the remaining tones were positioned off resonance. These measurements were performed without the additional amplifier in the RX branch, and the limited SDR output power required a reduction in the output power per probe tone, which generally resulted in degraded noise performance. Assuming the availability of 400 µMUX channels, we expect that the readout of the full target channel count will, in principle, be feasible with the current iteration of the SDR system. However, an additional amplifier at the SDR output will be required to achieve sufficient output power for optimized readout of all channels. In this configuration, the SDR electronics will generate tones with lower initial power, which are then amplified before entering the readout chain. This, however, degrades the signal-to-noise ratio of each tone amplitude, potentially affecting the system's overall noise performance.

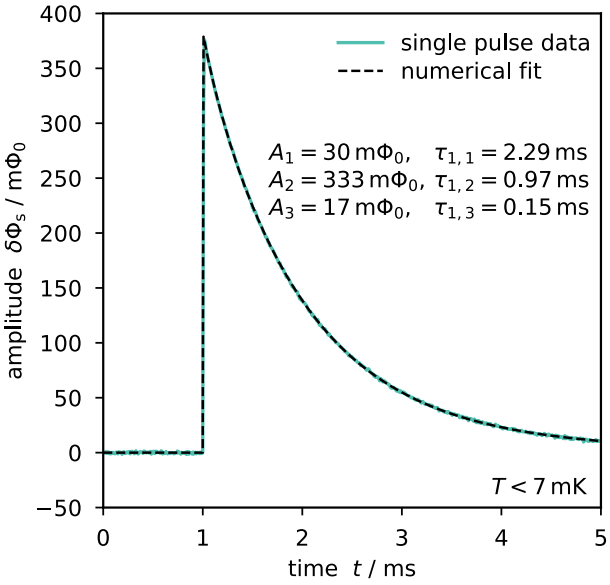

Fig. 5.14: Detector signal with positive polarity acquired in the 4.455 GHz µMUX channel at $T < 7\,\mathrm{mK}$. The signal shape can be described, according to equation 5.6, by the sum of three exponential functions. The corresponding amplitudes A_i and decay times $\tau_{1,i}$ are listed in the figure.

Figure 5.14 shows a single detector event with positive polarity recorded in µMUX channel 8 at $f_\mathrm{r} = 4.455\,\mathrm{GHz}$. The pulse corresponds to a K_α event with an energy of approximately 12.6 keV. While the flux-ramp repetition rate, and thus the effective sampling rate of the system, is insufficient to resolve the signal rise time, the signal decay can be investigated. As in the experiments reported in [Mül25], the decay is well described by a sum of three exponential components, indicating the presence of three independent heat capacities and thermal conduction pathways. The fit function applied in figure 5.14 is given by

$$\delta\Phi_\mathrm{s}(t) = \Theta(t - t_0) \cdot (A_1 e^{-\frac{t-t_0}{\tau_{1,1}}} + A_2 e^{-\frac{t-t_0}{\tau_{1,2}}} + A_3 e^{-\frac{t-t_0}{\tau_{1,3}}}), \tag{5.6}$$

Here, t_0 is the start time of the event, $\tau_{1,i}$ represents the decay times of the individual exponential components, A_i indicates the corresponding amplitudes, and Θ denotes the heaviside function. The decay times $\tau_{1,i}$ and amplitudes A_i found for the applied function are listed in figure 5.14.

The dominant contribution corresponds to a decay time of $\tau_{1,2} = 0.97\,\mathrm{ms}$, which is consistent with the designed thermal decay through the combined absorber and sensor heat capacity and the weak thermal link shown in figure 5.2 (b). Minor deviations from the results in [Mül25] are expected since the MMCs used here employ absorbers that are only half as thick, and the detector heat capacity depends on both temperature and persistent current. Additionally, a slower signal decay with $\tau_{1,1} = 2.29\,\mathrm{ms}$ is observed, the origin of which is not yet understood. This component contributes only weakly to the total signal amplitude, in contrast to [Mül25], where a decay time of similar magnitude accounted for approximately half of the total signal, depending on temperature. A fast decay component with $\tau_{1,3} = 0.15\,\mathrm{ms}$ is also observed, in agreement with [Mül25], and can be attributed to a heat capacity subsystem associated with quadrupole moments of erbium atoms embedded in the gold host material.

The total pulse amplitude cannot be directly compared to the measurements reported in [Mül25], as it depends on several parameters, including the SQUID inductances and the heat capacity of the MMCs. The latter is strongly dependent on both the persistent current and the MMC operation temperature. In particular, the operation temperature is hard to determine and would require a dedicated investigation of the pulse shape as a function of the mixing chamber platform temperature. As such measurements were not within the scope of this thesis, they have not been performed.

Event detection with the SDR system was successfully performed, with all 14 channels operating simultaneously. However, the activity in the channels with connected MMCs was only $\sim 0.1\,\mathrm{Bq}$ per detector pixel, rendering the acquisition of a high-statistics decay spectrum time-intensive. In addition, the MMCs exhibited temperature variations on timescales of a few seconds that must be corrected for [Mül25]. This correction can be achieved using an additional asymmetric MMC pixel that contains only sensor material and no absorber, thereby recording solely the base temperature of the experimental setup. Such a temperature pixel was not included in the present setup. Alternatively, temperature drifts can be corrected by tracking the pulse height of a spectral line over time or by monitoring the pre-trigger baseline level. However, the low activity of each pixel is insufficient to reliably apply these correction methods. Consequently, no high-resolution spectrum could be recorded.

5.6.3 Description of the data analysis using an exemplary readout channel

For each channel, we investigated the noise performance for both open-loop and FRM readout, as well as the channel linearity. While a time trace acquired in FRM readout is directly expressed in terms of the magnetic flux applied to the rf-SQUID, determining the open-loop noise in terms of flux first requires measuring the transfer coefficient between the voltage V_{DDC} of the transmitted probe tone in the SDR inputs digital down converter (DDC), and the magnetic flux Φ_{ext} applied to the rf-SQUID. In addition, the open-loop flux noise depends not only on the probe tone power and frequency but also on the flux bias applied to the rf-SQUID, which must be optimized to achieve the best noise performance. We performed all measurements at $T = 600\,\mathrm{mK}$, where the paramagnetic response of the MMC sensor material is suppressed to prevent detector signals from perturbing the noise measurements.

To determine the transfer coefficient at a given magnetic flux bias, we measured the amplitude of the transmitted probe tone in the SDR electronics' digital downconverter (DDC) as a function of the applied magnetic flux. This was achieved by generating a $3.358\,\mathrm{Hz}$ sawtooth ramp signal in the modulation coil with a total amplitude of $240\,\mu\mathrm{A}$ using the SQUID electronics. We calculated the applied flux corresponding to each modulation current using the modulation coil coupling $M_{\mathrm{mod}}^{-1} = 115.1\,\mu\mathrm{A}/\Phi_0$, which was determined from the VNA measurements, as discussed in section 5.5. The resulting measurement is shown in figure 5.15 (a). The DDC voltage is given in arbitrary units. However, changes in voltage can be converted into changes in magnetic flux by determining the derivative $\mathrm{d}V_{\mathrm{DDC}}/\mathrm{d}\Phi_{\mathrm{ext}}$ (see figure 5.15 (b)). Prior to calculating the

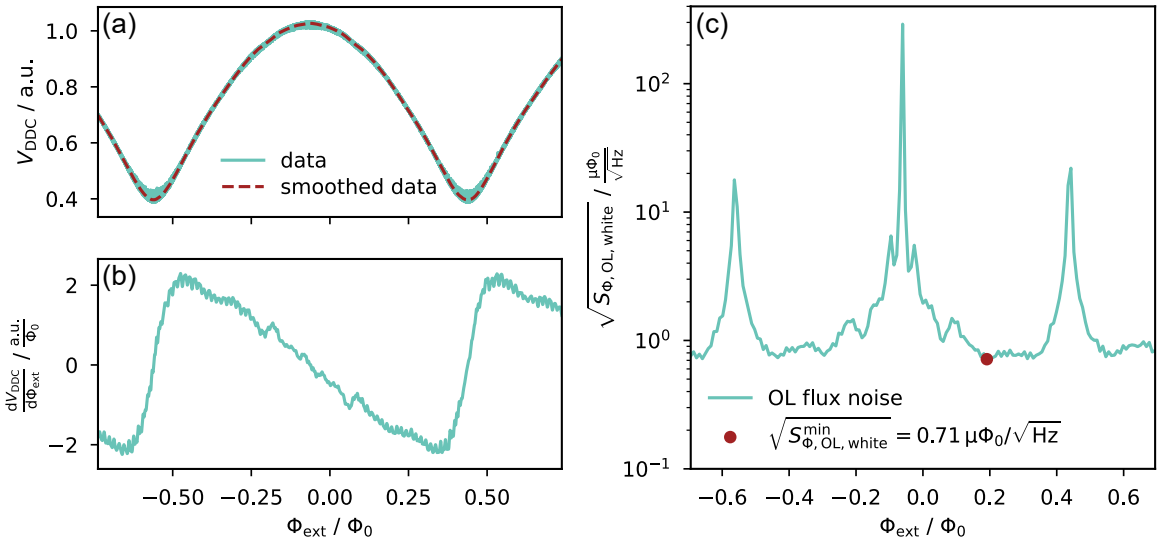

Fig. 5.15: Parameter optimization for the open-loop flux noise measurement in the 4.455 GHz µMUX channel. (a) Voltage V_{DDC} of the transmitted probe tone in the digital down converter (DDC) as a function of the applied flux through the rf-SQUID modulation coil. The data was smoothed to calculate the derivative. (b) Derivative of the smoothed data in (a). The derivative is used as transfer coefficient V_Φ to calculate flux noise from voltage noise in open-loop readout. (c) Open-loop white noise level as a function of the applied flux through the rf-SQUID modulation coil. The red circle marks the flux bias with the lowest open-loop white noise.

derivative, the data were smoothed using a boxcar filter with a window width of 0.1 mΦ_0.

To determine the optimal flux bias Φ_{ext}, we acquired open-loop noise traces at multiple magnetic flux bias points over a range exceeding 1 Φ_0. The flux bias was stepped by 1 µA in the modulation coil current, corresponding to 0.9 mΦ_0. For each noise trace, the corresponding flux noise spectrum was determined using the transfer coefficient shown in figure 5.15 (b), and the white noise level was extracted. The resulting magnetic flux white noise level as a function of flux bias is shown in figure 5.15 (c).

The spikes in figure 5.15 (c) correspond to flux bias points where the transfer coefficient approaches zero. In contrast, the best noise performance is observed at flux biases where the transfer coefficient is large. In the example channel, the minimum white noise level was found to be $0.71\,\mu\Phi_0/\sqrt{\mathrm{Hz}}$ at a flux bias of 0.19 Φ_0. The corresponding open-loop noise spectrum is shown in figure 5.16 (a). The noise spectrum obtained in FRM readout for the same channel and identical probe tone parameters is shown in figure 5.16 (b).

The open-loop noise spectrum was calculated from a noise trace comprising one million samples acquired at a sampling rate of 15.625 MHz, whereas the FRM noise spectrum was calculated from a noise trace with five million samples acquired at a sampling rate of 122 kHz. Although several spurious tones are visible in the spectra, the channel

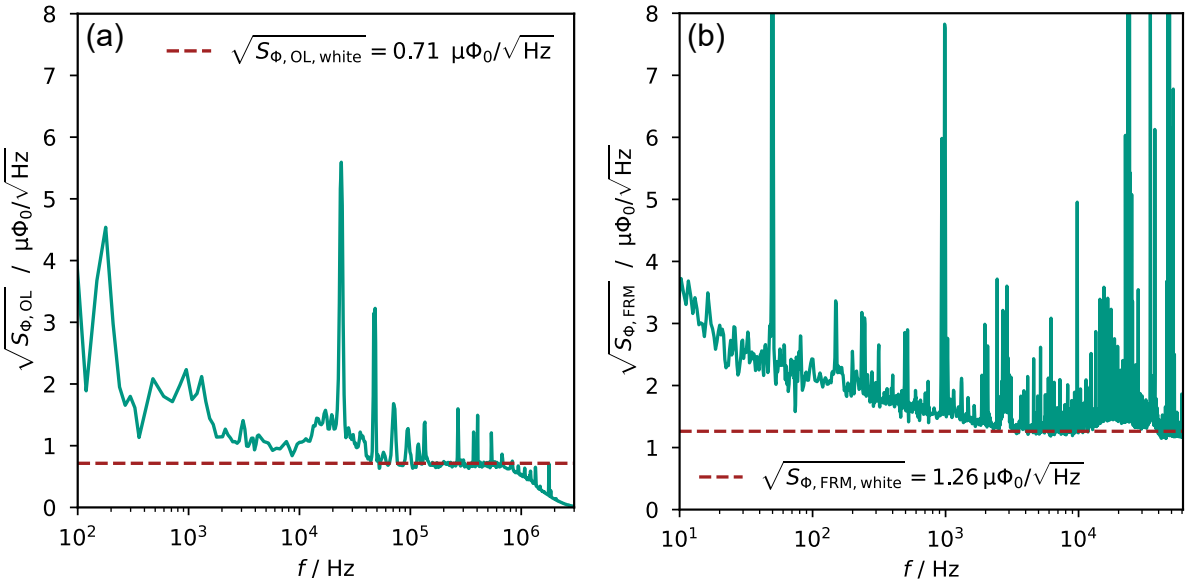

Fig. 5.16: Flux noise spectra of the 4.455 GHz µMUX channel. (a) Open-loop flux noise. (b) Flux-ramp-demodulated noise. The red dashed line marks the white noise level in each plot.

nonetheless exhibits a low white noise level of $1.26\,\mu\Phi_0/\sqrt{\mathrm{Hz}}$ in FRM readout, which corresponds to the noise performance during actual detector readout.

The origin of the spurious tones cannot be identified with certainty. However, simultaneous noise measurements performed in two separate channels reveal a strong correlation in FRM readout, both for the $1/f$ noise below 1 kHz and for the parasitic tones. This indicates that these contributions are either applied simultaneously to all channels via the modulation line or are generated in the TX or RX paths of the SDR electronics. In both cases, further optimization of the room temperature electronics is required. No correlation was observed for the white noise component, as expected for noise dominated by the HEMT amplifier.

Compared to open-loop readout, the white noise level in FRM readout is increased by a factor of 1.77, which slightly exceeds the theoretical minimum degradation of $\sqrt{2}$ (see section 2.6). This additional degradation is attributed to the exclusion of the transient regions at the beginning and end of each flux-ramp ($\alpha = 0.8$), combined with the non-sinusoidal shape of the probe tone amplitude in the DDC during each ramp [Ric21b].

Finally, the linearity of the µMUX channel was investigated. For this, we applied a 3.358 Hz triangle signal with a peak-to-peak amplitude of 240 µA to the modulation line. This signal was superimposed on the flux-ramp signal, enabling the measurement of the slow ramp in FRM readout. The top panel of figure 5.17 shows the measured flux in the µMUX channel as a function of the applied flux through the modulation line. Multiple ramp periods are overlaid in the same plot to reduce the influence of momentary perturbations. The data were fitted with a linear function, and the resulting residual is shown in the bottom panel of figure 5.17. The peak-to-peak amplitude of

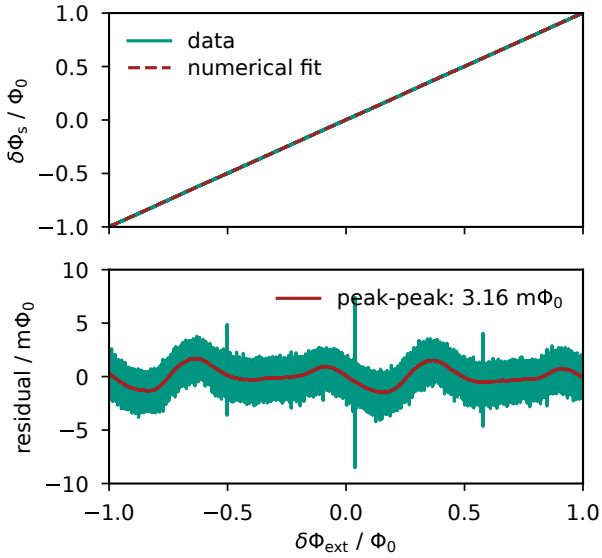

Fig. 5.17: Linearity measurement of the 4.455 GHz µMUX channel. The top plot shows the acquired flux signal in FRM readout as a function of the magnetic flux applied through the rf-SQUID modulation coil. The data was fitted with a linear function. The resulting residuals are shown in the bottom plot. The residuals were smoothed by averaging 100 neighboring points. The solid red line shows these smoothed residuals.

the residuals provides a measure of the non-linearity of the µMUX readout. To extract this value, the residuals were first smoothed using a first-order Savitzky–Golay filter with a window length of 1000 samples, thereby suppressing noise. This analysis yields a non-linearity of 3.16 mΦ_0, representing an improvement by a factor of two compared to the previous iteration of the full µMUX system [Ric21b].

5.7 Noise performance and readout optimization of the full µMUX system

All µMUX channels, 14 in total, were characterized using the procedure described in section 5.6.3, providing an overview of the µMUX system performance across the full operating frequency range from 4 GHz to 8 GHz. The noise performance of each channel is shown as a function of channel frequency in figure 5.18 (a), for both open-loop and FRM readout. Excellent noise performance is observed across all µMUX channels, with the open-loop flux noise consistently remaining below 1 $\mu\Phi_0/\sqrt{\text{Hz}}$ and a mean value of $(0.7 \pm 0.1)\,\mu\Phi_0/\sqrt{\text{Hz}}$. As expected, the mean FRM noise level is increased relative to the open-loop noise to $(1.4 \pm 0.2)\,\mu\Phi_0/\sqrt{\text{Hz}}$, corresponding to a current noise of $(19 \pm 3)\,\text{pA}/\sqrt{\text{Hz}}$ referred to the input coil, and it remains below $2\,\mu\Phi_0/\sqrt{\text{Hz}}$ for all channels. The single outlier at 6 GHz was traced to an incorrect demodulation frequency setting and was therefore excluded from the calculation of the mean noise performance.

The achieved noise performance is significantly lower than that demonstrated with the previous iteration of the SDR system ($2.5\,\mu\Phi_0/\sqrt{\text{Hz}}$) [Ric21b] and represents the lowest reported noise performance for a µMUX optimized for MMC readout. When expressed in terms of current noise, the present system achieves noise levels comparable to state-of-the-art µMUX devices optimized for TES readout [Mat17, Ben19, Gro25]. However, the noise performance of different µMUX devices is not directly comparable because the SQUID and input coil inductances vary between designs. A more suitable figure of

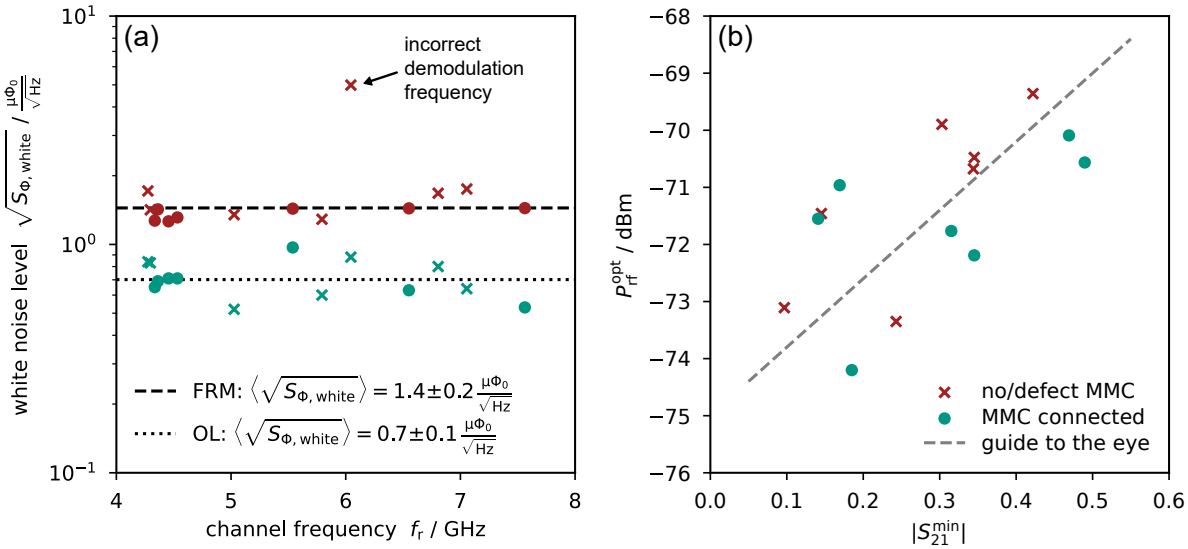

Fig. 5.18: (a) White noise level of all operated µMUX channels plotted against channel frequency. Circles indicate channels with functional MMCs connected, while crosses denote channels without detectors. Green data correspond to open-loop (OL) measurements, and red data correspond to FRM measurements. The black dashed and dotted lines mark the average white noise level in FRM and OL readout, respectively. The outlier in FRM readout at ∼6 GHz occurred due to an incorrect setting of the demodulation frequency and was excluded from the calculation of the mean noise. (b) Optimal readout power $P_{\mathrm{rf}}^{\mathrm{opt}}$ at which the noise measurements were performed as a function of the resonance curve minimum $|S_{21}^{\mathrm{min}}|$.

merit is therefore the intrinsic SQUID energy sensitivity $\epsilon = S_\Phi/(2L_\mathrm{S})$ and the input-referred coupled energy sensitivity $\epsilon_\mathrm{c} = \epsilon/k_\mathrm{in}^2$, where k_in denotes the magnetic coupling factor between the SQUID loop and the input coil. Using this metric, our µMUX system achieves $\epsilon = 158\,h$ and $\epsilon_\mathrm{c} = 374\,h$, which is approximately 10 to 15 times higher than the energy sensitivity of state-of-the-art two-stage dc-SQUIDs [Bau22]. However, the µMUX device with the best reported noise performance to date [Nak20] yields $\epsilon = 265\,h$ and $\epsilon_\mathrm{c} = 540\,h$, assuming a coupling constant of $k_\mathrm{in} = 0.7$ [Nak19]. This demonstrates that the present system exhibits excellent performance among state-of-the-art µMUX readout systems.

We do not see a difference in noise performance between channels with MMCs connected and those without, indicating that the overall noise performance is dominated by the readout system rather than by the MMCs. Furthermore, no correlation is found between the intrinsic quality factor Q_i of the channels and their individual noise levels, indicating that resonator losses do not limit the noise performance. This behavior deviates from previous observations for earlier devices [Ric23] and can be partially explained by successful µMUX and fabrication process optimization. However, this behavior can also partially be attributed to the individual adjustment of the power of each probe tone. A degradation in noise performance is expected for decreasing Q_i due to shal-

lower resonances (larger $|S_{21}^{\min}|$), which result in a smaller amplitude modulation of the transmitted probe tone. However, a lower Q_i also leads to a smaller current I_T in the µMUX load inductance, assuming the same readout power P_rf (see equation 2.24 and 2.29). Consequently, the µMUX power dependence becomes relevant only at higher readout powers, resulting in larger optimal readout power $P_\mathrm{rf}^\mathrm{opt}$ for such low-Q_i. Higher readout powers therefore improve the signal-to-noise ratio, compensating for the reduced modulation amplitude.

Figure 5.18(b) shows the optimal readout power $P_\mathrm{rf}^\mathrm{opt}$ obtained during the optimization described in section 5.6.1 as a function of the resonance depth $|S_{21}^{\min}|$. The on-chip power was estimated following the same procedure as described in section 5.6.1. As expected, $P_\mathrm{rf}^\mathrm{opt}$ increases with increasing $|S_{21}^{\min}|$. At first glance, one might assume that increasing the readout power is an effective way to compensate for the reduced noise performance observed in earlier works [Ric21b]. However, the increase in optimal readout power entails several disadvantages. These include the requirement for higher SDR output power and higher saturation power of the HEMT amplifier. More importantly, the combination of increased readout power and reduced Q_i leads to higher power dissipation in the µMUX and potentially in the MMC. The resulting parasitic heat load may become significant when reading out hundreds of detectors and elevate the MMC operation temperature, thus degrading the energy resolution. Consequently, optimizing the intrinsic quality factor of the µMUX channels remains a key objective in µMUX design.

The linearity across all channels varied significantly, resulting in a mean peak-to-peak non-linearity of $(4.1 \pm 2.6)\,\mathrm{m}\Phi_0$. Although this value is larger than the non-linearity reported in section 5.6.3, it remains lower than the peak-to-peak non-linearity of $6.2\,\mathrm{m}\Phi_0$ observed in the previous iteration of the SDR system. This improvement is likely due to improved trimming of the raw ramp signals before flux-ramp demodulation, which removes the transient region following each ramp reset.

The results presented here confirm that the multiplexed readout consistently achieves excellent noise performance and linearity across all channels. Although microwave power leakage into the MMCs, which could potentially affect the achievable energy resolution, was not investigated in this work, the consistently low flux-noise levels demonstrate that the readout system is fully functional and well suited for high-resolution, large-scale MMC experiments.

6. Advanced microwave SQUID multiplexer model incorporating readout power effects and Josephson junction inhomogeneities

The µMUX often determines the overall noise performance of the detector system, making optimization of its design and operation parameters essential. This requires accurate models that reliably predict µMUX behavior and enable precise device characterization. The analytical model introduced in [Weg22] accurately describes the dependence of µMUX characteristics on microwave probe tone power under typical operation conditions. It has thus become a core component of simulation frameworks used for µMUX optimization [Sch23b, Red24]. However, its validity is limited to SQUID screening parameters $\beta_\mathrm{L} < 0.6$, whereas values up to $\beta_\mathrm{L} < 1$ are of practical interest. To address this, we developed a numerical µMUX model that accurately describes the power dependence of µMUX devices up to $\beta_\mathrm{L} < 1$.

In this chapter, we describe the structure of our simulation framework, previously presented in [Nei25b], and compare its results with those obtained from the analytical model and experimental data. Furthermore, the framework supports arbitrary current–phase relations of the Josephson tunnel junction, enabling, for the first time, the modeling of µMUX devices comprising junctions with inhomogeneous tunnel barrier thickness. We analyze the effects of such inhomogeneities in comparison with those arising from the screening parameter and demonstrate that including them in the µMUX model significantly improves agreement with experimental observations.

6.1 Limitations of the analytical µMUX model

In chapter 2.3.2, we introduced the analytical model from [Weg22] describing the power dependence of the µMUX. The µMUX characteristics are primarily determined by the flux dependence of the effective load inductance $L_{\mathrm{T,eff}}$, which can be derived from the current I_S circulating in the rf-SQUID as a function of the current I_T in the load inductor. For this, we introduced the following expression:

$$\begin{aligned} I_\mathrm{S}(t) &= -I_\mathrm{c}\sin(\varphi_\mathrm{tot}) \\ &= -I_\mathrm{c}\sin\left[\varphi_\mathrm{ext} + \varphi_\mathrm{rf}\sin(\omega t) + \beta_\mathrm{L}\frac{I_\mathrm{S}(t)}{I_\mathrm{c}}\right], \end{aligned} \tag{6.1}$$

with the total normalized magnetic flux φ_tot threading the rf-SQUID loop, the quasi-static flux φ_ext applied via the modulation and input coils, the time-dependent flux $\varphi_\mathrm{rf}\sin(\omega t)$ generated by the current in the load inductor induced by the applied probe tone, and the screening flux $\varphi_\mathrm{scr}(t) = \beta_\mathrm{L} I_\mathrm{S}(t)/I_\mathrm{c}$, which arises from the current circulating in the rf-SQUID.

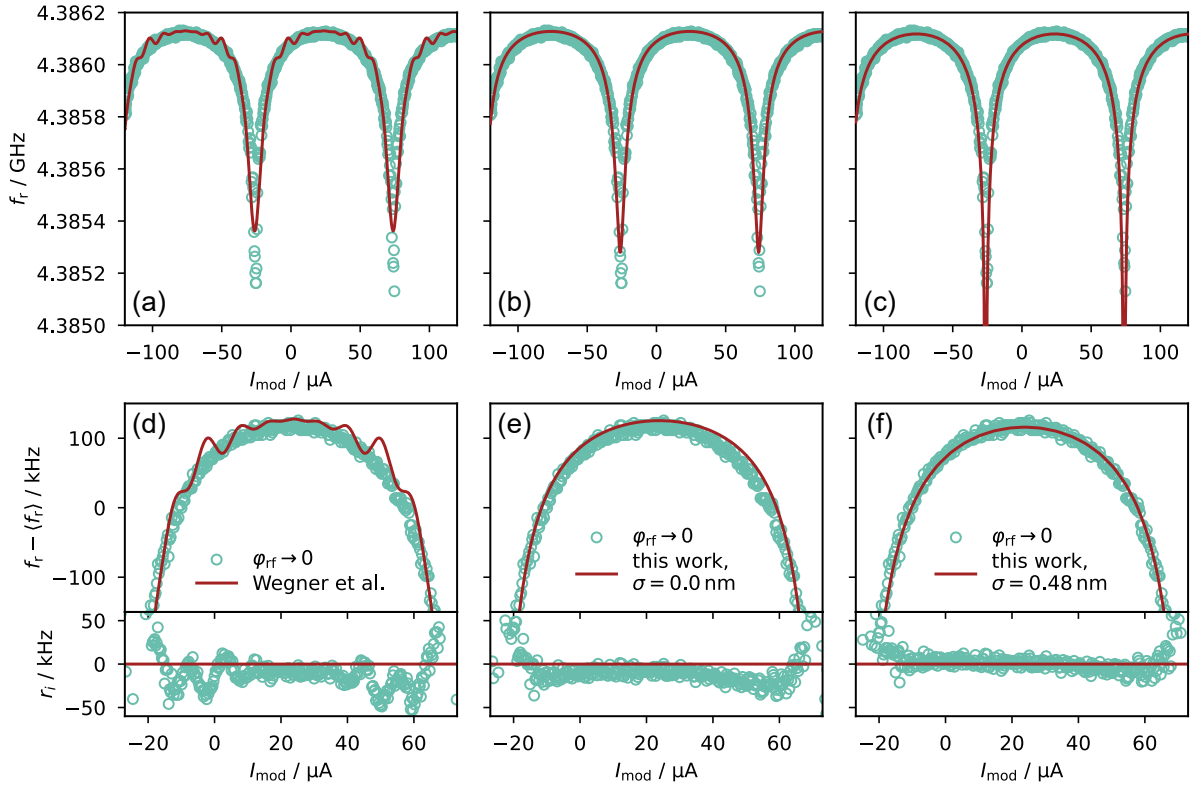

Fig. 6.1: Measured resonance frequency dependence $f_r(I_{mod})$ on the modulation coil current I_{mod} for a µMUX channel with $\beta_L > 0.6$. The corresponding resonance curves were recorded with low VNA output power, corresponding to the limit $\varphi_{rf} \to 0$. (a) Fit to the data using the analytical model from [Weg22], described in section 2.3.2. (b) Fit using the model presented in this thesis, assuming an ideal (i.e., perfectly homogeneous) Josephson tunnel junction barrier. (c) Fit with our new model assuming an inhomogeneous tunneling barrier thickness with Gaussian probability density distribution characterized by a mean barrier thickness $\bar{d} = 2\,\text{nm}$ and standard deviation $\sigma = 0.48\,\text{nm}$). (d)-(f) Magnified views of the fits in the panels above, where $\langle f_r \rangle = 4.386\,\text{GHz}$ denotes the resonance frequency averaged over I_{mod}. The residuals r_i of the fits are plotted at the bottom of the figure, with the red line marking $r_i = 0$. The best agreement between model and data is achieved using the model that includes a finite tunnel barrier inhomogeneity.

Since there is no closed-form solution for $I_S(t)$, the model presented in [Weg22], which we discussed in 2.3.2, employs an analytical, 10^{th}-order Taylor expansion in β_L to approximate a solution. This analytical model shows excellent agreement with experimental data for screening parameters $\beta_L < 0.6$. However, due to the inherent limitations of the Taylor expansion, the model deviates from the expected behavior and exhibits unphysical features beyond its valid range. As an example, figures 6.1(a) and (d) show the resonance frequency shift of a µMUX channel with $\beta_L \approx 0.65$, measured with a probe tone power of $\varphi_{rf} \to 0$ and fitted using the analytical model. In fact, we fitted the analytical model, as well as the models introduced in the following sections,

simultaneously to data acquired at four different readout powers (see figure 6.7), using maximum-likelihood fits [Dem20]. Since our setup for this measurement did not include magnetic shielding, the data collected at the lowest readout power were excluded from the fit for resonance frequencies below 4.3856,GHz, as here the strong dependence of the resonance frequency on the externally applied magnetic flux results in the largest uncertainties. The fit with the analytical model exhibits unphysical ripples that become even more pronounced as β_L increases. Although the model can, in principle, be extended to higher values of β_L, this would require a substantially higher order in the Taylor expansion, rendering the approach in fact impractical.

6.2 Numerical solution of the µMUX power dependence

Instead of increasing the order of the Taylor expansion, a more efficient and scalable approach is to solve equation 6.1 numerically. Figure 6.2 shows a flowchart of our algorithm for computing $I_\mathrm{S}(t)$. With $I_\mathrm{S}(t)$ calculated, we can determine its time-derivative, which allows us to find the current i_ind induced in the load inductor using equation 2.41, and subsequently the effective load inductance $L_\mathrm{T,eff}$ and the full µMUX characteristics using equations 2.43 and 2.39, respectively.

Assuming the current-phase relation $I_\mathrm{S,JJ}(\varphi)$ of the utilized Josephson junction, and thus the current-flux relation $I_\mathrm{S}(\varphi_\mathrm{tot})$ of the rf-SQUID, is known, the algorithm begins at step 1 by determining the time evolution of the supercurrent in the rf-SQUID as a function of the externally applied flux φ_ext for a given flux amplitude of the microwave probe tone φ_rf. This is accomplished using a fixed-point iteration method. The supercurrent is computed iteratively, where the n-th iteration is given by

$$I_{\mathrm{S},n}(t) = I_\mathrm{S,JJ}(-\varphi_{\mathrm{tot},n}(t)). \tag{6.2}$$

Here, $\varphi_{\mathrm{tot},n}$ denotes the total normalized flux at the n-th iteration, calculated with the relation

$$\varphi_{\mathrm{tot},n}(t) = \varphi_\mathrm{ext} + \varphi_\mathrm{rf}\sin(\omega t) + \beta_\mathrm{L}\frac{I_{\mathrm{S},n-1}(t)}{I_\mathrm{c}}. \tag{6.3}$$

The iteration begins with a random guess $\varphi_{\mathrm{tot},0} \in [0,2\pi)$ and the series is computed until it converges at iteration $n = N$, as defined by the stopping criterion

$$|\varphi_{\mathrm{tot},N} - \varphi_{\mathrm{tot},N-1}| < \epsilon_\varphi, \tag{6.4}$$

where ϵ_φ is a specified numerical tolerance. The final value $I_\mathrm{S} \equiv I_{\mathrm{S},N}$ then provides the desired supercurrent $I_\mathrm{S}(\varphi_\mathrm{ext},\varphi_\mathrm{rf},t)$. To reduce computation time, we apply acceleration techniques such as Aitken's delta-squared process [Saa25]. Our method reliably converges for all tested rf-SQUID parameters. However, in the case of a hysteretic rf-SQUID (i.e., $\beta_\mathrm{L} > 1$), the result will depend on the initial guess $\varphi_{\mathrm{tot},0}$, and not all theoretically valid solutions can be found using this approach.

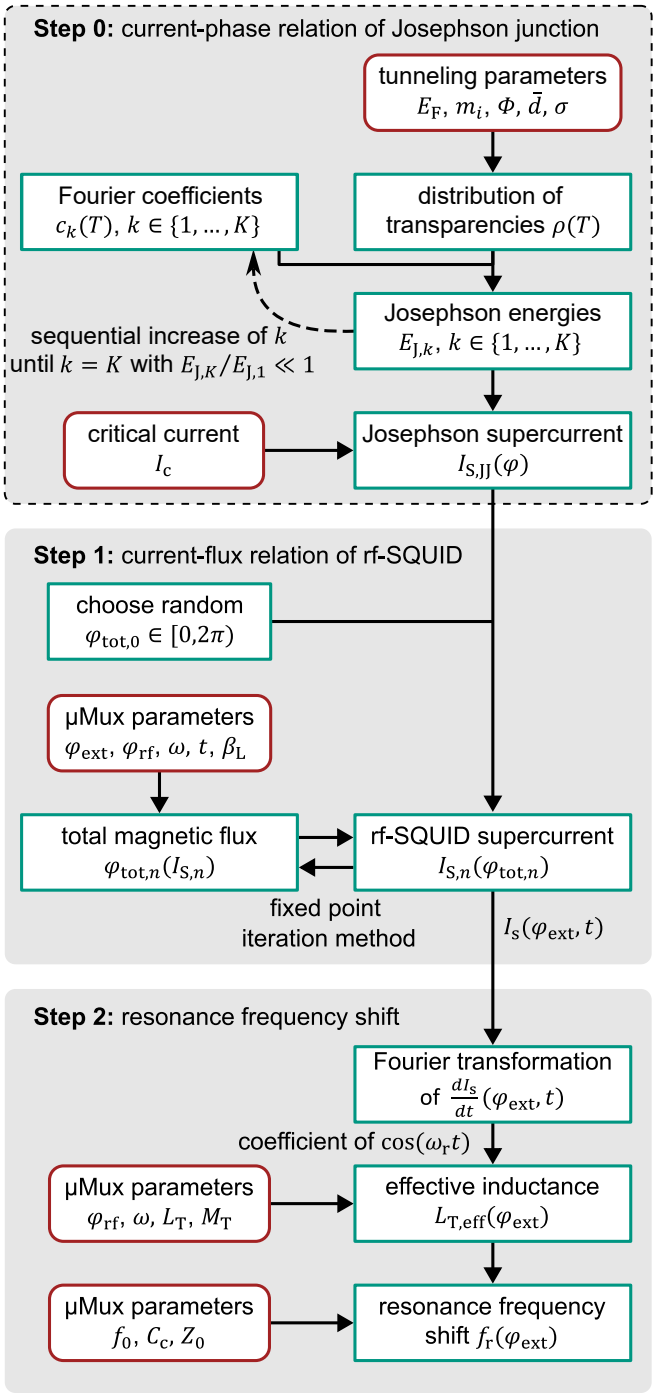

Fig. 6.2: Flowchart outlining our numerical simulation framework. Red, rounded boxes indicate user-defined input parameters, while green, rectangular boxes represent calculations of respective quantities. An optional step (Step 0) allows deriving the current phase relation of a Josephson tunnel junction with inhomogeneous barrier thickness. Step 1 determines the current-flux relation of the rf-SQUID as a function of the externally applied magnetic flux. Step 2 calculates the resonance frequency shift using the current-flux relation obtained in step 1.

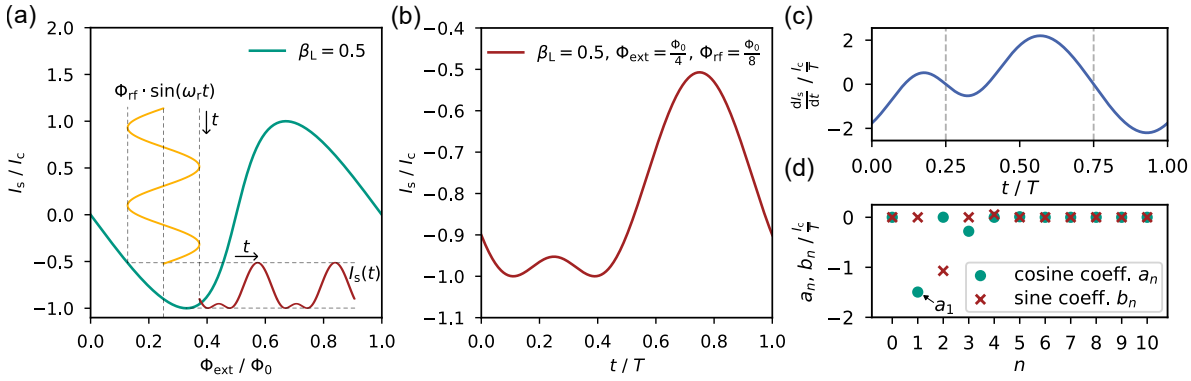

Fig. 6.3: rf-SQUID supercurrent and its time derivative, calculated using our advanced µmodel, are shown. (a) SQUID's current–flux relation (green solid line). The calculated SQUID response (red solid line) to a microwave signal (yellow solid line) with amplitude $\Phi_{rf} = \Phi_0/8$, applied at a flux offset $\Phi_{ext} = \Phi_0/4$, is schematically depicted. (b)+(c) Time-dependence of the supercurrent $I_S(t)$ and its time derivative, which result from the same microwave signal depicted in (a). The time derivative is anti-symmetric at $\pm T/4$ (gray dashed lines). It contains multiple frequency components, which are extracted using a discrete Fourier transform. The corresponding cosine and sine coefficients a_n and b_n are shown in (d). When we later calculate the effective load inductance $L_{T,\mathrm{eff}}$, only the first Fourier coefficient a_1 is relevant, as all other components either do not populate the resonator or vanish.

Step 1 of our algorithm allows for the calculation of the SQUID supercurrent as a function of the externally applied flux, as shown in figure 6.3(a) for a representative SQUID with $\beta_L = 0.5$. To determine the induced current $i_{ind}(t)$ in the load inductor, the time derivative $\mathrm{d}I_s/\mathrm{d}t$ of $I_S(t)$ is required. Therefore, we calculate the SQUID current as a function of time for one oscillation period $T = 1/f_r$. An exemplary curve for $I_S(t)$ is depicted in figure 6.3(b), assuming a microwave probe tone with amplitude $\Phi_{rf} = \Phi_0/8$ and an external flux bias $\Phi_{ext} = \Phi_0/4$.

Step 2 begins with computing the time derivative using a forward difference approximation:

$$\frac{\mathrm{d}I_S(t)}{\mathrm{d}t} \approx \frac{I_S(t+\delta t) - I_S(t)}{\delta t}, \tag{6.5}$$

where $\delta t \ll T$ is chosen to be sufficiently small. Figure 6.3(c) shows $\mathrm{d}I_S(t)/\mathrm{d}t$ over one oscillation period. It cannot be described by a simple sine function and therefore consists of multiple frequency components in addition to ω. Consequently, according to equation 2.41, we expect $i_{ind}(t)$ to also consist of multiple frequency components. However, due to the resonance condition 2.39, only the fundamental frequency $\omega \approx \omega_r$ populates the resonator. Higher harmonics do not meet the resonance condition and are therefore suppressed by destructive interference. Therefore, the time derivative $\mathrm{d}I_S(t)/\mathrm{d}t$ is evaluated over one oscillation period T and the ω-component is determined using a discrete Fourier transform. Because of the anti-symmetry of $\mathrm{d}I_S(t)/\mathrm{d}t$ at $t = T/4$

and $t = -T/4$[1], it can be shown that the corresponding sine coefficient b_1 must be zero. For this reason, only the first cosine coefficient a_1 is needed to calculate $i_{\mathrm{ind}}(t)$ using equation 2.41:

$$i_{\mathrm{ind}}(t) = -\frac{M_{\mathrm{T}}}{\omega L_{\mathrm{T}}} a_1 \sin(\omega t). \tag{6.6}$$

The induced current is phase shifted by $\pi/2$ due to the complex impedance $i\omega L_{\mathrm{T}}$ of the load inductor and therefore oscillates in phase with the current $i_{\mathrm{T}}(t)$. The resulting effective load inductance $L_{\mathrm{T,eff}}$, calculated using equation 2.43, is time-independent and can be used with equation 2.39 to determine the resonance frequency. Using this numerical approach, the µMUX resonance shift can be evaluated as a function of φ_{ext} and φ_{rf} for any non-hysteretic rf-SQUID. Thus, under the assumption of a junction current-phase relation $I_{\mathrm{S,JJ}}(\varphi) = I_{\mathrm{c}} \sin(\varphi)$, any µMUX with $\beta_{\mathrm{L}} < 1$ can be modeled, making this model more general compared to the analytical model described in [Weg22].

Figure 6.4 compares both models, assuming a µMUX channel with a screening parameter of $\beta_{\mathrm{L}} = 0.9$. This parameter exceeds the applicable range of the analytical model, resulting in the significant ripples observed in figure 6.4(a). In contrast, our numerical model does not display these ripples and shows excellent agreement in the limit of low readout powers $\Phi_{\mathrm{rf}} \to 0$ with the exact but power-independent model described in [Mat11, Kem17a]. When both models are evaluated for varying microwave probe tone power Φ_{rf} (see figure 6.4(b)), our numerical model shows the expected decrease in the resonance frequency shift with increasing readout power. For screening parameters $\beta_{\mathrm{L}} < 0.6$, we observe only negligible deviations between the resonance shift predicted by both models. However, for $\beta_{\mathrm{L}} > 0.6$, the ripples in the analytical model result in significant deviations, with these deviations being more pronounced at lower readout powers. Consequently, only our model converges to the power-independent exact solution for $\Phi_{\mathrm{rf}} \to 0$.

A fit of the data shown in figure 6.1 using our numerical model shows significantly better agreement with the measured data (see figure 6.1(b) and (e)) than the analytical model. This improvement becomes particularly evident in the residuals r_i, where the numerical model eliminates the unphysical ripples present in the analytical model. Moreover, the overall agreement between model and data, quantified by the fit's coefficient of determination value R^2, increases from 94.6 % to 95.5 %. However, the numerical model still underestimates the total resonance frequency shift and overestimates the resonance frequency between the modulation coil currents $I_{\mathrm{mod}} \approx 0\,\mu\mathrm{A}$ and $I_{\mathrm{mod}} \approx 50\,\mu\mathrm{A}$, corresponding to $\Phi_{\mathrm{ext}} \approx \pm\Phi_0/4$, suggesting an incomplete understanding of the behavior of this µMUX channel.

The current-phase relation $I_{\mathrm{S,JJ}}(\varphi)$ used in equation 6.2 can be any well-defined, contin-

[1] We define $\varphi_{\mathrm{app}} = \varphi_{\mathrm{ext}} + \varphi_{\mathrm{rf}} \sin(\omega t)$ as the flux applied to the rf-SQUID, which is symmetric around $t = \pm T/4$. By definition, for a non-hysteretic rf-SQUID, the implicit expression $\varphi_{\mathrm{tot}} = \varphi_{\mathrm{app}} + \beta_{\mathrm{L}} I_{\mathrm{S}}(\varphi_{\mathrm{tot}})/I_{\mathrm{c}}$ has a unique solution for each value of φ_{app}. This means the mapping of φ_{app} to φ_{tot} is single-valued, and φ_{tot} is a well-defined function of φ_{app}, which inherits the symmetry of φ_{app} around $t = \pm T/4$. Since $I_{\mathrm{S}}(\varphi_{\mathrm{tot}}) = I_{\mathrm{S,JJ}}(-\varphi_{\mathrm{tot}})$ is also uniquely defined for any φ_{tot}, I_{S} also inherits the symmetry around $t = \pm T/4$, making its time derivative $\mathrm{d}I_{\mathrm{S}}/\mathrm{d}t$ anti-symmetric around $t = \pm T/4$.

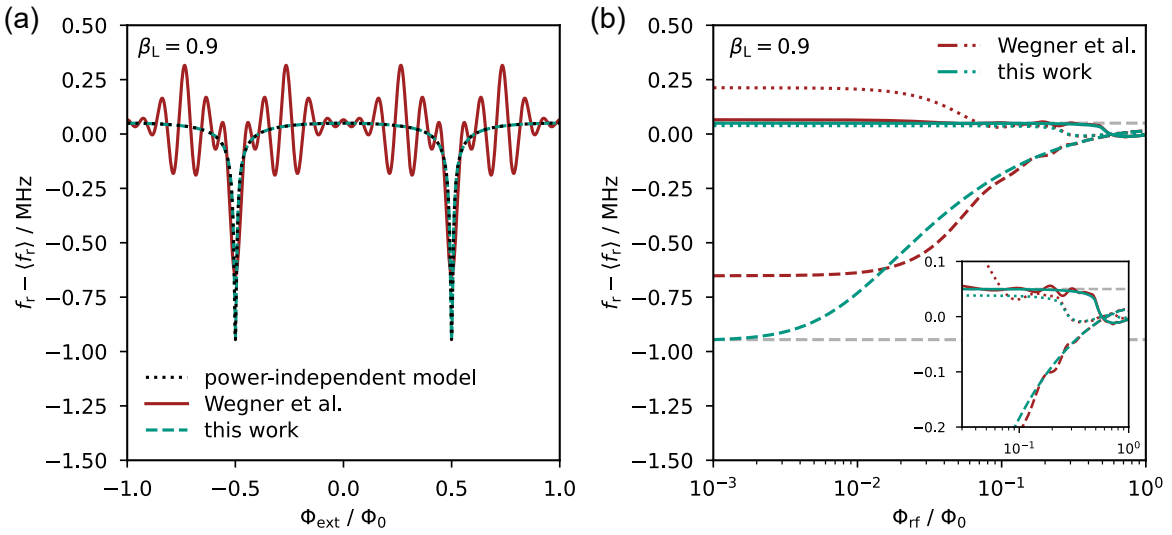

Fig. 6.4: Comparison between the analytical µMUX model presented in [Weg22] and the present numerical model, assuming an rf-SQUID with screening parameter $\beta_L = 0.9$. (a) Dependence of the resonance frequency f_r on the applied magnetic flux in the limit of negligible power of the microwave probe tone ($\Phi_{rf} \to 0$). $\langle f_r \rangle = 5\,\mathrm{GHz}$ denotes the resonance frequency averaged over Φ_{ext}. (b) Resonance frequency as a function of microwave probe tone power Φ_{rf}. The solid green and red line corresponds to $\Phi_{ext} = n\Phi_0$, the dashed green and red line to $\Phi_{ext} = (n+1/2)\Phi_0$, and the dotted green and red line to $\Phi_{ext} = (n \pm 1/4)\Phi_0$. The dashed light gray lines mark the minimum and maximum resonance frequency predicted by the power-independent model. The numerical model shows the expected behavior and matches the exact power-independent solution in the low-power limit, while the analytical model exhibits ripples caused by the limitations of its Taylor expansion. The inset shows a zoom near $\Phi_{rf} \approx 0.6\,\Phi_0$, where the resonance frequencies of the different flux states intersect for the first time.

uous function. This flexibility allows us to consider current–phase relations that deviate from the conventional sinusoidal form. Consequently, our numerical model can simulate µMUX devices based on non-tunneling-type Josephson junctions, such as Dayem bridges or 3D nanobridges, simply by inserting the appropriate current–phase relation. The approach can also improve the description of devices based on Josephson tunnel junctions. As shown in the following section, the fit to the data in figure 6.1 can be much improved by replacing the well-known sinusoidal current-phase relation of a Josephson tunnel junction with a more complex description, which accounts for inhomogeneities in the Josephson tunnel junction's barrier thickness.

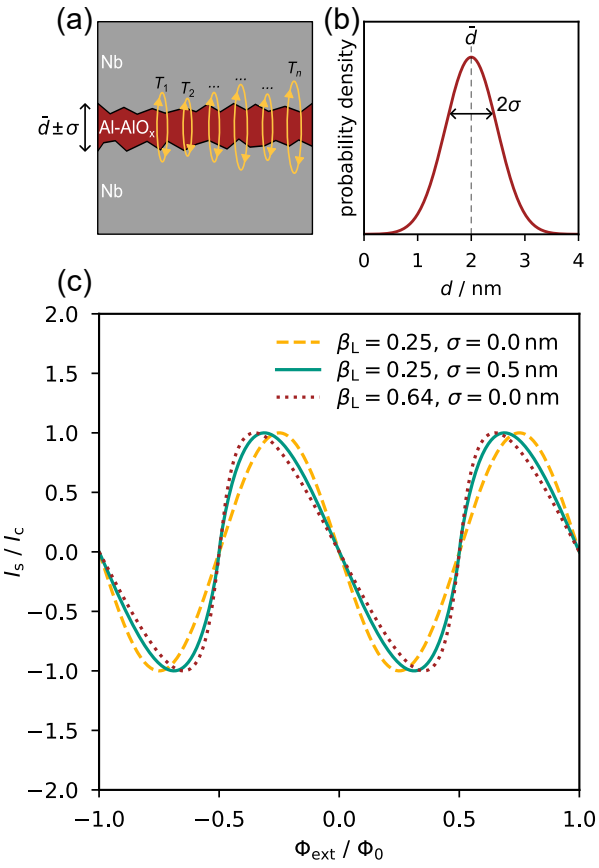

Fig. 6.5: Effect of an inhomogeneous tunnel barrier with a mean thickness $\bar{d} = 2\,\mathrm{nm}$ and a standard deviation $\sigma = 0.5\,\mathrm{nm}$ on the SQUIDS current-flux relation $I_S(\Phi_{ext})$. (a) Schematic cross section of a Nb/Al-AlO$_x$/Nb Josephson tunnel junction with an inhomogeneous barrier thickness. As the barrier thickness varies along the junction, the transmission probabilities T_1 to T_N of the N individual conduction channels also vary. (b) Assumed tunnel barrier thickness probability density distribution, a Gaussian distribution centered at the mean thickness $\bar{d}$. (c) Current–flux relation of an rf-SQUID with $\beta_L = 0.25$ for a homogeneous tunnel barrier (yellow, dashed line), for an inhomogeneous barrier with $\sigma = 0.5\,\mathrm{nm}$ (green, solid line), and for a homogeneous junction with a screening parameter $\beta_L = 0.64$ (red, dotted line). Similar to an increased screening parameter, the barrier inhomogeneity causes the current–flux relation to appear skewed.

6.3 Inclusion of Josephson tunnel junction barrier inhomogeneities into the µMUX model

So far, we have used a sinusoidal current-phase relation $I_{S,JJ} = I_c \sin(\varphi)$, which assumes a homogeneous tunnel barrier and low transmission probability. However, in practice, the tunnel barrier of actual Josephson tunnel junctions displays a certain degree of roughness. For instance, in [Ada24], it was demonstrated that Nb/Al-AlO$_x$/Nb based window-type junctions exhibit significant spatial variation in the critical current density across the cross-section of the tunnel barrier. Furthermore, Willsch *et al.* showed that superconducting qubits relying on Al/AlO$_x$Al Josephson tunnel junctions cannot be accurately modeled using a purely sinusoidal current-phase relation [Wil24]. Instead, they proposed a mesoscopic model of tunneling through an inhomogeneous AlO$_x$ barrier.

To incorporate inhomogeneous barriers into our advanced µMUX model, the current-phase relation $I_{S,JJ}(\varphi)$ used in step 1 in figure 6.2 is replaced by a relation directly derived from the mesoscopic model. This requires the introduction of an additional calculation step (step 0 in figure 6.2), in which the current-phase relation is derived using the mesoscopic model proposed in [Wil24]. The model assumes a rough tunneling barrier between the two junction electrodes, as illustrated in figure 6.6(a). Locally,

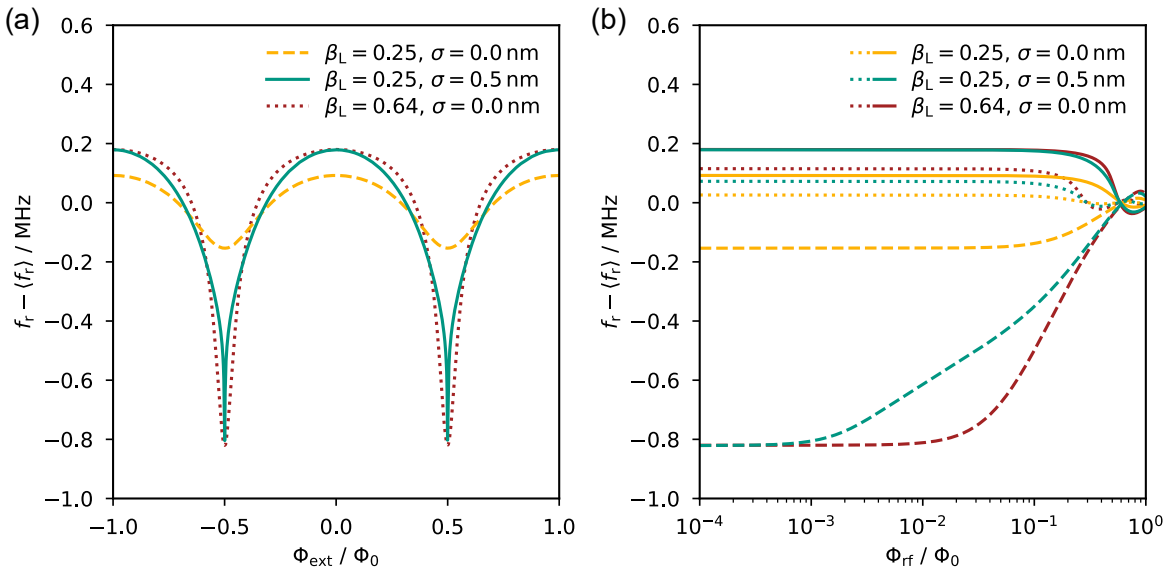

Fig. 6.6: The figures show the effect of an inhomogeneous tunnel barrier as depicted in figure 6.5 on the µMUX characteristics. (a) Resonance frequency shift of µMUX devices using the same SQUID parameters as in figure 6.5, with $\langle f_r \rangle = 5\,\mathrm{GHz}$. (b) Power dependence of the resonance frequency shift for external magnetic flux values $\Phi_{ext} = n\Phi_0$ (solid line), $\Phi_{ext} = (n + 1/2)\Phi_0$ (dashed line), and $\Phi_{ext} = (n \pm 1/4)\Phi_0$ (dotted line). The effects of barrier inhomogeneity and increased screening parameter are qualitatively similar, however, they are distinct. This becomes evident in the significantly steeper resonance frequency shift of the inhomogeneous device near $(n + 1/2)\Phi_0$ in panel (a), as well as the reduced resonance frequency at $(n \pm 1/4)\Phi_0$, visible in panel (a) and, as a function of probe tone powers, in panel (b).

the barrier is described as a rectangular potential of thickness d and height ϕ. The local thickness d follows a Gaussian distribution with mean $\bar{d}$ and standard deviation σ, as depicted in figure 6.6(b). Within this model, assuming operation well below the critical temperature, the current-phase relation of the Josephson junction is expressed as a Fourier series in terms of the Josephson energies $E_{J,k}$:

$$I_{S,JJ}(\varphi) = \frac{1}{\Phi_0} \sum_{k=1}^{\infty} k E_{J,k} \sin(k\varphi). \tag{6.7}$$

The Josephson energies depend on the junction parameters and can be expressed as

$$E_{J,k} = \frac{\Delta}{4} \frac{N}{k} \int_0^1 \mathrm{d}T\, \rho(T) c_k(T), \tag{6.8}$$

where Δ denotes the superconducting energy gap of the junction electrodes and N the number of conduction channels across the junction barrier. The Fourier coefficients $c_k(T)$ depend solely on the transmission probability T and are independent of the

parameters specific to the junction

$$c_k(T) = \begin{pmatrix} 2k-2 \\ k-1 \end{pmatrix} \frac{(-1)^{k+1}T^k}{16^{k-1}} \cdot {}_2F_1\left(k-\frac{1}{2}, k+\frac{1}{2}; 2k+1; T\right),$$

where ${}_2F_1$ denotes the hypergeometric function.

The distribution of transmission probabilities T across the conduction channels is described by the function $\rho(T)$. For the mesoscopic model with Gaussian barrier thickness distribution, the distribution $\rho(T)$ is given by [Wil24]

$$\rho(T) = \frac{2}{1+\mathrm{Erf}(\tilde{d}/\sqrt{2}\tilde{\sigma})} \frac{1}{2T\sqrt{1-T+a^2T}} \cdot \frac{1}{\sqrt{2\pi}\tilde{\sigma}} \exp\left(-\frac{(f(T)+\alpha)^2}{2\tilde{\sigma}^2}\right),$$

where $\mathrm{Erf}(x)$ is the error function, $\tilde{d} = \bar{d}/d_0$, $\tilde{\sigma} = \sigma/d_0$, and

$$d_0 = \hbar/\sqrt{2m_\mathrm{i}\phi}, \tag{6.9}$$

$$a^2 = \frac{1}{4}\left(\sqrt{\frac{m_\mathrm{i}\phi}{m_e E_\mathrm{F}}} - \sqrt{\frac{m_e E_\mathrm{F}}{m_\mathrm{i}\phi}}\right)^2, \tag{6.10}$$

$$f(T) = \log\left(\frac{\sqrt{T}}{\sqrt{1-T}+\sqrt{1-T+a^2T}}\right), \tag{6.11}$$

$$\alpha = \tilde{d} + \log(a). \tag{6.12}$$

Here, E_F denotes the Fermi energy of the junction electrodes, m_e the mass of the free electron, and m_i the effective electron mass in the band of the junction barrier closest to the energy of the tunneling electrons.

Since the total number of conduction channels N is generally unknown, the absolute values of the Josephson energies $E_{\mathrm{J},k}$ cannot be determined. However, the relative magnitudes of the Josephson energies are sufficient to reconstruct the current-phase relation up to a scaling factor. The scaling factor can be determined by normalizing $I_{\mathrm{S,JJ}}(\varphi)$ so that its maximum corresponds to the critical current I_c.

The Josephson energies $E_{\mathrm{J},k}$ alternate in sign and decrease exponentially with increasing k. The algorithm computes these energies up to $k = K$, such that

$$\left|\frac{E_{\mathrm{J},K}}{E_{\mathrm{J},1}}\right| < \epsilon_E \tag{6.13}$$

where $\epsilon_E \ll 1$ represents a sufficiently small numerical threshold. For larger inhomogeneities σ, the Josephson energies decrease at a slower rate, which necessitates the inclusion of terms with higher k. In contrast, for homogeneous barriers, it is sufficient to consider only the first Josephson energy, simplifying equation 6.7 to the well-known sinusoidal current-phase relation.

To apply this model to our µMUX devices, which are based on Nb/Al-AlO_x/Nb Josephson tunnel junctions, we assume a typical barrier thickness of $\bar{d} = 2\,\mathrm{nm}$, a barrier height of $\phi = 1\,\mathrm{eV}$, and an effective electron mass of $m_\mathrm{i} = 0.75 m_e$ [Jun09, Rip02]. For the Fermi energy of niobium, we use $E_\mathrm{F} = 5.32\,\mathrm{eV}$ [Ash76]. The numerical tolerances were set to $\epsilon_\varphi = 10^{-10}$, $\delta t = 10^{-6} T$, and $\epsilon_E = 10^{-10}$.

Figure 6.6(c) shows the current-flux relation of an rf-SQUID, calculated using our numerical model. We compare the cases of a homogeneous and an inhomogeneous tunnel barrier and also examine the effect of an increased screening parameter. The inhomogeneity is set to $\sigma = 0.5\,\mathrm{nm}$, leading to significant higher-order contributions from the Josephson energies ($|E_{\mathrm{J},2}/E_{\mathrm{J},1}| \approx 3.9\,\%$, $|E_{\mathrm{J},3}/E_{\mathrm{J},1}| \approx 0.9\,\%$, ...). As a result, the current-flux relation of the SQUID appears skewed, resembling the effect caused by a large screening parameter. The curve becomes steeper around $\Phi_\mathrm{ext} = (n + 1/2)\Phi_0$ and shallower around $\Phi_\mathrm{ext} = n\Phi_0$. Consequently, the total resonance shift (see figure 6.6(d)) increases and becomes more asymmetric around the average resonance frequency $\langle f_\mathrm{r} \rangle$. While the inhomogeneity can produce the same total resonance frequency shift around f_0 as the screening parameter, the overall shape of this shift is distinct. This becomes particularly evident when comparing the power dependence of both cases (see figure 6.6(e)). For the inhomogeneous tunnel barrier, the resonance frequency at $\Phi_\mathrm{ext} = (n \pm 1/4)\Phi_0$ is lower, and the reduction in total resonance frequency shift begins at lower readout powers Φ_rf. Because the effects of junction inhomogeneity and large screening parameters are qualitatively similar, neglecting inhomogeneity during device characterization could result in an incorrect estimate of the device's screening parameter.

We fitted our numerical model incorporating an inhomogeneous tunnel barrier to the data presented in figure 6.1(c) and (f). For this, we again assume a mean barrier thickness of $\bar{d} = 2\,\mathrm{nm}$, a barrier height of $\phi = 1\,\mathrm{eV}$, an effective electron mass of $m_\mathrm{i} = 0.75\,m_\mathrm{e}$ in the barrier, and a niobium Fermi energy of $E_\mathrm{F} = 5.32\,\mathrm{eV}$. Only the inhomogeneity σ is added as additional free fit parameter. The best agreement between the data and the model was achieved with an inhomogeneity of $\sigma = 0.48\,\mathrm{nm}$, representing a notable improvement over the homogeneous barrier model. The R^2 value is improved from 95.5 % to 97.4 % and the slight curvature of the residuals r_i observed in the homogeneous model is reduced. The same model applied to data taken from the same device at higher readout powers Φ_rf is shown in figure 6.7. We observe excellent agreement between the model and measurement even at $\Phi_\mathrm{rf} = 0.78\,\Phi_0$, which exceeds the typically applied readout powers. This demonstrates that our advanced model remains accurate across the full range of screening parameters and readout powers relevant for µMUX operation.

Although the measured data strongly suggest the presence of inhomogeneities in tunnel barrier thickness in the measured µMUX device, it is important to note that the exact distribution of barrier thickness, as well as the exact tunneling parameters E_F, m_i, and Φ, remain unknown. The critical current densities reported in [Ada24] show spatial variations that deviate from the simple Gaussian thickness distribution assumed in our Gaussian approach. Additionally, fabrication-related defects may create high-

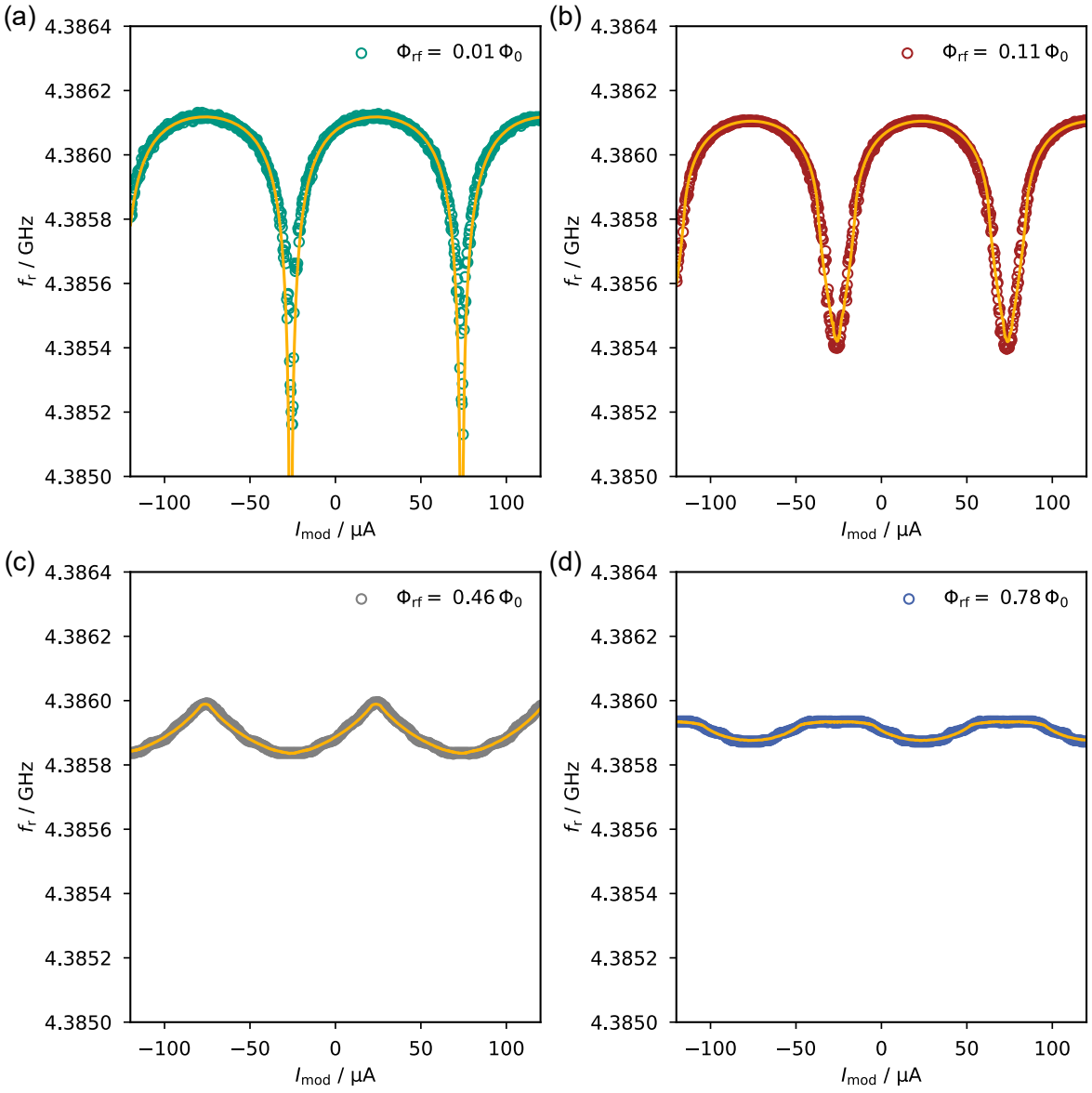

Fig. 6.7: Dependence of the measured resonance frequency $f_r(I_{mod})$ on the modulation coil current I_{mod} for microwave probe tone powers ranging from $\Phi_{rf} = 0.01\,\Phi_0$ to $\Phi_{rf} = 0.78\,\Phi_0$. The yellow lines represent the numerical model assuming a junction inhomogeneity of $\sigma = 0.48\,\text{nm}$, showing excellent agreement with the measured data.

transparency conduction channels that are not accounted for by the Gaussian model. However, such deviations from the assumed transmission probability distribution $\rho(T)$ are expected to produce qualitatively similar effects. Consequently, minor discrepancies between the model and the experimental data can likely be attributed to uncertainties in the actual form of $\rho(T)$.

6.4 Impact of our advanced µMUX model

The model presented in this chapter extends established µMUX power-dependent models to include SQUID screening parameters up to $\beta_L < 1$, thereby covering the full range of practically relevant design parameters before µMUX devices become hysteretic at $\beta_L = 1$. As demonstrated in section 6.2, for devices with $\beta_L > 0.6$ the numerical model significantly improves agreement with experimental data compared to existing models, enabling reliable characterization and simulation-based optimization of µMUX devices across the full parameter range of interest.

Moreover, the current-phase relation of the Josephson junction assumed in the model can be easily modified, allowing for the inclusion of µMUX devices based on non-tunneling-type Josephson junctions as well as tunnel junctions with inhomogeneous barriers. We have shown that the effects of such inhomogeneities are qualitatively similar to, yet distinct from, those of the screening parameter, making their inclusion essential for accurate characterization. As shown in section 6.3, incorporating these effects yields improved agreement with measurements, even at readout powers beyond typical operating conditions.

The importance of this model for µMUX characterization was already illustrated in section 5.5, where barrier inhomogeneities significantly influenced the extracted channel parameters. It will be further applied in chapter 7. Overall, the model provides a versatile framework for the analysis and design of µMUX devices and can be readily integrated into simulation tools for optimizing next-generation µMUX readout systems.

7. Microwave SQUID multiplexing in the K_u frequency band

State-of-the-art microwave SQUID multiplexer systems, such as the one discussed in chapter 5, demonstrate excellent noise levels of $(1.4 \pm 0.2)\,\mu\Phi_0/\sqrt{\text{Hz}}$. Nevertheless, there remains significant room for improvement before reaching the limits predicted by simulations [Sch23b]. However, even these predicted noise levels of approximately $0.6\,\mu\Phi_0/\sqrt{\text{Hz}}$ are still sufficiently high to dominate the overall noise budget when reading out MMCs. Consequently, novel concepts are required to further reduce the readout noise.

As discussed in chapter 2.8, the operation of µMUX devices at higher resonance frequencies presents a particularly promising approach, as it simultaneously offers several advantages, including improved time resolution, an increased multiplexing factor, and reduced device dimensions. However, the implications of increased resonance frequency on noise performance are not immediately apparent from the underlying theoretical expressions, and the practical feasibility of such devices has yet to be demonstrated.

Both aspects are addressed in this chapter. Using numerical simulations, we first identify optimal operating parameters and evaluate the noise performance of µMUX devices with resonance frequencies up to 50 GHz. We then describe the design iterations that enabled the realization of the first of its kind µMUX devices operating between 15.3 GHz and 17.6 GHz. Finally, we discuss the measured performance of these devices and demonstrate that their behavior is accurately described by the established µMUX models.

7.1 Performance prediction for a microwave SQUID multiplexer operating at resonance frequencies above 10 GHz

As discussed in chapter 2.8, operating µMUX devices at resonance frequencies $f_\text{r} > 10\,\text{GHz}$ provides several benefits, including improved time resolution, increased multiplexing factor, and reduced device footprints. However, the implications on the noise performance are less clear and require further investigation. For this, it is beneficial to recall the equations describing the open-loop noise of CPW and lumped-element-based µMUX devices:

$$S_{\Phi,\text{system}}^{\text{CPW}} = \frac{k_\text{B} T_{\text{N,system}}}{\pi \eta_0 f_\text{r}} \frac{Q_\text{c}}{Q_\text{l}} \frac{L_\text{S}}{\beta_\text{L} - \beta_\text{L}^3} \left(\sum_{ij} \frac{\partial p_{i,j}}{\partial \varphi_\text{ext}} \bigg|_{\Phi_\text{ext}=\Phi_\text{ext}^\text{opt}} \right)^{-2} \left(\frac{f_\text{r}}{f_0} \right)^2 \tag{7.1}$$

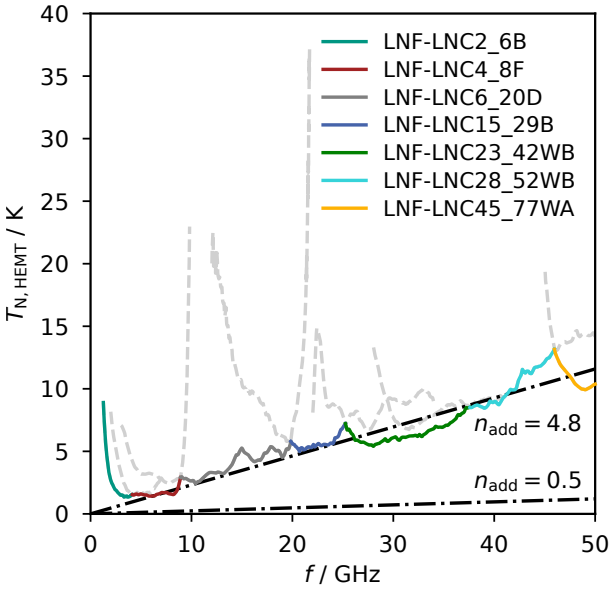

Fig. 7.1: Noise temperature of selected state-of-the-art cryogenic ultra-low-noise HEMT amplifiers from the Swedish company *Low Noise Factory AB*[1]. The different amplifier models are labeled by their model number. For each operation frequency, only the best performing amplifier is shown as a solid colored line. The other amplifiers at the same frequency are shown as gray dashed lines. The black dashdotted lines represent the noise temperature corresponding to a constant added noise of 4.8 and 0.5 photons, respectively.

$$S_{\Phi,\mathrm{system}}^{\mathrm{LEMWR}} = \frac{k_\mathrm{B} T_{\mathrm{N,system}}}{\pi \eta_0 f_\mathrm{r}} \frac{Q_\mathrm{c}}{Q_\mathrm{l}} \frac{L_\mathrm{S}}{\beta_\mathrm{L} - \beta_\mathrm{L}^3} \left(\sum_{ij} \frac{\partial p_{i,j}}{\partial \varphi_\mathrm{ext}} \bigg|_{\Phi_\mathrm{ext}=\Phi_\mathrm{ext}^\mathrm{opt}} \right)^{-2} \tag{7.2}$$

The µMUX noise performance depends on various competing parameters. In particular, it is inversely proportional to the µMUX resonance frequency f_r, promising lower readout noise at elevated operation frequencies. Most other relevant parameters, such as the quality factors $Q_\mathrm{c}/Q_\mathrm{l}$, the relative resonance frequency shift η_0, or the SQUID parameters L_S and β_L, are, in theory, independent of the operating frequency and are therefore not expected to negatively affect the noise performance when operating a µMUX at higher frequencies. However, this is not the case for the system noise temperature $T_{\mathrm{N,system}}$, which is dominated by the HEMT noise temperature $T_{\mathrm{N,HEMT}}$. An ideal phase-insensitive linear amplifier is ultimately limited by the standard quantum limit (SQL) and adds at least half a photon of noise referred to the input per unit bandwidth, yielding a noise temperature $T_{\mathrm{N,QL}} = hf/(2k_\mathrm{B})$ that is proportional to frequency. However, the noise performance of state-of-the-art cryogenic ultra-low-noise HEMT amplifiers lies about an order of magnitude above this limit.

In recent years, the range of commercially available cryogenic microwave components has expanded considerably, including ultra-low-noise HEMT amplifiers with operation frequencies exceeding 100 GHz. To quantify their frequency-dependent noise performance, we collected data on the noise performance of a selection of state-of-the-art HEMT amplifiers. Figure 7.1 shows the dependence of the noise temperature on the operation frequency. We assume a hypothetical ideal HEMT amplifier that covers the entire frequency range up to 50 GHz and exhibits the best available noise level at each frequency. The noise temperature of this amplifier increases approximately linearly with frequency and can be approximated by an additional noise of 4.8 photons, roughly an order of magnitude higher than that of quantum-limited amplifiers.

[1]Datasheets available at lownoisefactory.com (accessed December 2025).

To assess how the increasing amplifier noise competes with the expected decrease in flux noise, we evaluated the expected µMUX noise performance using the simulation framework described in [Sch23b]. Whereas equations 7.1 and 7.2 translate the voltage noise generated by the readout system, which is characterized by its noise temperature, into an equivalent flux noise in open-loop readout, the simulation framework includes additional effects and noise sources. Specifically, it accounts for the finite response time of the resonator, as well as SQUID noise and TLS noise in the resonator. The simulation results presented in the following section correspond to the case of flux-ramp demodulated readout and hence reflect the actual operating conditions.

The simulations were based on lumped-element resonators capacitively coupled to a 50 Ω transmission line, with parameters chosen to match µMUX devices developed for the ECHo experiment [Gas17, Ric21b, Ahr22]. Each resonator had an inductance of $L = 2\,\mathrm{nH}$, a load inductance of $L_\mathrm{T} = 152\,\mathrm{pH}$, and a capacitance adjusted to set the target resonance frequency. The coupling quality factor Q_c was chosen assuming $Q_\mathrm{i} = 10^5$ to yield the desired bandwidth. The SQUID inductance and screening parameter were set to 46.1 pH and 0.4, and the inductive coupling between load inductor and SQUID was adjusted such that the total resonance frequency shift equaled the resonance bandwidth ($\eta = 1$). For µMUX operation and readout, we assumed a software-defined radio system equivalent to that described in chapter 5, with a flux-ramp amplitude of $1\,\Phi_0$, a repetition rate of $\sim 122\,\mathrm{kHz}$, and a sampling rate of 15.625 MHz. The probe tone was placed 100 kHz above the resonance frequency f_r. For the amplifier noise temperature, we used the data shown in figure 7.1, resulting in simulations of µMUX readout systems that, in principle, can be realized with available technology.

We varied the probe tone power P_exc as well as the resonance bandwidth Δf_BW and evaluated the white noise level for various resonance frequencies between 2 GHz and 50 GHz. Figure 7.2(a) shows the resulting flux noise levels as a function of P_exc for a µMUX operated at 16 GHz. The optimal readout tone power, $P_\mathrm{exc}^\mathrm{opt}$, is identified at the minima of the curves, which correspond to the lowest attainable flux noise, $\sqrt{S_{\Phi,\mathrm{white}}^\mathrm{min}}$, for each combination of µMUX resonance frequency and bandwidth. Below this power, the noise performance degrades as the SNR of the transmitted probe tone decreases. At higher readout power, the non-linearity of the SQUID response becomes significant, reducing the overall resonance frequency shift over a single flux ramp and consequently diminishing the variation of the transmitted probe tone power and degrading the SNR.

Figure 7.2(b) shows the minimum white noise level as a function of the resonance frequency. For a fixed bandwidth of $\Delta f_\mathrm{BW} = 1\,\mathrm{MHz}$, the white noise level increases overall with increasing resonance frequency. This trend can primarily be attributed to the increase of the ratio $Q_\mathrm{c}/Q_\mathrm{l} = 1 + Q_\mathrm{c}/Q_\mathrm{i}$ at higher resonance frequencies. At low frequencies, where $Q_\mathrm{c} \ll Q_\mathrm{i}$, the ratio approaches $Q_\mathrm{c}/Q_\mathrm{l} \approx 1$. In contrast, maintaining a constant bandwidth at higher resonance frequencies requires $Q_\mathrm{c} \propto f_\mathrm{r}$ to increase, while Q_i is assumed to remain constant. As a result, $Q_\mathrm{c}/Q_\mathrm{l}$ increases, leading to a degradation in noise performance.

This effect can be mitigated either by a substantial increase in Q_i or by a reduction of

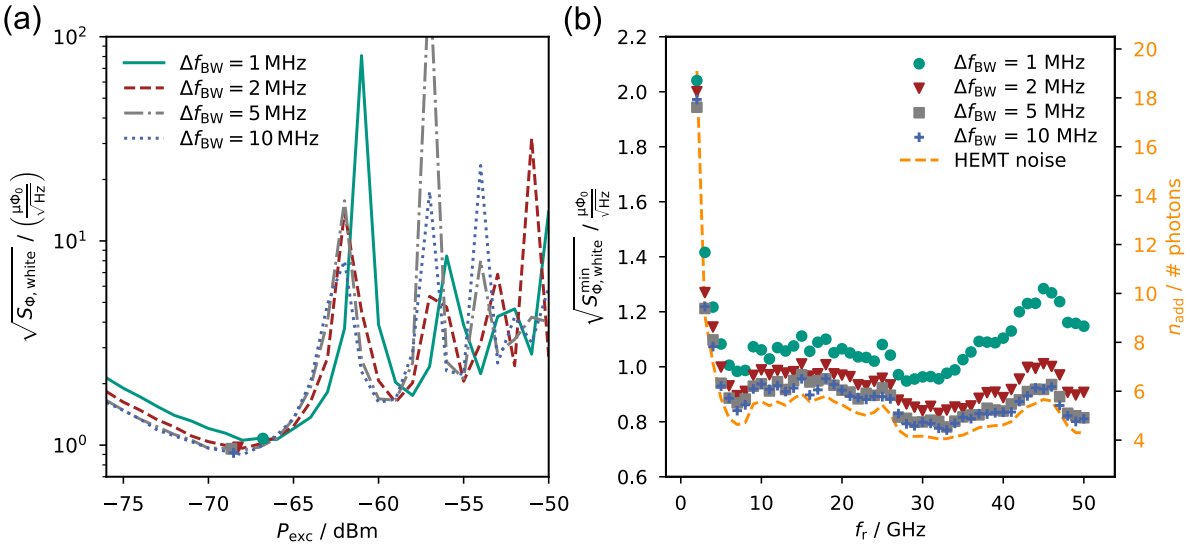

Fig. 7.2: Simulated noise performance of a fictitious µMUX operated between 2 GHz and 50 GHz assuming for each frequency the use of the best HEMT amplifier shown in figure 7.1. (a) FRM white noise level as a function of the on-chip readout tone power for a µMUX channel at 16 GHz assuming different values of the bandwidth Δf_{BW}. The minima correspond to the parameter $\sqrt{S^{\mathrm{min}}_{\Phi,\mathrm{white}}}$ plotted in (b). (b) lowest white noise level as extracted from (a) as a function of frequency. The dashed yellow line describes the assumed added noise of the HEMT amplifiers in number of photons.

Q_c. The latter corresponds to operation with larger channel bandwidths. Accordingly, figure 7.2 shows that increasing the bandwidth improves the noise performance, causing the noise to grow more slowly with resonance frequency. However, this improvement saturates, and the noise cannot be reduced indefinitely. Simulations show no significant performance difference between devices with $\Delta f_{\mathrm{BW}} = 5\,\mathrm{MHz}$ and $\Delta f_{\mathrm{BW}} = 10\,\mathrm{MHz}$. At large bandwidths, the frequency dependence of the flux noise is instead dominated by the added noise n_{add} of the HEMT amplifier, where $T_{\mathrm{N,HEMT}} = n_{\mathrm{add}} hf/k_{\mathrm{B}}$ is calculated from the noise temperatures in figure 7.1.

These results imply that simply increasing the operating frequency of state-of-the-art µMUX devices leads to a degradation in noise performance. However, by simultaneously exploiting a portion of the broader available frequency range through an increase in channel bandwidth, it is possible to mitigate this degradation. Such an approach enables significant improvements in noise performance compared to state-of-the-art devices working in the $4 - 8\,\mathrm{GHz}$ frequency range while simultaneously enhancing the multiplexing factor.

Operating µMUX at higher frequencies and achieving such low noise levels, however, requires a considerable increase in the power of the readout excitation tone (see figure 7.3 (a)). This increase is somewhat mitigated for larger channel bandwidths, but comparing, for example, the optimal readout power $P^{\mathrm{opt}}_{\mathrm{exc}}$ at 6 GHz and 32 GHz still shows an increase of approximately 8 dB. Nevertheless, these readout power levels can

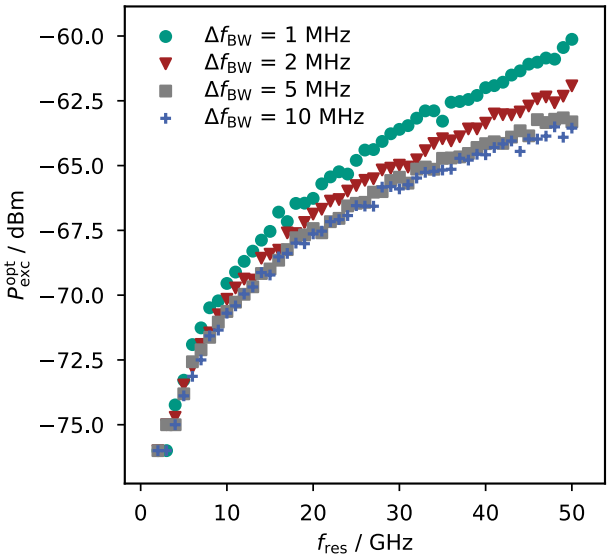

Fig. 7.3: Optimum excitation tone powers for µMUX devices between 2 GHz and 50 GHz with varying channel bandwidths. The readout powers correspond to the simulated minimum white noise levels shown in figure 7.2 (b)

be handled by HEMT amplifiers at these frequencies without encountering significant nonlinearities or power saturation. For example, a low gain amplifier operating at a frequency of 6 GHz[2] exhibits an input third-order intercept point (IIP3) of −32 dBm, while an amplifier operating at 32 GHz[3] shows an IIP3 of −24 dBm, which is also 8 dB higher. Consequently, linearity and power saturation are not expected to pose limiting factors for high-frequency µMUX devices.

7.2 Design iterations towards first K_u band µMUX devices

Motivated by the promising simulation results presented in the previous section, initial steps were taken toward the development of µMUX devices operating in the K_u band (12 GHz to 18 GHz). In [Hau23], both CPW $\lambda/4$ resonators and lumped-element resonators with resonance frequencies up to 20 GHz were fabricated using the available processes at IMS. Both designs exhibited intrinsic quality factors of $Q_i = \mathcal{O}(10^5)$, confirming that the losses within the resonator are sufficiently low to achieve the desired µMUX performance.

We chose CPW $\lambda/4$-resonators as the first resonator technology to realize a 16 GHz µMUX. While lumped element resonators offer a reduced footprint and avoid resonance harmonics, CPW resonators are the most commonly employed in µMUX devices. This is largely due to their reliable frequency tunability through adjustment of the transmission line length. In the initial approach, the CPW resonators developed in [Hau23] were combined with the established rf-SQUID design from [Ric23]. The resulting chip layout is shown in figure 7.4, labeled as *Hifr-Mux-01*.

The design consists of 12 µMUX channels arranged in 1 GHz steps between 9 GHz

[2]LNF-LNC4_8F_LG, Cryogenic Low Noise Amplifier, Low Noise Factory AB, Göteborg, Sweden
[3]LNF-LNC23_42B, Cryogenic Low Noise Amplifier, Low Noise Factory AB, Göteborg, Sweden

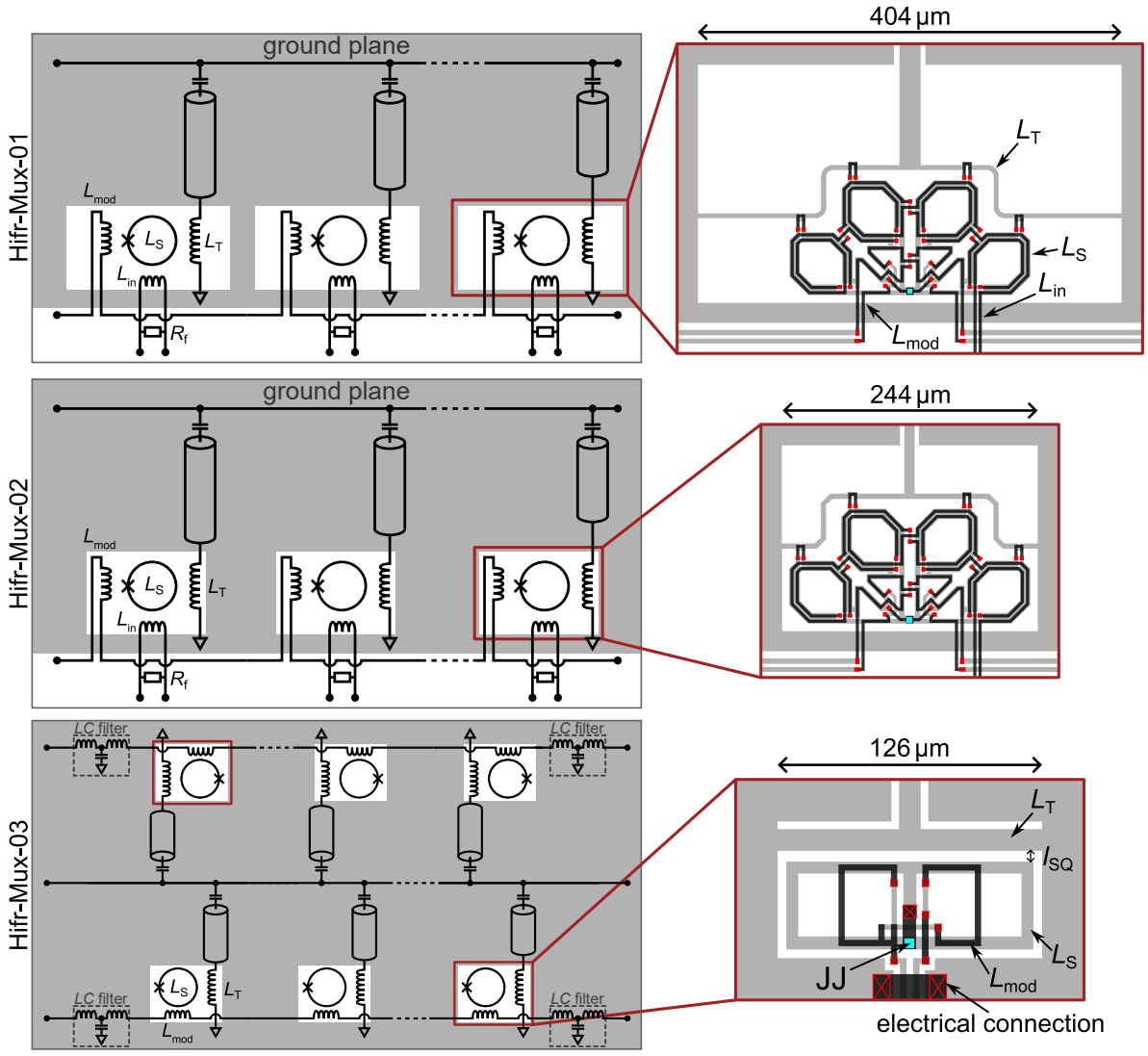

Fig. 7.4: Equivalent circuits of the chips and rf-SQUID layouts for the three design iterations leading to the final K_u band µMUX. The equivalent circuits are shown on the left. The gray area denotes the ground plane, which covers most of the chip while leaving a cutout around the rf-SQUIDs. In the first two designs, *Hifr-Mux-01* and *Hifr-Mux-02*, the ground plane ends above the modulation line. In the third iteration, *Hifr-Mux-03*, it extends to the bottom of the chip and also surrounds the modulation line, enabling ground connections between the chip and the µMUX housing from all sides. The layouts of the rf-SQUIDs is depicted on the right. The Nb bottom layer is shown in gray, and the top Nb wiring layer in black. Electrical connections between the two layers (vias) are highlighted in red. The load inductor and the size of the cut-out in the ground plane was reduced in scale from the first design to the second design. In the third iteration the rf-SQUID was redesigned with a minimalistic gradiometric layout, further reducing the scale of the resonator load circuit. However, this layout does not include an input coil and therefore does not constitute a fully operational µMUX channel.

Tab. 7.1: Exemple design parameters of a 16.5 GHz µMUX channel from design *Hifr-Mux-03*. The resonator parameters were derived from the µMUX design specifications, Sonnet simulations, and parameters extracted from the characterization of design *Hifr-Mux-02*, discussed in section 4.2. The rf-SQUID inductances and magnetic couplings were taken from InductEx simulations.

µMUX parameters

Parameter	Value
f_r	16.5 GHz
Δf_BW	1 MHz
$\Delta f_\mathrm{r}^\mathrm{max}$	1 MHz
β_L	0.4

Resonator parameters

Parameter	Value
f_0	17.033 GHz
l_res	1818 µm
C_c	1.83 fF

rf-SQUID parameters

Parameter	Value
L_S	49.6 pH
L_T	19.5 pH
L_mod	171 pH
M_T	1.52 pH
M_mod	35.5 pH
I_c	2.66 µA

and 20 GHz. The feedline design was adapted from [Hau23]. Like the resonators, it features an inner conductor width of 20 µm and a slot width of 5 µm. The ground plane extends to the chip edge above the feedline and to the modulation line below, which is positioned directly beneath the rf-SQUIDs. Bond pads for the rf-SQUID input coils and the filter resistors are located along the bottom chip edge. All channels were designed for a bandwidth and resonance shift of 1 MHz ($\eta_0 = 1$) with $\beta_\mathrm{L} = 0.4$. However, combining the 4 GHz rf-SQUID with the 16 GHz resonators did not yield functional µMUX channels. Only shallow and broad resonances were observed, exhibiting minimal distortion induced by the modulation current.

Several improvements were implemented in the subsequent wafer *Hifr-Mux-02*. In [Loh24], CPW resonators with varying dimensions were designed, all having a characteristic impedance of 50 Ω. The analysis revealed that an inner conductor width of 10 µm and a slot width of 4 µm yielded the highest intrinsic quality factor, with $Q_\mathrm{i} = \mathcal{O}(5 \cdot 10^5)$ in the range of 8 - 14 GHz. Consequently, these CPW dimensions were adopted for all subsequent designs. In addition, the load inductor was miniaturized. Estimating the maximum length scale l_max for lumped-element microwave circuits using an effective dielectric constant $\epsilon_\mathrm{r,eff} \approx 6.15$ for the CPW structures gives $l_\mathrm{max} = c/(20\sqrt{\epsilon_\mathrm{r,eff}} f_\mathrm{max}) \approx 300\,\mu\mathrm{m}$ for a maximum target frequency of $f_\mathrm{max} = 20\,\mathrm{GHz}$, with the downscaled load inductor remaining well below this limit. Finally, the ground planes on both sides of the feedline were interconnected behind the feedline taper, thereby improving the grounding of the circuit. The chip consists of 16 µMUX channels placed between 4.5 GHz and 19.5 GHz in 1 GHz steps with 1 MHz bandwidth and peak-to-peak frequency shift. While the µMUX channels below 8.5 GHz demonstrated intrinsic quality factors $\mathcal{O}(10^5)$, leading to well-defined resonance curves, we observed a decrease in the quality factor towards higher frequencies. Functional µMUX channels were observable up to $\sim$ 12.5 GHz, beyond which only harmonics of lower-frequency µMUX channels could be identified.

For the third design (*Hifr-Mux-03*), the rf-SQUID was redesigned to further reduce the device's scale, aiming to minimize radiation losses. The rf-SQUID was designed in a minimalistic gradiometric layout, removing the input coil, and with a SQUID inductance of $L_S = 50\,\mathrm{pH}$ and $\beta_L = 0.4$. As a result, no detector can be coupled to the µMUX channel, and thus the chip does not constitute a fully operational µMUX device. The coupling between load inductor and rf-SQUID was adjusted through the distance l_{SQ} between the two elements. This method requires dimensional accuracy on the order of hundreds of nanometers in the fabricated microstructure since a 100 nm deviation results in a $\sim 5\,\%$ deviation in the resonance frequency shift.

Using the standard IMS fabrication process with a critical current density of $j_c = 23\,\mathrm{A/cm^2}$ for the Josephson tunnel junctions, the required side length of the junction for this rf-SQUID design is 3.4 µm. In conjunction with a minimum via size of 2.5 µm for the existing fabrication process, this requirement dictates an alignment precision of $< 0.5\,\mu\mathrm{m}$ during the photolithography process. To alleviate this requirement, the critical current density was decreased by extending the oxidation time during the trilayer fabrication process from 3.5 h to 10 h. Using the relation $j_c \propto (p_{ox} t_{ox})^{-0.64}$[Ada24], this results in an expected reduction of the critical current density by a factor of two.

The chip design comprises 32 µMUX channels, with half of these channels coupled from one side and the other half from the opposite side to the feedline. The µMUX channels were arranged in 250 MHz steps from 12 GHz to 19.75 GHz. Table 7.1 lists the example design parameters for a 16.5 GHz µMUX channel. To establish the target coupling between the resonator and the SQUID, a distance of $l_{SQ} = 5.4\,\mu\mathrm{m}$ was specified. The area previously occupied by the bond pads of the input coils has been replaced with an extension of the ground plane to the lower edge of the chip. This arrangement enables grounding from all sides when mounted within the sample holder. To connect the ground plane on both sides of the modulation line, the modulation line has been fully covered by a Nb bridge between the two planes.

We effectively suppressed power leakage from the rf-SQUID into the input coil by removing it from the design, and an additional *LC* filter was integrated at each end of the modulation line to further reduce leakage through this path. The filter, designed with an inductance of 132 nH and a capacitance of 12 pF, yields a cutoff frequency of 126 MHz. To enhance mechanical compatibility with the sample holder, We increased the overall length of the chip to 15.5 mm, resulting in shorter bond wires between the chip's feedline and the feedline on the housing's rf-circuit board. For all subsequent measurements, we selected the number of bond wires connecting the feedline to be ≥ 5 in order to minimize the effects of the impedance mismatch caused by the inductance of the bond wires.

Figure 7.5 presents the frequency dependence of the transmission parameter for chip *A4* of design *Hifr-Mux-03*. To minimize the baseline ripple, we applied a Savitzky-Golay filter with a polynomial order of 5 and a window width of 2000, corresponding to 200 MHz. The transmission curves of the individual µMUX channels remain largely unaffected by this filtering process due to their significantly narrower bandwidth. Out of the 32 fabri-

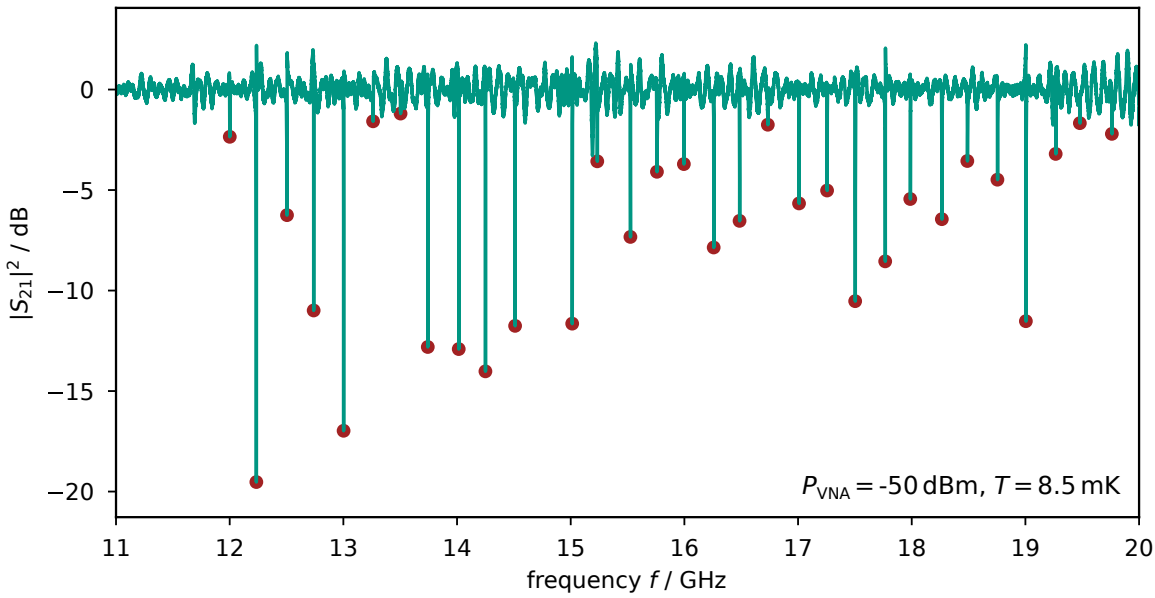

Fig. 7.5: Transmission measurement of chip *A4* of design *Hifr-Mux-03*. The baseline was corrected using a Savitzky-Golay filter. The red circles indicate the resonance frequency of identified µMUX channels. The data was recorded with a VNA output power of $P_{\mathrm{VNA}} = -50\,\mathrm{dBm}$ at $T = 8.5\,\mathrm{mK}$, using the microwave setup described in chapter 3.6.

cated µMUX channels, 31 could be identified. However, some resonances remained shallow, exhibiting intrinsic quality factors on the order of only a few thousand. In contrast, most channels demonstrated intrinsic quality factors of $Q_{\mathrm{i}} = \mathcal{O}(10^4)$. This resulted in well-defined resonance curves, having an average bandwidth of $\langle \Delta f_{\mathrm{BW}} \rangle = 2.3\,\mathrm{MHz}$ that is slightly broader than the design specification.

All tested µMUX channels exhibited a shift of the resonance frequency with changing modulation current. The transmission measurements for various magnetic biases of an example channel are depicted in figure 7.6 (a). Although the resonance bandwidth $\Delta f_{\mathrm{BW}} = 1.2\,\mathrm{MHz}$ is in good agreement with the design parameter, it is evident that the peak-to-peak resonance frequency shift is significantly larger than one bandwidth. In figure 7.6 (b) the µMUX model described in chapter 6 has been applied to fit the measured flux-dependence of the resonance frequency of the considered µMUX channel. The model describes the data accurately, assuming a screening parameter of $\beta_{\mathrm{L}} = 0.72$ and a junction barrier inhomogeneity of $\sigma = 0.38\,\mathrm{nm}$ with a mean barrier thickness of $\bar{d} = 2\,\mathrm{nm}$. The unexpectedly large screening parameter suggests a higher than intended critical current. In contrast, the characterization of test junctions from the border region of the wafer yielded a critical current density of $10.3\,\mathrm{A/cm^2}$, slightly lower than the target value of $11.5\,\mathrm{A/cm^2}$. This, combined with the observed barrier thickness inhomogeneity, indicates significant inhomogeneities in the spatial distribution of the critical current density across the wafer. The overall too large peak-to-peak resonance

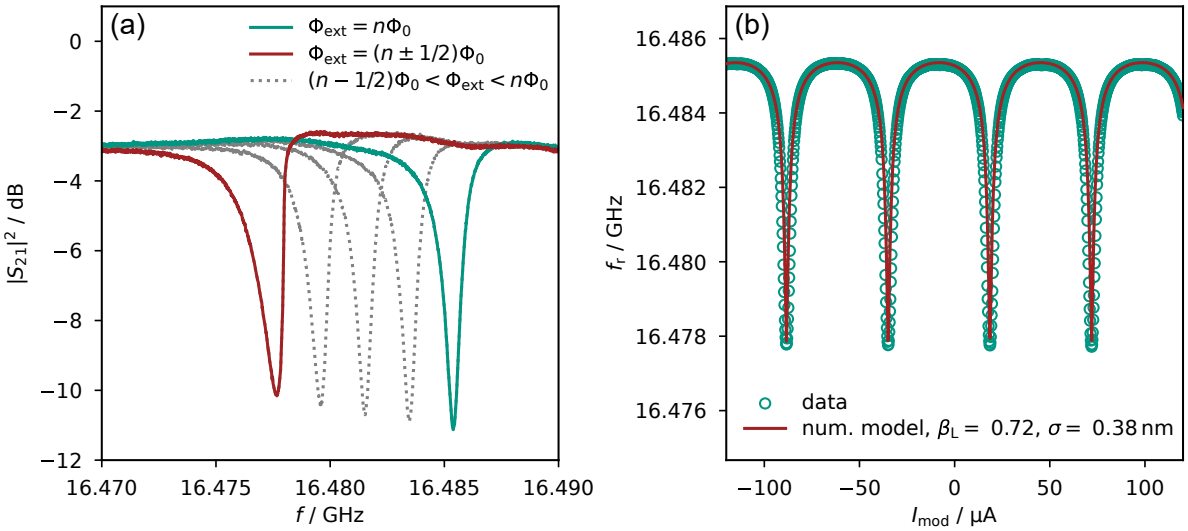

Fig. 7.6: Resonance frequency shift measurements of the 16.5 GHz channel of chip A4 of design *Hifr-Mux-03*. (a) Frequency dependence of the transmission parameter $|S_{21}|^2$ for varying flux bias. The measurement was performed with a vector network analyzer (VNA) with a VNA output power of $P_{VNA} = -44$ dBm and a temperature of $T = 8.5$ mK. (b) Resonance frequency as a function of applied modulation current. The solid line shows the result of a fit based on the numerical model described in chapter 6.

frequency shift can, on one hand, be attributed to this excessively high critical current density. On the other hand, as we will discuss in section 7.3.2, accurately simulating M_T in this design is challenging, as it strongly depends on the generally unknown current distribution in the ground plane surrounding the rf-SQUID, which can lead to peak-to-peak resonance frequency shifts of up to 6 times larger than anticipated.

While all µMUX channels displayed a periodic resonance frequency shift, some channels showed characteristics $f_r(\varphi_{ext})$ that cannot be explained by any existing µMUX model (see figure 7.7). These channels exhibit sudden jumps in the resonance frequency occurring periodically in steps of $1\,\Phi_0$. To investigate whether this behavior might be traced back to a screening parameter $\beta_L > 1$ resulting in a hysteretic rf-SQUID, the resonance shift of these channels has been measured for increasing as well as decreasing flux biases. However, no hysteresis could be observed.

As demonstrated in chapter 4.3, when a fixed complex load is inductively coupled to the rf-SQUID, the circuit connected to the resonator of the µMUX channels may satisfy the resonance condition for specific flux biases, leading to jumps in the resonance frequency of the µMUX channels. While such resonances are typically attenuated by the filter resistor included in the input circuit or by the normal conducting electronics connected to the modulation line, the design *Hifr-Mux-03* suppressed this effect through the inclusion of the *LC*-filter at the end of the modulation line. Furthermore, the modulation line coupled to the rf-SQUIDs should be regarded as a transmission line, given that it is longer than l_{max}. This configuration introduces previously unconsidered complex and

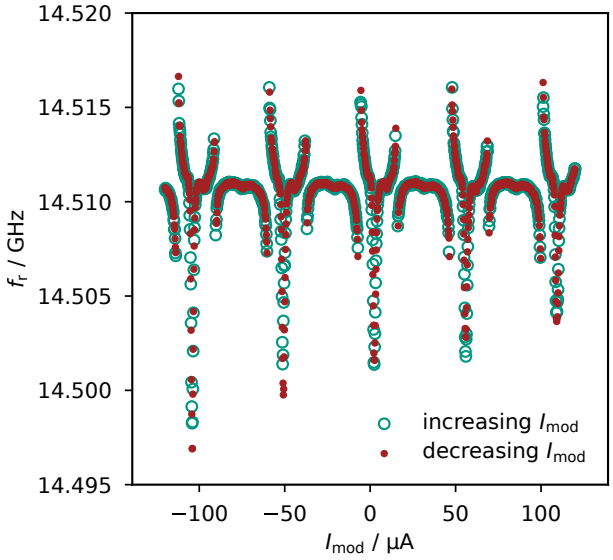

Fig. 7.7: Measured flux dependence of the resonance frequency shift of the 14.5 GHz µMUX channel on chip *A4* of design *Hifr-Mux-03*. The resonance frequency was determined from the minima of the resonance curves obtained from measurements with a VNA, with a VNA output power of $P_{VNA} = -50\,dBm$ at a temperature of $T = 8.9\,mK$. The modulation current was first increased from $-120\,\mu A$ to $120\,\mu A$ and subsequently decreased stepwise over the same range.

flux-dependent loads that may contribute to the observed resonance frequency jumps. To mitigate such resonances in future designs, the attenuation factor of the modulation line was increased by applying a resistive layer over the modulation line, allowing induced eddy currents to dampen high-frequency signals.

The measurements of this chip have demonstrated that µMUX devices operating in the K_u band with high intrinsic quality factors are feasible. However, the practical implementation of K_u band µMUX devices still faces two challenges. First, it remains to be shown that the frequency jumps observed in figure 7.7 can be mitigated, resulting in µMUX channels that can be reliably described by our µMUX models. Second, a complete µMUX device must include an input coil, which significantly increases the complexity of the resonator load circuit.

7.3 First complete K_u band µMUX devices

This section discusses the design and characterization of the first complete µMUX prototype devices for MMC readout, incorporating both an input and a modulation coil and operating in the K_u band. First, a CPW microwave resonator based µMUX design will be discussed. Afterwards, to demonstrate the potential for a further reduced design footprint, a lumped-element-based µMUX design will be presented.

7.3.1 Design of the K_u band µMUX chip

The first complete µMUX prototype device operating in the K_u band has been fabricated with design *Hifr-Mux-07*. Figure 7.8 shows a micrograph of chip *B5* of the design *Hifr-Mux-07*, the characterization of which will be discussed in sections 7.3.2 and 7.3.3. To trap magnetic flux quanta that potentially penetrate the ground plane in various

regions of the chip, the ground plane is perforated with 4 µm × 4 µm square holes arranged on a 8 µm × 8 µm grid. The rf-SQUID design incorporates an input coil, with the corresponding bond pads placed at the lower edge of the chip. Furthermore, the ground plane surrounds the individual bond pads. The individual sections of the ground plane, divided by the modulation and input lines, are interconnected by niobium bridges that are spread by ∼ 300 µm. The lines have been completely covered by the SiO_2 layer, and in addition, a layer of Au:Pd is placed on top of the lines in the sections between the bridges to dampen high-frequency signals through induced eddy currents, thus suppressing resonances that build along the input and modulation lines.

The chip features 18 µMUX channels, arranged with a 80 MHz frequency spacing between 15.32 GHz and 16.68 GHz. For the calculation of the resonator lengths, an effective permittivity of $\epsilon_{\mathrm{r,eff}} = 5.86$ was assumed, which was extracted from the measured resonance frequency of the bare resonators on chip *A4* from design *Hifr-Mux-02* (see section 4.2). Each channel is designed for a bandwidth of $\Delta f_{\mathrm{BW}} = 1\,\mathrm{MHz}$ and a peak-to-peak resonance frequency shift of $\Delta f_{\mathrm{r}}^{\mathrm{max}} = 2\,\mathrm{MHz}$ with an rf-SQUID screening parameter of $\beta_{\mathrm{L}} = 0.4$.

Following the results in the previous section and those discussed in chapter 4, the rf-SQUID has been redesigned to include an input coil, thereby forming a complete µMUX channel. The rf-SQUID is realized in a simple first-order gradiometric layout. This version has been further miniaturized compared to the design *Hifr-Mux-03*. To minimize transmission line effects between the input coil and the filter resistor, the resistor $R_{\mathrm{f}} = 3\,\Omega$ was placed as close as possible to the rf-SQUID. The coupling strength between load inductor and rf-SQUID is set by adjusting the width $l_{M_{\mathrm{T}}}$ (see figure 7.8). The coupling coil is part of the SQUID loop, making the SQUID inductance dependent on $l_{M_{\mathrm{T}}}$ (see figure 7.9), which must be considered for µMUX channel design. Table 7.2 presents the resulting rf-SQUID parameters for an example µMUX channel, with a resonance frequency of 15.32 GHz. To cover the limited frequency range from 15.32 GHz to 16.68 GHz only slight variations of $l_{M_{\mathrm{T}}}$ were required, spanning from 13.5 µm to 11.7 µm, resulting in mutual inductances M_{T} between 2.18 pH and 1.99 pH and SQUID inductances between 43.3 pH and 42.7 pH. The input coil remains largely unaffected by these changes with $L_{\mathrm{in}} = 330\,\mathrm{pH}$. This inductance is significantly lower than the inductance of typical MMCs ($L \sim 1.5\,\mathrm{nH}$). Therefore, future µMUX designs for practical MMC readout should make further adjustments to the input coil design to achieve impedance matching.

To investigate the impact of the different components of the rf-SQUID on the intrinsic quality factor of the µMUX channel operating at such high operation frequencies, not all channels on chip *B5* were designed to be a complete µMUX channel. This allows investigations similar to those made in section 4.2. Starting from the lowest resonance frequency, three channels were designed as complete µMUX channels, and for another three, only the filter resistor R_{f} was removed. For the following design variants, two channels were employed for redundancy. One variant has the input coil removed, and another variant has the modulation coil removed, effectively preventing microwave leakage into each line. The next design variant includes neither the input coil nor the

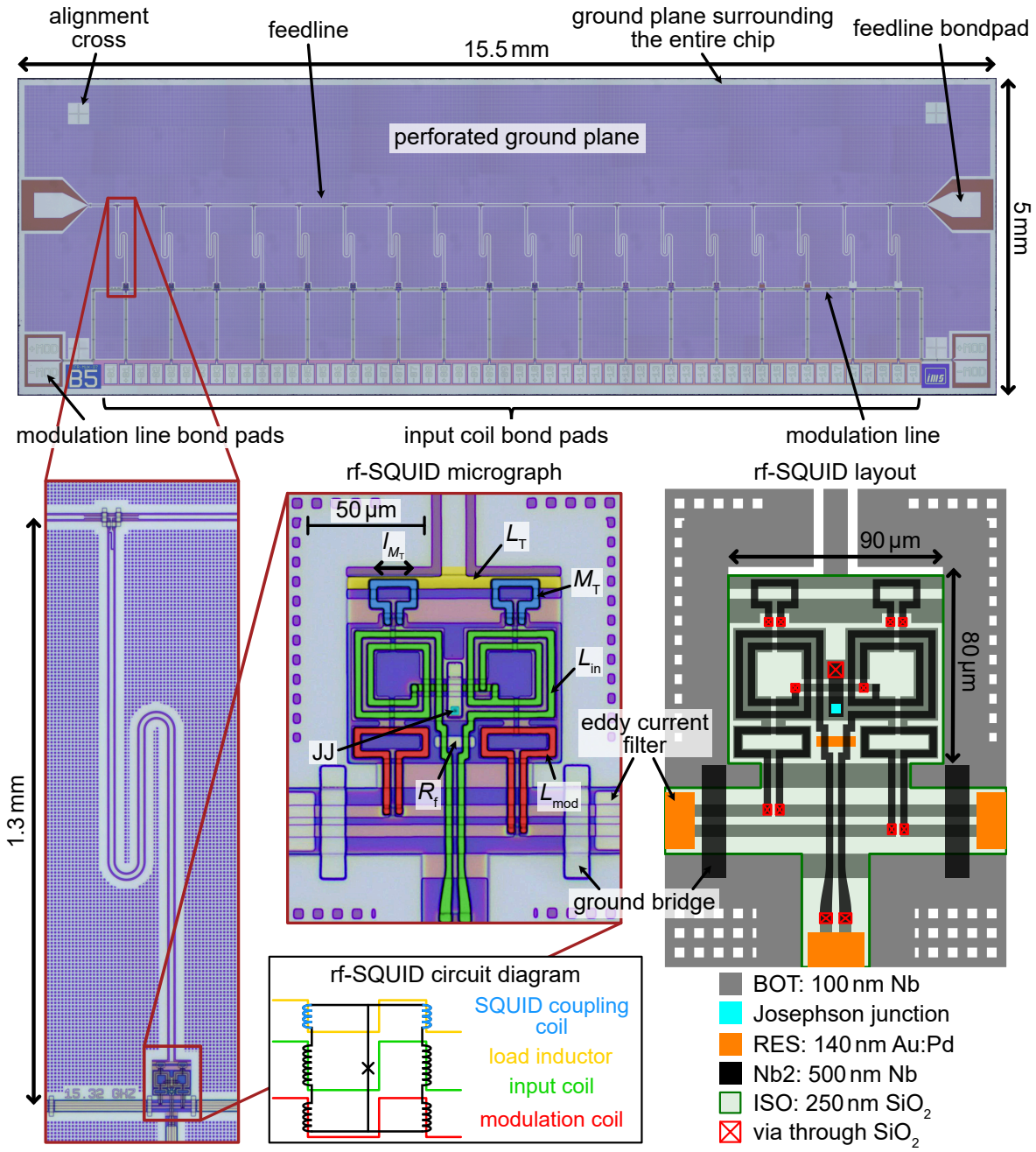

Fig. 7.8: Micrographs of chip *B5* of design *Hifr-Mux-07*. At the top an image of the entire chip is shown. The bottom left shows a zoomed-in view of a single µMUX channel. The center shows a zoomed-in view of the rf-SQUID. In the image, the device's different inductors have been colored for easier identification. In the bottom center the circuit diagram of the rf-SQUID has been sketched, using the same color codes as in the image above. On the right the layout of the rf-SQUID design is depicted, with all the electrical connections between the niobium layers marked.

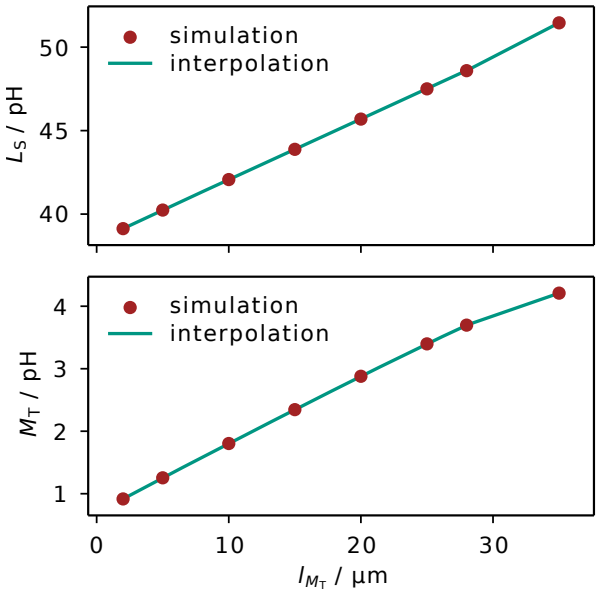

Fig. 7.9: Dependence of the SQUID inductance L_S and the SQUID-resonator coupling M_T on the coupler length l_{M_T} of the rf-SQUID design on *Hifr-Mux-07*, as determined from inductance simulations using InductEx. The individual simulated data points are connected by linear interpolation, allowing L_S and M_T to be evaluated for arbitrary coupler lengths within the simulated parameter range.

Tab. 7.2: rf-SQUID design parameters of the 15.32 GHz µMUX channel of chip *B5* of design *Hifr-Mux-07*. The values were determined through simulations using InductEx.

l_{M_T}	L_T	L_{in}	L_{mod}	L_S	M_T	M_{in}	M_{mod}	I_c
13.5 µm	14.8 pH	330 pH	163 pH	43.3 pH	2.18 pH	59.3 pH	19.4 pH	3.04 µA

modulation coil, followed by a variant in which the Josephson junction is replaced with a simple via, thereby eliminating potential losses due to low sub-gap resistances in the junction. The final two design variants result in a resonator solely terminated by the load inductor and another with no load. Since the resonator lengths were designed for complete µMUX channels, especially for the last design variants, which consist only of bare resonators, significantly higher resonance frequencies of ~ 17 GHz are expected.

7.3.2 Characterization of the µMUX chip

For characterization, the µMUX was installed in a copper housing and cooled to 20 mK, where the transmission parameter S_{21} was measured using a vector network analyzer (VNA). The µMUX chip was connected to one of the channels of the cryogenic rf-switch. Another channel had no device under test (DUT), with the input channel of the switch directly connected to the corresponding output channel of the switch. A transmission spectrum of the µMUX device over the full relevant frequency range is shown in figure 7.10. At first, the data were corrected using an equivalent S_{21} measurement obtained from the channel without a DUT and by calculating the ratio of the acquired transmission parameters ($S_{21}^{\text{corrected}} = S_{21}/S_{21}^{\text{noDUT}}$). The ripple in the baseline after this correction was reduced compared to the uncorrected S_{21} data. However, it remained significant (± 5 dB in the shown frequency range). Compared to established calibration methods, the employed correction cannot account for reflections and impedance

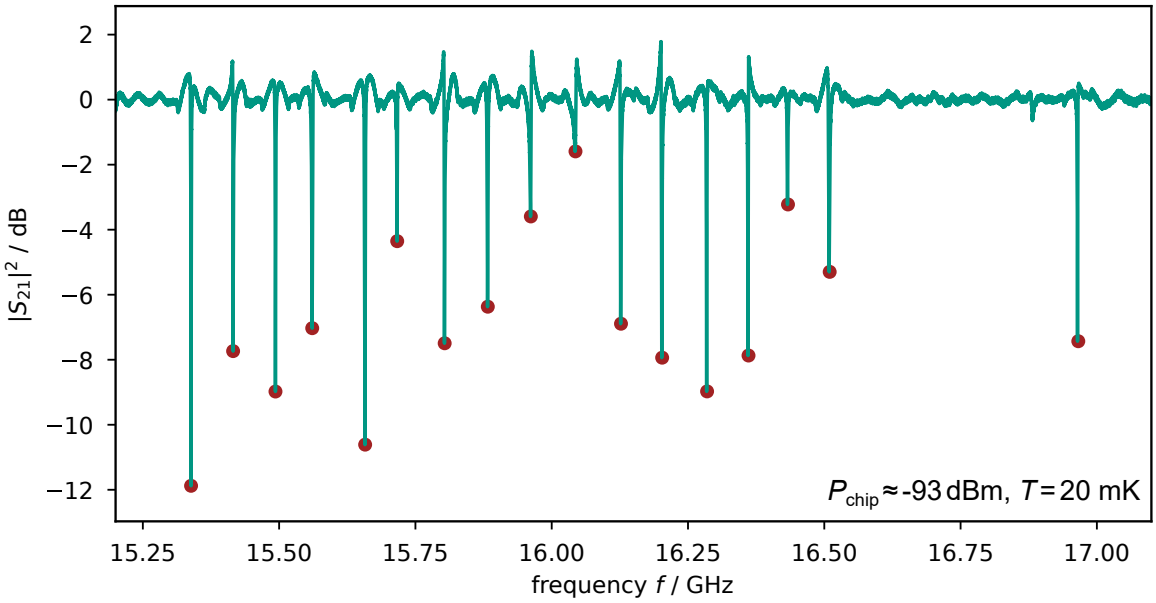

Fig. 7.10: Transmission parameter measurement of chip *B5* of design *Hifr-Mux-07*. The baseline was corrected using a second measurement through a another channel of the cryogenic rf-switch, as well as a third order Savitzky-Golay filter with a 50 MHz wide window. The red circles indicate the identified µMUX channels. The data was recorded with an on chip microwave power of $P_{\mathrm{chip}} \approx -93\,\mathrm{dBm}$ at $T = 20\,\mathrm{mK}$, with no current applied to the modulation line $I_{\mathrm{mod}} = 0\,\mu\mathrm{A}$.

mismatches between the DUT and the cryogenic transmission line. Additionally, the different electrical lengths through the µMUX and the channel without the DUT result in phase differences between the two measurements. Consequently, the impact of the cryogenic microwave measurement on the transmission measurement setup cannot be entirely removed from the data through this method. Only frequency-dependent effects, such as cable losses along the measurement chain, can be normalized. Therefore, the data were corrected with an additional third order Savitzky-Golay filter, with a window length of 50 MHz. In the corrected data, all designed resonances are clearly identifiable, with the exception of one of the two bare resonators around 17 GHz.

The resonance frequency spacing of the channels, excluding the bare resonator, was determined to be $79 \pm 5\,\mathrm{MHz}$, which aligns well with the design parameter of 80 MHz. The measured bandwidth, shown in figure 7.11, is, however, larger than intended. This deviation is partially attributed to the design assumption $Q_{\mathrm{i}} \gg Q_{\mathrm{c}}$, which is not applicable to the actual µMUX channels, where Q_{i} is only slightly larger than the designed $Q_{\mathrm{c}} = \mathcal{O}(16000)$(figure 7.11). Furthermore, the precise adjustment of the coupling capacitance poses an increasing challenge, as the required coupling capacitance scales with $C_{\mathrm{c}} \propto f_{\mathrm{r}}^{-3/2}$ for a constant resonance bandwidth, resulting in a decreasing coupler size with increasing frequency. Consequently, at higher frequencies, the resonance bandwidth becomes increasingly sensitive to small geometric variations during fabrication.

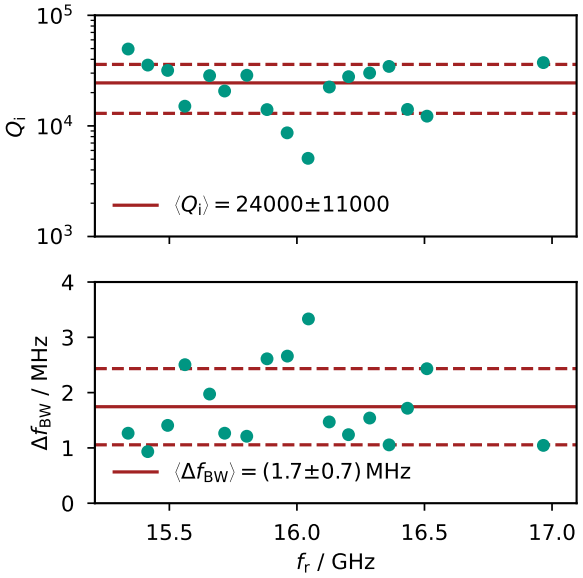

Fig. 7.11: Intrinsic quality factor and bandwidth of the resonances measured on chip *B5* of design *Hifr-Mux-07*. Individual results are shown in green, while the mean value and its standard deviation across the chip are indicated in red. The parameters were extracted using the circle-fit algorithm described in section 3.8.1 applied to the transmission measurement shown in figure 7.10.

Despite variations in the complexity of the resonator load circuits across channels, no clear trend of Q_i for decreasing complexity with increasing resonance frequency is apparent. Consequently, radiation losses and microwave leakage in the load circuit were not the primary factors influencing the intrinsic quality factor. This demonstrates that the effects discussed in section 4.2 were effectively mitigated through the new miniaturized rf-SQUID design.

To characterize the individual µMUX channels, the transmission curves of the different channels have been measured for different values of the externally applied flux bias. The flux bias was generated by a current running through the modulation coil, which was varied from $-125\,\mu A$ to $125\,\mu A$. The transmission curves were measured using a vector network analyzer (VNA) with an output power of $P_{VNA} = -50\,dBm$, resulting with an approximate attenuation of $\sim 53\,dB$ in an on chip power of $P_{chip} \approx -103\,dBm$. For the first three complete µMUX channels, the measurements were repeated at multiple output power levels ranging from $-65\,dBm$ to $-10\,dBm$. An example transmission curve measurement is shown in figure 7.12 (a). While the periodic resonance frequency shift is clearly observed, the resonance depth decreases significantly around $\Phi_{ext} = (n + 1/2)\Phi_0$. This phenomenon may be attributed to a low subgap resistance in the Josephson junctions of the rf-SQUIDs [Weg18]. Also, the eddy current filters placed on the input and modulation line can introduce considerable flux bias dependent losses (section 4.3).

The resonance frequency can be well described by our µMUX models, as shown in figure 7.12 (b). No significant contributions of the junction barrier inhomogeneity could be discerned. Therefore, it was neglected in the applied fit. The total resonance shift is larger than designed and can partially be traced back to deviations in the screening parameter β_L. These deviations can be attributed to inhomogeneities in the critical current across the wafer. As discussed in section 7.4, for the case of the lumped-

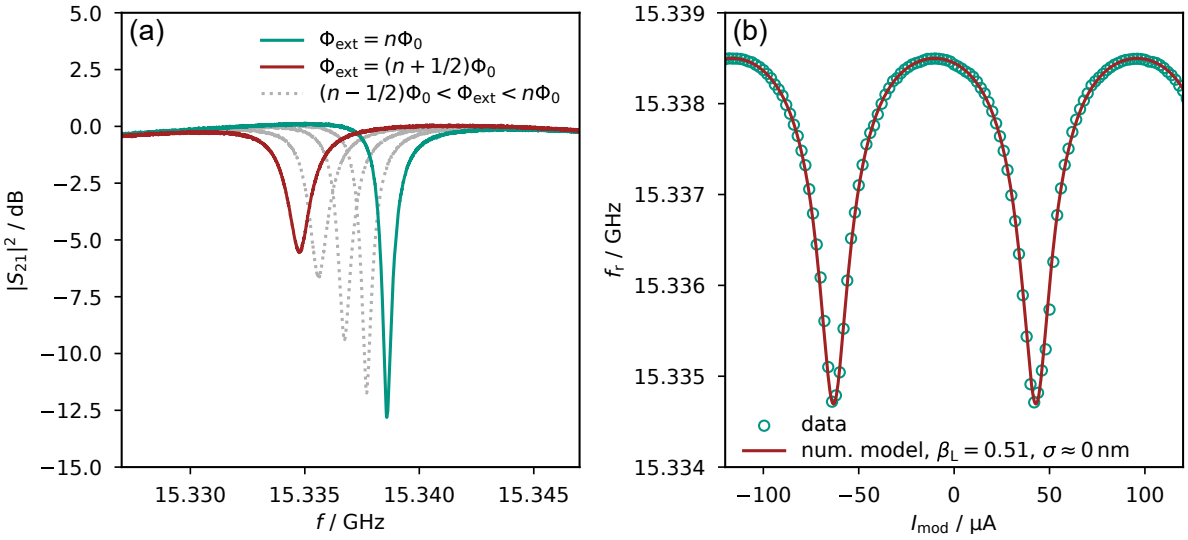

Fig. 7.12: Resonance shift of the 15.32 GHz µMUX channel, acquired at $T = 20$ mK with a VNA output power of $P_{VNA} = -45$ dBm, corresponding to an on-chip power of $P_{chip} \approx -98$ dBm. (a) Transmission curves of the µMUX channel for different flux bias values. (b) Resonance frequency as a function of the modulation current. The solid line shows the result of a fit based on the numerical model described in chapter 6.

element µMUX, the measured screening parameter is smaller than expected, despite the rf-SQUID design being identical and the chip being fabricated on the same wafer. These variations in the critical current may arise from minor discrepancies in the dimensions of the 3.6 µm × 3.6 µm Josephson junctions, as well as variations in the critical current density across the wafer.

Additionally, the ratio M_T^2/L_S shows a significant deviation from the simulated values, a trend observed across all characterized channels. Since only the first eight channels on the chip contained an rf-SQUID with coupled modulation line, only these channels were characterized. The determined parameters are listed in table 7.3. While the measured ratio $\langle M_T^2/L_S \rangle = (0.17 \pm 0.02)$ pH deviates significantly from the simulated 0.11 pH, the measured coupling M_{mod} between the rf-SQUID and the modulation coil aligns well with our simulations. Consequently, not the InductEx simulations in general, but specifically the simulation settings of L_S or M_T need to be optimized.

When reevaluating our simulations, we noticed that the accurate simulation of M_T is particularly challenging, more so than assumed in our initial simulations. To maintain a compact overall layout of the rf-SQUID, the ground plane surrounding the SQUID is kept at a minimal distance. As a result, the current distribution within the ground plane significantly influences the coupling strength M_T. In the original simulations, the ports defining the load inductance were positioned at the end of the CPW resonator: one in the inner conductor and the other in the ground plane, to the left and right of it. This placement assumed that all current flowing through the load inductor returns through the ground plane to the end of the resonator, effectively screening the current

Tab. 7.3: Overview of the measured µMUX channel parameters characterizing the rf-SQUIDs coupled to the microwave resonators. The parameters were extracted from transmission curve measurements using a VNA operated with an output power of $P_{\mathrm{VNA}} = -50\,\mathrm{dB}$ under different values of the external flux bias that was applied by running a dc current through the modulation line. Only the first eight channels of chip *B5* of design *Hifr-Mux-07* are shown, as the remaining channels either lacked a modulation line or had no rf-SQUID coupled.

Channel	Type	$f_{\mathrm{r}}^{\mathrm{off}}$ / GHz	$\Delta f_{\mathrm{r}}^{\mathrm{max}}$ / MHz	β_{L}	$\frac{M_{\mathrm{T}}^2}{L_{\mathrm{S}}}$ / pH	M_{mod} / pH
1	complete	15.3375	3.81	0.51	0.15	19.5
2	complete	15.4147	6.19	0.65	0.14	19.5
3	complete	15.4923	3.89	0.52	0.14	19.6
4	no R_{f}	15.5629	6.88	0.61	0.18	19.5
5	no R_{f}	15.6567	7.61	0.64	0.18	19.5
6	no R_{f}	15.7176	8.88	0.66	0.19	19.4
7	no L_{in}	15.8047	8.20	0.64	0.19	19.3
8	no L_{in}	15.8857	9.09	0.65	0.20	19.3

in the inner conductor. However, if a portion of the current flows toward the ground bridges, crossing the modulation line beneath each rf-SQUID, mutual inductances up to 2.5 times higher than expected may occur. Therefore, to achieve an accurate simulation of M_{T}, the current distribution in the ground plane must be thoroughly understood.

The three complete µMUX channels were further characterized by examining the power dependence of the resonance frequency shift (figure 7.13). The total resonance shift decreases with increasing readout powers, as predicted by our µMUX models. This behavior is critical for the simulations discussed in section 7.1, as they rely on these models to optimize the readout tone power to achieve the best SNR. The model applied to the data in figure 7.13 takes into account that the intrinsic quality factor Q_{i} is flux dependent. The power dependence of Q_{i} is approximated using an exponential function of readout power. Minor deviations between the model and the determined resonance frequencies may occur due to distortion of the resonance curve at high readout powers, leading to inaccuracies during the circle-fit routine. Additionally, the applied model does not consider the power dependence of the resonance frequency, which may arise from self-heating at high microwave probe tone powers.

Fitting the power dependence of the resonance frequency shift enables the determination of the attenuation A_{TX} of the transmission side of the cryogenic readout chain. To accomplish this, the mutual inductance between the load inductor and the rf-SQUID M_{T} is crucial. We can calculate M_{T} from the experimentally derived ratio $M_{\mathrm{T}}^2/L_{\mathrm{S}}$, assuming that only M_{T} significantly deviates from simulations due to the aforementioned currents in the ground plane, while L_{S} remains consistent. This yields $M_{\mathrm{T}} \approx 2.5\,\mathrm{pH}$. Using this value, we can evaluate the attenuation $A_{\mathrm{TX}} \approx (53 \pm 1)\,\mathrm{dB}$ around 15.4 GHz from the µMUX power dependence fits applied to the three complete µMUX channels. The uncertainty in the attenuation is introduced by the pronounced baseline ripples at these

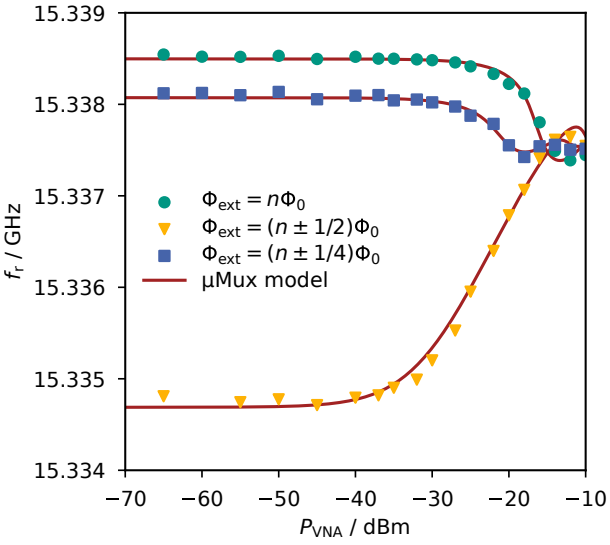

Fig. 7.13: Measured power dependence of the resonance shift of the 15.32 GHz µMUX channel at $T = 20\,\mathrm{mK}$. The resonance frequency is shown as a function of the VNA output power P_{VNA} for different values of the externally applied flux Φ_{ext}. The numerical fits are based on the µMUX model described in chapter 6, assuming negligible junction barrier inhomogeneity and additionally approximating Q_{i} as an exponential function of P_{VNA}. The attenuation installed on the transmission line was determined to be approximately $A_{\mathrm{TX}} \approx (53 \pm 1)\,\mathrm{dB}$.

frequencies, which introduce frequency-dependent variations of $\sim 1\,\mathrm{dB}$, even within the resonance shift range of a single channel. The determined attenuation is significantly higher than the installed attenuation of 40 dB. However, higher attenuation is expected due to the additional attenuation of the installed coaxial cables. With the determined attenuation of 46 dB at 4 GHz, this results in an average slope of the attenuation of $\sim 0.6\,\mathrm{dB/GHz}$. This agrees with the predictions made in [Ahr22] for an equivalent readout chain.

7.3.3 Open-loop noise performance of the K_u band µMUX

To compare the noise performance of the K_u band µMUX devices to the noise performance of conventional µMUX operating in the range of 4-8 GHz, additional noise measurements were performed for the 15.32 GHz µMUX channel. Since the SDR setup utilized for the noise measurements in chapter 5 has only a bandwidth of 4-8 GHz, the noise measurements had to be performed using an alternative setup and only the open-loop noise performance could be investigated.

The measurement setup is sketched in figure 7.14. A signal generator[4] is connected to the TX line of the cryogenic readout chain, where distributed 40 dB of attenuation is installed. This, combined with the attenuation from cables and individual RF components, results in a total attenuation of $A_{\mathrm{TX}} = (53 \pm 1)\,\mathrm{dB}$ at the µMUX input for an operation frequency of $\sim 15.3\,\mathrm{GHz}$, as determined from the µMUX power dependence in the previous section. On the RX line, the signals are amplified by a cryogenic HEMT amplifier followed by a room temperature amplifier, connecting to a signal analyzer[5]. The net gain, accounting for the attenuation from cables and RF components in the RX line, is $G_{\mathrm{RX}} = (52 \pm 1)\,\mathrm{dB}$. This value was calculated using the S_{21} parameter at

[4] Agilent, N5183A MXG Microwave, Analog Signal Generator
[5] Agilent, N9020A-526, MXA Signal Analyzer

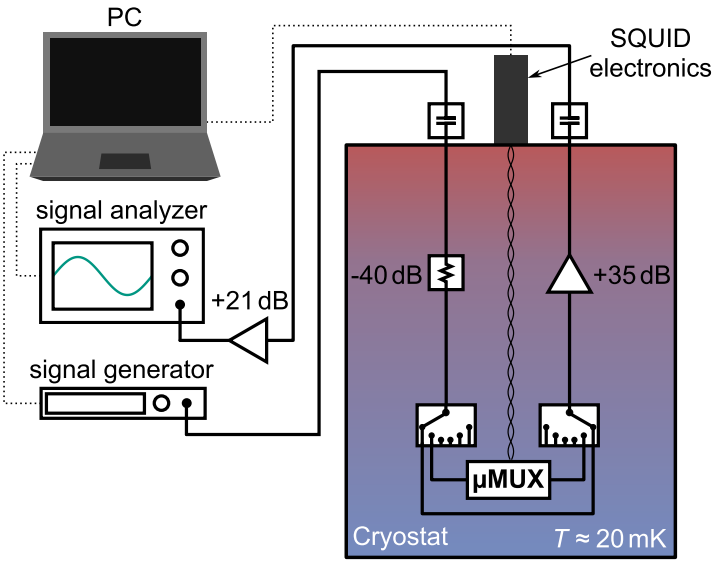

Fig. 7.14: Sketch of the setup used for open-loop flux noise measurements at $\sim$ 15.3 GHz. The installed attenuators, combined with the cable attenuation in the transmitting path, results in a total attenuation of $A_{\mathrm{TX}} = (53 \pm 1)$ dB. The net gain , including the cable attenuation, on the receiver side is $G_{\mathrm{RX}} = (52 \pm 1)$ dB. SQUID electronics, signal analyzer and signal generator are software controlled.

$\sim$ 15.3 GHz in combination with the attenuation A_{TX}. At the cryostat's mixing chamber stage, the rf-switches are installed, allowing for switching between measuring the actual μMUX and a simple transmission line. The modulation line current is controlled using the SQUID electronics, which, like the signal generator and analyzer, is controlled by software from a PC.

Before each noise spectrum acquisition, the transfer coefficient $\partial A/\partial\Phi$ between the transmitted signal amplitude A and the applied magnetic flux must be determined. For this, a square current signal was applied to the modulation line, with a peak-to-peak amplitude of $\Delta I_{\mathrm{mod}} = 1\,\mu\mathrm{A}$ and an adjustable modulation current offset I_{mod}. The signal generator produces an excitation tone at a frequency f_{exc}, while the signal analyzer records a trace of the amplitude of the transmitted tone (see figure 7.15 (a)). The acquired amplitude trace reveals the presence of the applied square signal. However, a slow drift in signal amplitude is also observed, potentially due to inadequate magnetic shielding. The amplitude of the acquired square signal can still be calculated by determining the levels of the various signal plateaus and taking the differences between adjacent plateaus. From this analysis, the transfer coefficient $\partial A/\partial I_{\mathrm{mod}}$ can be determined. When combined with the measured mutual inductance $M_{\mathrm{mod}}^{-1} = 106\,\mu\mathrm{A}/\Phi_0$, this allows for the calculation of the overall transfer coefficient $\partial A/\partial\Phi = M_{\mathrm{mod}}^{-1}(\partial A/\partial I_{\mathrm{mod}})$.

Noise traces were acquired with a sampling rate of 7 MHz over 0.25 s and the noise spectrum was calculated using the Welch method described in section 3.8.2. The amplitude noise spectrum S_A as well as the converted flux noise spectrum $\sqrt{S_\Phi}$ is shown in figure 7.15 (b). We observe a pronounced $1/f$ noise contribution below 700 kHz and a steep cutoff above 3 MHz that is related to the bandwidth of the spectral analyzer. The white noise level is extracted by averaging the noise value between 800 kHz and 1.3 MHz.

To minimize readout noise, the flux bias, excitation tone frequency f_{exc}, and microwave power P_{SG} must be optimized. The flux bias was optimized by performing multiple

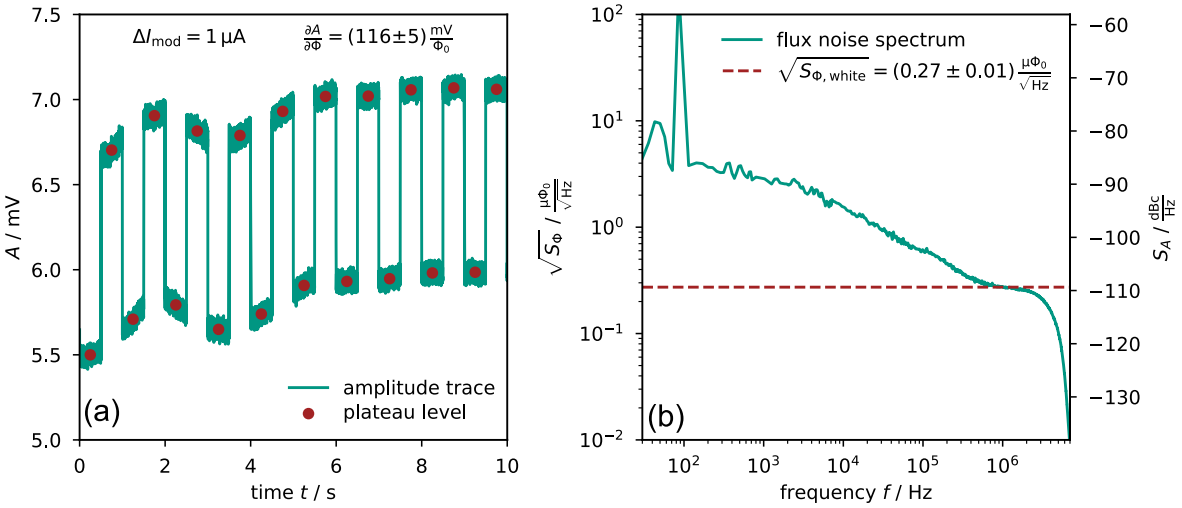

Fig. 7.15: (a) Amplitude time trace measurement used for the determination of the transfer coefficient $\partial A/\partial\Phi$ of the 15.32 GHz µMUX channel, using an excitation tone at $f_{exc} = 15.337\,65$ GHz and a signal generator output power of $P_{SG} = -25$ dBm. A 1 Hz square wave current signal with a peak-peak amplitude of $\Delta I_{mod} = 1\,\mu A$ and an offset of $I_{mod} = -59\,\mu A$ was applied to the modulation line using the SQUID electronics. The red circles mark the determined amplitude levels of the plateaus of the measured square wave. (b) Noise spectrum calculated from another amplitude time trace measurement performed with the same signal generator settings and modulation line current, however without the square signal. The amplitude noise spectrum S_A was converted into flux noise using the transfer coefficient determined in (b). The white noise level is indicated with a red dashed line.

measurements of the transfer coefficient and amplitude time traces across a range of flux bias values, covering more than a flux quantum. The white noise level was recorded for each current. At the flux bias value yielding the lowest white noise level, measurements were repeated with sweeps of the excitation tone frequency. Finally, the excitation tone power was optimized. Figure 7.16 shows the results of such measurements when performing a frequency sweep of the excitation tone. The overall measurement shape is determined by the frequency dependence of the transfer coefficient. Low transfer coefficients far away from resonance lead to high flux noise levels, while optimal flux noise performance is observed on the resonance flanks. At the resonance frequency, the transfer coefficient is again low, resulting in the spike observed at the center of figure 7.16. The best noise performance was achieved for a flux bias of $\Phi_{ext} = -0.46\,\Phi_0$, an excitation tone set at $f_{exc} = 15.337\,65$ GHz on the left flank of the resonance curve, and a tone power of $P_{SG} = -25$ dBm. The corresponding noise spectrum is depicted in figure 7.15 (b).

The measured white noise level is $\sqrt{S^{min}_{\Phi,white}} = (0.27 \pm 0.01)\,\mu\Phi_0/\sqrt{Hz}$, which is comparable to that of state-of-the-art two-stage dc-SQUID readout systems [Man21]. For

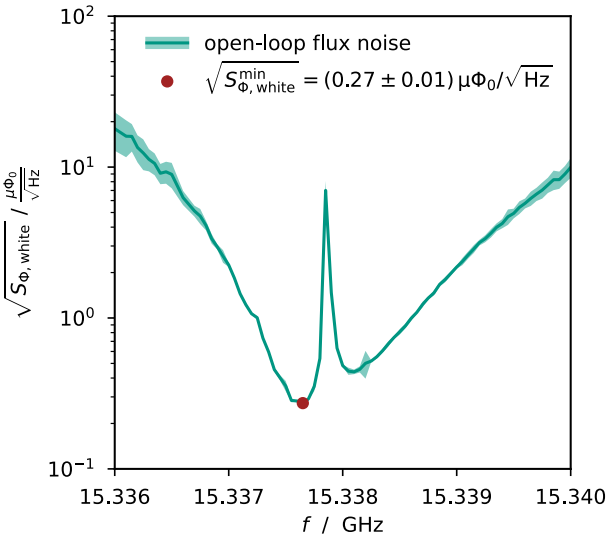

Fig. 7.16: Measured flux white noise level as a function of the excitation tone frequency. The sweep was performed with a modulation current bias of $I_{\mathrm{mod}} = -59\,\mu\mathrm{A}$ and a signal generator output power of $P_{\mathrm{SG}} = -25\,\mathrm{dBm}$. The white noise level is displayed as a green line, with the brighter green span marking the 1σ error range resulting from the uncertainty in the transfer coefficient determination. The minimal noise level is marked with a red circle at an excitation tone frequency of $f_{\mathrm{exc}} = 15.337\,65\,\mathrm{GHz}$.

FRM readout, a degradation of the readout noise is anticipated, particularly due to the high ratio between the peak-to-peak resonance shift and the resonator bandwidth $\eta_0 \approx 3$. This high value results in a large transfer coefficient, leading to low flux noise in open-loop readout. However, in FRM readout, the signal of the excitation tone over one flux ramp period becomes less sinusoidal, which results in a significant noise degradation.

The measured optimum flux white noise level corresponds to an amplitude noise level of $S^{\min}_{A,\mathrm{white}} = -109\,\mathrm{dBc}$. This noise level is expected to be dominated by the systems noise quantified by the system noise temperature and not by the µMUX chip. To validate this, the SNR of a transmitted excitation tone through the transmission line without DUT was analyzed, effectively removing all noise contributions from the µMUX itself. The dependence of the white noise level on the microwave power of a probe tone applied at 15.3 GHz is presented in figure 7.17. An improvement in the noise spectral density can be observed with increasing tone power, as expected from the noise introduced by the additive system noise temperature. At high probe tone powers, the noise value levels out due to the contribution of a multiplicative noise source $S^{\mathrm{mult}}_{A,\mathrm{white}}$, which is proportional to the probe tone power. The total amplitude white noise spectrum $S_{A,\mathrm{white}}$ can hence be described by

$$S_{A,\mathrm{white}} = S^{\mathrm{mult}}_{A,\mathrm{white}} + \frac{k_{\mathrm{B}} T^{\mathrm{ADC}}_{\mathrm{N}}}{P_{\mathrm{ADC}}}, \tag{7.3}$$

where $T^{\mathrm{ADC}}_{\mathrm{N}}$ denotes the additive noise temperature referred to the input of the signal analyzer, and P_{ADC} denotes the tone power at that input. From this, the system noise temperature $T_{\mathrm{N}} = T^{\mathrm{ADC}}_{\mathrm{N}}/G_{\mathrm{RX}}$ can be calculated. A numerical fit applied to the data in figure 7.17 yields a system noise temperature of $T_{\mathrm{N}} = (6.6 \pm 1.9)\,\mathrm{K}$ and a multiplicative noise contribution of $S^{\mathrm{mult}}_{A,\mathrm{white}} = -114\,\mathrm{dBc/Hz}$. The determined noise temperature agrees well with the expected system noise temperature of $\sim 7\,\mathrm{K}$, which is dominated by the noise temperature of the utilized HEMT amplifier. At the optimal readout power of $P_{\mathrm{SG}} = -25\,\mathrm{dBm}$, the system noise level is measured to be $S_{A,\mathrm{white}} =$

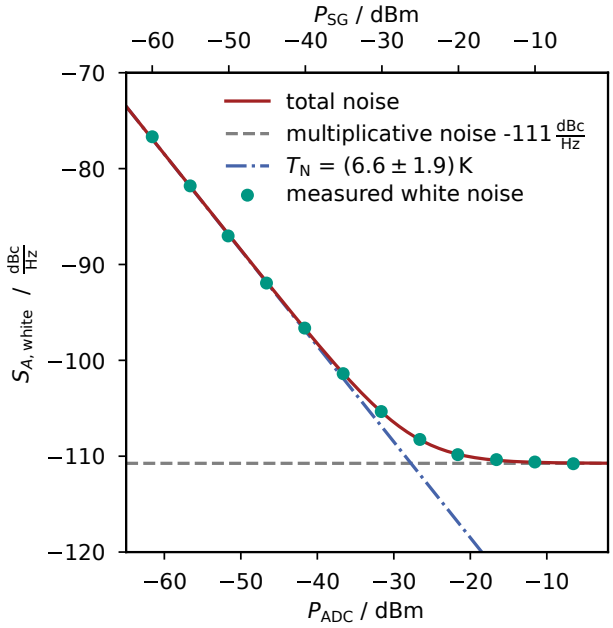

Fig. 7.17: White noise level as determined from amplitude time trace measurements at an microwave probe tone frequency $f_{exc} = 15.3\,\text{GHz}$ through the transmission line in the cryostat without DUT as a function of the signal generator output power P_{SG}. The total noise, fitted with the red solid curve, can be described as a combination of the system noise quantified by the noise temperature T_N, indicated with the blue dash dotted line, and a multiplicative noise contribution, shown with the gray dashed line.

−111 dBc/Hz, comparable to the value of −109 dBc/Hz as measured for the µMUX. The small difference is likely attributed to the reduced transmitted power of the probe tone applied to the flank of the µMUX resonance curve. Therefore, as expected, the white noise level for the µMUX is dominated by the noise introduced by the readout chain. However, at a readout power of $P_{SG} = -25\,\text{dBm}$, this noise is not dominated by the HEMT but rather by a multiplicative noise contribution arising from random fluctuations in the system parameters of the measurement setup. Consequently, the investigated 15.32 GHz µMUX channel can potentially achieve an even lower flux noise level with a more sophisticated measurement setup.

7.4 Lumped-element K_u band µMUX devices

To demonstrate the possibility of a significantly reduced device footprint when utilizing elevated µMUX operation frequencies, the design *Hifr-Mux-07* contains multiple chips with lumped-element microwave resonator-based µMUX (LEMWR MUX) devices. A micrograph of a single channel of such a device is presented in figure 7.18 (a) together with an equivalent circuit diagram in figure 7.18 (b). This design employs the same coupling capacitor, load inductor, and rf-SQUID configuration as the CPW-based µMUX discussed in the previous section. The lumped-element resonator comprises an interdigital capacitor (IDC) C positioned between the coupling capacitor C_C and ground, in parallel with an inductor L, which is connected in series with the load inductor L_T, also linked to ground.

The lumped-element design results in a significantly smaller footprint compared to CPW based $\lambda/4$-resonators. The resonator only takes an area of 220 µm × 170 µm, which is already smaller than the typical 250 µm × 250 µm microcalorimeter absorber. Addition-

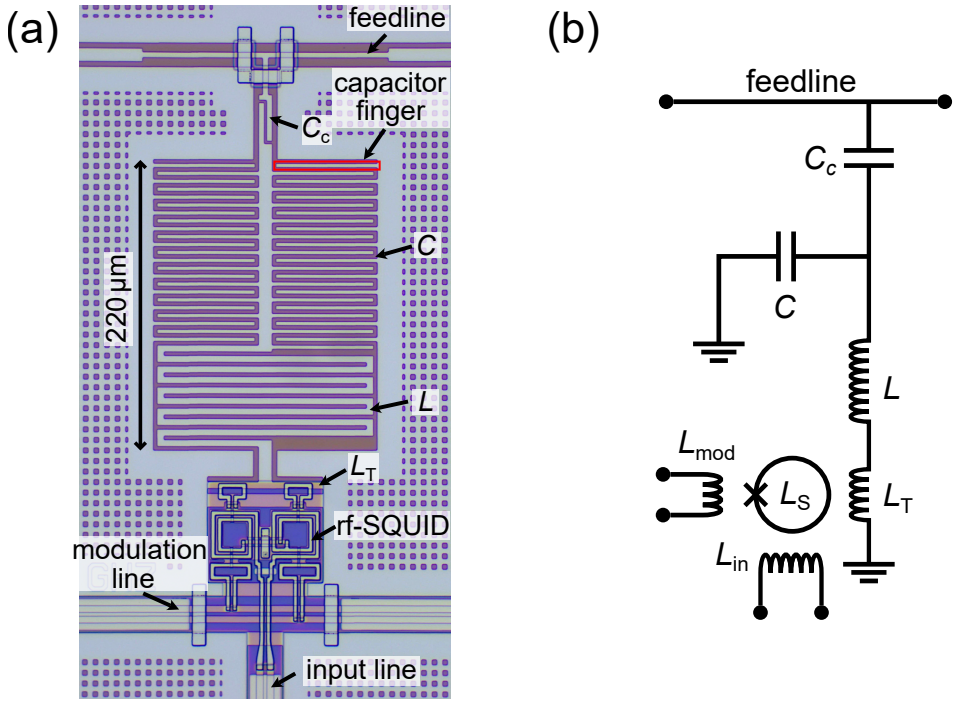

Fig. 7.18: (a) Micrograph of a lumped-element µMUX channel on chip *B6* from design *Hifr-Mux-07* with a target resonance frequency of 15.57 GHz. (b) Equivalent circuit diagram of the lumped-element µMUX channel shown in (a).

Tab. 7.4: Design parameters of the lumped-element µMUX channels on chip *B6* from design *Hifr-Mux-07*. The parameters are based on simulations using Sonnet and InductEx.

$f_{r,sim}$	$\Delta f_{BW,sim}$	$N_{fingers}$	L	C_c	L_T	L_S	M_T
15.57–16.85 GHz	1–1.2 MHz	47–38.5	523 pH	2.53 fF	14.8 pH	43.5 pH	2.35 pH

ally, further miniaturization is possible. The size of the capacitor can be reduced while maintaining its capacitance by using a material with high relative permittivity to cover the IDC fingers. Additionally, the inductance can be enhanced by employing a spiral inductor design and a conductor material with high kinetic inductance. Together, these approaches will yield µMUX devices that fit comfortably within the footprint of most existing microcalorimeters.

The LEMWR MUX chips contain 18 µMUX channels that share identical design parameters, with the exception of the varying number of IDC fingers. The simulated design parameters are listed in 7.4. The inductance of the resonator was simulated with InductEx. The interdigital capacitor C was designed iteratively based on Sonnet simulations to achieve resonance frequencies between 15.57 GHz and 16.85 GHz for varying numbers of IDC fingers $N_{fingers}$. Only the resonator designs corresponding to the highest and lowest resonance frequencies were simulated, while $N_{fingers}$ was varied in steps of

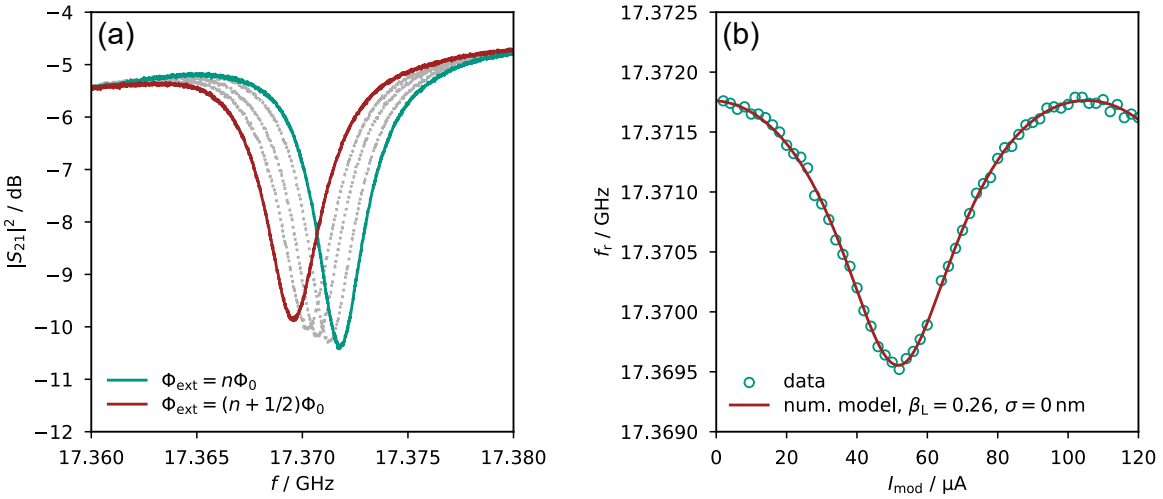

Fig. 7.19: Resonance shift of one of the LEMWR MUX channels, acquired at $T = 10\,\mathrm{mK}$ with a VNA output power of $P_{\mathrm{VNA}} = -35\,\mathrm{dBm}$, corresponding to an on-chip power of $P_{\mathrm{chip}} \approx -89\,\mathrm{dBm}$. (a) Transmission spectrum of the µMUX channel at varying flux bias. (b) Resonance frequency as a function of the modulation current.

0.5 fingers for the intermediate resonance frequencies. For the simulated inductances L, L_{T}, and the mutual inductance M_{T}, a resonance frequency shift of $\Delta f_{\mathrm{r}}^{\mathrm{max}} = 1.7\,\mathrm{MHz}$ is expected across all channels.

While lumped-element microwave resonators occupy a smaller footprint than CPW $\lambda/4$-resonators with the same resonance frequency, achieving precise resonance frequency placement is significantly more challenging. Dimensional deviations occurring during fabrication of about 0.1 µm in a CPW have a negligible effect on the resonance frequency. In contrast, similar deviations in the IDC of the lumped-element resonator used here can lead to resonance frequency shifts of approximately 1.5 % [Rea20], demonstrating the substantially higher sensitivity of lumped-element designs to fabrication variations.

The measured resonance frequencies deviate significantly from the simulated values. The observed resonances fall between 16.1 GHz and 17.4 GHz corresponding to a deviation from the design of $\sim$ 3.6 %. Furthermore, the resonance spacing is highly inhomogeneous, leading to substantial overlap among resonance curves. The inhomogeneous spacing is likely caused by local variations in the geometry of the IDC across the chip. As a result, most channels could not be accurately characterized. An exception is the µMUX channel with a measured resonance frequency at 17.37 GHz whose resonance curve is shown in figure 7.19 (a). The resonance exhibits a bandwidth of $\Delta f_{\mathrm{BW}} = 3\,\mathrm{MHz}$ and a peak-to-peak frequency shift of $\Delta f_{\mathrm{r}}^{\mathrm{max}} = 3.3\,\mathrm{MHz}$, both of which exceed the expected parameters from the design. The increased bandwidth can be primarily attributed to the intrinsic quality factor of $Q_{\mathrm{i}} = 11\,000$, which is similar to the coupled quality factor of $Q_{\mathrm{c}} = 12\,500$. Although Q_{c} is slightly lower than the target value of $\sim 15\,500$, the low Q_{i} dominates and effectively more than doubles the resulting bandwidth. The resonance frequency shift is mainly influenced by the rf-

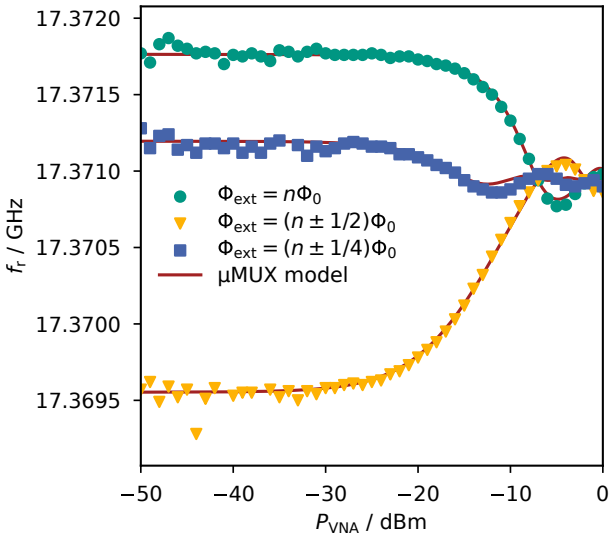

Fig. 7.20: Measured power dependence of the resonance shift of the investigated LEMWR MUX channel, measured at $T = 10\,\mathrm{mK}$. The resonance frequency is shown as a function of the VNA output power P_{VNA} for different values of the externally applied flux Φ_{ext}. The numerical fits are based on the µMUX model described in chapter 6, assuming negligible junction barrier inhomogeneity and additionally approximating Q_{i} as an exponential function of P_{VNA}. The attenuation installed on the transmission line was determined to be approximately $A_{\mathrm{TX}} \approx (54 \pm 1)\,\mathrm{dB}$.

SQUID's screening parameter β_{L}, the inductances L, L_{S}, and L_{T}, as well as the mutual inductance M_{T} (see equation 2.48). We extracted a β_{L} from the resonance frequency dependence on the modulation current shown in figure 7.19 (b) and yielded a screening parameter of $\beta_{\mathrm{L}} = 0.26$, which is smaller than the design value of 0.4 and even smaller than the parameters found in section 7.3.2 for chip *B5* with CPW µMUX channels . Since the SQUID design remains consistent across the two chips, this suggests spatial inhomogeneity in the junction's critical current across the wafer. This may be due to variations in critical current density or discrepancies in the realized junction side lengths. Based on the smaller β_{L}, we would expect a smaller than intended resonance shift. Therefore, significant deviations from simulations in the achieved inductances and mutual inductances must be present. Accurate simulations of the inductances L and L_{T}, as well as the resonator SQUID coupling M_{T}, are particularly challenging due to the current distribution in the ground plane in close proximity to the resonator. This especially affects M_{T}, which is the dominant quantity influencing the resonance shift. Considering exclusively deviations in the mutual inductance, we get $M_{\mathrm{T}} = 3.24\,\mathrm{pH}$, which deviates by 38 % from the simulated value.

We also investigated the power dependence of the resonance frequency shift of the LEMWR MUX. For this, we measured the resonance curve for multiple readout powers at the flux bias values $n\Phi_0$, $(n \pm 1/2)\Phi_0$, and $(n \pm 1/4)\Phi_0$. The extracted resonance frequencies as a function of the VNA readout power are presented in figure 7.20. We observe excellent agreement between our µMUX model and the measured data. This validates that our µMUX model accurately describes both CPW-based and lumped-element-based µMUX devices operating in the K_u band. Using the calculated mutual inductance M_{T}, we extract the attenuation A_{TX} from the fitted model in figure 7.20. We find $A_{\mathrm{TX}} = (54 \pm 1)\,\mathrm{dB}$ of attenuation at 17.37 GHz, which agrees with the value obtained for 15.4 GHz in section 7.3.2.

The strong agreement between measurements and µMUX model confirms that K_u band µMUX devices are both feasible and that the underlying assumptions made for the

simulations presented in section 7.1 are valid, not only within the frequency range of 4 GHz to 8 GHz but also at higher frequencies in the K_u band. Combined with the prior validation of the simulation framework using µMUX data around 4 GHz [Sch23b], this further supports the reliability of the simulation results. Future experiments will require a complete µMUX readout chain, including a suitable software-defined radio system, to thoroughly evaluate the predicted performance and to utilize the enhanced multiplexing factor, time resolution, and noise levels.

Additionally, the results presented in this thesis represent an important first step toward significantly reduced µMUX footprints. Such reductions are expected to have a significant impact on future large-scale microcalorimeter arrays by reducing layout complexity and enabling more compact detector assemblies.

8. Conclusion and Outlook

Superconducting microcalorimeters are a key enabling technology for upcoming and near-future experiments that require detectors with sub-electronvolt energy resolution or aim to detect rare processes. They combine near-unity quantum efficiency with record energy resolution. Moreover, recent advances in micro- and nanofabrication technologies have enabled the production of large microcalorimeter arrays comprising thousands of detectors, thereby enabling experiments that demand high statistics or improved spatial or angular resolution. However, the operation of large detector arrays at millikelvin temperatures inherently poses the challenge of developing a suitable multiplexing scheme that manages system complexity, cost, and parasitic heat load on the experimental stage. In this regard, microwave SQUID multiplexers (µMUXs) [Irw04, Mat08, Kem17a] represent the current state of the art, as they combine a high multiplexing factor with low on-chip power dissipation and large bandwidth per readout channel. While µMUXing has already enabled the simultaneous readout of hundreds of microcalorimeters, their noise performance falls short of what is provided by two-stage dc-SQUID setups [Fag06] used for individual microcalorimeter readout. As a result, for magnetic microcalorimeters (MMCs), µMUX readout already limits the achievable energy resolution in large-scale arrays. Further optimization and novel concepts for reducing µMUX readout noise are therefore essential for next-generation experiments.

State-of-the-art µMUX devices exhibit noise levels well above those predicted by numerical simulation frameworks [Sch23b], indicating significant potential for improvement. This discrepancy can largely be attributed to unintended microwave power losses within the µMUX channels [Ric23], which reduce resonance depth and consequently decrease the modulation amplitude of the probe tones. In addition, existing simulation frameworks are based on analytical models with a restricted range of validity [Weg22] and therefore do not cover the full parameter range relevant for device optimization. This prohibits the full optimization of the design parameters of current µMUX designs.

To surpass present noise limitations and approach the performance of single-detector readout systems, more advanced µMUX concepts are required. Prominent approaches include the integration of quantum-limited kinetic-inductance traveling-wave parametric amplifiers (KITWPAs) into the cryogenic amplification chain [Mal23] and the implementation of tone-tracking readout schemes [Ker18]. Both strategies, however, introduce substantial technical challenges, including complex biasing circuits, limited saturation power, and stringent demands on room-temperature electronics.

In this thesis, we established the infrastructure required for state-of-the-art µMUX development at the Institute of Micro- and Nanoelectronic Systems (IMS). This includes an electromagnetic simulation based design workflow for µMUX channels with arbitrary design parameters, the implementation of a dedicated microfabrication process, the

development of a cryogenic housing for operation in a dilution refrigerator, the design and installation of a complete cryogenic readout chain, and the creation of software tools for device characterization. These capabilities enabled the realization of state-of-the-art µMUX devices and the targeted investigation of the major limitations in current µMUX readout systems.

We showed that integrating the rf-SQUID into the µMUX channel design introduces additional dominant loss mechanisms compared to a bare microwave resonator and showed that loading the µMUX channels modulation coil and input coil introduces even higher losses, limiting the µMUX channels resonance depth. This finding underscores the importance of accounting for the microwave behavior of the nominally dc circuitry. We therefore systematically investigated the influence of the dc load. In particular, we demonstrated that the placement of the filter resistor shunting the input coil strongly affects the intrinsic quality factor. Minimizing the distance between the filter resistor and the input coil suppresses distributed-element behavior, which could otherwise lead to significant microwave power dissipation in the resistor. We developed a quantitative model describing the losses associated with the filter resistor and showed that they determine the flux dependence of the intrinsic quality factor in our devices. Furthermore, we demonstrated that filter resistors reduce the total resonance-frequency shift of a µMUX channel, making their inclusion essential when calculating design parameters and aiming for precise µMUX characteristics. Finally, we analyzed the impact of arbitrary complex loads connected to the dc circuitry and observed discontinuities in the µMUX characteristics. These effects can be mitigated in practical implementations of future µMUX designs by selecting sufficiently small filter resistances. However, a compromise must be made, keeping the Johnson noise introduced by the filter resistor in mind.

Using the design and fabrication processes established in this thesis, we realized a dedicated µMUX device that was deployed in the first full-fledged µMUX readout system for MMCs [Nei25a]. A complete µMUX readout system requires complex room temperature electronics to handle probe tone generation and digital demultiplexing. This is commonly implemented using a software defined radio (SDR) system. The SDR system [Mus24] deployed in our µMUX setup was developed for the ECHo experiment [Gas17] and represents the latest generation of SDR systems for µMUX readout of MMCs. It provides up to 400 readout channels covering the frequency range from 4 to 8 GHz. For the acquisition of detector events, we coupled MMCs [Mül24] to the µMUX input coils and installed them in a dedicated cryogenic measurement setup equipped with a ^{83}Rb/$^{83\mathrm{m}}$Kr source. The fabricated µMUX device provided 14 channels, 7 of which were connected to MMCs. The µMUX channel resonance frequencies were distributed across the full 4 and 8 GHz band, enabling validation of the SDR system over its entire operational bandwidth. Simultaneous acquisition of detector signals on all installed channels confirmed proper multiplexed operation. A comparison of pulse shapes recorded with the µMUX system and those obtained using individual dc-SQUID readout demonstrated faithful signal reproduction. By optimizing probe-tone frequencies and amplitudes for minimal noise, we achieved an average flux noise level

of $(1.4 \pm 0.2)\,\mu\Phi_0/\sqrt{\mathrm{Hz}}$ in flux-ramp–demodulated readout across all channels. This corresponds to a reduction of 44 % compared to the previous SDR generation. From the measured energy sensitivity $\epsilon = 158\,h$ and coupled energy sensitivity $\epsilon_\mathrm{c} = 374\,h$, we demonstrate that our system provides excellent performance even among state-of-the-art µMUX systems. Together with the demonstrated linearity across all channels, these results confirm that our system is fully functional and well suited for high-resolution, large-scale MMC experiments.

We developed an advanced numerical model describing the power dependence of µMUX devices. In contrast to the earlier model presented in [Weg22], which loses validity for screening parameters $\beta_\mathrm{L} > 0.6$, our approach extends the applicable range to the full practically relevant range up to $\beta_\mathrm{L} < 1$. This is achieved through a fully numerical calculation of the rf-SQUID current–flux relation and its time-dependent response to probe tones of arbitrary amplitude. We demonstrated that this numerical treatment significantly improves agreement with experimental data. In addition, the model allows for arbitrary current–phase relations of the Josephson junction forming the rf-SQUID. We used this capability to investigate the impact of a skewed current–phase relation arising from tunneling-barrier inhomogeneities in Josephson tunnel junctions. Such skewness modifies the µMUX characteristics in a way that resembles an increased screening parameter, yet produces distinct signatures that allow the two effects to be differentiated. Accurate modeling of barrier inhomogeneities is therefore essential for reliable µMUX characterization. By incorporating these effects, the model further improves agreement with measurements, both at low probe-tone powers and at power levels well above those typically used in µMUX readout. Overall, the developed framework provides a powerful tool for the design and analysis of future µMUX devices and is well suited for integration into simulation environments aimed at optimizing next-generation µMUX designs across the full relevant parameter space.

Finally, we presented a novel approach to improving µMUX noise performance by increasing the µMUX channels resonance frequencies. Using simulations based on our µMUX models, we evaluated device performance for resonance frequencies up to 50 GHz. These simulations show that merely increasing the operating frequency does not, by itself, reduce readout noise. However, if the expanded frequency range is exploited to increase the bandwidth per channel, a clear improvement in predicted noise performance emerges compared to current state-of-the-art devices. In addition to enhanced noise performance, such devices offer improved time resolution and higher multiplexing factors. Their reduced physical dimensions further facilitate the realization of large microcalorimeter arrays with near-complete focal-plane coverage. Electromagnetic simulations indicate that µMUX devices operating in the $\mathrm{K_u}$ frequency band (12–18 GHz) can already be made sufficiently compact to fit beneath a typical microcalorimeter absorber. We presented the design iterations leading to the first prototype µMUX operating above 16 GHz and demonstrated that its behavior is accurately captured by our µMUX models. A redesigned rf-SQUID enabled the realization of the first complete high-frequency µMUX devices incorporating both a modulation coil and an input coil, as required for practical detector readout. Based on this rf-SQUID design, we developed

two µMUX variants operating around 16 GHz: one employing a $\lambda/4$ resonator and one based on a lumped-element resonator. The latter achieves device dimensions smaller than those of a typical microcalorimeter absorber. Both device types were characterized, confirming the feasibility of K_u band µMUX operation and demonstrating excellent agreement with our models. Initial open-loop noise measurements yielded a flux noise level as low as $(0.27 \pm 0.01)\,\mu\Phi_0/\sqrt{\text{Hz}}$, comparable to state-of-the-art two-stage dc-SQUID systems [Man21] and to µMUX systems employing KITWPAs in the cryogenic chain [Mal23]. The measured noise was not limited by the amplifier noise temperature but instead by multiplicative noise contributions, suggesting that further improvements are achievable with an optimized measurement setup. This excellent noise performance, combined with the strong agreement between measurement and our µMUX models, confirms that K_u band µMUX devices are not only technically feasible but also a promising route toward future µMUX systems with lower readout noise, smaller device footprints, improved time resolution, and increased multiplexing capability.

In summary, this thesis established the complete development infrastructure for microwave SQUID multiplexers at IMS, spanning design tools, microfabrication processes, and the full cryogenic readout chain. Building on this foundation, we addressed several of the most significant challenges in current µMUX systems, identifying the dominant microwave power loss mechanisms and extending existing µMUX models to cover the full practically relevant parameter space. The deployed µMUX readout system enables large-scale, high-resolution MMC-based experiments. In combination with the demonstrated feasibility of operating µMUX devices in the K_u frequency band, these results contribute to the development of ultra-large-scale microcalorimeter arrays. They thereby support future experiments in fields such as particle physics, astrophysics, and materials science that require sub-electronvolt energy resolution, high statistics, or angular resolution.

A. Appendix

A.1 Current in the lumped-element resonator inductor

A.1.1 Induced current by a probe tone applied on-resonance

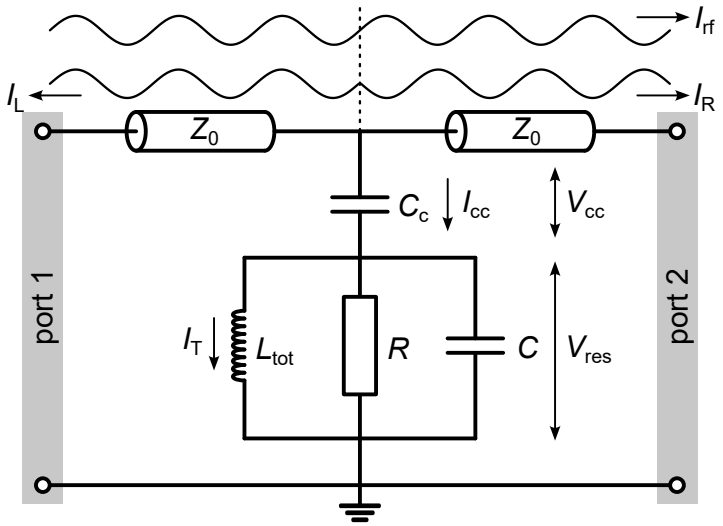

Fig. A.1: Equivalent circuit diagram of a lumped-element resonator.

Figure A.1 shows the equivalent circuit of a lumped-element resonator. The resonance frequency is given by

$$\omega_\mathrm{r} \approx \frac{1}{\sqrt{L_\mathrm{tot}(C + C_\mathrm{c})}} \tag{A.1}$$

and the coupling quality factor by

$$Q_\mathrm{c} = \frac{2}{Z_0 \omega_\mathrm{r}^3 L_\mathrm{tot} C_\mathrm{c}^2}. \tag{A.2}$$

At resonance, the energy stored within the resonator oscillates between the magnetic field in L_tot and the electric fields in C and C_c (assuming large R):

$$E_\mathrm{L} = E_\mathrm{C} + E_\mathrm{cc} \tag{A.3}$$

$$\frac{1}{2} L_\mathrm{tot} |I_\mathrm{T}|^2 = \frac{1}{2} C |V_\mathrm{res}|^2 + \frac{1}{2} C_\mathrm{c} |V_\mathrm{cc}|^2 \tag{A.4}$$

With $|V_\mathrm{res}| = \omega_\mathrm{r} L_\mathrm{tot} |I_\mathrm{T}|$ and $|V_\mathrm{cc}| = |I_\mathrm{cc}|/(\omega_\mathrm{r} C_\mathrm{c})$, we obtain:

$$\frac{1}{2}L_{\mathrm{tot}}|I_{\mathrm{T}}|^2 = \frac{1}{2}C\omega_{\mathrm{r}}^2 L_{\mathrm{tot}}^2|I_{\mathrm{T}}|^2 + \frac{1}{2}\frac{|I_{\mathrm{cc}}|^2}{\omega_{\mathrm{r}}^2 C_{\mathrm{c}}} \tag{A.5}$$

$$\Rightarrow \quad |I_{\mathrm{T}}|^2 = |I_{\mathrm{cc}}|^2 \frac{1}{\omega_{\mathrm{r}}^2 C_{\mathrm{c}} L_{\mathrm{tot}}(1-\omega_{\mathrm{r}}^2 LC)} \tag{A.6}$$

$$\Rightarrow \quad |I_{\mathrm{T}}| = |I_{\mathrm{cc}}| \frac{1}{\omega_{\mathrm{r}}^2 L_{\mathrm{tot}} C_{\mathrm{c}}} \tag{A.7}$$

To determine $|I_{\mathrm{cc}}|$, we analyze the current waves propagating along the feedline. At resonance, the resonator reflects the incident current waves, establishing a voltage node and a current antinode (in the ideal case of $Q_{\mathrm{i}} \to \infty$).

The various current waves are depicted in figure A.1. By symmetry, the two current waves I_{R} and I_{L} generated at the resonator must propagate identically to the left and to the right.

$$I_{\mathrm{L}} = I_{\mathrm{R}} \tag{A.8}$$

The total amplitude of the current exiting the resonator can therefore be expressed as

$$I_{\mathrm{cc}} = -(I_{\mathrm{L}} + I_{\mathrm{R}}) = -2I_{\mathrm{R}} \tag{A.9}$$

(The sign depends on the defined direction of I_{cc}.)

The third current wave propagates to the right from the source and is defined by the applied incident power.

$$I_{\mathrm{rf}} = \sqrt{\frac{2P_{\mathrm{rf}}}{Z_0}} = \frac{V_{\mathrm{rf}}}{Z_0} \tag{A.10}$$

with V_{rf} representing the equivalent incident voltage wave amplitude.

By definition, the scattering parameter is given by

$$S_{ij} = \frac{b_i}{a_j} \qquad \text{with} \quad a_k = 0 \quad \forall\, k \neq j \tag{A.11}$$

with a_i and b_i representing the incident and reflected power waves at port i.

$$a_i = \frac{V_i^+}{\sqrt{2Z_0}} = \sqrt{\frac{Z_0}{2}} I_i^+ \tag{A.12}$$

$$b_i = \frac{V_i^-}{\sqrt{2Z_0}} = \sqrt{\frac{Z_0}{2}} I_i^- \tag{A.13}$$

V_i^+ and V_i^- represent the incident and reflected voltage waves, respectively, while I_i^+ and I_i^- denote the incident and reflected current waves at port i.

In our circuit, we have

$$a_1 = \sqrt{P_{\mathrm{rf}}} = \frac{V_{\mathrm{rf}}}{\sqrt{2Z_0}} = \sqrt{\frac{Z_0}{2}} I_{\mathrm{rf}} \tag{A.14}$$

$$a_2 = 0 \tag{A.15}$$

$$b_1 = S_{11} a_1 \tag{A.16}$$

$$b_2 = S_{21} a_1 \tag{A.17}$$

On resonance, we have $S_{21}(\omega_{\mathrm{r}}) = S_{21}^{\mathrm{min}} \approx Q_{\mathrm{l}}/Q_{\mathrm{i}}$, resulting in

$$b_2(\omega_{\mathrm{r}}) = S_{21}^{\mathrm{min}} a_1 = \frac{Q_{\mathrm{l}}}{Q_{\mathrm{i}}} \sqrt{\frac{Z_0}{2}} I_{\mathrm{rf}} \tag{A.18}$$

However, by definition, b_2 is also expressed through I_2^-, which represents the sum of the wave I_{rf} and I_{R}:

$$b_2(\omega_{\mathrm{r}}) = \sqrt{\frac{Z_0}{2}} I_2^- = \sqrt{\frac{Z_0}{2}} (I_{\mathrm{rf}} + I_{\mathrm{R}}) = \sqrt{\frac{Z_0}{2}} (I_{\mathrm{rf}} - \frac{I_{\mathrm{cc}}}{2}) \tag{A.19}$$

Using equations A.18 and A.19 we get

$$\sqrt{\frac{Z_0}{2}} (I_{\mathrm{rf}} - \frac{I_{\mathrm{cc}}}{2}) = \frac{Q_{\mathrm{l}}}{Q_{\mathrm{i}}} \sqrt{\frac{Z_0}{2}} I_{\mathrm{rf}} \tag{A.20}$$

$$\Rightarrow I_{\mathrm{cc}} = 2 \left(1 - \frac{Q_{\mathrm{l}}}{Q_{\mathrm{i}}} \right) I_{\mathrm{rf}} \tag{A.21}$$

$$= 2 \frac{Q_{\mathrm{l}}}{Q_{\mathrm{c}}} \frac{V_{\mathrm{rf}}}{Z_0} \tag{A.22}$$

Inserting equation A.22 into equation A.7 yields

$$|I_{\mathrm{T}}| = 2 \frac{Q_{\mathrm{l}} |V_{\mathrm{rf}}|}{Q_{\mathrm{c}} \omega_{\mathrm{r}}^2 L_{\mathrm{tot}} C_{\mathrm{c}} Z_0} \tag{A.23}$$

Using the definition of Q_{c}, we get

$$|I_\mathrm{T}| = 2|V_\mathrm{rf}|\sqrt{\frac{Q_\mathrm{l}^2}{Q_\mathrm{c}^2\omega_\mathrm{r}^4 L_\mathrm{tot}^2 C_\mathrm{c}^2 Z_0^2}} \tag{A.24}$$

$$= 2|V_\mathrm{rf}|\sqrt{\frac{Q_\mathrm{l}^2}{2Q_\mathrm{c}\omega_\mathrm{r} L_\mathrm{tot} Z_0}} \tag{A.25}$$

$$= \sqrt{4\frac{Q_\mathrm{l}^2}{Q_\mathrm{c}}\frac{P_\mathrm{rf}}{\omega_\mathrm{r} L_\mathrm{tot}}} \tag{A.26}$$

This equation is identical to the one found in [Ahr22], differing only by a factor of 2.

A.1.2 Induced current by a probe tone applied off-resonance

Using equations A.14, A.17, and A.19 we can derive the relation

$$I_\mathrm{cc} = 2(1 - S_{21})I_\mathrm{rf} \tag{A.27}$$

between the amplitude I_rf of the incoming current wave and the amplitude I_cc of the current in the coupling capacitor.

Using Kirchhoff's law, we can relate the currents in the lumped elements of the resonator

$$I_\mathrm{cc} = I_\mathrm{T} + I_\mathrm{loss} + I_\mathrm{C} \tag{A.28}$$

$$I_\mathrm{T} = \frac{V_\mathrm{res}}{i\omega L_\mathrm{tot}} \tag{A.29}$$

$$I_\mathrm{loss} = \frac{V_\mathrm{res}}{R} \tag{A.30}$$

$$I_\mathrm{C} = i\omega C V_\mathrm{res}. \tag{A.31}$$

Here, I_T, I_loss, and I_C denote the currents in the resonators inductor L_tot, resistor R, and capacitor C, respectively. ω is the frequency of the applied probe tone and V_res is the voltage across the resonator without the coupling capacitor.

Using equations A.28 to A.31 and the relation $Q_\mathrm{i} = R/(\omega L)$ for the intrinsic quality factor of lumped-element resonators, we obtain

$$I_\mathrm{T} = \frac{I_\mathrm{cc}}{1 - \omega^2 L_\mathrm{tot} C + i/Q_\mathrm{i}} \tag{A.32}$$

$$= \frac{2(1 - S_{21})I_\mathrm{rf}}{1 - \omega^2 L_\mathrm{tot} C + i/Q_\mathrm{i}}. \tag{A.33}$$

By inserting equation 2.20 and using equation A.2 to eliminate C from the expression,

we obtain

$$I_{\mathrm{T}} = 2\frac{Q_{\mathrm{l}}}{Q_{\mathrm{c}}}\frac{1}{\left(1+2iQ_{\mathrm{l}}\left(\frac{\omega}{\omega_{\mathrm{r}}}-1\right)\right)\left(1-\frac{\omega^2}{\omega_{\mathrm{r}}^2}+\omega^2\sqrt{\frac{2L_{\mathrm{tot}}}{Z_0\omega_{\mathrm{r}}^3Q_{\mathrm{c}}}}+\frac{i}{Q_{\mathrm{i}}}\right)}\frac{V_{\mathrm{rf}}}{Z_0}. \tag{A.34}$$

On resonance, i.e. $\omega = \omega_{\mathrm{r}}$, and for large intrinsic quality factors Q_{i}, this expression simplifies to equation A.23.

A.2 Controller circuit of the cryogenic rf-switches

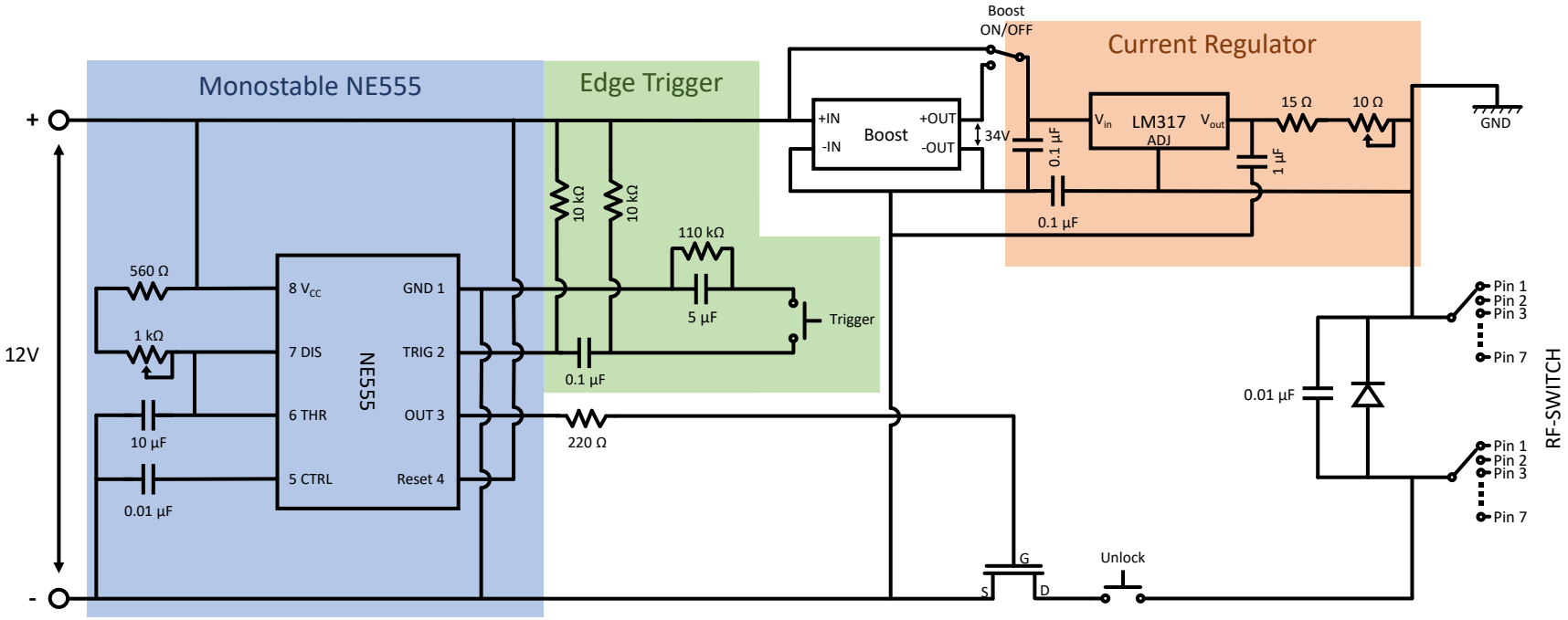

Fig. A.2: Equivalent circuit diagram of the controller for the latching rf-switches used in the cryogenic readout chain. The controller operates at room temperature and drives the rf-switches by applying current pulses of approximately $\sim 62.5\,\mathrm{mA}$ with durations below 15 ms to the switch pins. The pulse duration is set by a monostable NE555 circuit, while the current amplitude is limited by a simple LM317-based current regulator. A pulse is initiated by the trigger button and is applied to the rf-switch only when the unlock button is pressed simultaneously. The pulse height and duration can be adjusted by the variable resistors in the monostable NE555 circuit and LM317-based current regulator. While a supply voltage of 12 V is sufficient for switching at millikelvin temperatures, a boost converter is required for operation at room temperature due to the residual resistivity ratio of the latching switch coils ($RRR \approx 100$), where the coil resistance exceeds $500\,\Omega$.

A.3 Effective load impedance under the influence of the input circuit

The load inductor coupled to the rf-SQUID and input coil forms a circuit, as shown in figure A.3, with an effective load impedance $Z_{\mathrm{L,eff}}(\varphi_{\mathrm{tot}})$ that depends on the total flux $\varphi_{\mathrm{tot}} = 2\pi\Phi_{\mathrm{tot}}/\Phi_0$ through the rf-SQUID. To derive the effective load impedance, we express the voltage across each inductor as:

$$V_{\mathrm{T}} = i\omega L_{\mathrm{T}} I_{\mathrm{T}} + i\omega M_{\mathrm{T}} I_{\mathrm{S}} + i\omega M_{\mathrm{p}} I_{\mathrm{in}} \tag{A.35}$$

$$V_{\mathrm{S}} = i\omega L_{\mathrm{S}} I_{\mathrm{S}} + i\omega M_{\mathrm{T}} I_{\mathrm{T}} + i\omega M_{\mathrm{in}} I_{\mathrm{in}} = -Z_{\mathrm{JJ}}(\varphi_{\mathrm{tot}}) I_{\mathrm{S}} \tag{A.36}$$

$$V_{\mathrm{in}} = i\omega L_{\mathrm{in}} I_{\mathrm{in}} + i\omega M_{\mathrm{p}} I_{\mathrm{T}} + i\omega M_{\mathrm{in}} I_{\mathrm{S}} = -Z_{\mathrm{in}} I_{\mathrm{in}} \tag{A.37}$$

Where $Z_{\mathrm{JJ}}(\varphi_{\mathrm{tot}})$ denotes the junction impedance and Z_{in} the impedance of the filter resistor and detector shunting the input coil. Using this set of equations, we can derive the effective load impedance as $Z_{\mathrm{L,eff}} = V_{\mathrm{T}}/I_{\mathrm{T}}$, yielding:

$$Z_{\mathrm{L,eff}}(\varphi_{\mathrm{tot}}) = i\omega \left(L_{\mathrm{T}} - \frac{M_{\mathrm{p}}^2 (L_{\mathrm{S}} + \frac{Z_{\mathrm{JJ}}(\varphi_{\mathrm{tot}})}{i\omega}) + M_{\mathrm{T}}^2 (L_{\mathrm{in}} + \frac{Z_{\mathrm{in}}}{i\omega}) - 2M_{\mathrm{in}} M_{\mathrm{T}} M_{\mathrm{p}}}{(L_{\mathrm{S}} + \frac{Z_{\mathrm{JJ}}(\varphi_{\mathrm{tot}})}{i\omega})(L_{\mathrm{in}} + \frac{Z_{\mathrm{in}}}{i\omega}) - M_{\mathrm{in}}^2} \right) \tag{A.38}$$

It is important to note that this solution does not account for the modulation coil. However, the influence of the input coil, due to its stronger magnetic coupling, is typically expected to be the dominant factor affecting the load impedance.

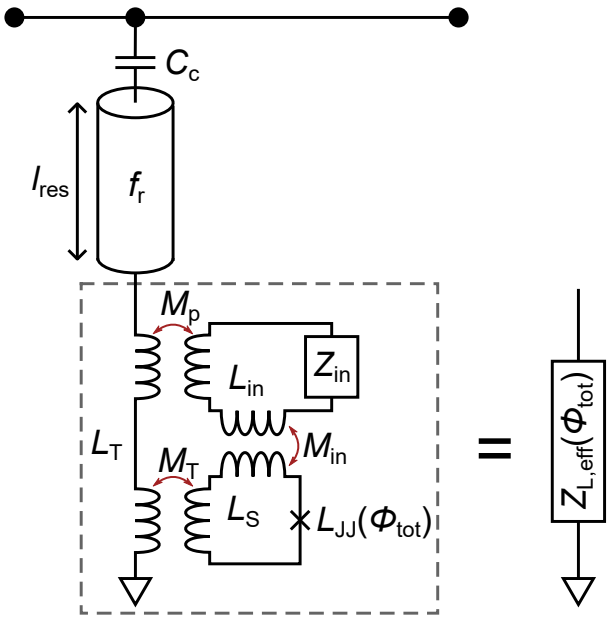

Fig. A.3: Equivalent circuit diagram of a single µMUX channel. The load inductor coupled to the rf-SQUID and input circuit forms an effective flux dependent load impedance $Z_{\mathrm{L,eff}}(\Phi_{\mathrm{tot}})$.

A.4 Influence of the filter resistor

When assuming an ideal Josephson junction we can describe the junction impedance Z_{JJ} in equation A.38 with the inductance $L_{\mathrm{JJ}}(\varphi_{\mathrm{tot}}) = \Phi_0/(2\pi I_{\mathrm{c}} \cos(\varphi_{\mathrm{tot}}))$ yielding:

$$Z_{\mathrm{L,eff}}(\varphi_{\mathrm{tot}}) = i\omega \left(L_{\mathrm{T}} - \frac{M_{\mathrm{p}}^2 L_{\mathrm{SQ}} + M_{\mathrm{T}}^2 (L_{\mathrm{in}} + \frac{Z_{\mathrm{in}}}{i\omega}) - 2M_{\mathrm{in}} M_{\mathrm{T}} M_{\mathrm{p}}}{L_{\mathrm{SQ}} (L_{\mathrm{in}} + \frac{Z_{\mathrm{in}}}{i\omega}) - M_{\mathrm{in}}^2} \right) \tag{A.39}$$

$$= i\omega \left(L_{\mathrm{T}} - \frac{\begin{array}{c}(M_{\mathrm{p}}^2 L_{\mathrm{SQ}} + M_{\mathrm{T}}^2 (L_{\mathrm{in}} + \frac{\Im[Z_{\mathrm{in}}]}{\omega}) - 2M_{\mathrm{in}} M_{\mathrm{T}} M_{\mathrm{p}} - iM_{\mathrm{T}}^2 \frac{\Re[Z_{\mathrm{in}}]}{\omega}) \\ \cdot (L_{\mathrm{SQ}} (L_{\mathrm{in}} + \frac{\Im[Z_{\mathrm{in}}]}{\omega}) - M_{\mathrm{in}}^2 + iL_{\mathrm{SQ}} \frac{\Re[Z_{\mathrm{in}}]}{\omega})\end{array}}{(L_{\mathrm{SQ}} (L_{\mathrm{in}} + \frac{\Im[Z_{\mathrm{in}}]}{\omega}) - M_{\mathrm{in}}^2)^2 + (L_{\mathrm{SQ}} \frac{\Re[Z_{\mathrm{in}}]}{\omega})^2} \right) \tag{A.40}$$

with

$$L_{\mathrm{SQ}} = L_{\mathrm{S}} (1 + \frac{Z_{\mathrm{JJ}}}{i\omega}) = L_{\mathrm{S}} (1 + (\beta_{\mathrm{L}} \cos(\varphi_{\mathrm{tot}}))^{-1}) \tag{A.41}$$

if we only connect a filter resistor to the input coil ($Z_{\mathrm{in}} = R_{\mathrm{f}}$) the expression simplifies to

$$Z_{\mathrm{L,eff}} = i\omega \left(L_{\mathrm{T}} - \frac{(M_{\mathrm{p}}^2 L_{\mathrm{SQ}} + M_{\mathrm{T}}^2 L_{\mathrm{in}} - 2M_{\mathrm{in}} M_{\mathrm{T}} M_{\mathrm{p}} - iM_{\mathrm{T}}^2 \frac{R_{\mathrm{f}}}{\omega})(L_{\mathrm{SQ}} L_{\mathrm{in}} - M_{\mathrm{in}}^2 + iL_{\mathrm{SQ}} \frac{R_{\mathrm{f}}}{\omega})}{(L_{\mathrm{SQ}} L_{\mathrm{in}} - M_{\mathrm{in}}^2)^2 + (L_{\mathrm{SQ}} \frac{R_{\mathrm{f}}}{\omega})^2} \right) \tag{A.42}$$

We can use the real part of this expression to calculate the effect on the intrinsic quality factor with:

$$Q_{\mathrm{f}}(\varphi_{\mathrm{tot}}) = \frac{\pi Z_0}{4\Re[Z_{\mathrm{L,eff}}(\varphi_{\mathrm{tot}})]} \approx \frac{\pi Z_0}{4R_{\mathrm{f}}} \frac{(L_{\mathrm{in}} L_{\mathrm{SQ}}(\varphi_{\mathrm{tot}}) - M_{\mathrm{in}}^2)^2}{M_{\mathrm{T}}^2 M_{\mathrm{in}}^2 + L_{\mathrm{SQ}}(\varphi_{\mathrm{tot}})(M_{\mathrm{p}}^2 L_{\mathrm{SQ}}(\varphi_{\mathrm{tot}}) - 2M_{\mathrm{in}} M_{\mathrm{T}} M_{\mathrm{p}})} \tag{A.43}$$

The imaginary part on the other hand yields the effective load inductance with:

$$L_{\mathrm{T,eff}}(\varphi_{\mathrm{tot}}) = \frac{\Im[Z_{\mathrm{L,eff}}(\varphi_{\mathrm{tot}})]}{\omega} \tag{A.44}$$

$$= L_{\mathrm{T}} - \frac{(M_{\mathrm{p}}^2 L_{\mathrm{SQ}} + M_{\mathrm{T}}^2 L_{\mathrm{in}} - 2M_{\mathrm{in}} M_{\mathrm{T}} M_{\mathrm{p}})(L_{\mathrm{SQ}} L_{\mathrm{in}} - M_{\mathrm{in}}^2) + L_{\mathrm{SQ}} M_{\mathrm{T}}^2 \frac{R_{\mathrm{f}}^2}{\omega^2}}{(L_{\mathrm{SQ}} L_{\mathrm{in}} - M_{\mathrm{in}}^2)^2 + (L_{\mathrm{SQ}} \frac{R_{\mathrm{f}}}{\omega})^2} \tag{A.45}$$

In the limit of large filter resistors ($R_{\mathrm{f}} \to \infty$), corresponding to an open input circuit, the last terms in both the numerator and the denominator dominate, yielding the well-known expression

$$L_{\mathrm{T,eff}}(\varphi_{\mathrm{tot}}) = L_{\mathrm{T}} - \frac{M_{\mathrm{T}}^2}{L_{\mathrm{S}}} \frac{\beta_{\mathrm{L}} \cos(\varphi_{\mathrm{tot}})}{1 + \beta_{\mathrm{L}} \cos(\varphi_{\mathrm{tot}})} \tag{A.46}$$

However, the filter resistor is typically selected to be small, ensuring that the cut-off frequency ω_{c} is significantly lower than the resonance frequency ω_{r} of the µMUX:

$$\omega_{\mathrm{c}} = \frac{R_{\mathrm{f}}}{L_{\mathrm{in}}} \ll \omega_{\mathrm{r}} \tag{A.47}$$

Using ω_{c}, we obtain:

$$L_{\mathrm{T,eff}}(\varphi_{\mathrm{tot}}) = L_{\mathrm{T}} - \frac{(M_{\mathrm{p}}^2 L_{\mathrm{SQ}} + M_{\mathrm{T}}^2 L_{\mathrm{in}} - 2M_{\mathrm{in}} M_{\mathrm{T}} M_{\mathrm{p}})(L_{\mathrm{SQ}} L_{\mathrm{in}} - M_{\mathrm{in}}^2) + \frac{\omega_{\mathrm{c}}^2}{\omega^2} L_{\mathrm{SQ}} M_{\mathrm{T}}^2 L_{\mathrm{in}}^2}{(L_{\mathrm{SQ}} L_{\mathrm{in}} - M_{\mathrm{in}}^2)^2 + \frac{\omega_{\mathrm{c}}^2}{\omega^2} L_{\mathrm{SQ}}^2 L_{\mathrm{in}}^2} \tag{A.48}$$

Taking into account that $\omega_{\mathrm{c}}^2/\omega^2 \ll 1$ we can neglect the last terms in both the numerator and denominator, resulting in:

$$L_{\mathrm{T,eff}}(\varphi_{\mathrm{tot}}) \approx L_{\mathrm{T}} - \frac{M_{\mathrm{p}}^2 L_{\mathrm{SQ}} + M_{\mathrm{T}}^2 L_{\mathrm{in}} - 2M_{\mathrm{in}} M_{\mathrm{T}} M_{\mathrm{p}}}{L_{\mathrm{SQ}} L_{\mathrm{in}} - M_{\mathrm{in}}^2} \tag{A.49}$$

$$= L_{\mathrm{T}} - \frac{M_{\mathrm{p}}^2 L_{\mathrm{S}} + \beta_{\mathrm{L}} \cos(\varphi_{\mathrm{tot}})(M_{\mathrm{p}}^2 L_{\mathrm{S}} + M_{\mathrm{T}}^2 L_{\mathrm{in}} - 2M_{\mathrm{in}} M_{\mathrm{T}} M_{\mathrm{p}})}{L_{\mathrm{S}} L_{\mathrm{in}} + \beta_{\mathrm{L}} \cos(\varphi_{\mathrm{tot}})(L_{\mathrm{S}} L_{\mathrm{in}} - M_{\mathrm{in}}^2)} \tag{A.50}$$

Bibliography

[Ada24] F. Adam, C. Enss, S. Kempf, Anodization-free fabrication process for high-quality cross-type Josephson tunnel junctions based on a Nb/Al-AlO_x/Nb trilayer, *Supercond. Sci. Technol.*, **37**(8), 085013, 2024, doi:10.1088/1361-6668/ad59cf.

[Agr25] A. Agrawal, V. V. Alenkov, P. Aryal, J. Beyer *et al.*, Improved limit on neutrinoless double beta decay of ^{100}Mo from AMoRE-I, *Phys. Rev. Lett.*, **134**(8), 082501, 2025, doi:10.1103/PhysRevLett.134.082501.

[Ahr22] F. K. Ahrens, *Cryogenic read-out system and resonator optimisation for the microwave SQUID multiplexer within the ECHo experiment*, Dissertation, University of Heidelberg, 2022, doi:10.11588/heidok.00032038.

[Aka23] H. Akamatsu, W. B. Doriese, J. A. B. Mates, B. D. Jackson *et al.*, Signal readout for transition-edge sensor X-ray imaging spectrometers, in *Handbook of X-ray and Gamma-ray Astrophysics*, 1–48, Springer Nature Singapore, Singapore, 2023, doi:10.1007/978-981-16-4544-0_24-1.

[Alp25] B. K. Alpert, M. Balata, D. T. Becker, D. A. Bennett *et al.*, Most stringent bound on electron neutrino mass obtained with a scalable low-temperature microcalorimeter array, *Phys. Rev. Lett.*, **135**(14), 141801, 2025, doi:10.1103/s9vl-7n24.

[And72] P. W. Anderson, B. I. Halperin, C. M. Varma, Anomalous low-temperature thermal properties of glasses and spin glasses, *The Philosophical Magazine: A Journal of Theoretical Experimental and Applied Physics*, **25**(1), 1–9, 1972, doi:10.1080/14786437208229210.

[Ash76] N. W. Ashcroft, N. D. Mermin, *Solid State Physics*, Saunders College Publishing, 1976.

[Bah03] I. Bahl, *Lumped elements for RF and microwave circuits*, Microwave Library, Artech House, Norwood, MA, 2003.

[Bar57] J. Bardeen, L. N. Cooper, J. R. Schrieffer, Theory of superconductivity, *Phys. Rev.*, **108**(5), 1175–1204, 1957, doi:10.1103/PhysRev.108.1175.

[Bar09] R. Barends, *Photon-detecting superconducting resonators*, Dissertation, Technische Universiteit Delft, 2009.

[Bar11] R. Barends, J. Wenner, M. Lenander, Y. Chen *et al.*, Minimizing quasiparticle generation from stray infrared light in superconducting quantum circuits, *Appl. Phys. Lett.*, **99**(11), 113507, 2011, doi:10.1063/1.3638063.

[Bau22] F. Bauer, *Rauscharme Stromsensor-dc-SQUIDs mit Impedanzanpassung für metallische magnetische Kalorimeter*, Dissertation, University of Heidelberg, 2022, doi:10.11588/heidok.00032001.

[Ben19] D. A. Bennett, J. A. B. Mates, S. R. Bandler, D. T. Becker *et al.*, Microwave SQUID multiplexing for the Lynx x-ray microcalorimeter, *J. Astron. Telesc. Instrum. Syst.*, **5**(02), 1, 2019, doi:10.1117/1.JATIS.5.2.021007.

[Bot11] D. Bothner, T. Gaber, M. Kemmler, D. Koelle *et al.*, Improving the performance of superconducting microwave resonators in magnetic fields, *Appl. Phys. Lett.*, **98**(10), 102504, 2011, doi:10.1063/1.3560480.

[Bur08] A. Burck, *Entwicklung großflächiger mikrostrukturierter magnetischer Kalorimeter mit Au:Er- und Ag:Er-Sensoren für den energieaufgelösten Nachweis von Röntgenquanten und hochenergetischen Teilchen*, Dissertation, University of Heidelberg, 2008, doi:10.11588/heidok.00008832.

[Che99] J. A. Chervenak, K. D. Irwin, E. N. Grossman, J. M. Martinis *et al.*, Superconducting multiplexer for arrays of transition edge sensors, *Applied Physics Letters*, **74**(26), 4043–4045, 1999, doi:10.1063/1.123255.

[Cla04] J. Clarke, A. I. Braginski, *The SQUID handbook: Fundamentals and technology of SQUIDs and SQUID systems v. 1*, The SQUID Handbook. Set, Wiley-VCH Verlag, Weinheim, Germany, 2004.

[Col00] R. E. Collin, *Foundations for Microwave Engineering*, IEEE Press Series on Electromagnetic Wave Theory, John Wiley & Sons, Nashville, TN, 2 edition, 2000.

[Cro12] M. Croce, M. Bacrania, E. Bond, D. Dry *et al.*, Ultra-high resolution alpha particle spectrometry with transition-edge sensor microcalorimeters, *J. Low Temp. Phys.*, **167**(5-6), 955–960, 2012, doi:10.1007/s10909-011-0419-0.

[Dem20] H. Dembinski, P. Ongmongkolkul, C. Deil, H. Schreiner *et al.*, scikit-hep/iminuit, 2020, doi:10.5281/zenodo.3949207.

[Dob21] B. Dober, Z. Ahmed, K. Arnold, D. T. Becker *et al.*, A microwave SQUID multiplexer optimized for bolometric applications, *Appl. Phys. Lett.*, **118**(6), 062601, 2021, doi:10.1063/5.0033416.

[Dor06] W. Doriese, J. Beall, W. Duncan, L. Ferreira *et al.*, Progress toward kilopixel arrays: 3.8eV microcalorimeter resolution in 8-channel SQUID multiplexer, *Nuclear Instruments and Methods in Physics Research Section A: Accelerators, Spectrometers, Detectors and Associated Equipment*, **559**(2), 808–810,

2006, Proceedings of the 11th International Workshop on Low Temperature Detectors, doi:10.1016/j.nima.2005.12.146.

[Dor16] W. B. Doriese, K. M. Morgan, D. A. Bennett, E. V. Denison *et al.*, Developments in Time-Division Multiplexing of X-ray Transition-Edge Sensors, *Journal of Low Temperature Physics*, **184**, 389–395, 2016, doi:10.1007/s10909-015-1373-z.

[Dru07] D. Drung, C. Abmann, J. Beyer, A. Kirste *et al.*, Highly Sensitive and Easy-to-Use SQUID Sensors, *IEEE Transactions on Applied Superconductivity*, **17**(2), 699–704, 2007, doi:10.1109/TASC.2007.897403.

[Eom12] B. H. Eom, P. K. Day, H. G. LeDuc, J. Zmuidzinas *et al.*, A wideband, low-noise superconducting amplifier with high dynamic range, *Nat. Phys.*, **8**(8), 623–627, 2012, doi:10.1038/nphys2356.

[Fag06] R. L. Fagaly, Superconducting quantum interference device instruments and applications, *Review of Scientific Instruments*, **77**(10), 101101, 2006, doi:10.1063/1.2354545.

[Far24] F. Faramarzi, R. Stephenson, S. Sypkens, B. H. Eom *et al.*, A 4–8 GHz kinetic inductance traveling-wave parametric amplifier using four-wave mixing with near quantum-limited noise performance, *APL Quantum*, **1**(3), 036107, 2024, doi:10.1063/5.0208110.

[Fit21] R. P. Fitzgerald, B. K. Alpert, D. T. Becker, D. E. Bergeron *et al.*, Toward a new primary standardization of radionuclide massic activity using microcalorimetry and quantitative milligram-scale samples, *J. Res. Natl. Inst. Stand. Technol.*, **126**(126048), 126048, 2021, doi:10.6028/jres.126.048.

[Fle05] A. Fleischmann, C. Enss, G. Seidel, *Metallic Magnetic Calorimeters*, 151–216, Springer Berlin Heidelberg, Berlin, Heidelberg, 2005, doi:10.1007/10933596_4.

[Fri44] H. T. Friis, Noise Figures of Radio Receivers, *Proc. IRE*, **32**(7), 419–422, 1944, doi:10.1109/JRPROC.1944.232049.

[Gao07] J. Gao, J. Zmuidzinas, B. A. Mazin, H. G. LeDuc *et al.*, Noise properties of superconducting coplanar waveguide microwave resonators, *Applied Physics Letters*, **90**(10), 102507, 2007, doi:10.1063/1.2711770.

[Gao08a] J. Gao, *The Physics of Superconducting Microwave Resonators*, Dissertation, California Institute of Technology, 2008.

[Gao08b] J. Gao, M. Daal, J. M. Martinis, A. Vayonakis *et al.*, A semiempirical model for two-level system noise in superconducting microresonators, *Appl. Phys. Lett.*, **92**(21), 212504, 2008, doi:10.1063/1.2937855.

[Gao08c] J. Gao, M. Daal, A. Vayonakis, S. Kumar *et al.*, Experimental evidence for a surface distribution of two-level systems in superconducting lithographed microwave resonators, *Appl. Phys. Lett.*, **92**(15), 152505, 2008, doi:10.1063/1.2906373.

[Gar22] R. Gartmann, N. Karcher, R. Gebauer, O. Krömer *et al.*, Progress of the ECHo SDR Readout Hardware for Multiplexed MMCs, *Journal of Low Temperature Physics*, **209**, 726–733, 2022, doi:10.1007/s10909-022-02854-1.

[Gas17] L. Gastaldo, K. Blaum, K. Chrysalidis, T. Day Goodacre *et al.*, The electron capture in 163Ho experiment – ECHo, *European Physical Journal: Special Topics*, **226**(8), 1623–1694, 2017, doi:10.1140/epjst/e2017-70071-y.

[Gia24] A. Giachero, M. Vissers, J. Wheeler, L. Howe *et al.*, Kinetic inductance traveling wave amplifier designs for practical microwave readout applications, *J. Low Temp. Phys.*, **215**(3-4), 152–160, 2024, doi:10.1007/s10909-024-03078-1.

[Glo57] R. E. Glover, M. Tinkham, Conductivity of superconducting films for photon energies between 0.3 and $40kT_c$, *Phys. Rev.*, **108**(2), 243–256, 1957, doi:10.1103/PhysRev.108.243.

[Goe16] J. Goetz, F. Deppe, M. Haeberlein, F. Wulschner *et al.*, Loss mechanisms in superconducting thin film microwave resonators, *J. Appl. Phys.*, **119**(1), 015304, 2016, doi:10.1063/1.4939299.

[Gro25] J. C. Groh, Z. Ahmed, J. Austermann, J. Beall *et al.*, Demonstration of a 1820 channel multiplexer for transition-edge sensor bolometers, *Appl. Phys. Lett.*, **127**(15), 2025, doi:10.1063/5.0290914.

[Häh20] S. Hähnle, N. v. Marrewijk, A. Endo, K. Karatsu *et al.*, Suppression of radiation loss in high kinetic inductance superconducting co-planar waveguides, *Appl. Phys. Lett.*, **116**(18), 182601, 2020, doi:10.1063/5.0005047.

[Ham24] M. Hampel, A. Almela, J. Bonaparte, J. B. Neira *et al.*, The magnetic microbolometer: A proposal for QUBIC next gen, *J. Low Temp. Phys.*, **217**(3-4), 401–408, 2024, doi:10.1007/s10909-024-03203-0.

[Hau23] L. Hauswald, *Characterization of superconducting microwave resonators for quantum sensing applications*, Master's thesis, Karlsruhe Institute of Technology, 2023.

[Hay24] R. Hayakawa, D. Fukuda, K. Hattori, F. Hirayama *et al.*, Demonstration of simultaneous optical transition-edge sensors readout using microwave SQUID multiplexer with 5 MHz flux ramp modulation, *J. Low Temp. Phys.*, **215**(3-4), 170–176, 2024, doi:.1007/s10909-024-03080-7.

[Hir13] F. Hirayama, S. Kohjiro, D. Fukuda, H. Yamamori *et al.*, Microwave SQUID Multiplexer for TES Readout, *IEEE Transactions on Applied Superconductivity*, **23**(3), 2500405–2500405, 2013, doi:10.1109/tasc.2012.2237474.

[Hir17] F. Hirayama, T. Irimatsugawa, H. Yamamori, S. Kohjiro *et al.*, Interchannel Crosstalk and Nonlinearity of Microwave SQUID Multiplexers, *IEEE Trans. Appl. Supercond.*, **27**(4), 1–5, 2017, doi:10.1109/TASC.2016.2638082.

[Hoe64] B. J. C. v. d. Hoeven, P. H. Keesom, Specific heat of niobium between 0.4 and 4.2°K, *Phys. Rev.*, **134**(5A), A1320–A1321, 1964, doi:10.1103/PhysRev.134.A1320.

[Irw04] K. D. Irwin, K. W. Lehnert, Microwave SQUID multiplexer, *Applied Physics Letters*, **85**(11), 2107–2109, 2004, doi:10.1063/1.1791733.

[Irw05] G. Irwin, K.D.and Hilton, *Transition-Edge Sensors*, 63–150, Springer Berlin Heidelberg, Berlin, Heidelberg, 2005, doi:10.1007/10933596_3.

[Irw09] K. D. Irwin, Shannon Limits for Low-Temperature Detector Readout, *AIP Conference Proceedings*, **1185**(1), 229–236, 2009, doi:10.1063/1.3292320.

[Irw10] K. D. Irwin, M. D. Niemack, J. Beyer, H. M. Cho *et al.*, Code-division multiplexing of superconducting transition-edge sensor arrays, *Superconductor Science and Technology*, **23**(3), 034004, 2010, doi:10.1088/0953-2048/23/3/034004.

[Jon24] D. Jones, R. Singh, J. Austermann, J. A. Beall *et al.*, Qualification of microwave SQUID multiplexer chips for Simons Observatory, *J. Low Temp. Phys.*, **216**(1-2), 50–56, 2024, doi:10.1007/s10909-024-03102-4.

[Jos62] B. D. Josephson, Possible new effects in superconductive tunnelling, *Phys. Lett.*, **1**(7), 251–253, 1962, doi:10.1016/0031-9163(62)91369-0.

[Jos64] B. D. Josephson, Coupled Superconductors, *Rev. Mod. Phys.*, **36**(1), 216–220, 1964, doi:10.1103/RevModPhys.36.216.

[Jun09] H. Jung, Y. Kim, K. Jung, H. Im *et al.*, Potential barrier modification and interface states formation in metal-oxide-metal tunnel junctions, *Phys. Rev. B*, **80**, 125413, 2009, doi:10.1103/PhysRevB.80.125413.

[Kar22] N. Karcher, *Ausleseelektronik für magnetische Mikrokalorimeter im Frequenzmultiplexverfahren*, Dissertation, Karlsruher Institut für Technologie (KIT), 2022, doi:10.5445/IR/1000148040.

[Kau78] R. L. Kautz, Picosecond pulses on superconducting striplines, *J. Appl. Phys.*, **49**(1), 308–314, 1978, doi:10.1063/1.324387.

[Kem12] S. Kempf, *Entwicklung eines Mikrowellen-SQUID-Multiplexers auf der Grundlage nicht-hysteretischer rf-SQUIDs zur Auslesung metallischer magnetischer Kalorimeter*, Dissertation, Heidelberg University Library, 2012, doi:10.11588/heidok.00013620.

[Kem16] S. Kempf, A. Ferring, C. Enss, Towards noise engineering: Recent insights in low-frequency excess flux noise of superconducting quantum devices, *Appl. Phys. Lett.*, **109**(16), 162601, 2016, doi:10.1063/1.4965293.

[Kem17a] S. Kempf, M. Wegner, L. Deeg, A. Fleischmann *et al.*, Design, fabrication and characterization of a 64 pixel metallic magnetic calorimeter array with integrated, on-chip microwave SQUID multiplexer, *Supercond. Sci. Technol.*, **30**(6), 065002, 2017, doi:10.1088/1361-6668/aa6d17.

[Kem17b] S. Kempf, M. Wegner, A. Fleischmann, L. Gastaldo *et al.*, Demonstration of a scalable frequency-domain readout of metallic magnetic calorimeters by means of a microwave SQUID multiplexer, *AIP Adv.*, **7**(1), 015007, 2017, doi:10.1063/1.4973872.

[Kem18] S. Kempf, A. Fleischmann, L. Gastaldo, C. Enss *et al.*, Physics and Applications of Metallic Magnetic Calorimeters, *Journal of Low Temperature Physics*, 1–15, 2018, doi:10.1007/s10909-018-1891-6.

[Ker18] S. A. Kernasovskiy, S. E. Kuenstner, E. Karpel, Z. Ahmed *et al.*, SLAC microresonator radio frequency (SMuRF) electronics for read out of frequency-division-multiplexed cryogenic sensors, *J. Low Temp. Phys.*, **193**(3-4), 570–577, 2018, doi:10.1007/s10909-018-1981-5.

[Kim18] G. B. Kim, C. C. Flynn, S. Kempf, L. Gastaldo *et al.*, Development of MMC Gamma Detectors for Precise Characterization of Uranium Isotopes, *Journal of Low Temperature Physics*, **193**(5), 1236–1242, 2018, doi:10.1007/s10909-018-1978-0.

[Kim23] H. Kim, Y.-H. Kim, K.-R. Woo, Cryogenic particle detection based on magnetic microcalorimeters for rare event searches, *Eur. Phys. J. Plus*, **138**(6), 2023, doi:10.1140/epjp/s13360-023-04068-0.

[Koc07] R. H. Koch, D. P. DiVincenzo, J. Clarke, Model for $1/f$ Flux noise in SQUIDs and qubits, *Phys. Rev. Lett.*, **98**(26), 2007, doi:10.1103/PhysRevLett.98.267003.

[Koh14] S. Kohjiro, F. Hirayama, H. Yamamori, S. Nagasawa *et al.*, White noise of Nb-based microwave superconducting quantum interference device multiplexers with NbN coplanar resonators for readout of transition edge sensors, *J. Appl. Phys.*, **115**(22), 223902, 2014, doi:10.1063/1.4882118.

[Kov25] N. Kovač, F. Adam, S. Kempf, M.-C. Langer *et al.*, Comparison of the detector response and calibration function of metallic microcalorimeters for X-ray photons and external electrons, *Nucl. Instrum. Methods Phys. Res. A*, **1080**(170662), 170662, 2025, doi:10.1016/j.nima.2025.170662.

[Koz12] A. Kozorezov, Energy down-conversion and thermalization in metal absorbers, *J. Low Temp. Phys.*, **167**(3-4), 473–484, 2012, doi:10.1007/s10909-011-0426-1.

[Kra88] J. D. Kraus, *Antennas*, McGraw-Hill, Inc, 2 edition, 1988.

[Kra24] M. Krantz, F. Toschi, B. Maier, G. Heine *et al.*, Magnetic microcalorimeter with paramagnetic temperature sensors and integrated dc-SQUID readout for high-resolution x-ray emission spectroscopy, *Applied Physics Letters*, **124**(3), 032601, 2024, doi:10.1063/5.0180903.

[Kro23] B. von Krosigk, K. Eitel, C. Enss, T. Ferber *et al.*, DELight: A Direct search Experiment for Light dark matter with superfluid helium, *SciPost Phys. Proc.*, 016, 2023, doi:10.21468/SciPostPhysProc.12.016.

[Kum08] S. Kumar, J. Gao, J. Zmuidzinas, B. A. Mazin *et al.*, Temperature dependence of the frequency and noise of superconducting coplanar waveguide resonators, *Appl. Phys. Lett.*, **92**(12), 123503, 2008, doi:10.1063/1.2894584.

[Li18] D. Li, B. K. Alpert, D. T. Becker, D. A. Bennett *et al.*, TES X-ray spectrometer at SLAC LCLS-II, *J. Low Temp. Phys.*, **193**(5-6), 1287–1297, 2018, doi:10.1007/s10909-018-2053-6.

[Lik86] K. K. Likharev, *Dynamics of Josephson junctions and circuits*, Taylor & Francis, London, England, 1986.

[Loh24] L. F. Lohrke, *Optimierung von supraleitenden Resonatoren für SQUID-basierte Multiplexverfahren*, Bachelor's thesis, Karlsruhe Institute of Technology, 2024.

[Maa22] A. Maatz, *Entwicklung und Charakterisierung von supraleitenden Resonatoren für die Quantensensorik*, Master's thesis, Karlsruhe Institute of Technology, 2022.

[Mac10] P. Macha, S. H. W. van der Ploeg, G. Oelsner, E. Il'ichev *et al.*, Losses in coplanar waveguide resonators at millikelvin temperatures, *Appl. Phys. Lett.*, **96**(6), 062503, 2010, doi:10.1063/1.3309754.

[Mal21] M. Malnou, M. Vissers, J. Wheeler, J. Aumentado *et al.*, Three-Wave Mixing Kinetic Inductance Traveling-Wave Amplifier with Near-Quantum-Limited Noise Performance, *PRX Quantum*, **2**, 010302, 2021, doi:10.1103/PRXQuantum.2.010302.

[Mal23] M. Malnou, J. A. B. Mates, M. R. Vissers, L. R. Vale *et al.*, Improved microwave SQUID multiplexer readout using a kinetic-inductance traveling-wave parametric amplifier, *Applied Physics Letters*, **122**(21), 214001, 2023, doi:10.1063/5.0149646.

[Man21] F. Mantegazzini, S. Allgeier, A. Barth, C. Enss *et al.*, Multichannel read-out for arrays of metallic magnetic calorimeters, *J. Instrum.*, **16**(08), P08003, 2021, doi:10.1088/1748-0221/16/08/P08003.

[Man25] A. Mangu, B. Westbrook, S. Beckman, L. Corbett *et al.*, The Simons Observatory: Design, optimization, and performance of low-frequency detectors, *J. Low Temp. Phys.*, **218**(1-2), 21–28, 2025, doi:10.1007/s10909-024-03234-7.

[Mat58] D. C. Mattis, J. Bardeen, Theory of the anomalous skin effect in normal and superconducting metals, *Phys. Rev.*, **111**(2), 412–417, 1958, doi:10.1103/PhysRev.111.412.

[Mat08] J. A. B. Mates, G. C. Hilton, K. D. Irwin, L. R. Vale *et al.*, Demonstration of a multiplexer of dissipationless superconducting quantum interference devices, *Applied Physics Letters*, **92**(2), 023514, 2008, doi:10.1063/1.2803852.

[Mat11] J. A. B. Mates, *The Microwave SQUID Multiplexer*, Dissertation, University of Colorado, 2011.

[Mat12] J. A. Mates, K. D. Irwin, L. R. Vale, G. C. Hilton *et al.*, Flux-ramp modulation for SQUID multiplexing, *Journal of Low Temperature Physics*, **167**(5-6), 707–712, 2012, doi:10.1007/s10909-012-0518-6.

[Mat17] J. A. B. Mates, D. T. Becker, D. A. Bennett, B. J. Dober *et al.*, Simultaneous readout of 128 X-ray and gamma-ray transition-edge microcalorimeters using microwave SQUID multiplexing, *Applied Physics Letters*, **111**(6), 062601, 2017, doi:10.1063/1.4986222.

[Mat19] J. A. B. Mates, D. T. Becker, D. A. Bennett, B. J. Dober *et al.*, Crosstalk in microwave SQUID multiplexers, *Appl. Phys. Lett.*, **115**(20), 202601, 2019, doi:10.1063/1.5116573.

[Maz04] B. A. Mazin, *Microwave Kinetic Inductance Detectors*, Dissertation, California Institute of Technology, 2004.

[Maz06] B. A. Mazin, P. K. Day, K. D. Irwin, C. D. Reintsema *et al.*, Digital readouts for large microwave low-temperature detector arrays, *Nucl. Instrum. Methods Phys. Res. A*, **559**(2), 799–801, 2006, doi:10.1016/j.nima.2005.12.208.

[McC21] H. McCarrick, E. Healy, Z. Ahmed, K. Arnold *et al.*, The Simons Observatory microwave SQUID multiplexing detector module design, *Astrophys. J.*, **922**(1), 38, 2021, doi:10.3847/1538-4357/ac2232.

[McR20] C. R. H. McRae, H. Wang, J. Gao, M. R. Vissers *et al.*, Materials loss measurements using superconducting microwave resonators, *Rev. Sci. Instrum.*, **91**(9), 091101, 2020, doi:10.1063/5.0017378.

[Mül24] M. Müller, M. Rodrigues, J. Beyer, M. Loidl *et al.*, Magnetic microcalorimeters for primary activity standardization within the EMPIR project PrimA-LTD, *Journal of Low Temperature Physics*, 1–9, 2024, doi:10.1007/s10909-024-03048-7.

[Mül25] M. Müller, *Magnetische Mikrokalorimeter für die Aktivitätsstandardisierung und die Messung fundamentaler Zerfallsdaten in der Radionuklidmetrologie*, Dissertation, Karlsruher Institut für Technologie (KIT), 2025, doi:10.5445/IR/1000181097.

[Mus24] T. Muscheid, R. Gartmann, N. Karcher, F. Schuderer *et al.*, Full-Scale Readout Electronics for the ECHo Experiment, *Journal of Low Temperature Physics*, **217**, 456–463, 2024, doi:10.1007/s10909-024-03213-y.

[Nak19] Y. Nakashima, F. Hirayama, S. Kohjiro, H. Yamamori *et al.*, Investigation of large coupling between TES X-ray microcalorimeter and microwave multiplexer based on microstrip SQUID, *IEEE Trans. Appl. Supercond.*, **29**(5), 1–5, 2019, doi:10.1109/TASC.2019.2905688.

[Nak20] Y. Nakashima, F. Hirayama, S. Kohjiro, H. Yamamori *et al.*, Low-noise microwave SQUID multiplexed readout of 38 x-ray transition-edge sensor microcalorimeters, *Appl. Phys. Lett.*, **117**(12), 2020, doi:10.1063/5.0016333.

[Nar20] M. Naruse, M. Kuwata, T. Ando, Y. Waga *et al.*, Niobium-based kinetic inductance detectors for high-energy applications, *IEICE Trans. Electron.*, **E103.C**(5), 204–211, 2020, doi:10.1587/transele.2019SEI0001.

[Nei25a] M. Neidig, T. Muscheid, R. Gartmann, L. E. A. Perez *et al.*, Full-scale microwave SQUID multiplexer readout system for magnetic microcalorimeters, 2025, arXiv:2509.07671, doi:10.48550/arXiv.2509.07671.

[Nei25b] M. Neidig, M. Wegner, S. Kempf, Advanced microwave SQUID multiplexer model incorporating readout power effects and Josephson junction inhomogeneities, 2025, arXiv:2512.09600, doi:10.48550/arXiv.2512.09600.

[Nie10] M. D. Niemack, J. Beyer, H. M. Cho, W. B. Doriese *et al.*, Code-division SQUID multiplexing, *Applied Physics Letters*, **96**(16), 163509, 2010, doi:10.1063/1.3378772.

[Nsa14] I. Nsanzineza, B. L. T. Plourde, Trapping a single vortex and reducing quasiparticles in a superconducting resonator, *Phys. Rev. Lett.*, **113**(11), 117002, 2014, doi:10.1103/PhysRevLett.113.117002.

[Phi87] W. A. Phillips, Two-level states in glasses, *Rep. Prog. Phys.*, **50**(12), 1657–1708, 1987, doi:10.1088/0034-4885/50/12/003.

[Poz98] D. M. Pozar, *Microwave Engineering*, John Wiley & Sons, Inc., 4 edition, 1998.

[Pro15] S. Probst, F. B. Song, P. A. Bushev, A. V. Ustinov *et al.*, Efficient and robust analysis of complex scattering data under noise in microwave resonators, *Rev. Sci. Instrum.*, **86**(2), 024706, 2015, doi:10.1063/1.4907935.

[Qui14] C. M. Quintana, A. Megrant, Z. Chen, A. Dunsworth *et al.*, Characterization and reduction of microfabrication-induced decoherence in superconducting quantum circuits, *Appl. Phys. Lett.*, **105**(6), 062601, 2014, doi:10.1063/1.4893297.

[Rea20] T. M. Reader, U. Hanke, E. Halvorsen, T. Grande *et al.*, A unified approach for the calculation of in-plane dielectric constant of films with interdigitated electrodes, *Smart Mater. Struct.*, **29**(11), 115039, 2020, doi:10.1088/1361-665X/abb4b9.

[Red24] M. E. G. Redondo, N. A. Müller, J. M. Salum, L. P. Ferreyro *et al.*, Optimal demodulation domain for microwave SQUID multiplexers in presence of readout system noise, *J. Appl. Phys.*, **136**(11), 2024, doi:10.1063/5.0222656.

[Ric21a] D. Richter, L. Hoibl, T. Wolber, N. Karcher *et al.*, Flux ramp modulation based MHz frequency-division dc-SQUID multiplexer, *Applied Physics Letters*, **118**(12), 122601, 2021, doi:10.1063/5.0044444.

[Ric21b] D. P. Richter, *Multikanal-Auslesung von metallischen magnetischen Kalorimetern mittels eines vollständigen Mikrowellen-SQUID-Multiplexer-Systems*, Dissertation, University of Heidelberg, 2021, doi:10.11588/heidok.00030266.

[Ric23] D. Richter, M. Wegner, F. Ahrens, C. Enss *et al.*, Simultaneous MMC Readout Using a Tailored μMUX Based Readout System, *IEEE Transactions on Applied Superconductivity*, **33**(5), 1–5, 2023, doi:10.1109/TASC.2023.3264200.

[Rip02] W. H. Rippard, A. C. Perrella, F. J. Albert, R. A. Buhrman *et al.*, Ultrathin Aluminum Oxide Tunnel Barriers, *Phys. Rev. Lett.*, **88**, 046805, 2002, doi:10.1103/PhysRevLett.88.046805.

[Rog03] J. Rogers, C. Plett, *Radio Frequency Integrated Circuit Design*, Microwave Library, Artech House, Norwood, MA, 2003.

[Rot18] J. Rothe, G. Angloher, P. Bauer, A. Bento *et al.*, TES-Based Light Detectors for the CRESST Direct Dark Matter Search, *Journal of Low Temperature Physics*, **193**(5), 1160–1166, 2018, doi:10.1007/s10909-018-1944-x.

[Saa25] Y. Saad, Acceleration methods for fixed-point iterations, *Acta Numer.*, **34**, 805–890, 2025, doi:10.1017/S0962492924000096.

[Sag11] J. M. Sage, V. Bolkhovsky, W. D. Oliver, B. Turek *et al.*, Study of loss in superconducting coplanar waveguide resonators, *J. Appl. Phys.*, **109**(6), 063915, 2011, doi:10.1063/1.3552890.

[San19] O. Sander, N. Karcher, O. Kromer, S. Kempf *et al.*, Software-Defined Radio Readout System for the ECHo Experiment, *IEEE Transactions on Nuclear Science*, **PP**, 1–1, 2019, doi:10.1109/TNS.2019.2914665.

[Sch22] C. Schuster, M. Wegner, C. Enss, S. Kempf *et al.*, Flux ramp modulation based hybrid microwave SQUID multiplexer, *Applied Physics Letters*, **120**(16), 162601, 2022, doi:10.1063/5.0087994.

[Sch23a] F. Schuderer, *SDR Electronics Based Readout of a Microwave SQUID Multiplexer*, Master's thesis, Karlsruhe Institute of Technology, 2023.

[Sch23b] C. Schuster, M. Wegner, S. Kempf, Simulation framework for microwave SQUID multiplexer optimization, *Journal of Applied Physics*, **133**(4), 044503, 2023, doi:10.1063/5.0135124.

[Sch25] M. Schmelz, E. Heinz, K. Peiselt, G. Zieger *et al.*, Scalable Microwave SQUID Multiplexer Readout Architecture for TES-Based THz Security Camera, *IEEE Transactions on Applied Superconductivity*, **35**(3), 1–5, 2025, doi:10.1109/TASC.2025.3545212.

[She17] S. Sheldon, M. Sandberg, H. Paik, B. Abdo *et al.*, Characterization of hidden modes in networks of superconducting qubits, *Appl. Phys. Lett.*, **111**(22), 222601, 2017, doi:10.1063/1.4990033.

[Sim01] R. N. Simons, *Coplanar Waveguide Circuits, Components, and Systems*, Wiley Series in Microwave and Optical Engineering, John Wiley & Sons, Nashville, TN, 2001.

[Son09] C. Song, T. W. Heitmann, M. P. DeFeo, K. Yu *et al.*, Microwave response of vortices in superconducting thin films of Re and Al, *Phys. Rev. B Condens. Matter Mater. Phys.*, **79**(17), 2009, doi:10.1103/PhysRevB.79.174512.

[Sta04] G. Stan, S. B. Field, J. M. Martinis, Critical field for complete vortex expulsion from narrow superconducting strips, *Phys. Rev. Lett.*, **92**(9), 097003, 2004, doi:10.1103/PhysRevLett.92.097003.

[Ste02] L. Stephan, J. P. Coupez, E. Rius, C. Person *et al.*, Integration of various types of compensated dielectric bridges for mm coplanar applications, in *1996 IEEE MTT-S International Microwave Symposium Digest*, IEEE, 2002, doi:10.1109/MWSYM.1996.508468.

[Ste19] T. R. Stevenson, M. A. Balvin, S. R. Bandler, A. M. Devasia *et al.*, Magnetic calorimeter option for the Lynx x-ray microcalorimeter, *J. Astron. Telesc. Instrum. Syst.*, **5**(02), 1, 2019, doi:10.1117/1.JATIS.5.2.021009.

[Szy23] P. Szypryt, N. Nakamura, D. T. Becker, D. A. Bennett *et al.*, A tabletop X-ray tomography instrument for nanometer-scale imaging: Demonstration of the 1,000-element transition-edge sensor subarray, *IEEE Trans. Appl. Supercond.*, **33**(5), 1–5, 2023, doi:10.1109/TASC.2023.3256343.

[Tol16] S. Tolpygo, V. Bolkhovsky, T. Weir, A. Wynn *et al.*, Advanced fabrication processes for superconducting very large scale integrated circuits, *IEEE Trans. Appl. Supercond.*, 1–1, 2016, doi:10.1109/TASC.2016.2519388.

[Ull15] J. N. Ullom, D. A. Bennett, Review of superconducting transition-edge sensors for x-ray and gamma-ray spectroscopy, *Superconductor Science and Technology*, **28**(8), 084003, 2015, doi:10.1088/0953-2048/28/8/084003.

[Vén18] D. Vénos, J. Sentkerestiová, O. Dragoun, M. Slezák *et al.*, Properties of83mKrconversion electrons and their use in the KATRIN experiment, *J. Instrum.*, **13**(02), T02012–T02012, 2018, doi:10.1088/1748-0221/13/02/T02012.

[Vis14] P. J. d. Visser, D. J. Goldie, P. Diener, S. Withington *et al.*, Evidence of a nonequilibrium distribution of quasiparticles in the microwave response of a superconducting aluminum resonator, *Phys. Rev. Lett.*, **112**(4), 047004, 2014, doi:10.1103/PhysRevLett.112.047004.

[Weg18] M. Wegner, *Entwicklung, Herstellung und Charakterisierung eines auf metallischen magnetischen Kalorimetern basierenden Detektorarrays mit 64 Pixeln und integriertem Mikrowellen-SQUID-Multiplexer*, Dissertation, University of Heidelberg, 2018, doi:10.11588/heidok.00025741.

[Weg22] M. Wegner, C. Enss, S. Kempf, Analytical model of the readout power and SQUID hysteresis parameter dependence of the resonator characteristics of microwave SQUID multiplexers, *Superconductor Science and Technology*, **35**(7), 075011, 2022, doi:10.1088/1361-6668/ac6d15.

[Wel67] P. D. Welch, The Use of Fast Fourier Transform for the Estimation of Power Spectra: A Method Based on Time Averaging Over Short, Modified Periodograms, *IEEE Transactions on Audio and Electroacoustics*, **15**, 70–73, 1967, doi:10.1109/TAU.1967.1161901.

[Wel04] F. C. Wellstood, C. Urbina, J. Clarke, Flicker (1/f) noise in the critical current of Josephson junctions at 0.09–4.2K, *Appl. Phys. Lett.*, **85**(22), 5296–5298, 2004, doi:10.1063/1.1826236.

[Wen11] J. Wenner, M. Neeley, R. C. Bialczak, M. Lenander *et al.*, Wirebond crosstalk and cavity modes in large chip mounts for superconducting qubits, *Supercond. Sci. Technol.*, **24**(6), 065001, 2011, doi:10.1088/0953-2048/24/6/065001.

[Wil24] D. Willsch, D. Rieger, P. Winkel, M. Willsch *et al.*, Observation of Josephson harmonics in tunnel junctions, *Nature Physics*, **20**(5), 815–821, 2024, doi:10.1038/s41567-024-02400-8.

[Yoo01] J. Yoon, J. Clarke, J. M. Gildemeister, A. T. Lee *et al.*, Single superconducting quantum interference device multiplexer for arrays of low-temperature sensors, *Applied Physics Letters*, **78**(3), 371–373, 2001, doi:10.1063/1.1338963.

[Yos20] D. R. W. Yost, M. E. Schwartz, J. Mallek, D. Rosenberg *et al.*, Solid-state qubits integrated with superconducting through-silicon vias, *Npj Quantum Inf.*, **6**(1), 2020, doi:10.1038/s41534-020-00289-8.

[Yu23] C. Yu, Z. Ahmed, J. C. Frisch, S. W. Henderson *et al.*, SLAC microresonator RF (SMuRF) electronics: A tone-tracking readout system for superconducting microwave resonator arrays, *Rev. Sci. Instrum.*, **94**(1), 014712, 2023, doi:10.1063/5.0125084.

[Zmu12] J. Zmuidzinas, Superconducting Microresonators: Physics and Applications, *Annual Review of Condensed Matter Physics*, **3**(1), 169–214, 2012, doi:10.1146/annurev-conmatphys-020911-125022.

Acknowledgments

During my time as a PhD student, I experienced the steepest learning curve of my life. This journey brought its share of struggles and challenges that I might not have overcome without the many people who supported me along the way.

First, I want to express my deepest gratitude to my supervisor, Prof. Dr. Sebastian Kempf, for giving me the opportunity to work on such a fascinating topic. Your extensive expertise and invaluable guidance, paired with the freedom to pursue my own ideas, enabled my personal growth while simultaneously allowing me to achieve concrete results in my project.

I especially want to thank my fellow PhD students, Constantin, Michael, Lena, Nik, Friedrich, Jesús, Nahuel, and Juan Ma, as well as Mathias and Fabienne: for all the fruitful and productive conversations, as well as those of a more entertaining nature; for the many fun movie and game nights; for making sure I eat my fair share of healthy and unhealthy snacks at the office; and for the unforgettable experiences around many conferences. Thank you for listening to my complaints whenever my perfect experimental setups failed or the computer refused to understand my perfect code, and for enduring my uninvited vocal performances. You made my time at IMS the most enjoyable.

I also thank the other employees at IMS: Alexander Stassen for his reliable support with any technical issue related to our deposition chambers, Stefan Ziegler and the workshop team for the fabrication and solution oriented approach to all of my mechanical setups, Frank Ruhnau for the fast and extensive IT related support, Stefan Wünsch for the many helpful microwave electronics related conversations, and Doris Duffner and Helga Scherer for supporting me in anything related to administration, where I was usually clueless.

I am grateful for the many talented students that I had the honor of supervising during my time at IMS. Without your contributions, the scope of my thesis would not have been possible. I also thank my fellow PhD students at IPE, Timo and Robert, for providing the SDR system and helping me set it up, as well as for the quick answers to any related questions I had.

Special thanks go to the graduate school KSETA for funding a large part of my work during my thesis and offering workshops and courses, where I got to expand my scientific horizon and meet lots of interesting people.

Finally, I want to thank my parents for always supporting me, not only during my time as a Ph.D. student, but throughout my life. You sparked my interest in physics early on and enabled me to pursue my studies in the first place. Thank you for everything!